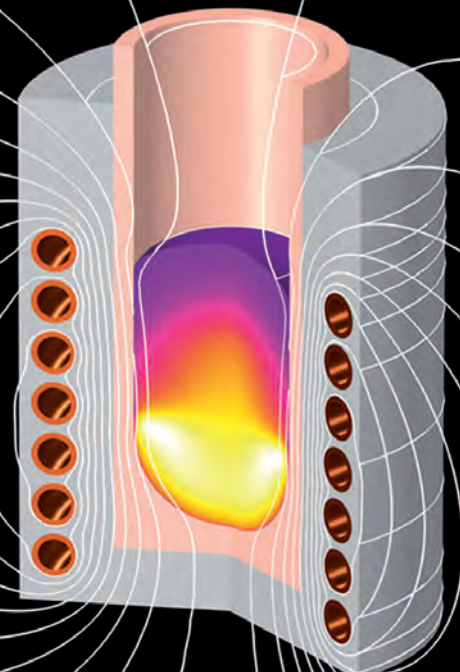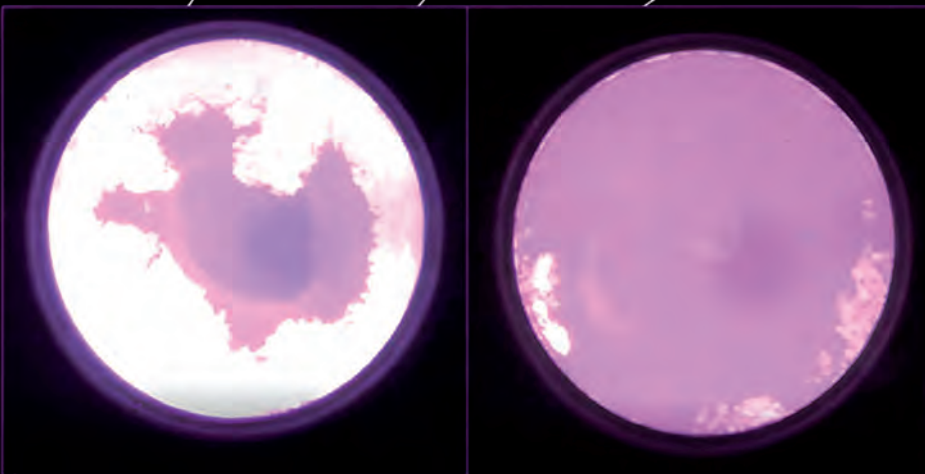**Mondragon
Unibertsitatea**

DOCTORAL THESIS

ENHANCEMENT OF VACUUM INDUCTION MELTING THROUGH NUMERICAL
AND EXPERIMENTAL INVESTIGATION

PABLO GARCIA MICHELENA | Arrasate-Mondragón, 2023

PhD Course in Applied Engineering

Enhancement of Vacuum Induction Melting through Numerical and Experimental Investigation

Pablo García Michelena

Supervised by:

Dr. Xabier Chamorro Sánchez

Dr. Nuria Herrero Dorca

Dr. Emilio Ruiz Reina

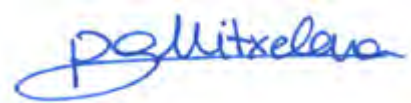Mechanical and industrial production department

Mondragon Unibertsitatea

July 2023

Declaration of Originality

I hereby declare that this thesis, and the work presented in it with its results, were carried out entirely by me at the Mechanical and Manufacturing Department of the University of Mondragon's Polytechnic School. All sources, references, and literature used during the elaboration of this work are properly cited and listed in complete reference to the due source.

Pablo García Michelena

July 2023

Copyright and reproduction rights

Agradecimientos

Cuando comencé con la tesis, me advirtieron que sería una maratón a ritmo de sprint. En mi caso, ha sido más bien un "*tappone*" de 250 km de longitud con 5 puertos de montaña. Ahora que estoy llegando a la "*flame rouge*" o último kilómetro, me gustaría expresar mis agradecimientos.

En primer lugar, dar las gracias a mis directores, el Dr. Xabier Chamorro, la Dra. Nuria Herrero y el Dr. Emilio Ruiz-Reina, quienes, con su conocimiento y perspectiva en sus respectivos campos de especialización, han contribuido a la realización de esta tesis. Además, quisiera destacar que la dirección de una tesis no se limita únicamente al aspecto técnico, sino que también implica una dimensión humana, por el cual me siento especialmente agradecido.

También me gustaría agradecer por los recursos materiales y económicos proporcionados por el departamento de Mecánica y Producción Industrial de MGEP. Especialmente, quiero agradecer a todo el equipo de Fundi-NSF por tratarme como a uno más del equipo.

De igual manera, quiero expresar mi reconocimiento hacia el personal del departamento de tecnología de ITP Casting por su contribución a este trabajo facilitando información relevante y compartir su conocimiento.

A mis camaradas, Dani, Olaia, Andrea y Juanjo les agradezco todas las largas horas que hemos compartido en el laboratorio de conformado de Garaia, ya sea cocinando aleaciones, calibrando pirómetros o simplemente intentando escribir una página más de la tesis. De igual manera a todos los compañeros de la sala de doctorandos, tanto aquellos que han llegado antes a la meta como aquellos que aún están pedaleando.

No puedo olvidarme de mis queridos Pipas, Juantxo y Chache, quienes siempre encuentran una razón para reír y me han ayudado a afrontar el doctorado de una manera positiva y alegre. Agradezco de corazón el moscatel de Chipiona. A ustedes señores Doctores, amantes del mar y la playa, quiero recordarles que siempre tendrán un amigo y un hogar en Zarautz.

Euskarara pasatuz, nire eskerrik zintzoenak eman nahiko nizkieke kuadrilako lagunei, ez dutenek oraindik oso argi tesian zertan nabilen beti arazo berri batekin nabileko.

Amaierarako onena utzita, bihotzez eskertzen diot familiari azken urteotan emandako babesa eta laguntza. Nire osabei, Pablori eta Enriqueri, zientziarekiko eta teknologiarekiko jakin-mina pizteagatik; Amari eta Aitari eman didaten maitasunagatik eta heziketagatik, baita nire erabaki guztietan erakutsi duten aintzatespenagatik eta babesagatik ere; Ainhoari, anaia nagusiari eman dizkion gomendio guztiengatik, eta, akatsak egin ditudanean konpontzen lagundu izanagatik.

Eta Garaziri, zer esan eta dena ezin esan… zuk inork baina hobeto dakizu helmugara iristea kostatu zaidana, une oro nire alboan pedalei eragiten egon zarena, aldapan gora bultzatu nauena eta erori naizenean jaikitzen lagundu nauena, zu zara bidelagun hoberena.

Eskerrik asko!

Abstract

The aeronautic industry is renowned for its remarkable level of innovation and development of products and processes. A constant pursuit in this field is enhancing the thermodynamic efficiency of engine cycles through the utilization of high-performance materials like nickel-based alloys in turbine and compressor components. The complex and precise chemical composition of these alloys necessitates advanced manufacturing processes. To achieve components of superior metallurgical quality with complex geometries and near-net-shaped criteria, the investment casting technology and Vacuum Induction Melting (VIM) are effectively combined.

The success of VIM technology lies in its vacuum atmosphere, which minimizes oxidation and the removal of alloying chemical elements from the liquid metal, ensuring precise composition of the final component. Moreover, it achieves high electrical efficiency through magnetic induction and resistive heating within the metal, along with rapid melting cycles. Although, the complex control of the process is challenging due to the coexistence of multiple physical phenomena during melting and various process variables, hindering the process improvement. In this field, numerical tools based on models are the optimal choice due to their balance between accuracy, speed, and cost.

This research project aims to enhance the VIM process by developing multi-physics models encompassing the main physical phenomena, including magnetic fields, fluid dynamics, and heat transfer, in a coupled manner. These models will be integrated and capture the interactions between these different fields while also allowing for the study of the impact of various process variables and deepening the understanding of VIM technology.

To validate the theoretical studies, a comparison with experimental references is necessary. Therefore, specific experimental tests have been designed and conducted at the laboratory-scale VIM furnace to obtain real process references. In this manner, it has been possible to correlate with the numerical results and determine the uncertainty of the simulations. Once the validated tool is obtained, several case studies have been considered, incorporating different configurations of industrial-scale VIM furnaces and dynamic operating conditions based on real melting procedures. Finally, an improved melting procedure is proposed, aiming to increase thermal efficiency and reduce the process cycle time.

Resumen

La industria aeronáutica es reconocida por su notable nivel de innovación y desarrollo continuo de sus productos y procesos. En este campo, se persigue constantemente mejorar la eficiencia termodinámica de los ciclos de los motores mediante el uso de materiales de alto rendimiento, como las aleaciones base de níquel en los componentes de la turbina y compresor. La composición química compleja y precisa de estas aleaciones requiere procesos de fabricación avanzadas. Para lograr componentes de calidad metalúrgica superior, con geometrías complejas y criterios cercanos a la forma final, se combinan de manera efectiva las tecnologías de moldeo a la cera perdida y la fusión por inducción en vacío o Vacuum Induction Melting (VIM).

El éxito de la tecnología VIM radica en su atmósfera de vacío e inerte, que minimiza la oxidación y la eliminación de elementos aleantes del metal líquido, asegurando una composición precisa del componente final. Además, logra una alta eficiencia eléctrica mediante la inducción magnética y el calentamiento resistivo dentro del propio metal a fundir, junto con ciclos de fusión rápidos. Sin embargo, el control complejo del proceso presenta desafíos debido a la coexistencia de múltiples fenómenos físicos durante la fusión y diversas variables del proceso, dificultando la optimización del proceso. En este campo, las herramientas numéricas basadas en modelos es la solución óptima debido a su equilibrio entre precisión, velocidad y coste.

El objetivo de este proyecto de investigación es mejorar el proceso de fusión VIM mediante el desarrollo de modelos multi-físicos que abarquen los principales fenómenos físicos, incluyendo campos magnéticos, dinámica de fluidos y transferencia de calor y el acoplamiento entre las mismas. Estos modelos integrarán y capturarán las interacciones entre estos diferentes campos, permitiendo también el estudio del impacto de diversas variables del proceso, así como ahondar en la compresión de las dinámicas internas del proceso VIM.

Para validar los estudios teóricos, es necesaria una comparación y correlación con referencias experimentales. Por lo tanto, se han diseñado y realizado ensayos específicos en un horno VIM a escala de laboratorio para obtener referencias reales del proceso. Así, se han correlacionado con los resultados numéricos y determinado la incertidumbre de las simulaciones, pudiendo corregir la desviación en los casos necesarios. Una vez obtenida la herramienta validada, se han considerado varios casos de estudio, incorporando diferentes configuraciones de hornos VIM a escala industrial y condiciones operativas dinámicas basadas en condiciones operativas reales de fusión. En última instancia, se propone un procedimiento de fusión mejorado con el objetivo de aumentar la eficiencia térmica y reducir el tiempo del ciclo del proceso.

Laburpena

Industria aeronautikoa bere produktuen eta prozesuen etengabeko berrikuntza eta garapen maila nabarmenagatik aintzatesten da. Arlo horretan, hegazkin motorren ziklo termodinamikoaren eraginkortasuna etengabe hobetu nahi da, errendimendu handiko materialak erabiliz, hala nola nikel-oinarrizko superaleazioak turbina eta konpresoreen osagarrientzako. Nikel aleazio horien konposizio kimiko konplexu eta zehatzak fabrikazio metodo aurreratuak eskatzen ditu. Kalitate metalurgiko handiagoko osagaiak lortzeko, geometria konplexuekin eta azken formatik hurbil dauden irizpideekin, modu eraginkorrean konbinatzen dira argizari galduan moldekatzeko teknologiak eta hutsean indukzio bidezko fusioa edo Vacuum Induction Melting (VIM).

VIM teknologiaren arrakasta bere hutseko atmosfera eta inertean datza, metal likidoaren elementu aleatzaileen oxidazioa eta deuseztapena minimizatzen dituena, metalaren konposizio zehatza ziurtatuz. Gainera, eraginkortasun elektriko handia lortzen du indukzio magnetikoaren bitartez izan ere urtu beharreko metala zuzenean berotzen da energia elektrikoa bero erresistiboa bilakatuz eta horrela fusio ziklo azkarrak lortuaz. Hala ere, prozesuaren kontrol konplexuak erronkak ditu, fusioan zehar hainbat fenomeno fisiko eta prozesuaren hainbat aldagai batera ematen direlako honek prozesuaren optimizazioa zailtzen duelarik. Eremu honetan, modeloetan oinarritutako erremienta numerikoak dira soluziorik onena, doitasunaren, abiaduraren eta kostuaren arteko oreka dela eta.

Ikerketa-proiektu honen helburua VIM fusio-prozesua hobetzean datza, fenomeno fisiko nagusiak barne hartzen dituzten modelo multi-fisikoak garatuz, eremu magnetikoak, fluidoen dinamika eta bero-transferentzia. Modelo horiek eremu horien arteko elkarrekintzak modu integratu batean erreproduzituko dituzte, eta, era berean, prozesuko hainbat aldagairen inpaktua aztertzea eta VIM teknologiaren konpresioan sakontzea ahalbidetuko dute.

Emaitza numeriko teorikoak balioztatzeko, erreferentzia esperimentalekin alderatzea eta korrelazioa nahitaezkoa da. Horretarako, laborategiko eskalako VIM labe batean entsegu espezifikoak diseinatu eta burutu dira. Prozesuaren erreferentzia esperimental hauekin emaitza numerikoak alderatu izan dira eta simulazioen ziurgabetasuna zehaztu, eta behar izandako kasuetan errorea zuzenduz. Balioztatutako tresna definitu ondoren, hainbat estudio-kasu hartu dira kontuan, industria-eskalako VIM labeen konfigurazio desberdinak eta fusio prozedura errealetan oinarritutako baldintza operatibo dinamikoak ikertuaz. Azken batean, fusio prozedura hobetua proposatzen da, eraginkortasun termikoa handitzeko eta prozesuaren zikloaren denbora murrizteko.

List of Contents

List of Figures

List of Tables

List of Symbols

Notation	Unit	Description	Notation	Unit	Description
Latin Symbols					
A	Wb/m	Magnetic vector potential	**K**	Pa	Viscous stress tensor
A	m^2	Boundaries Area	L	H	Inductance
B	T	Magnetic flux density	L_0	V^2/K^2	Lorenz number
C_μ	-	Turbulence modeling constant	l_w	mm	Wall distance
C_p	J/ kg · K	Heat Capacity	l_c^*	-	Distance to cell center in viscous units
D	m	Distance	$\dot{m}$	kg/s	Mass flow rate
D	C/m^2	Electric displacement	n	-	Refractive index
e_b	W/m^2	Blackbody total emissive power	**n**	-	Normal vector
E	V/m	Electric field intensity	p	Pa	Pressure
F	-	View factor	P	kW	Power
$\mathbf{F_L}$	N/m^3	Lorentz volumetric force vector	**q**	W/m^2	Heat flux
$\mathbf{F_s}$	N/m^3	Surface tension force	Q	W/m^3	Heat source
g	m/s^2	Acceleration of gravity	r	mm	r-coordinate position
G	W/m^2	Surface irradiation	R	Ω	Resistance
h	$W/(m^2 K)$	Heat transfer coefficient	t	s	Time
H	A/m	Magnetic field	T	℃	Temperature
I	A	Current	**u**	m/s	Fluid velocity vector
I	-	Identity matrix	u^+	m/s	Velocity parallel to wall
j	-	Imaginary unit	u_τ	-	Friction velocity
J	W/m^2	Surface radiosity	V	V	Electric potential
J	A/m^2	Current density	y^+		Wall distance in viscous units
k	$m^2 \cdot s^2$	Turbulent kinetic energy	Z	mm	z-coordinate position
Greek Symbols					
α	m^2/s	Thermal diffusivity	μ_r	H/m	Relative magnetic permeability
τ	-	Transmission	μ_0	H/m	Magnetic permeability of space
γ	N/m	Surface tension	μ_T	Pa	Turbulent viscosity
δ	mm	Skin depth	ρ	kg/m^3	Density
δ_w^+	-	Wall lift-off	ρ_s	C/m^3	Electric charge density
ε	$m^2 \cdot s^3$	Turbulent dissipation rate	ρ_d	-	Diffusive reflectivity
ε_0	F/m	Electric permittivity of space	σ	S/m	Electrical conductivity
ε_r	F/m	Relative electric permittivity	σ_{SB}	-	Stefan-Boltzmann constant
ϵ	-	Emissivity	φ	deg	Phase shift

λ	W/(m · K)	Thermal conductivity		ϕ		Azimuthal direction
λ_{eff}	W/(m · K	Turbulent thermal conductivity		ω	rad/s	Angular frequency
μ	kg/(m · s)	Viscosity				

Nondimensional numbers

Pe	Peclet number	Pr	Prandtl number
Re	Reynolds number	Pr_T	Turbulent Prandtl number

Subscripts and addscripts

e	Source term	T	Turbulence
r	Radiation	app	Applied
st	Surface tension	dis	Dissipated
rh	Resistive heating	rad	Radiation
f	Frequency	ext	External
c	Coil	tang	Tangential

Acronyms

BSD	Backscattered scanning electron
SEM	Scanning Electron Microscopy
EDS	Energy-dispersive X-ray spectroscopy
CCIM	Cold Crucible Induction melting
DNS	Direct Numerical Simulation
DSC	Differential Scanning Calorimetry
FEM	Finite Element Method
IM	Induction Melting
LFA	Laser Flash Analysis
LES	Large Eddy Simulation
PDE	Partial Differential Equations
VIM	Vacuum Induction Melting
XRD	X-ray Diffraction
XRF	X-ray Fluorescence

Chapter 1

1. Introduction

The first chapter of this research provides an exposition of the underlying motivation that drove its development and a clear definition of the primary objectives. Subsequently, the chapter delves into a comprehensive explanation of the methodology employed to accomplish the proposed objectives.

1.1. Motivation

The industrial sectors of metallic material extraction and processing are considered to have a significant environmental impact, ranking second in energy and natural resource consumption indicators after the chemical industry [1]. In light of the renewed European directives for the next decade on energy and resource consumption, aimed at reducing electricity consumption by almost 30%, metal processing sectors are compelled to seek out new technologies and advanced manufacturing processes to enhance efficiency, save on raw materials, and sustained development [2]. Of the various processes used in metalworking, casting is recognized as one of the most efficient in terms of material utilization and specific energy consumption. However, the heating and melting of metals before casting remain energy-intensive, with an estimated 80 % of the energy consumption for final components occurring during the melting stage [3].

In this regard, over the last decades in the European scenario, with the increased energy costs and the constant threat of raw material imports, there has been a gradual reduction in foundries, with only those with higher productivity rates able to withstand [4]. However, worldwide production is expected to continue to increase, particularly in Europe, where an almost 15% increase is estimated [5]. In order to consolidate these forecasts, cost savings derived from energy and raw materials are critical to the consolidation and growth of production. To achieve these goals, advanced manufacturing and digitization of production means will be indispensable tools in reducing the need for raw materials and energy and meeting sustainable economic growth directives while consolidating production in Europe.
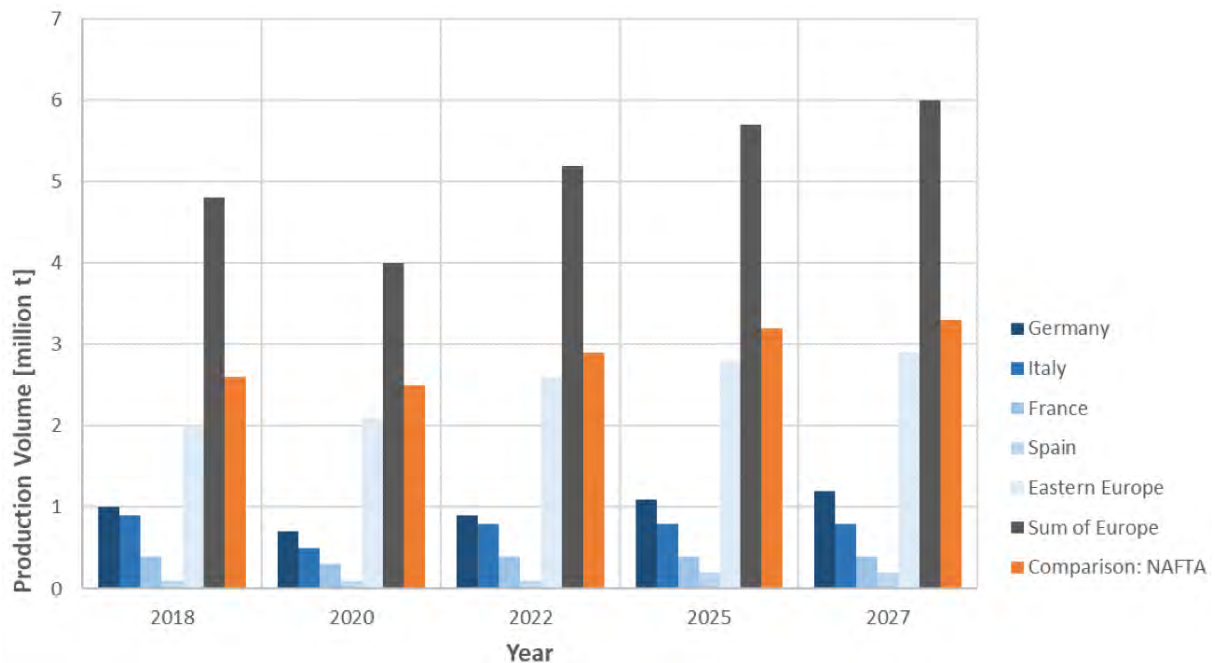
Figure 1-1. Projected production volume of the casting industry [5].

On the other side, the aeronautic industry is focusing on developing lighter and more efficient aircraft to enhance fuel consumption and reduce emissions in compliance with environmental regulations. With the expected growth in air transport, almost 40,000 new units are anticipated to replace the current fleet with more efficient models by 2040 [6]. Therefore, aero-engines are crucial in optimizing the thermodynamic cycle by raising combustion temperatures, and nickel-based superalloys are indispensable for achieving this goal due to their exceptional mechanical properties at high temperatures, currently constituting almost half of the engine components' weight [7].

The fabrication of such components, primarily through investment casting, is a challenging manufacturing process. This is due to the fact that Ni-based superalloys contain a complex combination of chemical elements that require precise compositional control to produce the necessary hardening mechanisms. Additionally, the high melting point above 1300 °C and the high reactivity of the elements make it challenging to achieve the desired narrow compositional margins, free of defects and inclusions. Consequently, vacuum induction melting (VIM) is the most appropriate method to process these components due to the controlled atmosphere during melting and its higher efficiency, localized heating capability, and greater operational flexibility. The electrical efficiency of the process is estimated to be as high as 65 % for non-ferrous alloys; however, it is still an intensive energy-demanding process with ample room for improvement of cycle times and defectiveness [8].

Although modern metallurgy employs measurement-based techniques to monitor and control operating conditions, controlling the VIM furnaces is challenging due to their high temperatures and inaccessibility. Therefore, employing numerical simulation techniques offers a cost-effective and efficient approach to optimizing the VIM process parameters; thus, the development of precise and experimentally validated numerical models that can reproduce the internal dynamics of the heating and melting process will allow for the study of the impact of different variables as a whole and enable simulation of various operating conditions. This, in turn, will aid in determining efficient conditions, minimizing melting times, and reducing energy consumption.

1.2. Objectives

The research project focuses on enhancing the vacuum induction melting (VIM) technology for efficient heating and melting of Inconel 718 superalloy, utilizing both numerical and experimental investigations. To accomplish this, the following specific objectives have been proposed:

i.   Develop an efficient modeling methodology capable of accurately simulating VIM's heating and melting process.

ii.   Create multi-physics numerical models that incorporate various physical phenomena and their interactions.

iii. Improve accuracy and reduce uncertainty trough experimental validation of theoretical results in a laboratory-scale facility.

iv.   Evaluate the impact of VIM variables in the melting process by studying specific case studies operating under large-scale industrial conditions.

v.   Enhance VIM efficiency by reducing energy consumption and melting process time.

These specific objectives guide the research project towards a deeper understanding of the VIM technology, its application to Inconel 718, and the development of practical solutions to optimize the process on both laboratory and industrial scales.

1.3. Methodology

The following section provides a concise and structured outline of the research plan's structure, detailing the steps to achieve the set objectives. It also serves as an introduction to the different sections that constitute the document. The work is organized into two major sections: a theoretical-numerical section and a practical-experimental section; these sections complement each other and form the core of the document Figure 1-2 illustrates the chapters comprising the dissertation.
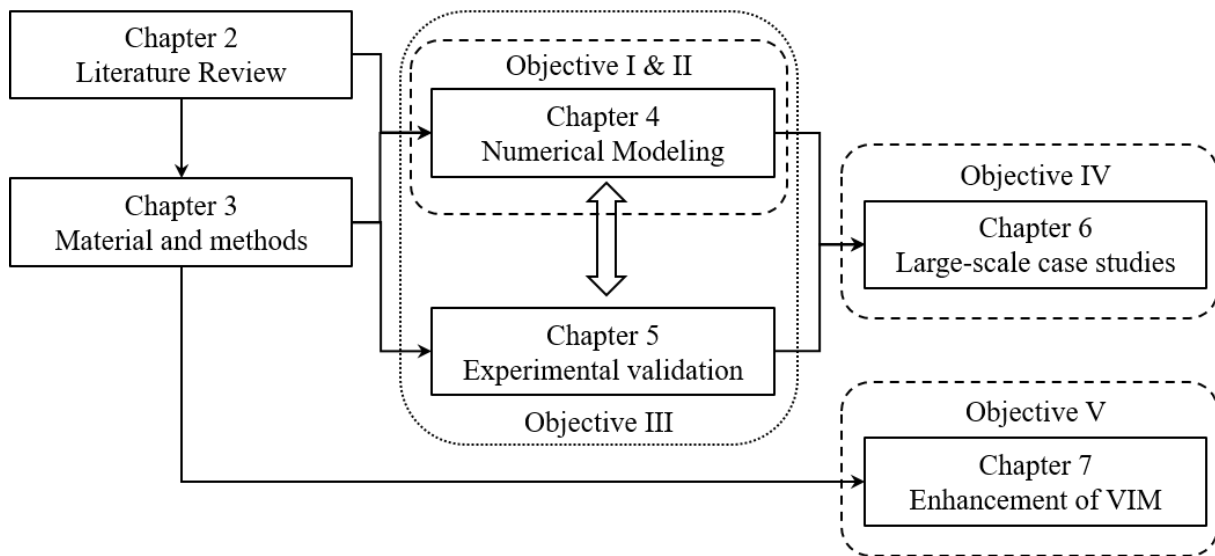
Figure 1-2. Document structure and research workflow.

Chapter 2, "Literature Review" establishes the theoretical framework, laying the foundations for subsequent sections. It comprehensively introduces the essential aspects of nickel-based superalloys, including their manufacturing, focusing on the melting process. Furthermore, it presents an overview of the state-of-the-art numerical models encompassing induction heating and flow transport modeling in liquid metals.

In Chapter 3, "Material and methods", the objective is first to determine the melting materials' thermophysical properties. It also provides detailed insights into the characteristics of the laboratory scale melting furnace, the calibration, and the measurement systems for the melting variables determining a standard operating procedure. The collected parameters and variables are employed to feed the numerical model.

Chapter 4, titled "Numerical Modeling," focuses on developing a comprehensive numerical model using the finite element method. This chapter thoroughly examines two distinct aspects. Firstly, it develops a magnetic induction model that explicitly addresses solid-state metal heating scenarios. Secondly, it explores the behavior of liquid metals and investigates the coupled phenomena of turbulent flow transport and heat transfer.

Chapter 5, titled "Experimental validation," aims to validate the theoretical results by conducting specific tests. The primary objective is to gather real process data through ad-hoc experimental tests, enabling the study of the coupled behavior of the process under dynamic operating conditions. The obtained experimental references are then used to perform additional simulations, and the numerical results are compared and correlated with the experimental data. This chapter provides a detailed analysis of the internal dynamics of the melting process and examines the model's response, including an assessment of uncertainty.

Chapter 6, titled "Large-scale case studies," aims to scale up the laboratory-scale numerical model to one and two orders of magnitude industrial facilities by considering specific case studies. This chapter builds upon the knowledge generated in previous sections and explores techniques to improve the practical application of the model in industrial settings.

In Chapter 7, titled "Enhancement of VIM efficiency," the influence of crucibles on the thermal efficiency of the melting process is compared based on the knowledge gained from previous chapters. The chapter proposes an optimized melting procedure and analyzes the metal and crucible reactivity.

Lastly, Chapter 8, titled "Conclusions and Future Lines," provides a comprehensive summary of the main findings of the research. It concludes by suggesting future research directions to advance further the VIM process and improvement of the presented model.

Chapter 2

2. Literature review

This initial chapter reviews the state of the art concerning the melting process of Ni-based superalloys. It briefly summarizes these special alloys' properties, microstructure, composition, and principal applications. Subsequently, it presents an overview of the specific manufacturing routes capable of producing components, emphasizing the casting processes. The document then delves into the VIM technology for melting Ni-based superalloys. It provides a detailed explanation of the operating principles and melting procedure, along with a description of the required equipment and their relationship with potential sources of metallurgical defects. Last, an exhaustive review of numerical modeling in induction melting technologies is conducted, followed by an update on the current situation, leading to potential avenues for further investigation. As a result, the conclusions drawn from this analysis identify possible approaches for process improvement.

2.1. Ni-based superalloys

Superalloys are specifically designed alloys with excellent mechanical, fatigue, and oxidation resistance properties at elevated operating temperatures exceeding 70 % of melting point. There can be found three main groups depending on the base element, cobalt (Co), iron-nickel (Ni-Fe), and nickel (Ni). The last ones, Ni-based superalloys, are the most widely employed due to their superior properties. The principal characteristics of Ni-based superalloys are mechanical resistance and ductility, excellent resistance against oxidation, and corrosion in an ample range of temperatures and aggressive chemical atmosphere environments [9]. Considering the time variable at elevated temperatures, creep resistance is required, and it is under these conditions that Ni-superalloys stand out above all alloys [10]. These properties result from a complex crystalline microstructure obtained with precise alloy composition, controlled and homogeneous solidification, and posterior heat treatments.

Due to these outstanding properties, Ni-based superalloys are commonly used in applications requiring to withstand high pressures in high temperatures and corrosive environments. Thus, typical applications are aeronautic, petrochemical, and nuclear. Perhaps the application for which Ni-based superalloys are recognized is aero-engines, where many components are manufactured with these alloys, such as turbine blades for high and low-pressure stages, compressor disks, combustion chambers, or different support housings [11]. Figure 2-1 shows two typical applications NGVs and the radial structure of a Trent XWB turbine.
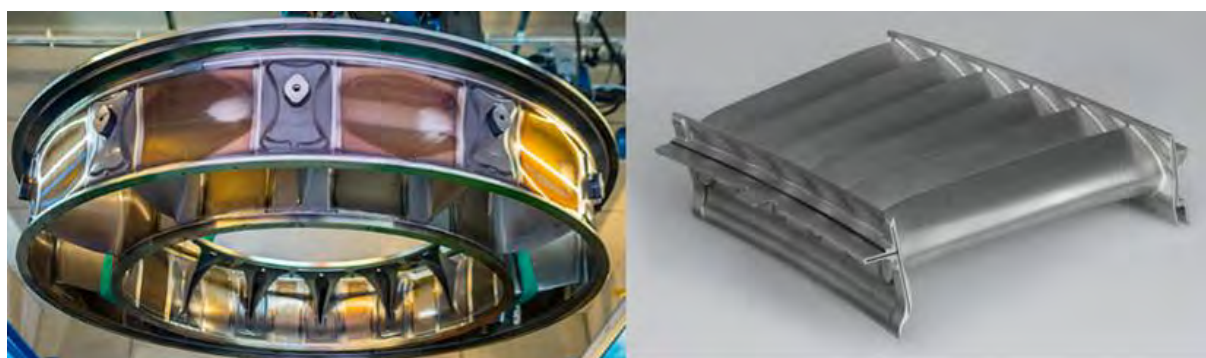
Figure 2-1. Ni-based superalloys made aeronautic components [12].

The Inconel 718 has become one of the most widespread superalloy due to its reasonable cost and availability ratio and excellent load and creep resistance [13]. The principal hardening mechanism is the

intermetallic precipitation of γ" Ni₃Nb-type phase in the FCC austenitic γ matrix. γ" is a precipitate with a BCT crystalline structure coherent with the γ. Hardening is achieved due to the difference in stiffness between the precipitates and the BCT and FCC structures matrix. Although it also exhibits γ' Ni₃(Al, Ti), the proportion of Al and Ti so that its precipitation is minimal. Additional hardening is provided by the solid solution hardening, acritude, and carbides. Alloying elements are crucial in forming the strengthening phases, which can be classified as stabilizers of the γ-phase and γ' or/and γ", phase carbide formers and elements that tend to segregate to the grain boundaries [14].

The chemical composition of the Inconel 718 is resumed in Table 2-1; it is composed of a complex amalgam of elements with a precise balance necessary to form the required microstructure. The alloy has less Ni than other alloys, does not contain cobalt, and has fewer strategic elements content, reducing the cost.

Table 2-1: Chemical composition of Inconel 718 superalloy.

Element	Ni	Fe	Cr	Nb	Mo	Ti	Al	Co	Cu	B
Comp. (wt. %)	52.3	Bal.	19	5.1	3	0.9	0.5	0.5	0.15	0.005

Regarding mechanical properties, yield, and ultimate strengths are satisfactory, and low cycle fatigue resistance and creep resistance in intermediate temperatures. In addition, it has excellent corrosion resistance, weldability, and formability properties, making it excellent for forging processes [15]. Among its applications, there are numerous components manufactured for the aircraft industry, power plants, and oil & gas [9]. It has been the standard turbine disk material for low-intermediate-temperature turbine disks for aircraft engines. An illustrative example is the General Electric CF6 engine employed on the Boeing 787, accounting for 34 % of the material in the Inconel 718 superalloy [7].

2.1.1. Manufacturing routes

Once the importance of the Ni-based superalloys, properties, composition, and applications have been explained, the manufacturing routes are introduced.

There are two main Ni-based superalloy products, castings and wrought. Regarding the last ones, hot-forming processes produce components with simple geometrical sheets, bars, profiles, or other pre-formed products. Typically, for performance Fe-Ni alloys where segregation is not an issue but high composition quality is required, casted pre-form is produced, and afterward hot worked to produce wrought components [16]. Due to their limited ductility, Ni-based superalloys cannot be effectively forged even at high temperatures. Consequently, precision casting is utilized as an alternative method. Before pouring the molten material into the mold, whether an ingot or scrap, it must undergo heating until it reaches a molten and superheated state. Various melting technologies are employed, such as gas, electric, or arc melting [17].

However, for the fabrication of aero-engine components, where high-metallurgical quality, complex geometry, and near-net-shaped criteria have to meet the benefits of the investment casting technology and Vacuum Induction Melting (VIM) is united [18]. This route is marked in red in the general outline presented in Figure 2-2. Moreover, it has to be noted that the controlled solidification makes it possible to vary the grain morphology, equiaxial, directional, or single crystal. In this way, it is possible to optimize the material's microstructure and, thus, the mechanical properties and behavior of the final component. This demonstrates the great versatility and interest of the investment casting process for nickel components [19].

Regarding the VIM procedure, it is necessary to emphasize the fast start-up and flexibility that offers induction technology. Moreover, induction heating of the metal provides high power densities, and higher heating rates than convection or radiation processes, as it is more localized, offering a more efficient process being the fastest and most electrically efficient technology. High production rates are achieved because of shorter melting times. In addition, when not in use, the induction power supply does not consume energy and does not require long start-up and shut-down times. [20].
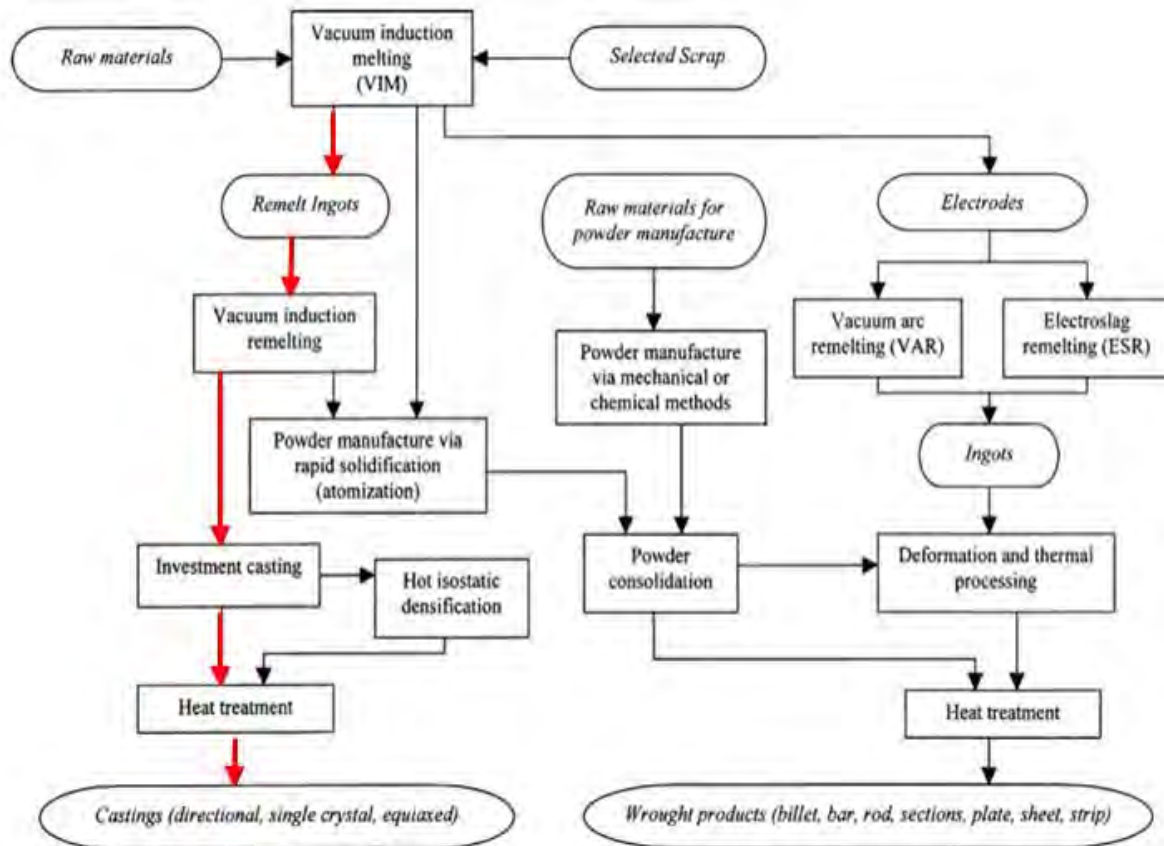
Figure 2-2. The general outline of fabrication routes for Ni-based superalloys components [17].

As observed, VIM outstands as an essential step from which the rest of the processes derive for casted or wrought components having two principal benefits which justify its predominance. Induction heating is contrary to other indirect melting processes; the metal is heated with induction, offering faster and energetically more efficiency. The vacuum chamber provides an inert atmosphere. The high reactive contents with rapid oxidation kinetics, such as Al, Cr, Ti, and Mn, demand a non-reactive atmosphere to ensure the liquid alloy's chemical composition. This is why VIM outstands from other melting technologies; the vacuum chamber minimizes O and N content atmosphere resulting in a microstructure with fewer inclusions and defects, ensuring correct chemical composition and reducing compositional variations in the melting charge [21].

2.2. VIM Technology

In the following lines, an introduction regarding the operating principles of the VIM process and the up-to-date technological aspects are described. The complex multi-physical phenomena associated with VIM technology can be summarized as follows: applying alternating current through a coil generates a time-harmonic magnetic field. This magnetic field induces eddy currents in an electrically conductive material in the opposite direction with an intensity proportional to the rate of magnetic flux. These induced currents dissipate energy through the Joule effect, heating the metal until it melts. Once the

material is fully molten, magnetic or Lorentz forces act as inertial forces, leading to the recirculation of the liquid metal and deformation of its top-free surface. Throughout this process, two sources of heat loss are present: 1) conduction from the molten charge through the melt-box until it dissipates on the water-cooled coils, and 2) radiation from the top surface (Figure 2-3).
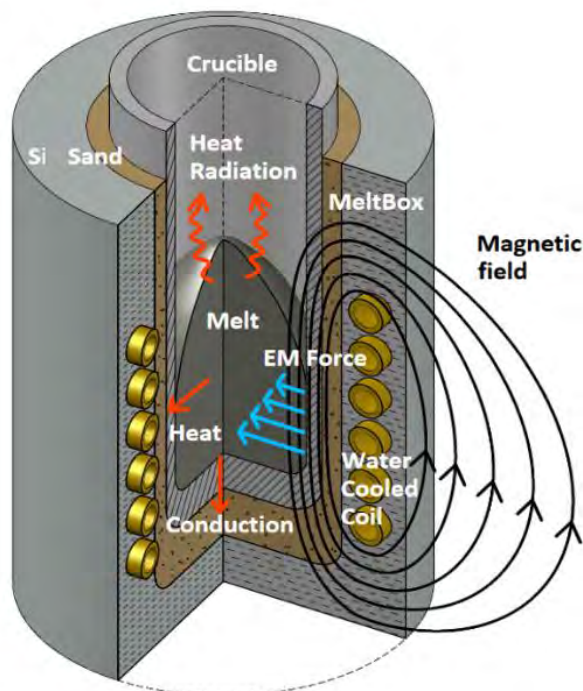
Figure 2-3. Depict of hot-crucible induction melting.

2.2.1. Components

The essential equipment of a VIM installation consists of melting and mold chambers, vacuum pumps, a power generator, and a control station. The melting and mold chambers can be shared or separated; they are usually airtight steel chambers connected to a high vacuum pumping system. When separated, they are also vacuumed separately to allow the furnace to operate semi-continuously. The coil is inside the melting chamber, is typically made of copper, and is arranged in a sinusoidal shape, folding various loops. It is usually coaxial, with an inner piping tube from where water flows for refrigeration; thus, a chiller is employed to cool down the water in a closed circuit. The coil is connected to a power generator that feeds the system with the necessary current and voltage to induce the magnetic field in the charge to melt. The charge is placed in a crucible consisting of two layers, a working layer and a reinforced layer. The first one, also known as a liner, is the interface between the metal and the crucible, where the ceramic-metal reactivity and erosion might affect the metallurgical quality and the presence of defects final component. The second, the reinforcing layer, protects the coil from a possible breakage of the active ceramic layer. The control station contains all the valve actuators, sensor instruments, and recorders for process management.

- **Coil**

The induction coil or inductor is the heart of the VIM furnace and must be installed in a robust cylindrical housing. In this manner, it also has the mechanical function of supporting the ceramic crucible in the radial direction. The coil must be fixed entirely utilizing magnetic yokes placed from side to side. A rectangular profile in the coil allows radial forces to be transferred from the crucible to the yokes. Which

also captures the magnetic field scattered outside the coil minimizing losses. Induction coils require higher electrical insulation capacity due to the increased danger of electric shock in low-pressure atmospheres. This is why the coil requires insulation made of epoxy resin and glass fiber coating to ensure stability and avoid discharges at operating voltages above 600V [22].

A varying magnetic field is generated through an AC circulating in a coil to generate the magnetic field and consequent induction heating. By folding multiple turns, the flux lines running longitudinally through the coil are strengthened, increasing the intensity of the magnetic field. Therefore, the number of coil loops, the position relative to the charge, and the section area significantly impact the field, the charge-coil magnetic coupling, and the consequent efficiency. For an optimum coil design and arrangement, additional aspects such as electrical conductivity and magnetization of melting material, mass to be melted, required stirring velocities, and process time must be considered [20].

In order to have a high varying current in the coil, an oscillatory RLC circuit is employed (Figure 2-4.a). The resistive component (R) corresponds to the charge to be heated, and the inductive component (L) is the inductor. Thus, capacitors (C) are connected to form a resonant circuit, which can be placed in series or parallel configuration, being series preferred for induction melting applications. The inductor and capacitor functions are in parallel.

When a pulse of energy is introduced, it is stored as electrostatic charge in the capacitor and released as current, while the coil is stored as a magnetic field and then released back to the capacitor. Thus the two components pass their stored energy back and forth, a phenomenon called oscillation, while the resistive component of the charge transforms the power into heat. The frequency at which energy is transferred back and forth is the frequency of the resonant circuit and is determined according to the capacitors' magnitude and the coil's inductance.

The resonance condition is achieved when the inductive and capacitive reactance is equal in magnitude but cancels each other as being switched 180° apart in phase. In this equilibrium, the impedance of the circuit is minimum while the current maximum and the resistance are balanced, which means that the energy released by the capacitor will equal the energy reached by the coil. Therefore, working near this resonant frequency is necessary for efficient heating [23].

- **Power generator**

As mentioned, the energy losses in the form of heating of the charge demand a power feed of the resonant circuit. The coil and capacitors are connected to a power generator or converters. These frequency inverters convert three-phase line voltage and frequency to single-phase power with the frequency required for the application. It is a combination of converter and inverter where the converter modifies the alternate current (AC) three-phase input line to direct current (DC), and the inverter changes the direct current to single-phase AC [24]. The load-matching process corresponds to the dimensioning of the capacitor tank to fit the desired resonant frequency, which is dependent on the previously mentioned coil inductance, work-piece material, and mass and process limitation regarding desired heating power and time [25].

In the case of series-connected capacitors tanks, they behave as current sources while the inverter is considered a voltage-fed inverter (Figure 2-4.a), fed with a constant voltage source of the converter. H-bridge type inverters are employed for most induction heating and melting applications due to their capacity to feed the same power with lower currents. For high-power inverters, medium-frequency supplies are available, up to 1 kHz for high-capacity furnaces and 10 kHz for low-capacity furnaces [26]. The DC voltage from the converter is modulated with a duty cycle controlling the four IGBTs by switching them on and off according to the power requirements (Figure 2-4.b). This way, the single-

phase AC output voltage is modulated, and amplitude and frequency are controlled by regulating the time they are switched on or off, while the disadvantage of this technique is the increased losses of the IGBT [24].
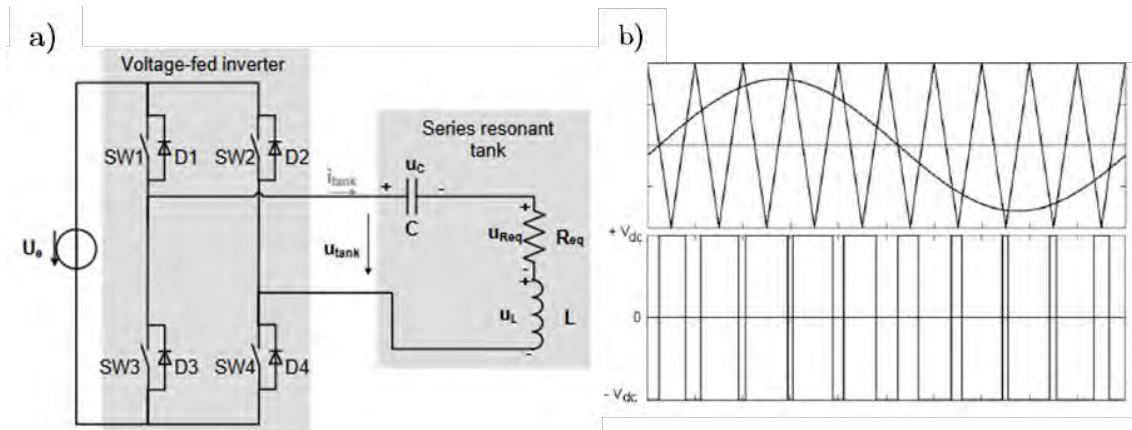
Figure 2-4. a)Voltage-fed series inverter configuration and b) AC modulation. Adapted from [26].

These inverters regulate the power, but the electronic control system adjusts the operating frequency and current according to the equivalent R-L-C circuit and tries to get close to the resonant frequency. As the power increases, the frequency drops towards the resonant frequency of the load; in parallel, the output power and current approach the maximum power. The power applied to load is regulated by the frequency, and at the resonant frequency, the power is maximum, but when moving away from this frequency, the power decreases. Therefore the current supplied by the inverter oscillates with a resonance frequency independently adapting to the high-power circuit between the furnace coil and the capacitor tank [26].

This enables a constant regulation of the power in the load. For example, when charge material is cold, magnetic, or scrapped, with high electrical resistance, maximum power is obtained at low current and low frequency but at maximum voltage. Alternatively, if the furnace is filled with melt, hence at low resistance, a higher current at a higher frequency provides the same power with a lower voltage. The problem with this control technique is that the phase between current and voltage is not zero outside the resonant frequency. This means that the inverter contributes reactive power that increases the current in the auxiliary components due to parasitic resistances. In addition, the inductance of the load to be melted varies, whether in a solid or liquid, so the generator is adjusted to the imposed active power [27].

- **Crucible and Liner**

The crucible and liner are other critical elements during induction melting, as the VIM process is also known as hot-crucible induction melting. The principle objective is to work as a vessel for the liquid metal. Thus it has to withstand the high melting temperatures of Ni-based superalloy over 1500 °C while being chemically stable and resistant to erosion. In this regard, the suited materials are refractory ceramics with low thermal conductivity that do not interfere with the magnetic field.

The crucible typically comprises two layers - the inner one is in contact with the liquid metal, denominated as liner. The interface between the ceramic and metal is critical as chemical interactions and reaction product formation might occur during high melting temperatures. Also, the physical erosion and thermo-mechanical loads due to the flow stirring promote the decomposition of the liner and the formation of oxides inclusions that might end in the casted components. The service life of conventional liners depends on the wear and cracking due to thermal cycling [28], while for high-added value applications, one-shot liners are employed.

The secondary layer, the reinforcement layer, acts as a coil protector in case of breakage and prevents leakage. It also has a higher insulating capacity to minimize heat conduction, as the radiation is the principal heat loss and the consequent process efficiency [29]. Thus, controlled employ of the crucibles is necessary to produce clean alloys with minimum oxide inclusions; its notable importance is discussed in more detail in 2.3. Crucibles for Ni-based superalloys melting

- **Chiller**

The heat through the crucible is dissipated in the coil, which must be continuously refrigerated to avoid damaging the copper windings. The chiller is responsible for cooling, utilizing the water flow at a controlled temperature through a closed, pressurized circuit. It is also employed to refrigerate the power generator's internal electronics and the capacitor tanks. Given that the VIM furnace is an installation with a significant thermal load, ensuring that all the furnace components work under optimum and safe conditions throughout the heating and melting process is vital. The cooling conditions will therefore affect the behavior of the components and the melting process itself.

2.2.2. Melting procedure

After describing the principle components of VIM equipment, the basic operating procedure is described with a detailed explanation of the principle stages detailing the good practices necessary to follow in order to ensure an excellent metallurgical quality of the final components. Figure 2-5 power-temperature time diagram shows a typical melting cycle for Ni-based superalloys. The temperature evolution is measured with a pyrometer, and the graph is normalized with the melting power. In addition, the vacuum chamber pressure is shown along with the subsequent process steps.
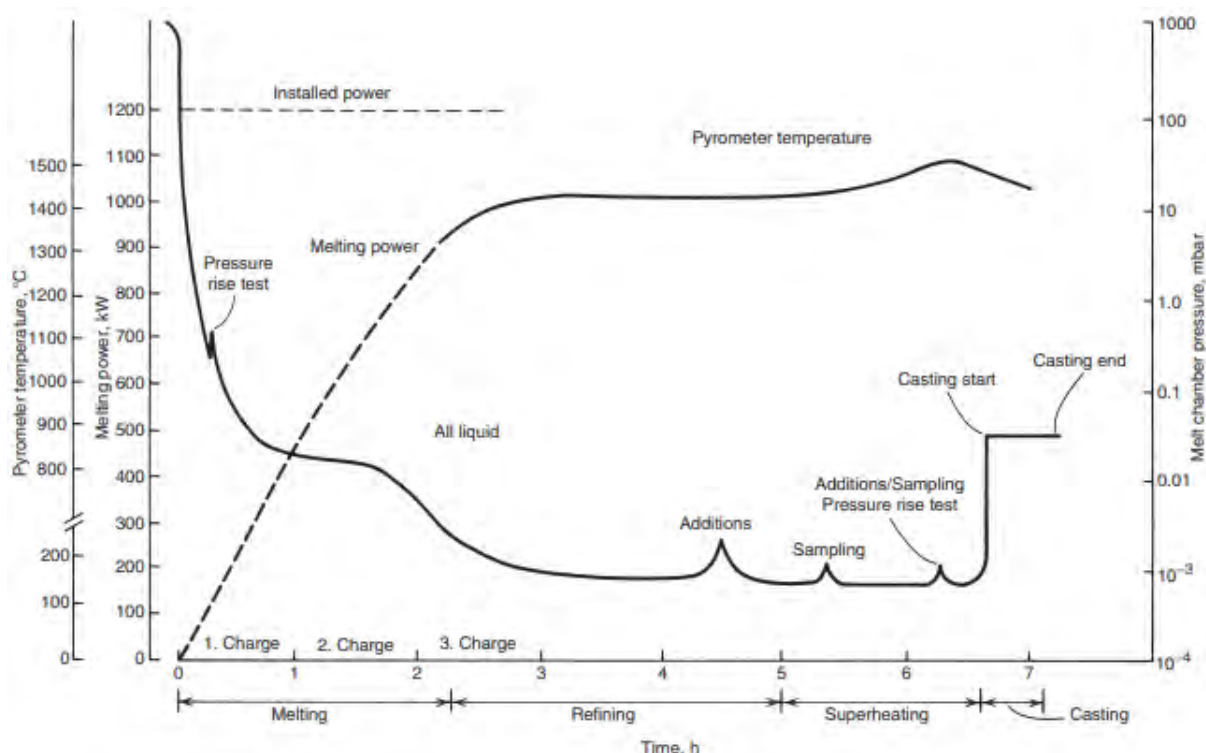
Figure 2-5. Typical vacuum induction melting procedure for Ni-based superalloys [30].

- **Melting**

Once the chamber is closed, the vacuum is created employing multiple pump systems, typically mechanical, rotary, or diffuser pumps, reaching a vacuum capacity of 10^{-1}-10^{-3} Pa. The initial charge contains the raw material with the additional alloying constituent without the reactive ones. The sequence of the charge placement is essential for progressive melting. Adding the rest of the alloying elements as more raw material is done without breaking the vacuum atmosphere through a bulk charger on a side or top of the furnace. Once ensuring that the furnace vacuum pressure has reached the mechanical limit, ingot or virgin material heating is commenced by inducing a magnetic field from an induction coil. After applying enough power and time solid-to-liquid transition of melting commences. During melt-down and posterior refining treatment steps, the vacuum chamber pressure must be controlled and maintained as low as possible [30].

- **Refining**

During the refining treatment, degassing and boiling reactions occur, removing the dissolved gases and eliminating the harmful trace elements to ensure a correct melt composition. For high mechanical demanding applications, eliminating deteriorated trace elements to ppm level is essential to obtain the necessary mechanical properties particularly sensitive to impurities. Among these elements, it can be mentioned that Ag, Bi, Cu, or Pb are critical, for example, in the stress rupture life for Inconel 718. Typically it can be easily eliminated as gas bubbles during VIM refinement due to their lower solubility in the melt or higher vapor pressure. The stirring increases the evaporation rate being very effective for removing high vapor-pressure metallic impurities [31].

However, in the case of more volatile chemical elements, such as Al and Ti, which are in less proportion for Inconel 718 superalloy, Moshtaghi and Safyari [32] evidenced that longer refining times lead to the diminution of Ti and Al content and the presence of higher oxygen content and Al_2O_3 inclusions and TiN nitrides. The presence of N has been related to the formation of brittle nitrides or carbonitrides and higher microporosity and inclusions with the consequent reduction of mechanical properties on Inconel 718 [33].

Nitrogen appearance has been related to raw material contamination and atmospheric contamination during melting due to poor vacuum conditions during VIM refining by obtaining levels < 20 ppm; however, nitride-forming solid elements such as Cr, Nb, Al, and Ti with high affinity with the N reducing the activity and makes removing it difficult [34]. Oxygen is also a harmful element that appears as a solid solution and inclusion due to the presence of oxide-forming elements like Al, Ti, and Cr. These inclusions might act as crack initiation and propagation paths; thus, the rupture life decreased for Ni-based superalloys with O content higher than 50 ppm. VIM produces low oxygen (<30 ppm) and carbon (<50 ppm) content components; however, the pressure-dependent removals are not effective in the presence of nitride, oxide, and carbide formers since the vacuum does not facilitate the dissociation.

- **Alloying and superheating**

After the refining stage, and when the melt is deoxidized, being almost free of oxygen and nitrogen content, the reactive alloying elements such as Al, Ti, or B are added, thus minimizing the possible reactions and loss of alloying effectiveness. The sequence of alloying additions is stepped by introducing mixing periods to ensure homogenization. After ensuring the correct metallurgical composition and the necessary compositional adjustment, the melt temperature increments to superheat temperature before pouring. For pouring, the coil and crucible are tilted and cast into a preheated mold [30].

During the process, the melt temperature has to be carefully controlled in order not to exceed and avoid the possible reaction with the crucible or the possible overheating of the melt lower vapor pressure alloying elements. However, the casted part could still have considerable amounts of slag from the products of refining and inclusions coming from the deterioration of the crucible [35].

2.2.3. Operating variables

Once the principle components related to the VIM technology and the operating procedure are defined, it will study the impact of some of the significant variables and their effect on the process. From the physical principle of induction heating seen in the previous section, it is possible to define a series of technological parameters of the melting process itself, which will determine the correct evolution of the melting of the charge. Although most works that study the effect of power and efficiency focus on cold crucible installations due to their more significant impact, they also lay the scientific and operational foundations for their application to VIM technology.

- **Power and efficiency**

The power variable is closely related to the efficiency of the process. As in all melting technologies, improving process efficiency has been a significant research issue. From a purely electric point of view, the magnetic coupling between the coil and the workpiece results is essential; in this regard, many contributions regarding induction heating can be found in the literature, while for induction melting processes, there are fewer references. For example, Baake et al. [36] claim that the efficiency for non-ferrous alloys tends to be lower than 60 %. The paramagnetic behavior of these alloys does not contribute to an effective coupling, and the higher electrical conductivity reduces the effectiveness of the induction heating, concentrating the heating on the surface. Figure 2-6 indicates the approximation of the possible efficiency of induction melting for various materials and the ratio between the skin depth and the workpiece diameter.
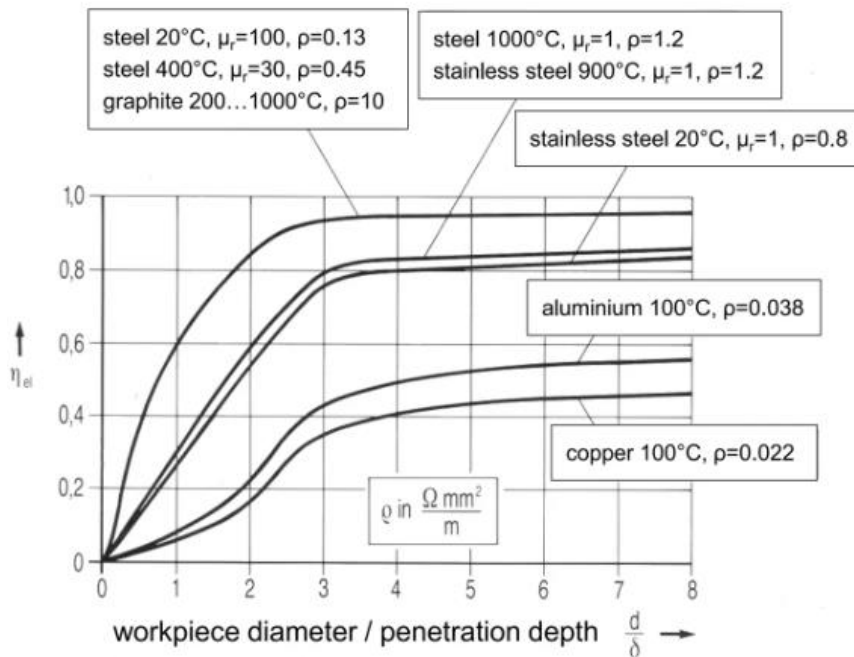
Figure 2-6. Induction melting efficiency for various materials and workpiece/skin depth ratio [36].

Additionally, there are electrical losses related to the parasitic losses of the cables and coaxial connections, and converter losses account for approximately 10 %. In this aspect, the designs of more

efficient coil configurations have been the principal approach. For example, the electrical efficiency of an induction melting furnace has been investigated by modifying the coil section configuration from a solid copper pipe to Litz wire, improving efficiency by 12 %. The power losses were experimentally by measuring the input corresponding to the power generator supply and the power losses of the coil and the rest of the connections, thus estimating the induced power in the charge [37].

Pericleous et al. [38] employed the calorimetric-balance approach to measuring heat losses and consequent process efficiency for CCIM. The author measured the energy balance by experimentally measuring the water flow and temperature difference between input and output water flow. In Figure 2-7 can be observed the power-temperature-time curve for the aluminum CCIM process detailing the power losses in the fingers and bottom and the temperature increase in response to power variations. Continuous heat losses were due to radiation and conduction effects, while the remaining induced power heated the load. The authors concluded that higher power causes a higher overheating of the melt, increasing up to a specific value that depends on the characteristics of the installation and the parameters. Above this characteristical limit, there was no consistent increase in superheat because the power gain only raised heat losses [39].
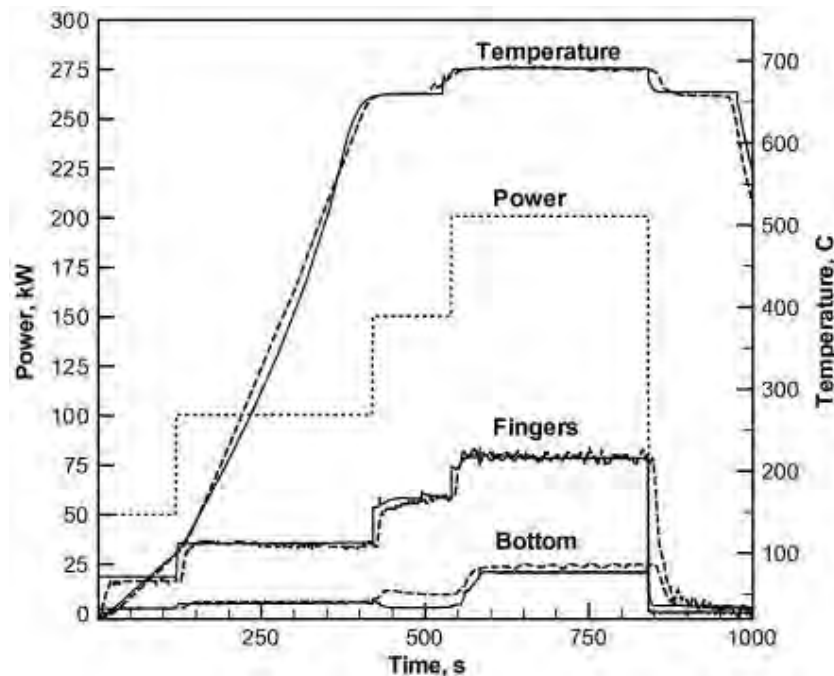
Figure 2-7. Power-temperature-time relation for ISM aluminum melting [38].

Another related substantial effect of the power is the variation of the flow field. Also, for a higher power, the magnetic field intensity is incremented the free surface profile deformation, thus incrementing the meniscus height. This reduces the contact surface between the melt and crucible and affects the magnetic coupling between the coil and melt. Spitans et al. [40] studied experimentally and numerically, reporting the free surface deformation for various current levels. Moreover, there is no superheat increment because the meniscus is maintained far from the crucible, reducing the electromagnetic coupling and hence, the total power generation in the melt [41].

- **Current and frequency**

The induced power in the charge is related to the oscillation frequency of an alternate current by a square root proportion. Thus, by maintaining the current, higher frequencies increase the induced heat. Although higher excitation frequencies increment the parasitic losses in the circuit; for a fixed coil current higher frequencies demand additional power to compensate for the increment of the losses. On

the contrary, constant power frequency reduction demands an increment of current, and an increment of the temperature has been reported [39]. The temperature variations for both fixed conditions and frequency variations are summarized in Table 2-2 for a TiAl alloy.

Table 2-2. Coil frequency effect on the maximum temperature for current and power [39].

f[kHz]	Constant Current			Constant Power		
	I [kA]	P [kW]	T [°C]	I [kA]	P [kW]	T [°C]
3.5	6.7	160	1565	8.04	220	1623
7	6.7	223	1588	6.7	220	1588
14	6.7	345	1615	5.59	220	1583

At high frequencies, it is possible to induce more power in the load; however, the power translates into much more localized heating on the load's surface due to the skin effect, which implies much more localized heating. However, with higher frequencies, the contact area between the crucible and the metal is incremented, leading to more significant heat conduction losses, which reduce the overheating temperature[41].

Regarding the effect of the fluid field, higher frequencies have been related to an increment of the interaction between the magnetic field and the free surface oscillations, requiring longer times to achieve a steady state. A sharper angle between the crucible wall and meniscus profile is produced while the final height is reduced, having a more planar surface, increasing the stability of the metal and reducing the perturbations even though the relative impact of the power is more pronounced [41].

- **Crucible diameter and filling level**

The increase in the crucible mass filling results in a better response to the load. The main reason lies in the increased induced power in the liquid metal due to the improvement of the magnetic coupling between the charge and the inductor. However, the temperature difference of the melt us is also increased. (Figure 2-8).
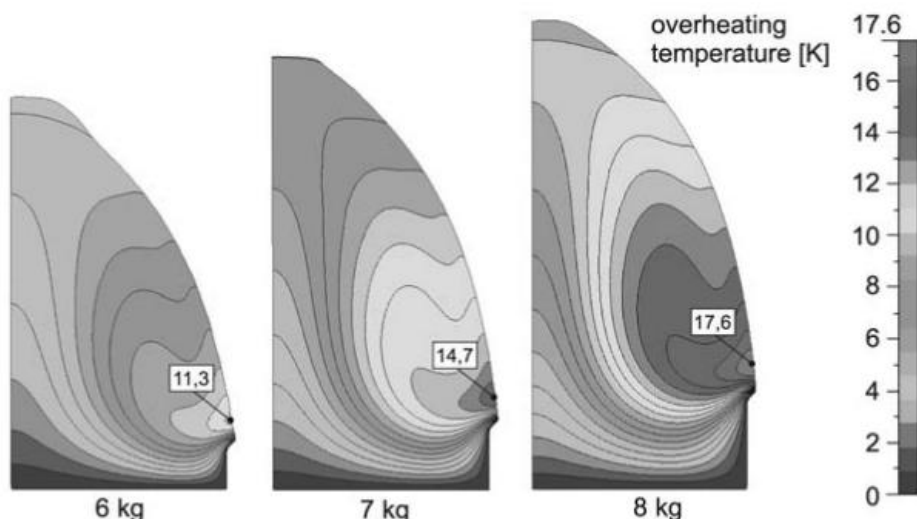
Figure 2-8. Temperature distribution comparison for TiAl melt in CCIM at different filling levels [41].

Similarly, an optimum charge height-diameter ratio (H/D) is essential for efficient heating. This is a crucial design parameter as it offers the opportunity to influence the shape of the free surface of the liquid metal and the metal flow velocity distribution. With the height increment, an extension of the

lower toroidal flow has been reported, incrementing the convective heat transfer effect and the consequent superheating temperature. Even if the heat conduction losses are incremented for higher H/D ratio crucibles, the electrical efficiency and, thus, the power induced in the liquid metal is enhanced. Therefore, the VIM melting process should be carried out with the filling level at maximum to obtain the best response, always considering possible instabilities of the metal surface and not exceeding the height of the coil [41].

- **Atmosphere and partial pressure**

The control of vacuum level and temperature leads to the control of the VIM melting and refining for Ni-based superalloys; thus, the type of atmosphere and partial pressure inside the vacuum chamber plays a crucial role in the alloy contamination and final composition [42].

For the Inconel 718 superalloy, the effect of vacuum pressure on mechanical properties was investigated. Four samples at a vacuum pressure of 10 Pa, 1 Pa, and 0.01 Pa were melted with an additional trial in argon gas at 500 Pa. Only Ti and Al variations were measured from the four melts, while other alloying elements remained unchanged. The chemical analysis concluded that under the argon atmosphere, there is more dissipation in Al and Ti, and for lower vacuum levels where the soluble oxygen content has increased, the formation of Al and TI oxides incremented. Higher vacuum levels reduce the tensile and yield strength of the samples due to higher evaporation of Al and Ti and the reduction of the strengthening γ'' phase [43].

The effect of the argon atmosphere is similar to a lower vacuum level; it increases the oxide inclusions and enhances the hardness. Therefore, the authors recommended the most suitable vacuum pressure level of 1 Pa. In addition to inhibiting oxidation, melting under an argon atmosphere also optimizes the temperature of the melt, an effect that seems to increase as the argon pressure increases. Thus, the lower the concentration of free oxygen in the atmosphere surrounding the molten metal, the lower the possibility of the metal reacting to form oxides that contaminate the final alloy [44].

2.3. Crucibles for Ni-based superalloys melting

As stated earlier, crucibles are of utmost importance in VIM melting as they significantly contribute to metal contamination in the form of inclusions, thereby posing a potential threat to the integrity of the final components. The decomposition of the crucible is a complex phenomenon driven by metal recirculation and high temperatures. It involves the simultaneous interplay of multiple phenomena, such as chemical reactivity, thermal diffusion, and physical erosion. Accurately describing and predicting this intricate process remains challenging due to its multifaceted nature. Next, an overview of the primary research conducted in the study of ceramic crucibles for melting Ni-based superalloys is introduced, highlighting the critical areas of investigation explored thus far.

2.3.1. Chemical reactivity

Chemical reactions between liquid metal and ceramic crucibles are one of the most relevant phenomena concerning metallurgical quality. This reactivity is known as the ability of a metal to form oxides and reaction products from atmospheric oxygen or at the cost of reducing some ceramic oxide compounds present in molds and crucibles.

The reactivity of metals is a complex process characterized by a combination of laws and phenomena varying with time and temperature. Understanding this behavior requires consideration of thermodynamics as a critical factor in analyzing the chemical stability of ceramic materials.

The formation of compounds is a kinematic process involving reactive chemical elements in the alloy interacting with the less stable ceramic crucible oxides. Since determining the compound formation rates is challenging, a steady-state approach is commonly adopted based on the concept of formation energy (ΔG^0_f). Also called Gibbs free energy, so the more negative $\Delta G0f$ is, the more stable the composite is. In the case of crucible-metal reactions, the ceramic's primary oxide is usually more stable than the potential oxides coming from the Ni-based superalloy. Figure 2-9 plots the Ellingham diagram of the standard free energy formation of the principle binary oxides.
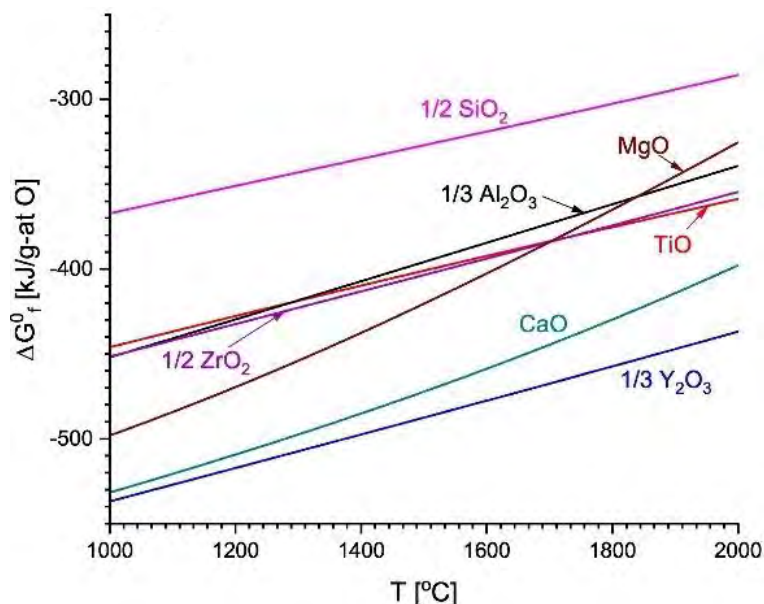
Figure 2-9. Formation of oxide refractories according to Gibbs free energy and temperature [45].

To date, numerous researchers have dedicated their studies to understanding the metal-ceramic interaction mechanisms that occur during the melting of Ni-based superalloys. Gusching [46] comprehensively analyzed the resulting reaction products when melting a Ni-Al-Hf-C alloy in crucibles made of different compositions, namely alumina (Al_2O_3), magnesia (MgO), and zirconia (ZrO_2). The study revealed that all three crucibles produced aluminum and hafnium oxides, with alumina tending to migrate to the surface and form a layer known as "dross." On the other hand, hafnium oxide was predominantly found at the bottom of the crucibles, although some mixing was observed.

The magnesia (MgO) crucible did not generate a continuous dross layer due to its high partial pressure, causing the dross to evaporate into the pumping system. In contrast, the alumina (Al_2O_3) and zirconia (ZrO_2) crucibles formed a continuous dross layer. Also, hafnium oxide stabilized zirconia, minimizing oxide transfer from ZrO_2 to the molten alloy. Consequently, the presence of hafnium oxide (HfO_2) created a continuous layer, enhancing the stability of the zirconia crucible. Therefore, Zr crucibles typically contained a certain amount of HfO_2. Conversely, in the case of the alumina crucible, HfO_2 did not provide stability to Al_2O_3, resulting in higher reactivity and the tendency to generate hafnium oxides that settled at the bottom of the crucible.

Sutton [47] investigated the formation of oxides in the interface between three types of crucibles, concluding that the stability to chemical reduction and dissociation of decreases in function of the oxygen content of the crucible and the type of reactive alloying elements Al, Ti, Hf, and Zr. The Al_2O_3 had the lowest inclusion content and least amount of oxides, while the MgO indicated higher indications of reactivity. As Zr has the lowest free energy formation, the first ZrO_2 oxide layer formed due to reduction with pure Al_2O_3 forming a ZrO_2 surface layer.

More recently, Gao et al. [48] studied the impact of alumina, magnesia, and spinel crucibles in forming oxide compounds and inclusions in the FGH4096 Ni-based superalloy. The authors concluded that physical erosion is the dominant effect for the Al_2O_3 crucible, while for MgO and spinel, there were dissolution and chemical reaction effects between the superalloy and crucible. The MgO formed a $MgAl_2O_4$ layer by a double-stage chemical reaction. First, the MgO reacted with the free Al of the alloy, forming an Al_2O_3 layer and dissolution of Mg in the alloy. Later, unstable internal wall-attached alumina inclusions were transformed into $MgAl_2O_4$, as evidenced by the dissolved Mg melt alloy.

Moreover, the dissolved Mg reduced the Al_2O_3 and Al-Ti oxides in the inclusions transforming them into stable Al-Mg oxides. This new stable layer prevents direct contact between the molten superalloy and the crucible wall, inhibiting erosion. However, for the Al_2O_3, no chemical reaction was found, while a higher mechanical erosion was detected due to the continuous electromagnetic stirring. The particles are detached and dispersed into the melt. According to the authors, some particles dissolved while others floated on the molten metal-free surface.
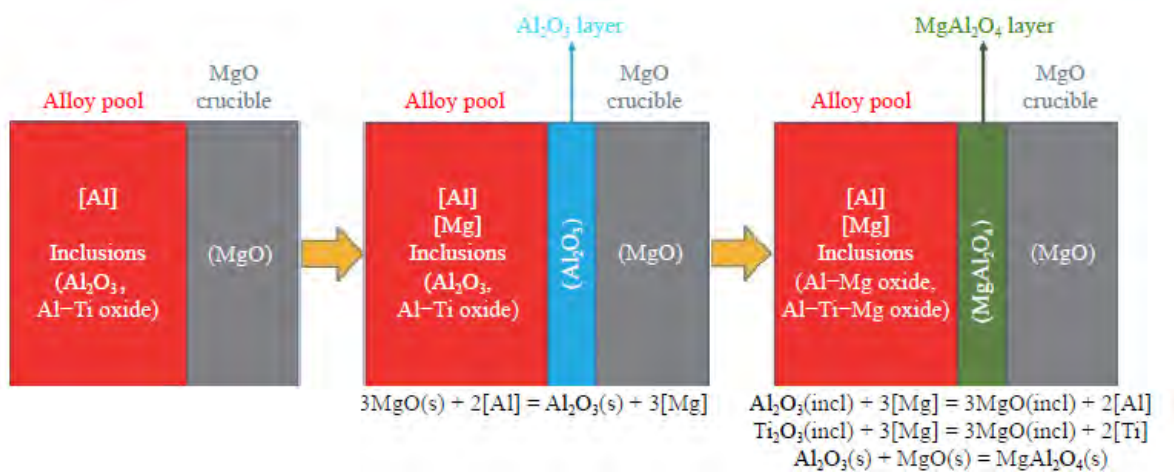
Figure 2-10. Depict of the superalloy–MgO crucible reaction mechanism during VIM [48].

2.3.2. Physical erosion

Even though the free energy formation alone does not entirely explain the reactivity between the molten metal and crucibles, the physical erosion due to the melt recirculation depends on the wetting angle, the surface porosity of the crucibles, and the time [49], Figure 2-11 illustrates the physical erosion mechanism.

The erosion is governed by the capillary effect and gravity, where the molten alloy with enough low viscosity penetrates the superficial pores of the crucible. Then the infiltrated metal commences eroding the grain boundaries of the crucible. Mechanical erosion depends on the convection force applied on the crucible surface due to the metal flow velocity field weakening the resistance of the crucible [50]. Wear increases rapidly once the initial surface has been detached due to the increment of the exposed surface, promoting further metal entrainment.

The loose particles can be dissolved following the previously mentioned chemical reactions or recirculate in the melt depending on the time and temperature. The continuous particle detachment and the dissolution on the melt promote the formation of a diffusive interface whose thickness depends on the vacuum pressure, superheat temperature, and time. As vacuum increases, melt contamination generally increases. The pore radius, surface tension, and wetting angle between the melt and crucible determine the erosion length [45].
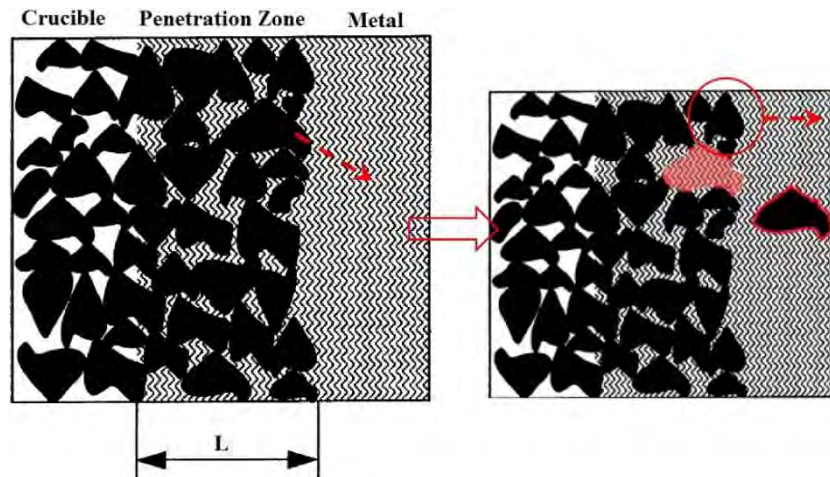
Figure 2-11. Depict of melt filtration into a crucible and entrainment of particles into the melt [45].

- **Wetting angle**

Wetting between the liquid metal and oxide substrate plays a crucial role in filtration and subsequent grain erosion. Numerous studies have been conducted to comprehend wetting phenomena at elevated temperatures, focusing on specific alloys and oxide substrates. Generally, it has been observed that higher non-wetting angles between the metal and the oxide layer lead to reduced filtration and superficial erosion.

The sessile drop test conducted at high temperatures serves as the standard characterization method, providing valuable insights into the wetting behavior. It has been established that wetting behavior is a thermally activated process, with the drop spreading rate following an Arrhenius-type equation [51].

Kanetkar [52] performed a sessile drop test at 1500 °C to investigate the surface tension and wetting angle of various alloy compositions, UD720, UD520, UD718, and Waspaloy, on alumina and zirconia substrates. Test results indicate that for the alumina substrate, a wetting behavior reports angles between 80° - 90°, while the zirconia substrate has a non-wetting with angles between 115° - 120°.

Valenza et al. [53] investigated Ni-based superalloys, Hf containing CMSX486 and IN738LC, with sapphire, alumina, mullite, and zirconia substrates under an argon atmosphere. Wetting angle measurements were based on the acquisition of high-resolution photographs. For Hf containing CMSX486, wetting behavior was reported for all the substrates ranging between 80° - 90°. For IN738LC, again, for all substrates except mullite, a wetting was reported.

- **Porosity**

The significance of porosity in the erosion of crucible surface layers becomes evident. Typically, researchers have studied metal infiltration into the crucible concerning the reaction duration. Detailed analyses examined the relationship between open porosity parameters and melting in this context. It is generally observed that higher porosity rates result in increased wettability and metal filtration, thereby intensifying erosion and causing crucible decomposition [54].

Kuang et al. [55] conducted tests on MgO, Al_2O_3, CaO, and Y_2O_3 coated MgO crucibles, all possessing an equal porosity of 20%, at a temperature of 1550 °C to measure melt infiltration. The results revealed notable differences among the coatings, with Y_2O_3-coated crucibles demonstrating nearly two orders of magnitude less erosion compared to MgO and CaO crucibles. Al_2O_3 also exhibited promising results, showing one order of magnitude less erosion. Subsequently, the effect of the compacting force of yttrium particles and sintering temperature was investigated for crucibles with porosities of 40%, 20%, and 15%.

The study established a logarithmic relationship between metal penetration and the duration of the melting process while maintaining a proportional relationship between porosity percentage and the extent of erosion [56].

The porosity is formed mainly during crucible fabrication, the principal methods being the pressing and sintering processes, where particles of various sizes are filled into a mold in the shape of the final crucible, and a compression force is applied and burned to obtain the desired shape and characteristics. Higher pressures and temperatures result in crucibles with lower porosity, higher compaction, and better mechanical properties [57]. Nevertheless, even if it might induce erosion, crucibles contain a minimum and controlled amount of porosity left to improve the thermal shock resistance [58].

2.3.3. Thermo-mechanical resistance

Another field of investigation for crucibles has been the thermal shock resistance due to the severe thermal and stress gradients present during Ni-based superalloys melting [59]. It is more critical for industrial-size crucibles, where large mass and long melting and refining times. The thermal cycling test determines the number of cycles a crucible material can withstand before cracking and breakage. Usually, ceramic crucibles have a relatively low thermal shock resistance compared to metal crucibles being a challenge in upgrading ceramic crucibles. Highly thermal resistance crucibles exhibit low thermal expansion coefficients, and the Young-modulus temperature dependence was determined as a critical factor for crucible resistance [60].

Furthermore, researchers have employed the Finite Element Method (FEM) to develop thermo-mechanical transient models capable of predicting stress-thermal fields and assessing the resulting damage to the liner [61]. In the modeling context, aluminum's energy consumption during melting and holding time was investigated considering the thermal properties of the crucibles [62]. Moreover, they have developed statistical models to estimate thermal conductivity, considering variables such as temperature or porosity. However, it should be noted that an increase in the number of dependent variables leads to a decay in the accuracy of these models [63].

Thermal conductivity depends on several principal physical variables, including bulk density, porosity, and microstructure [64]. In the case of polycrystalline oxides, grain orientation, size, and the presence of pores and impurities play a crucial role in determining heat conduction capacity. The last two aspects are particularly significant for thermal conduction, as higher porosity and lower crucible density reduce thermal conduction [65]. Therefore, it is recommended to conduct experimental measurements for each sample. While the measurement of refractories during metal solidification into molds has received considerable attention, the influence on crucibles or liners has not yet been investigated.

Despite the available reference values in databases and handbooks, considerable scattering is observed, limited to specific compositions, relatively low measuring temperatures, and the absence of a unified criterion for measuring techniques [66]. Regarding measurement methods, a comparison was made between four techniques for vermiculite and clay-based refractory crucibles to determine thermal conductivity. The study concluded that sample humidity, porosity, and heterogeneity contribute to a minimum discrepancy of 10% in the measurement results.

2.4. Numerical Modeling

After reviewing the technical aspects of the VIM process, the melting and refining procedure, and the principal process variables, it can be concluded that it is a complex melting technology. The coexistence of various physical fields and many variables requires solid experimental background for a proper melting procedure, where a slight deviation might negatively affect the final component. Therefore, incrementing the knowledge from a theoretical perspective is necessary to deepen the understanding of the influence of the process variables, melting procedures, and conditions, to name a few. In this regard, developing numerical models can be considered one of the best approaches due to their relative precision, flexibility, and reduced cost.

As mentioned, induction heating melting is a complex multi-physical phenomenon characterized by the simultaneous existence and interaction of magnetic, thermal, and fluid fields. To achieve comprehensive numerical modeling, each of these physics must be taken into account, and coupling. Consequently, the literature review has been structured based on the material state, specifically the solid and liquid phases.

This categorization thoroughly examines the research conducted across induction heating and melting phenomena. Lastly, it provides a dedicated review of studies investigating the coupled heat transfer in liquid metals. Next, the fundamental numerical methods and the most relevant results in this field are explained.

2.4.1. Review of induction heating modeling

Extensive and highly specialized literature discusses numerical methods used in induction heating. However, this document does not delve into the detailed analysis of these methods. A comprehensive overview of different numerical methods, including key authors and reference publications, can be found in Lavers' review. Among the various numerical methods, the most widely employed for induction heating applications is the FEM [67].

Induction heating involves coupling two phenomena that operate on different time scales. The electromagnetic problem consists of low- and medium-frequency sources (50 Hz-10 kHz), while the thermal problem can span several minutes. Coupled models utilize iterative time steps to compute the magnetic field based on temperature-dependent material properties. The resulting distribution of resistive losses drives the temperature solution, updating the material properties and recalculating the magnetic field at each time step [68]. Simplifying the problem, the electromagnetic and thermal coupling is commonly simulated in a 2-D axisymmetric computational domain [69]. Alternatively, the thermal problem can be discretized only in the workpiece, accounting for the thermal non-linearities of the materials, while solving the magnetic problem in the complete geometry [70].

Tavakoli [71] investigated the positioning of the coil and volumetric heating on the workpiece (Figure 2-12). The 2D steady-state power distribution and heating pattern for different heights of metal cylinders were studied. Height ratios below one between the workpiece and coil resulted in overheating and non-uniform heating power profiles along the workpiece length. Additionally, high-intensity heating at the workpiece edges led to longer coils, emphasizing the importance of accurately designing the coil length.
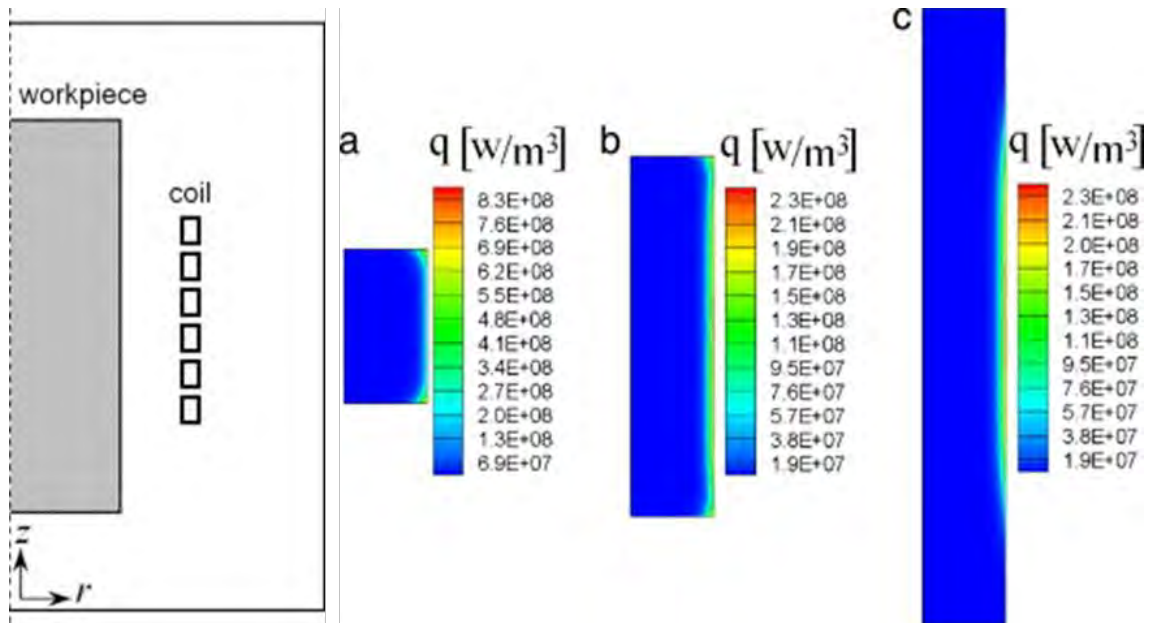
Figure 2-12. Power distribution in the workpiece with various heights ingots [71].

Moreover, the influence of coil shape on heating efficiency was examined, comparing circular, conical, square, and oval configurations. The study concluded that an oval shape provided the most uniform heating and greater efficiency for cylindrical ingot workpieces [72].

Another crucial aspect of numerical models involves correlating them with experimental results to determine appropriate boundary conditions. Yang et al. [73] developed a 2D FEM induction model to calculate heat and temperature transfer for three metals: aluminum, steel, and TiAlNb. The coupled transient model heated solid cylindrical workpieces implementing temperature-dependent thermo-physical properties. The model's validity was established by comparing the results with measurements from five thermocouples placed at different heights within the load, demonstrating an acceptable correlation. The heat transfer submodel accounted for conduction and radiation losses resulting in the temperature flattening. However, it should be noted that the transient temperature results only qualitatively reproduced the trend, as the impact of heat transfer by conduction and radiation increases with temperature.

Using PID control, Fisk [76] validated a coupled model that simulated the heating process in an Inconel 718 alloy. The model was compared against experimental thermocouple measurements, estimating the current and frequency parameters required to achieve the desired temperature in the workpiece.

Kranj et al. [74] studied induction heating for steel billets and the experimental measurement by thermographic images as an alternative to thermocouples. The results demonstrated good agreement between the experimental and numerical findings, emphasizing the significance of incorporating temperature-dependent thermal and electrical properties.

It has to be noted until now that it has considered the material in the solid state, as the liquid heat transfer mechanism demands the incorporation of the flow field and the turbulence behavior, which is discussed in the following section.

2.4.2. Induction melting review and modeling

- **Principles of induction melting**

The field that studies the interaction between magnetic fields and electrically conductive fluids is magneto-hydrodynamics [75]. When the coil carries an alternating current (Ji), it creates a magnetic field (**B**) that induces a current in the conductive fluid in the opposite direction (J_B) (Figure 2-13).
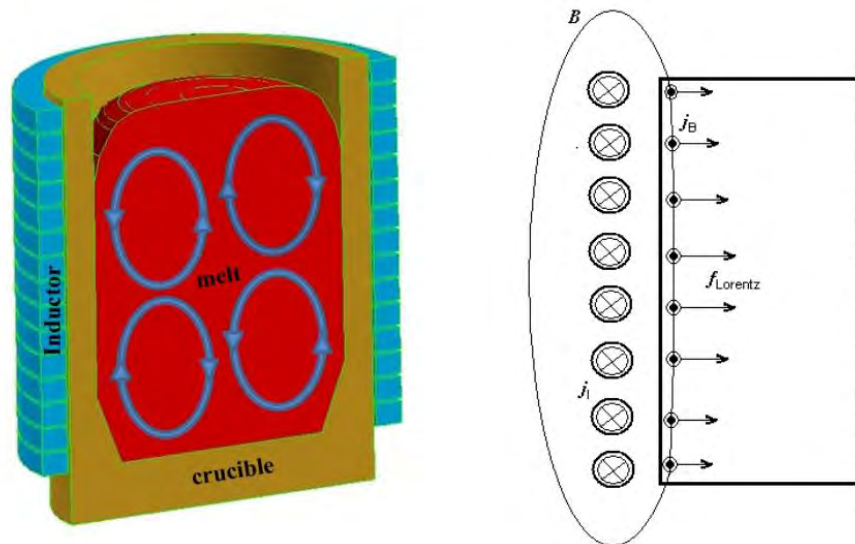
Figure 2-13. Depict of an induction furnace and axisymmetric Lorentz forces [76].

Additionally, these currents give rise to a new magnetic field that distorts the original field. At the boundary of the liquid metal, the magnetic field is a combination of the externally supplied field from the fixed alternating current coil and a field in the opposite direction generated by the induced currents in the metal. These changes in the magnetic field introduce strong non-linearity into the process. The cross product of the induced current (J_B) and the magnetic field vectors (**B**) is the Lorentz Force (F_L) and acts as an inertial term on the liquid metal, causing deformation of the free surface and the recirculation of the flow [76].

The velocity of a liquid metal generated by a single-phase AC magnetic field has been a matter of study; the first measurements focused on determining the flow pattern and averaged velocity. The first measurement employed a hot-film anemometer to measure average velocity, turbulent intensity, and time spectra. The main drawback of this method is the high metal thermal conductivity and temperature not being able to use for temperatures up to 100 °C [77]. Afterward, with the development of a permanent magnet probe with antipodal pair of electrodes, local velocities and turbulence of large vortices of molten metal up to 700 °C were measured [78].

In addition to the averaged flow velocity, turbulence fluctuations are significant. In this regard, Umbrashko [79] identified short and long-period velocity fluctuations with potential difference magnetic probes for the measurements. These velocity fluctuations are quantitatively described as the distribution of the melt flow's turbulent kinetic energy (k). The turbulent kinetic energy of the melt and the associated mass transport is proportional to the ratio of the specific power and frequency $k \approx P_m/f$ where the authors, the maximum turbulent energy is between the vortices of the averaged flow near the crucible wall.

The most intense pulsations of these low-frequency flow oscillations are located near the crucible wall between the main upper and lower vortices and have a characteristic period depending on the current inductor. The Lorentz force (F_L) and the harmonic magnetic field (**B**) can be divided into average and

oscillatory components. The averaged component is responsible for the volumetric motion being the source term for the Navier-Stokes equations. On the contrary, the oscillatory part introduces instabilities on the surface of the liquid metal. This component, with a twice oscillation frequency of the magnetic field, and various authors recommend taking into account if the field frequency is minimum < 5 Hz [80].

Possible reasons for these low-frequency oscillations are flow instability [77] and the continuous generation and dissipation of large-scale vortices represented by several peaks in spectral energy [81]. These low-frequency oscillations and high-frequency pulsations between the two vortices are the reason for the homogenization of temperature and material between the upper and lower parts of the melt. Moreover, it aids in separating the suspended oxides and thus favors the formation of deposits on the crucible wall [82].

- **Flow recirculation and turbulence modeling**

Extensive research has been conducted on magnetically driven metal flow phenomena, with a specific focus on the cases of induction melting. Initially, models were developed based on the general assumption that, for a low magnetic Reynolds number (Rm), the magnetic field propagation is significantly faster than the fluid velocity, allowing for the decoupling of the fluid flow. The fluid flow field and associated turbulence variables were solved using the RANS k-ε model and wall functions. Adhering to this criterion, the time-averaged velocity field was accurately reproduced, exhibiting a notable correlation with experimental observations. [83] [84].

An alternative k-ω turbulence model, as demonstrated by Bojarevics and Pericleous [85], exhibited potential adequacy for complex turbulent flows. This model takes into account nearly laminar fluid regions where turbulent viscosity μ_T approaches zero while simultaneously generating highly intense turbulence, such as in areas subjected to rotational body forces and near-wall layers. The authors concluded that it effectively reproduced the general flow structure and demonstrated good agreement with respect to local velocities and turbulence intensity levels [86].

In recent studies, Bulínski et al. [87] compared various turbulence models, including RNG k-ε, k-ω, and k-ω SST. These models demonstrated a consistent trend by accurately reproducing the recirculation effect. The only notable difference observed was in the magnitudes of the flow field, with the RNG k-ε approach yielding lower velocities than the rest, and the authors considered this model to be the most accurate.
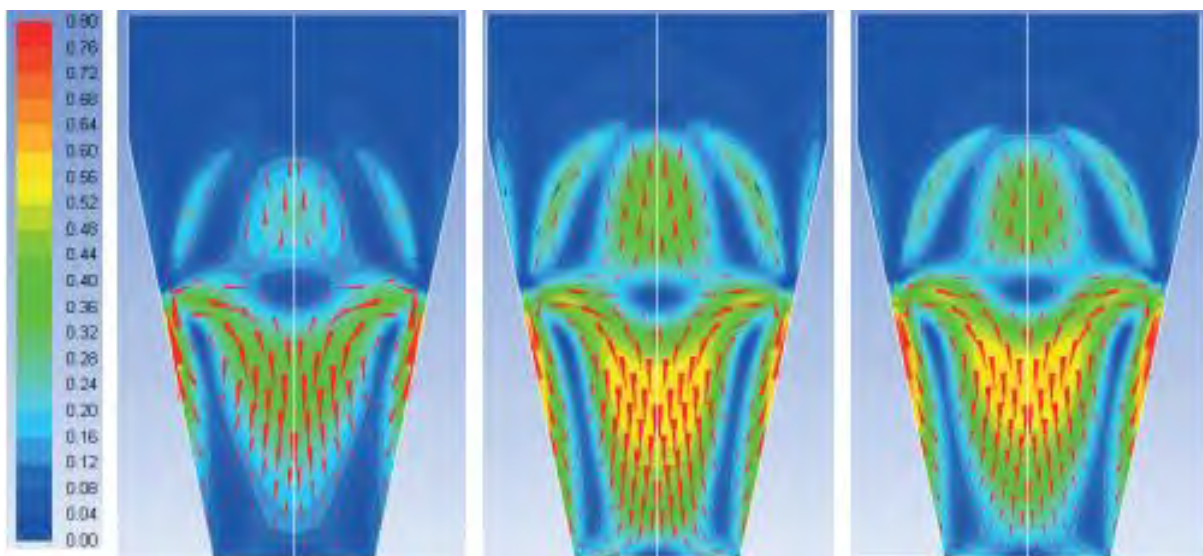
Figure 2-14. Velocity field comparison for turbulence models. Left, k-ε. Center, k-ω. Right, SST [87].

However, the main limitation of two-equation turbulence models lies in their assumption of isotropic turbulence, which leads to the consideration of effective viscosity as the sum of laminar and turbulent viscosity. To address this issue, Baake [88] developed an extended version of the standard k-ε model that incorporates additional factors and resolves turbulence using a low Reynolds k-ε approach. This modification successfully captured the additional turbulence generation caused by low-frequency fluctuations and achieved a qualitative agreement with experimental results.

Even the straightforward approach is the RANS formulation Large Eddy Simulation (LES) models are an alternative to two-equation turbulence models and are considered more suitable for complex turbulent flows [89]. The principle behind the LES turbulence approach is that the small-scale eddies are modeled, with a smaller size than the mesh size, while the higher eddies are resolved numerically. Thus it assumes that the large-scale eddies depend on the flow conditions while the behavior of small scales is isotropic. This way, LES modeling considers 3D unsteady turbulent motions and small-scale eddies. However, the computational requirement to resolve the necessary 3D transient model requires higher resources and time [76].

In this context, Kirpo [90] compared RANS turbulence models and LES Smagorinsky for a liquid metal flow confined in a cylindrical container. The comparison revealed a similar velocity profile, even in the case of LES, suggesting that the models adequately represent steady stated averaged flow conditions. However, unsteady situations exhibited a higher discrepancy, as the turbulent flow exhibited large-scale periodic instabilities in the melt, consistent with experimental observations.

Notably, the LES approach showed a turbulence viscosity one order of magnitude lower than that predicted by the k-ε model. In contrast, the RANS method predicted higher values at the center of the eddies, while lower values were observed between the eddies. This distribution reflected the characteristic behavior of the 2-D k-ε model and was also reported in 3-D transient models. Conversely, the sub-grid viscosity distribution in LES exhibited variations, with maximum values occurring in the vortices that interact within the near-wall region and between the eddies in the recirculated flows [91].

- **Free surface hydrodynamics**

The second effect of the Lorentz force is the magnetic pressure gradient that deforms the surface generating the characteristic convex meniscus profile of the free surface of the metal. Due to changing operational parameters, medium flow instabilities, and high turbulence kinetic energy values, free surface behavior can be remarkably unstable; a significant change in furnace operating current or frequency values can lead to free surface disturbances. The height of the meniscus at the center of the melt depends on the applied power and the root frequency of the coil current $h_m \approx k P_m / \sqrt{f}$. This deformation can be beneficial in reducing the contact area between the melt and the wall. The free surface deformation is the balance of hydrostatic and hydrodynamic forces, the magnetic pressure, and the contribution of the surface tension.

- **Free surface modeling**

The typical solution for calculating the free surface profile or "meniscus" in induction furnaces relies on determining a steady-state free surface computing in a 2D axisymmetric formulation and balancing the Lorentz force and hydrostatic pressure [92]. In the classical solution of the stationary meniscus in hydrostatic models, only the potential part of the Lorentz force is considered, ignoring the rotational part corresponding to the recirculation of the alloy [93].

More accurate 2D calculations of the meniscus shape were obtained by including the flow contribution. Assuming that the moving fluid does not influence the external magnetic field, the simulation was

divided into two tasks, electromagnetic and hydrodynamic, and solving them sequentially. The magnetic field was initially solved using ANSYS Classic®, determining the Lorentz force contribution, which acts as a mechanical momentum term for calculating the flow field. Then, the steady-state hydrodynamic flow was solved with ANSYS CFX® via the Eulerian approach with the volume of fluid (VOF) to track the free surface deformation [90].

A similar solution is proposed by Bulínski et al. [87], studying the mass transport of the flow and surface deformation profile geometry for aluminum melt in a coupled way by separating the calculation into two stages. Simulation results were validated with a 3D laser scanning projection and posterior triangulation by registering the reflection by a camera. The profile shape was correctly reproduced, with a slight deviation in the wall region due to the limitation of the laser and underestimation of the maximum height. In addition, the sensitivity analysis evaluated the influence of the liquid aluminum material properties, electrical conductivity, viscosity, surface tension, and wetting angle, concluding that electrical conductivity and the Lorentz Force have the most significant impact [94].

Even though this approach is valid as a first approximation, newer references and experimental results have indicated that the hydrodynamic component must be included for more precise modeling. Spitans [95] enhanced the turbulence of the recirculating flow computed with the RANS k-ω Shear Stress Transport (SST) turbulence model. The time interval is assumed to be small enough to modify the geometry during a step and can be considered a constant Lorentz force distribution. The data transfer between ANSYS CFX® and ANSYS Classic® was done with an external coupler. This coupler transferred free surface coordinates and connectivity among them, forming elementary polygons, and filtering was applied to avoid generating distorted elements on the surface.
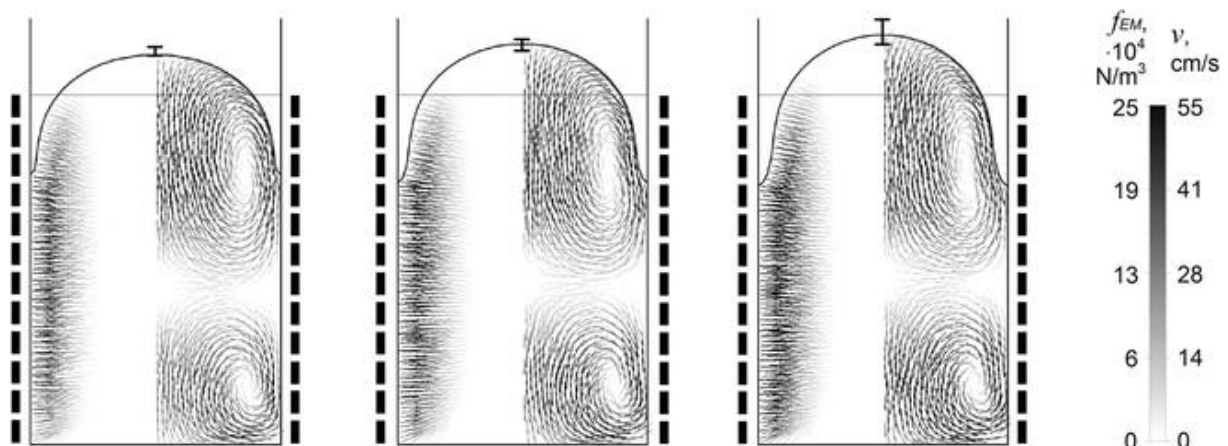
Figure 2-15. Lorentz force (left), steady-state flow pattern (right), and meniscus shape [95].

2.4.3. Liquid metal turbulent heat transfer

So far, the coupling of two isolated physical phenomena has been discussed, heating by magnetic induction and flow recirculation by the magnetic field. However, when the heat transfer mechanism is coupled to the flow recirculated by the magnetic force, the three physics union is achieved corresponding to the VIM process. It is in this last field that relates the mass and heat transfer in the melt where there is scarce literature.

For the specific case of liquid metal, it is considered a low Prandlt (Pr) number problem as it is in the order of magnitude between 10^{-2} and $10^{-3,}$ whereas for water and air, it is Pr 0.7 and 1, respectively. The same occurs for liquid metal's density and thermal conductivity, which are several orders higher. It even is possible to state that heat conduction plays a dominant role since the thermal diffusivity of liquid metal is larger than the kinematic viscosity.

Therefore the parameter that relates both thermal and velocity field with the turbulence is the turbulent Prandlt number (Pr_t). The Pr_t reflects the characteristics of turbulent flows, where heat transfer is primarily driven by convective mixing rather than molecular conduction, quantifying the ratio of turbulent momentum transfer to turbulent heat transfer within the fluid. In order to measure Pr_t at any boundary layer point, it is necessary to consider four components: the turbulent shear stress, the turbulent heat flux, the velocity gradient, and the temperature gradient. This difficulty makes direct measurements of Pr_t sparse and with a large scatter of the experimental data requiring the employ of numerical simulations.

Many attempts have been made to accurately model the turbulent heat transfer of liquid metal by employing DNS and wall-resolved LES methods, most related to metal-cooled nuclear reactors [96]. DNS involves the complete solution of the time-dependent Navier-Stokes and thermal energy equations for a turbulent flow. For example, for channel fluids, Abe and Kawamura [97] provided interesting results for various Re numbers up to $Re_t=1020$ and Pr down to 0.025. At Pr <0.2, it was evidenced that Pr_t was not constant depending on the wall distance, as seen in Figure 2-16.
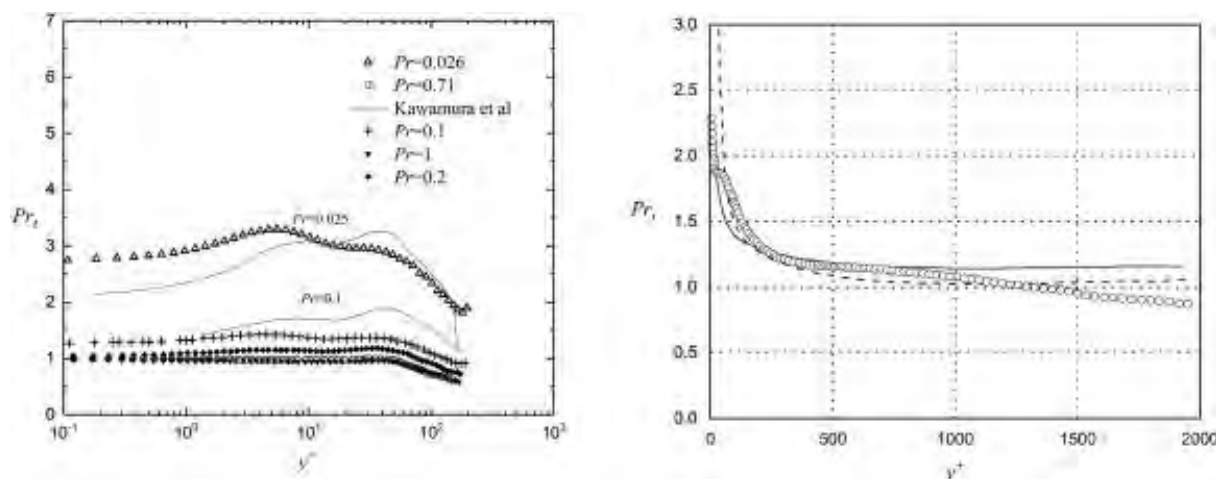
Figure 2-16. Turbulent-Prandlt-number (Prt) in the near-wall region [98].

The Pr_t decreased in the near-wall region where the turbulent viscous effect and heat flux coexist; thus, a fixed Pr_t value would produce unsatisfactory results. Bricteaux et al. [99] verified it by considering LES and DNS approaches and obtained a value of $Pr_t\approx2$ for LES and DNS simulation of the flow characteristics of liquid metals between two plates at moderate Reynolds numbers and Pr=0.01.

However, the DNS calculations reported to date are for low Reynolds numbers, so it is difficult to distinguish the log region as the sublayer merges almost directly into the developed flow region. Despite the rapid advancements in computational capabilities, these advanced high-fidelity numerical approaches still require significant computational resources. Furthermore, their applicability is limited to simple geometries and specific Re and Pr numbers values. Consequently, the RANS methods carry greater importance in engineering practice due to their lower computational costs.

A specific solution is introduced when the RANS models describe the flow, introducing a new dimensionless parameter that relates both phenomena. This parameter, known as the turbulent Prandtl number (Prt), establishes the ratio between the diffusivity of eddy momentum and heat transfer. The modified Prandtl mixing length approach applies isotropic eddy conductivities and introduces a thermal length scale, which depends on the distance from the wall and the molecular Prandtl number [98]. In this context, the temperature is derived from the velocity equations, with the heat flux considered an extension of the velocity field, assuming a similarity between turbulent heat and momentum transfer. However, it is important to note that thermal diffusivity tends to be faster than momentum diffusivity,

which presents a significant limitation to this assumption. The thermal boundary layer for liquid metals is significantly more prominent than air due to their higher thermal conductivity, leading to a notable difference in heat transfer. This distinction is illustrated in Figure 2-17.
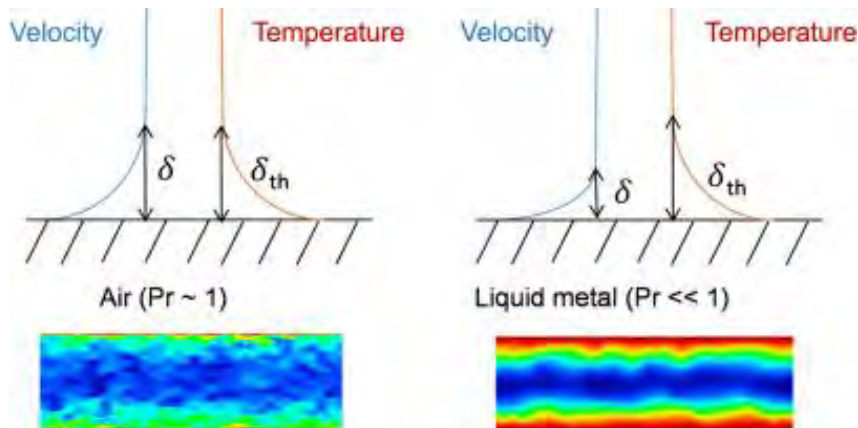
Figure 2-17. Turbulent boundary layer and structures for air and liquid metal [100].

Multiple studies have investigated the relationship between the fluid flow field in the boundary layer and the thermal field, utilizing the Pr_t analogy and considering local parameters such as wall distance (y+) and Pr adopting two principle approaches.

The first approach involves global models that consider the dependence of Pr_t on global flow parameters like Pr, Re, or Pe numbers. These models assume constant Pr_t values throughout the entire cross-section. A notable example is the approach proposed by Aoki and Reynolds [101]. The second approach utilizes local models, such as those developed by Kays and Crawford [102] and Weigand [103]. These models adjust Pr_t based on local spatial parameters and vary its values depending on flow parameters like the turbulent viscosity ratio (μ_t/μ), wall distance in viscous units, or the turbulent Peclet number $Pe_t = Pr(\mu_t/\mu)$. Duponcheel et al. [104] employed LES to study turbulent heat transfer in liquid metal flow between plates at a Reynolds number of Re = 2000. They compared different Pr_t models, including a constant $Pr_T = 0.85$, Kays' correlation, and Kays wall-resolved. Considering the normalized wall temperature and wall distance in viscous units, the comparison is depicted in Figure 2-18.
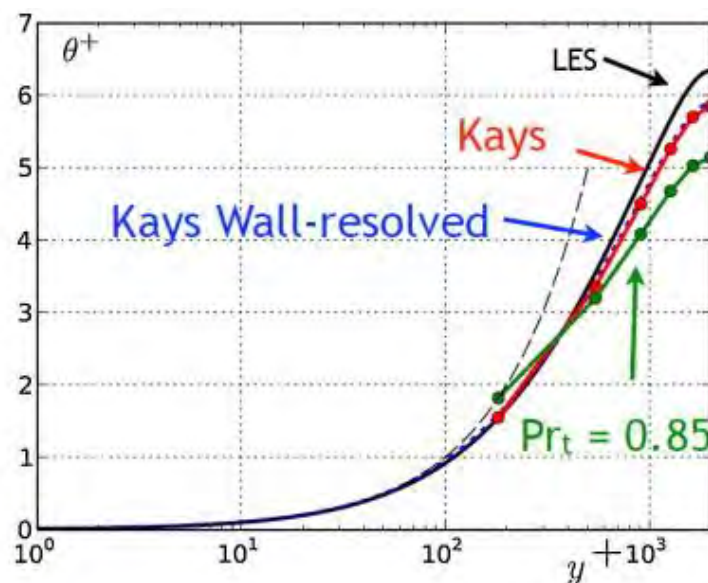
Figure 2-18. Comparison of temperature profiles for RANS at $Re_t=2\cdot10^3$ and Pr=0.01 [105].

Low Reynolds number models have shown promising results in near-wall modeling. A satisfactory solution can be achieved by establishing a connection between shear stress, heat transfer, and turbulence values at the first mesh point near the wall. This modified boundary condition was successfully tested using the SST turbulence model, yielding acceptable results [106]. Furthermore, a case study involving volumetric heating investigated the determination of heat flux in near-wall regions. A low Reynolds number k-ε turbulent model was applied, and various mesh configurations were examined while maintaining a fixed Prandtl number (Pr_t) value of 0.9 [107].

Therefore, it can be stated that there are no consistent criteria for selecting a specific Pr_t model. There is a notorious dependency on each modeling case where the flow field has a notable influence. In general, the different turbulence models should not undergo any change since their turbulent heat transfer mechanisms in these structures are always similar, so there should be an implicit relationship in these models, especially between the global and local turbulence models.

2.5. Critical Review

Ni-based superalloys consist of a complex and precise combination of chemical elements necessary to produce the required hardening mechanisms for superior mechanical properties. Their manufacturing involves intricate technologies to ensure precise metallurgical control. Among these processes, VIM stands out as one of the most effective methods for achieving the desired metallurgical composition. VIM eliminates high-pressure trace elements and gases by operating under a vacuum atmosphere, resulting in proper chemical compositions. The recirculation of the melt facilitates the interaction of alloying elements at the melt-vacuum interface, accelerating reactions and achieving rapid dissolution of alloy additions and homogenization of the melt. The vacuum environment prevents oxidation, enabling exceptional and reproducible control over the reactive elements in the alloy composition.

The crucible's importance in the VIM process is evident as it can introduce metallurgical defects in the form of inclusions due to physical erosion and chemical reactivity between the metal and ceramic material. Although appropriate practices during melting and refining can minimize such defects, their complete elimination is not guaranteed. Extensive research has focused on characterizing the reaction mechanisms dependent on factors like porosity, the chemical composition of the phases, wettability angle, and time. These factors are multifactorial and specific to each facility and melting procedure. However, the thermal aspect of crucibles has not been extensively studied, with the focus primarily on their thermo-mechanical resistance. The impact of the thermal conductivity of ceramic crucible materials on the VIM melting process and its efficiency has not been adequately considered.

The VIM fusion process relies on various factors and components that complicate its control, particularly the coil and power generator. Previous studies have demonstrated that operating variables related to these elements directly affect the melting process, influencing the speed and temperature of the metal. Variables such as frequency, current, and power directly impact the fusion process. Additionally, the power capacity of the generator and resonant frequency impose inherent limitations, restricting the melting capacity based on the material type and mass. The process variables become uncertain during melting, primarily influenced by the resonance coupling between the charge, coil, and power generator. Noncontact methods like pyrometers for continuous measurements or thermocouples for spot measurements are typically employed. Therefore, the characterization and control of these operating variables are crucial for ensuring a controlled and repeatable melting procedure.

Furthermore, the vacuum pressure within the chamber and the presence of residual air can impact the chemical composition by forming carbonitrides or oxides. The vacuum chamber itself, coupled with the high melting temperatures required for Ni-based superalloys and the presence of magnetic fields, pose

challenges in controlling and monitoring the melt. This makes it difficult to measure crucial process variables such as temperature, metal velocity, and free surface deformation.

Therefore, developing advanced numerical models becomes essential for a comprehensive understanding and accurate description of the VIM process. These models need to consider the complex interaction between different fields and be developed in a coupled manner. It is crucial to validate these models against experimental tests to assess uncertainty and error.

Previous studies have primarily focused on the coupling between magnetic fields and temperature increase in magnetic induction heating. The arrangement and geometrical characteristics of the charge on the coil play a critical role in magnetic coupling. Advanced models have incorporated the nonlinearity of material properties, which is particularly important for wide heating ranges. Temperature variation during the model validation process has commonly been measured using contact thermocouples. However, the correlation with experimental results continues to be scarce.

In the context of liquid metal modeling, extensive research has been conducted on metal recirculation and free surface deformation. It is important to note that simulations and experimental validations have primarily been carried out for melting furnaces open to the air due to technical challenges associated with vacuum chambers. The velocity field and stirring phenomenon have been investigated using various turbulence models, including RANS and LES. While RANS models cannot account for low-frequency velocity fluctuations, they have provided reliable results even for the averaged velocity field. The selection and implementation of turbulent models depend on the specific conditions of each case, and no standard criterion has been established. However, it is generally preferable to use RANS models that resolve the flow up to the wall for computing the thermal convection of the flow.

The modeling of the free surface profile has been conducted using computationally demanding fixed mesh methods. The calculations of the magnetic and flow fields have been performed using an uncoupled procedure. Various software programs and meshes have been employed, necessitating additional communication and data transfer subroutines. Therefore, an efficient modeling procedure will be developed that calculates the fields with a strong coupling by employing moving mesh methods.

Regarding heat transfer in turbulent flow, no specific references have been identified for the case of the induction melting process. The Prandtl number governs the relationship between fluid flow and heat transfer, which is exceptionally small for metallic flows and requires specific treatment. Although DNS and LES models that resolve the flow up to the wall are considered more reliable, they have limitations for flows with specific Reynolds numbers and relatively simple flow structures. Also, it has to consider their superior requirement of computational resources. Therefore, analytical relations based on the flow field relate to heat transfer. Applying turbulent RANS models incorporating the Prandtl turbulent number term (Prt) is valid. These analytical models establish relationships between the flow velocity field, turbulent characteristics, and heat transfer. Multiple formulations reviewed in the literature consider their suitability for specific flow cases, which can be implemented in the simulation of the induction melting process.

Chapter 3
3. Material and methods

The following chapter aims to characterize the melting material, Inconel 718, and the ceramic crucibles and establish a standard melting trial methodology. Initially, the chapter discusses the reported properties and measurement techniques employed in the literature for characterizing the melting Inconel 718. It then presents the techniques and measurements for obtaining experimentally selected material properties. Furthermore, the ceramic crucibles, which are as crucial as the alloy, are experimentally characterized in terms of their composition and thermal properties. These properties will be used as input for the numerical models developed in Chapter 4. Numerical modeling.

The second part of the chapter provides an overview of the laboratory-scale VIM furnace, which serves as a reference for developing the numerical model. The chapter explains the experimental setup designed to acquire and monitor process variables during melting. A standard heating and melting procedure is also established to ensure the reproducibility of subsequent melting trials. The chapter also explains the calibration process for sensors and the electrical measurements conducted during a melting test cycle.

3.1. Inconel 718: material properties

Thermal induction heating and melting processes, such as the VIM process, require consideration of material properties related to heat and fluid flow transport. These properties vary depending on the material's state, whether it is in a solid or liquid state. For solid materials, the specific thermophysical properties include density (ρ), specific heat capacity (C_p), thermal conductivity (λ), and emissivity (ε) at high temperatures. The difficulty of measuring these properties increases with temperature, and in the case of liquid metals, viscosity (μ) and surface tension (γ) are essential. Electrical resistivity (R) is also essential for the induction heating phenomena.

3.1.1.   Properties from literature

Thermophysical data available in the literature can be categorized into two main groups. The first group comprises analytical expressions based on elemental thermodynamic and phase transformation principles. While these expressions are generally accurate and reliable, they are limited to specific alloy compositions and may not consider the material's processing history. Data availability across the complete temperature processing range for the VIM process is also limited.

The second group of data concerns properties that have been experimentally determined. In such cases, the obtained values are constrained by the precision and accuracy of the equipment used, the analyzed temperature range, and the reactivity of the samples. This poses a particular challenge when dealing with samples in the liquid and mushy states due to convection effects and interactions with vessels and the surrounding medium.

Inconel 718 is widely employed but challenging to characterize, which explains the scarcity of references reporting experimental measurements. The requirement for high measurement temperatures and the alloy's oxidization tendency complicate acquiring accurate data. Table 3-1 provides an overview of the bibliographic references that report thermophysical property data for the Inconel 718 superalloy, including the material history of heat treatments or as-cast conditions, temperature range, measurement methods employed, and reported properties.

Table 3-1: Resume of principal references for Inconel 718 material properties

Author - Reference	Property	Temperature [°C]	Technique	Material
(McElroy 1978)[108]	R and λ	25-900	Direct Probe	N/A
(Pottlacher 2002) [109]	λ, C_p, ρ, R	727-1827	Pulse Heating	N/A
(Basak 2003) [110]	C_p and R	25-1200	Pulse Heating	As-cast
(Lee 2006) [111]	C_p	25-700	DSC	As-cast / H.T
(Agazhanov 2019) [112]	C_p, λ and α	25-1100	LFA /Dilatometry/DSC	As-cast
(Overfelt 1996) [113]	μ	1350-1475	Oscillating viscometer	As-cast
(Brooks 2001) [114]	μ and γ	1375-1500	Oscillating viscometer	N/A
(Hosaeus 2001) [115]	C_p and R	727-1827	Pulse Heating	As-cast
(Wang 2018) [116]	ρ	1250-1500	Electrostatic Levitation	N/A
(Mills 2002) [117]	Compilation	25-1600	LFA./Dilatometry/DSC	N/A
(O'Flynn 2020) [118]	λ	25-1000	LFA/Dilatometry/DSC	H.T

- **Thermal properties**

The references mentioned earlier employed transient methods to measure the thermal conductivity of the Inconel 718 superalloy. These methods include laser flash, hot disk, and hot wire techniques. Each method has advantages and drawbacks, and there is no consensus on the criterion for selecting the method depending on the characteristics of the material and the availability of standardized methods [119]. The authors determined thermal conductivity by multiplying the measured values of the three main thermophysical properties (density (ρ), specific heat capacity (C_p), and thermal diffusivity (α)).In all cases, the authors progressively increased the sample's temperature within the desired range, performing the corresponding measurements at each temperature step.

$$\lambda(T) = \alpha(T)C_p(T)\rho(T) \tag{3.1}$$

As is logical, this approach provides the most information, although its main problem is the requirement for more significant resources and the possibility of uncertainty and deviations. It is necessary to consider that measuring thermophysical properties can be challenging and may require careful consideration of the experimental setup, sample preparation, and data analysis to ensure accurate results.

Another commonly used method for measuring thermal conductivity is the ohmic pulse-heating technique, which involves resistive volumetric heating of alloy samples. This method estimates thermal conductivity from the electrical resistivity data by considering the Wiedemann-Franz law [120]. According to this law, the ratio between a metal's thermal and electrical resistivity is proportional to the temperature, and the Lorentz number gives the proportionality constant $L_0 = 2.45 \cdot 10^{-8}[V^2 \cdot K^{-2}]$.

$$\frac{\lambda(T)}{R(T)} = L_0 T \tag{3.2}$$

This technique deals with the solid-to-liquid phase transition being suitable for the measurement in the solid and liquid phases. The resolution in the microseconds scale allowed the calculation of the specific heat and the mutual dependencies between enthalpy, electrical resistivity, temperature, and density of the sample.

Figure 3-1 resumes the dependence of thermal conductivity on the temperature, calculated with the literature values shown in Table 3-1 and according to Equation 3.1. The data showed that the thermal conductivity was almost similar for all the authors at temperatures below 800 °C with a linear increment. Mills [117] reported a constant value at higher temperatures near liquidus, while Pottlacher et al. [109] indicated a continuous incremental. A similar trend for the heat capacity can be seen in Figure 3-2, starting in a linear incremental and having a sudden measurement increment at approximately 800 °C, which might be related to the dissolution of the precipitated phases [111]. In the liquid state, constant values were reported for both available references.
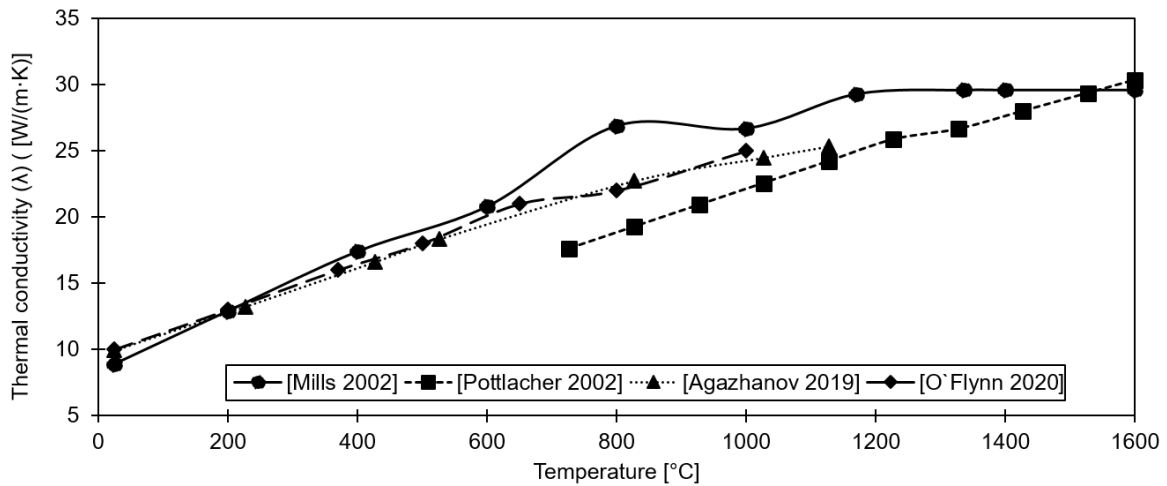
Figure 3-1. Reported thermal conductivity (λ) of selected references.
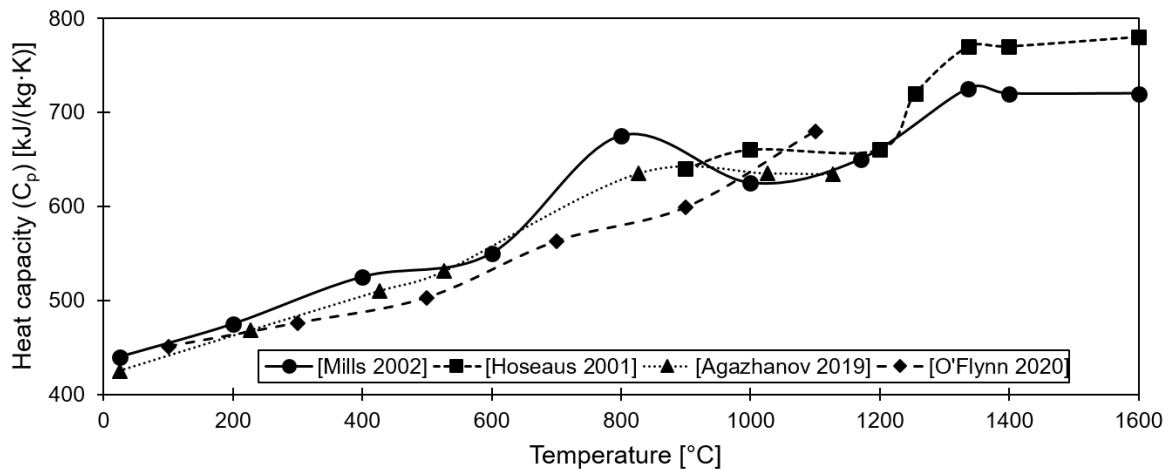
Figure 3-2. Reported heat capacity (C_p) of selected references.

- **Fluid properties**

Additional to the thermal properties when dealing with liquid-state material, specific parameters such as viscosity and surface tension must be considered for modeling fluid flow phenomena. However, for metallic materials in a liquid state, several difficulties arise due to the requirement of the equipment to cope with high temperatures, loss of sensitivity, and interaction with vessels. These difficulties make dynamic methods more suitable. Overfelt et al.[113] reported viscosity measurement on the oscillating viscometer technique. In the mentioned method, the molten metal was confined within a ceramic vessel suspended by a torsion pendulum. As the pendulum oscillates, the viscous dissipation of the molten metal within the vessel affects the motion by dampening the resulting oscillations. The viscosity of the molten metal can be determined by analyzing the time and logarithmic attenuation of the oscillation amplitude. Reported results are consistent, with similar values and a decreasing temperature trend for

the viscosity, while the surface tension maintains almost constant in the studied temperature range, summarized in Table 3-2.

Table 3-2. Resume of reported fluid properties of Inconel 718.

Reference	Temperature range [°C]	μ [mPa·s]	γ [N/m]
(Overfelt 1996) [113]	1350-1475	7.4 – 5.7	-
(Brooks 2001) [114]	1350-1600	7.6 – 5.2	1.82
(Mills 2002) [117]	1336-1500	7.2 – 5.3	1.88 - 1.86

- **Electrical resistivity**

Electrical resistivity, the inverse of conductivity, is another critical material property closely related to heat induction. Resistivity increases with temperature as the metal atoms and electrons' vibration energy is enhanced; thus is necessary to characterize the function of the temperature.

The most commonly used method is the four-probe potentiometric method, where the potential drop in the sample is measured by applying a constant current density [121]. Following this method, McElroy [108] measured Inconel 718 with two electrodes; however, the principal limitation resided in the relatively low temperature of the sample as the measuring devices were made of copper. Basak [110] increased the measuring range to 1200 °C. The results obtained by this author show that the resistivity gradually increased to almost 800 °C with a small peak due to the dissolution of the hardening precipitates and remained stable until the melting temperature. Hosaeus et al. [115] performed solid and liquid state measurements for Inconel 718 with the pulse heating method temperature ranging between 850 °C and 1500 °C increasing from 1.4 μΩ/m to 1.5 μΩ/m
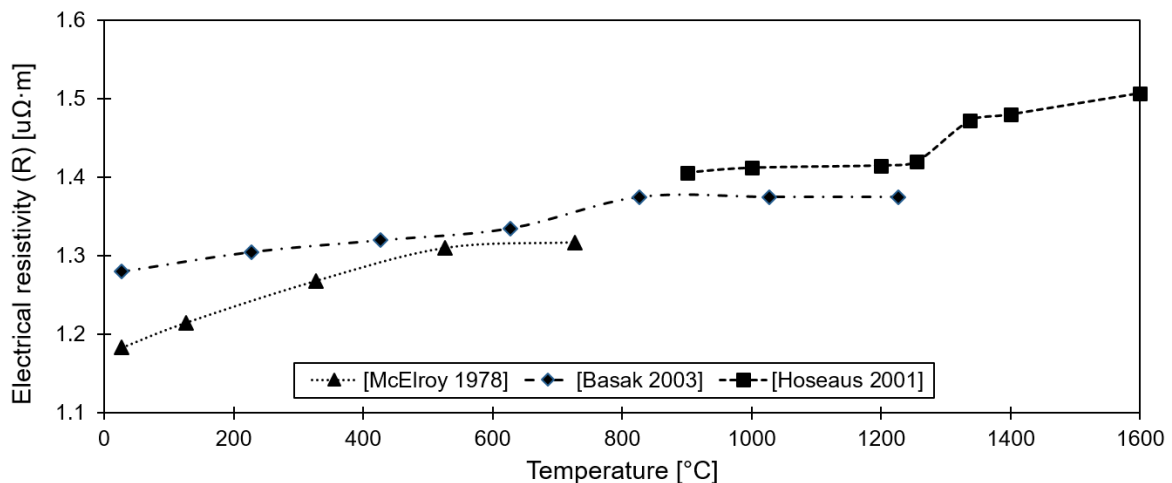
Figure 3-3. Electrical resistivity of selected references

- **Surface emissivity**

Several articles in the literature deal with the emissivity of Inconel 718 alloy; however, a notable disparity was found as there was a strong dependence on the surface quality of the sample, temperature, and the employed technique. In this regard, Keller et al. [122] completed a detailed resume by considering multiple aspects from which it can be concluded that the result depended principally on temperature, measurement method, and the sample surface finish and roughness, reporting spectral emissivity values varying between 0.2 and 0.8.

Considering the variability of emissivity measurements, it was decided to characterize it for the actual melting material. It is important to note that the testing material was provided by ITP Aero, which had already conducted experimental measurements in previous studies [123]. In its as-cast condition, the material was cut into samples using electro-discharge machining (EDM) while ensuring a surface for a Ra = 2.7 µm surface quality. The total hemispherical emissivity as a function of temperature (Figure 3-4) was derived by integrating the directional spectral emissivity values within the range of 2 to 12 µm, accounting for 90% of the total radiation.
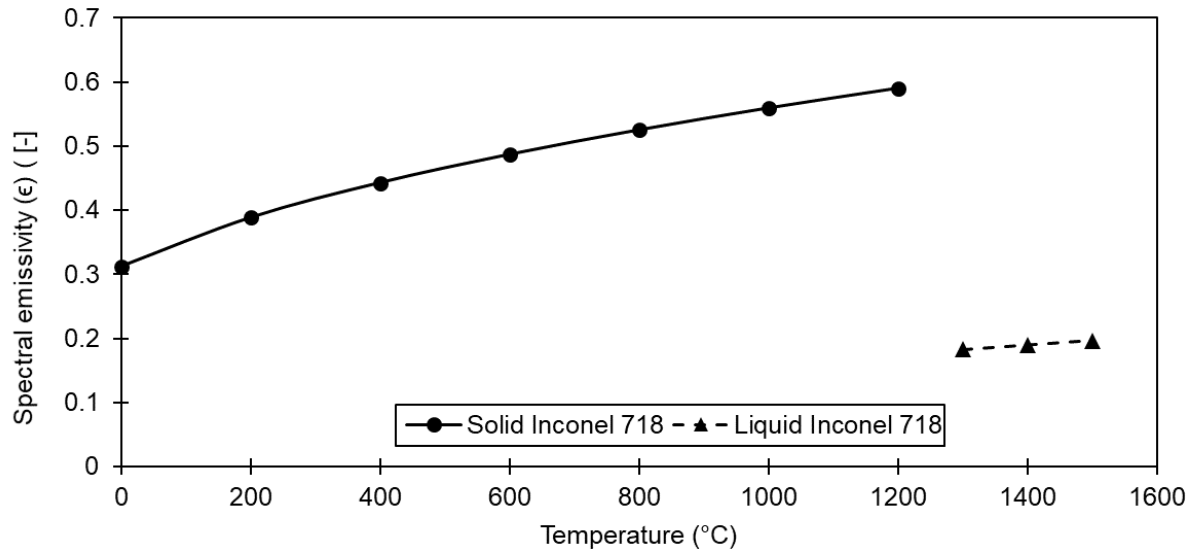
Figure 3-4. The normal spectral emissivity of solid and liquid Inconel 718.

3.1.2. Experimental characterization of Inconel 718

The thermal conductivity (λ) characterization involved measuring three fundamental thermophysical properties up to 1000 °C, and the obtained results are presented in Figure 3-6. The Wiedemann-Franz law was considered to establish the relationship between thermal conductivity and electrical resistivity. Regarding the liquid state of Inconel 718, a consistent behavior was observed for viscosity and surface tension, and the model will incorporate the references provided by Mills [117].

Samples for each test were extracted from an as-cast Inconel 718 bar produced by Cannon-Muskegon Corporation and supplied by ITP Aero. Subsequently, we used EDM to cut smaller ingots weighing 2 kg each, which were shaped into melting cylinders for the subsequent experimental trials.

Figure 3-5. a) As-cast Inconel 718 superalloy ingot. b) Samples for thermal characterization.

- **Density (ρ)**

Density was determined with the Linseis® L75 Platinum Series dilatometer; the prepared samples were cylinders of 5 mm diameter and 17 mm length. The test was performed in an argon atmosphere to minimize oxidation of the samples at high temperatures and avoid fluctuations in the reading. The results showed a linear decreasing trend over the whole measuring temperature range.

- **Specific heat capacity (C_p)**

The differential scanning calorimetry (DSC) technique was done to the samples with a Netzsch STA 449 F3 Jupiter®. The sapphire method is comparative, where three measurements follow identical conditions. The first two empty crucibles, made of Pt-Al_2O_3, are measured to calibrate the equipment following the complete DSC program. In the second one, a flat sapphire disk was inserted in one crucible with a mass approximate to the measuring sample, and the specific heat capacity was measured. Finally, the sapphire disk was changed to the Inconel 718 samples to measure the Cp. Three samples of each crucible were extracted, grounded to Ø 5 mm and 2 mm height dimensions, and fired to eliminate humidity before testing.

- **Thermal diffusivity (α)**

In the same manner, thermal diffusivity, which related the reaction velocity of a material to a temperature variation, was measured. Laser flash analysis (LFA) was done on the crucible samples with a Linseis LFA 1000®. The technique employs a millisecond duration irradiated energy pulse to the front face of the sample that was heated to measurement temperature. The detector placed on the backside measures the temperature increment. The samples were extracted from melting ingot and machined to obtain samples with dimensions of Ø 10 mm and 1 mm height with parallel faces.
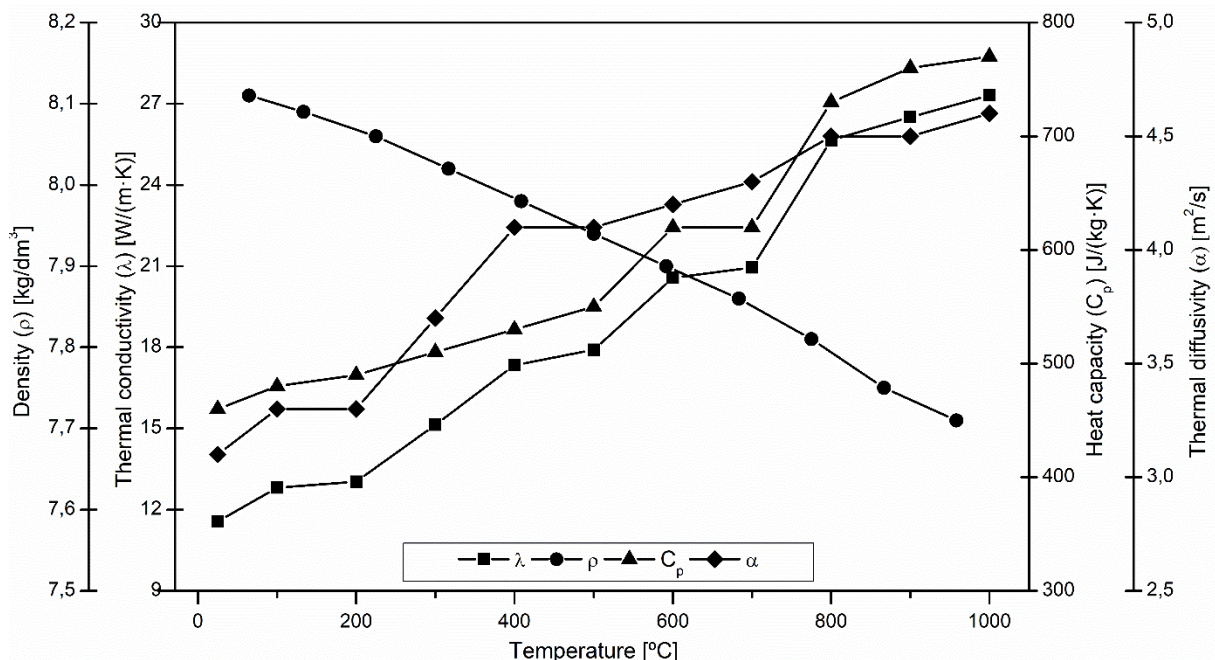
Figure 3-6. Thermophysical properties at solid-state for the as-cast Inconel 718 superalloy.

3.2. Ceramic crucibles: selection and characterization

From a metallurgical point of view, the ceramic crucible is as essential as the alloy to be melted for the VIM process. In the literature review, it has been evidenced that the effect of the crucible on the VIM efficiency has not been covered up to date as well no available reactivity studies for Inconel 718. Along the same line, ceramics' thermal properties depend on various factors such as the crystalline structure, porosity, and impurities. Thus, considering the standard measurements required to characterize each specific composition is not feasible. This section explains the selection and characterization of suitable crucible materials for melting Inconel 718.

3.2.1. Crucible material selection

The principal crucible composition selection criteria have been the capacity to withstand Inconel 18 superalloy melting temperatures, chemical inertness, availability, and its use in real industrial applications. Alumina (Al_2O_3), mullite ($Al_6Si_2O_{13}$), magnesia (MgO), and zirconia (ZrO_2) based crucibles were selected due to their notable composition difference, thus expecting higher performance differences. Also, no published results cover these ceramics compositions and Inconel 718 reactivity.

- **Composition of the crucibles**

Crucibles manufactured by Capital refractories LDT were selected for the characterization and posterior melting trials based on alumina (AL97I), magnesia (MG95I), mullite (ML72I), and zirconia (ZC93I). AL97I was considered the reference crucible material. All were manufactured by hot isostatic pressing process and had the exact final dimensions, inner Ø 62 mm and 160 mm height and outer Ø 75 mm and 175 mm height.

The material's composition and crystallographic structure must be characterized as they will influence the thermal properties of the crucibles and the ceramic-metal reactions. For this purpose, a combined semi-quantitative wave-diffraction X-ray fluorescence (XRF) and X-ray diffraction (XRD) analysis was done. XRD with a PANalytical Xpert PRO diffractometer equipped with a copper tube with a vertical goniometer was employed for the crystal structure and phase identification. The instrumental conditions used were a current generator of 40 kV and 40 mA with an angular sweep between 5° - 80°. The specific software PANalytical X'pert was used for phase identification in combination with the PDF database. The XRD pattern indicated that only oxide compounds were present on the crucibles.

A PANalytical model AXIOS was employed with an Rh tube and three detectors for the chemical compositional XRF. The semi-quantitative software used was based on the measurement of a set of scans, with different analyzing crystals, to determine different analyzers crystals, to determine the presence of the different elements. The semi-quantitative evaluation was performed based on the fundamental parameters method. The results are expressed in w.t. % of oxides in Table 3-3.

Table 3-3. Crucible chemical composition measured by XRF.

Crucible Reference	Chemical Analysis [wt. %]						
	Al_2O_3	SiO_2	MgO	CaO	Fe_2O_3	ZrO_2+HfO_2	Other
AL97I	94.4	4.4	-	0.2	0.5	-	0.5
MG95I	1.1	2.1	92.4	2.3	1.1	-	1.0
ML72I	71.0	24.3	-	1.4	1.1	-	2.2
ZC93I	1.7	1.2	-	4.5	0.4	91.0	1.2

3.2.2. Thermal characterization

The same strategy described for Inconel 718 was used for the thermal characterization. The thermal conductivity was established according to the product among the other three properties. Three samples for each composition were extracted from the new crucibles and polished with discs in a dry state.

- **Density (ρ)**

The density of the crucibles was assumed to be constant by assuming an insignificant thermal expansion. Thus, according to the standard ISO 18754:2020 method B the apparent density was determined by the mass-volume relation; the results are summarized in Table 3-4.

Table 3-4. Density measurement for the ceramic crucibles.

	MG95I	AL97I	ML72I	ZC93I
ρ [kg/m^3]	3050	2950	2320	4350

- **Specific heat capacity (C_P)**

DSC technique was done to the crucible samples with a Netzsch STA 449 F3 Jupiter®. The sapphire method is comparative; three measurements follow identical conditions. The first two empty crucibles, made of Pt-Al$_2$O$_3$, were measured to calibrate the equipment following the entire DSC program up to 1500 °C. In the second one, a flat sapphire disk was inserted in one crucible with a mass approximate to the measuring sample, and the specific heat capacity was measured. Finally, the sapphire disk was changed with the crucible samples with 2 mm height dimensions and fired to eliminate humidity before testing. Figure 3-7 resumed the obtained results with the corresponding measurement uncertainty.
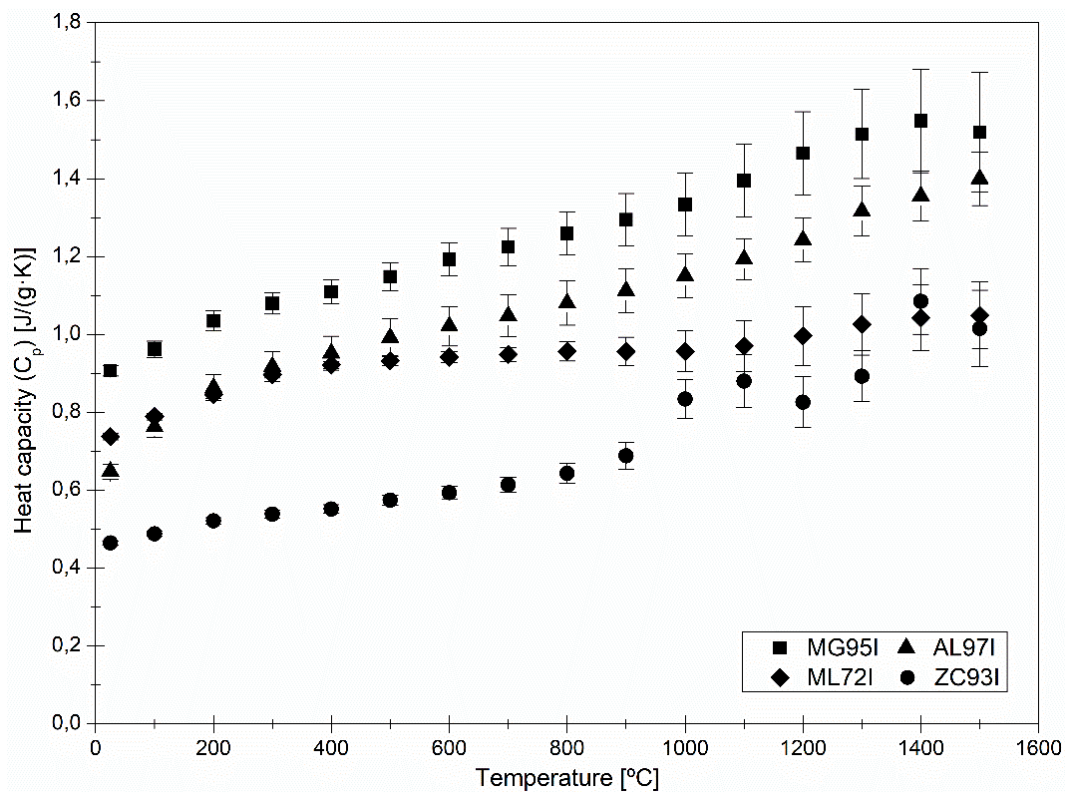
Figure 3-7. Measured heat capacity for the test crucible compositions.

The uncertainty of higher measuring temperatures increased considerably due to the decreased measurement sensitivity at high temperatures as the thermal resistance between the sensor and sample increased. Magnesia and alumina-based crucibles showed a higher heat capacity. Regarding mullite, it indicated a more linear performance maintaining stability at high temperatures. On the contrary, the zirconia-based crucible had the lowest Cp increasing rapidly once it surpassed the 1000 °C barrier; a possible reason could be the structure change from monoclinic to tetragonal at 1170 °C.

- **Thermal diffusivity (α)**

In the same manner, thermal diffusivity, which relates the reaction velocity of a material to a temperature variation, was measured. LFA was done on the crucible samples with a Linseis LFA 1000®. The technique employed a millisecond duration irradiated light energy pulse to the front face of the sample that was heated to measurement temperature. The infrared detector placed on the backside measures the temperature increment. The samples were extracted from the crucibles and grounded to obtain dimensions of Ø 10 mm and 1 mm height and parallel faces. The samples were coated with black paint to improve the heat absorption capacity. The characteristically logarithmic curve was acquired for the four crucibles, pointing to the averaged measurement with the corresponding standard deviation.
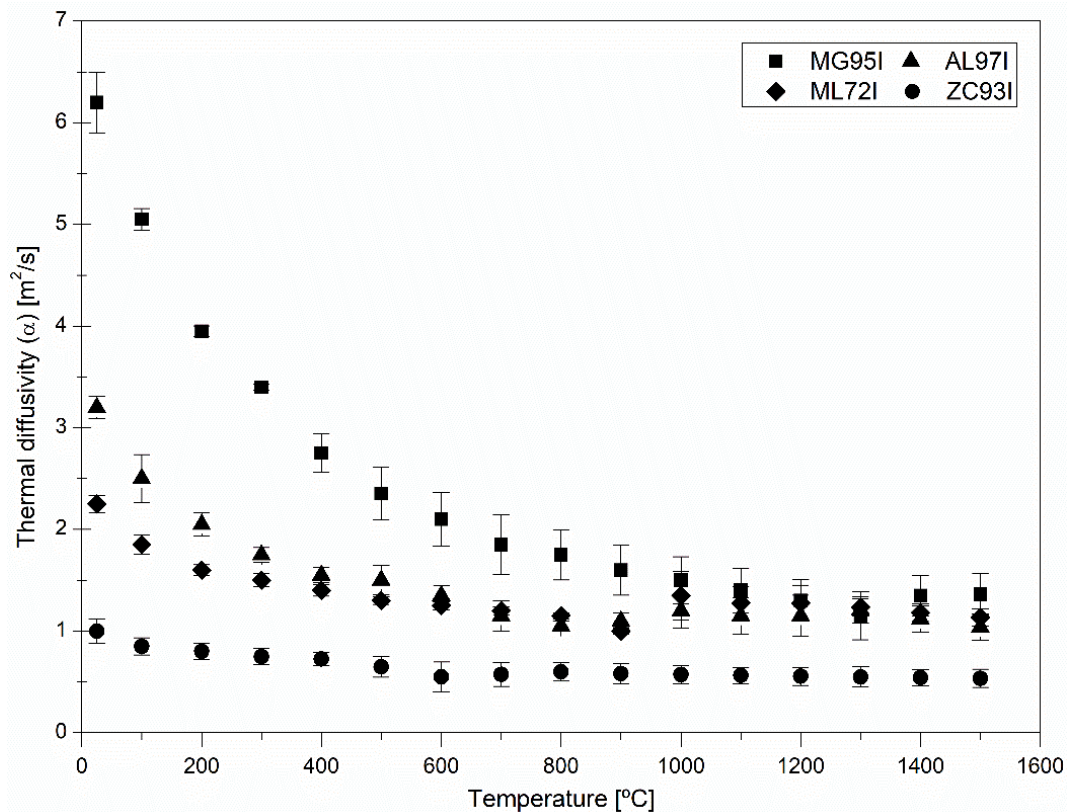
Figure 3-8. Measured thermal diffusivity for the test crucible compositions.

- **Thermal conductivity (λ)**

The thermal conductivity in Figure 3-9 was extrapolated as the product of the density, thermal diffusivity, and heat capacity. The obtained results represented the mean value and the deviation. The results indicated an exponentially decreasing trend of thermal conductivity, obtaining an almost stationary constant value for the highest temperature ranges, reproducing a similar trend as in the thermal diffusivity. Thus, results were more sensitive to this last parameter than the specific heat capacity. MG95I and AL97I-based crucibles indicated a greater thermal conductivity, especially at lower

temperatures, while ML72I had a more linear performance, maintaining constant even at higher temperatures and for the ZC93I.
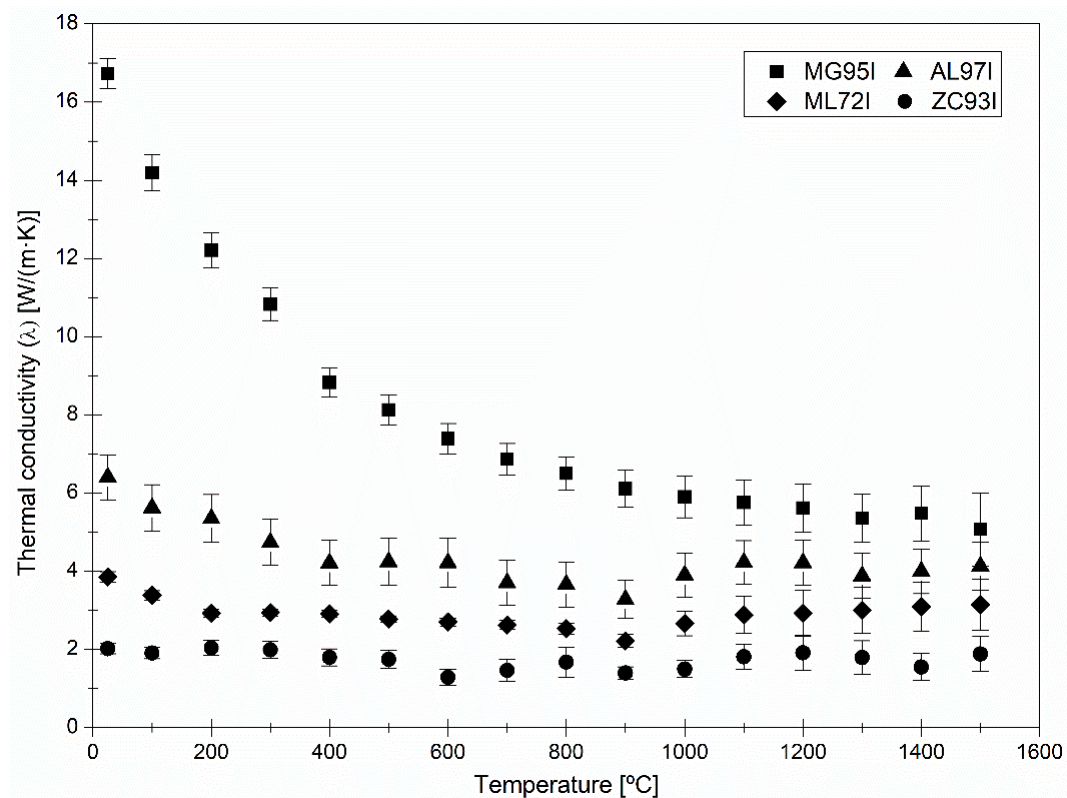
Figure 3-9. Measured thermal conductivity for the test crucible compositions.

3.3. Laboratory scale VIM furnace

The following section presents the vacuum induction melting equipment (Figure 3-10) employed for the trials and considered for the modeling. Mondragon Goi Eskola Politeknikoa (MGEP) has a semi-industrial scale facility for melting in a vacuum and/or protective atmosphere and with interchangeable crucible hot and cold crucible (CCIM/VIM) from SECO-WARWICK S.A. With a melting capacity of approximately 300 cm^3, this facility either allows for the melting of highly reactive and high melting point alloys by using the cold crucible configuration for titanium alloys with 1 kg capacity or through a hot crucible for Ni or Co base superalloys with 2 kg capacity.

For the hot crucible configuration, inside the vacuum chamber, the melt-box sub-assembly is placed, formed by the coil, a ceramic crucible, and the structural housing to hold both. It has to be noted that the melt-box was designed and manufactured by ITG Induktionsanlagen GmbH to adapt the electrical characteristics of the power generator. The seven-turn induction copper coil is electrically insulated to prevent short circuits and protected from thermal conduction heat losses with refractory cement based on Al_2O_3-CaO. The crucible is inserted inside the coil, which works as a recipient to contain the liquid metal. The melt-box is connected to a coaxial port, enabling tilting and metal pouring. This port is connected to a 100 kW and 10 kHz nominal frequency solid-state converter power supply fabricated by Alecto Systems LLC. The seven-turn induction copper coil and vacuum chamber are refrigerated with recirculating water by a single Parker-Hiross ICE® 116 kW chiller.

The vacuum chamber is made of stainless steel and has a cylinder shaper with an outer and inner diameter of 956 mm and 856 mm, respectively. The total length is 1013 mm, while the inner cavity is 867 mm long. The pumping system comprises a MICROVAC 149H rotary piston pump and an MB43

mechanical booster. The vacuum level obtained inside the chamber is in the order of 0.1 Pa. During operation, a constant argon flow of 1 Pa is added to stabilize the free surface and to minimize possible reactivity with the remaining air.
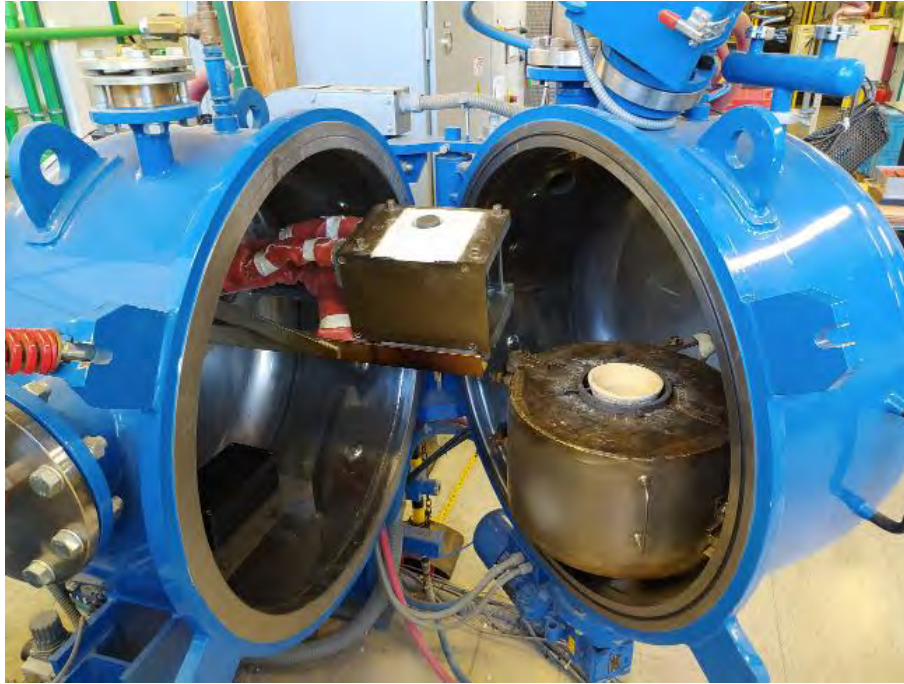
Figure 3-10. VIM facility, vacuum chamber, and hot crucible melt-box detail.

The installation also has a lance acting as a submersible thermocouple or adding alloys to the melt. Additionally, two video cameras are installed to visualize and control the melting and casting process. The old heating system inside the vacuum chamber enables molds to be heated from 500 °C to 1200 °C with heating ramps ranging from 5 °C to 50 °C/min. The equipment also offers the possibility of rotating the molds at a speed of up to 350 rpm for centrifugal casting and combining it with the mold heating system.

3.3.1. VIM process variables monitoring

The bibliographical review has concluded that the principal process variables that control the VIM process are the coil configuration and the applied power. Usually, the geometrical configuration, number of loops, and coil-to-charge distance are fixed. Thus power and time are the variables that can be adjusted during the process. Process variables are monitored and recorded in real-time with an in-house developed acquisition system to improve process control and achieve repetitive melting trials. Two four-channel universal analog inputs, NI-9207, were installed to acquire data from each sensor at 1 Hz, and the raw data was filtered and implemented in a graphical user interface (GUI) and displayed in the monitoring system.

The settled key variables are the applied power, melt temperature, heat losses, and thermal efficiency. The applied power signal can be obtained directly from the output of the power generator, while the electrical variables are measured during the melting trials. The metal temperature is controlled by adjusting the applied power, thus requiring measuring the response of the temperature variation on the metal. Therefore, choosing and calibrating a pyrometer for optimum process control is essential. In addition to the pyrometer temperature measurement, inside the vacuum chamber, a connection rack or thermocouples is placed with 5 input ports for coupling K, B, S, and C-type thermocouples whose reading is derived from the monitoring system.

- **Heat losses and thermal efficiency**

The heat losses and thermal efficiency were measured according to the calorimetric balance methodology presented by Chamorro et al. [124]. The heat losses correspond to conduction ($\mathbf{q_{dis}}$) and radiation ($\mathbf{q_{rad}}$). The first one was measured by evaluating the difference between the coil refrigeration water input and output temperature. For that, a calorimetric flow sensor displayed the water flow of the melt-box and two resistance temperature detectors for the water temperature inlet and outlet monitoring with 0.1 % error in the 0 °C – 100 °C measuring range. Additionally is necessary to measure the water flow to multiply with the heat capacity of the water.

$$\mathbf{q_{dis}} = \dot{m} \cdot C_p \cdot (T_{out} - T_{in}). \tag{3.3}$$

Conversely, the radiation was estimated according to the liquid metal top surface temperature, surface area, emissivity, and Stefan-Boltzmann constant.

$$\mathbf{q_{rad}} = \epsilon \cdot \sigma_{SB} \cdot A \cdot T^4 \tag{3.4}$$

Thus thermal efficiency was derived as the relation between the heat sources and the applied power.

$$\eta = \frac{\mathbf{q_{dis}} + \mathbf{q_{rad}}}{P_c} \tag{3.5}$$

3.3.2. Pyrometer calibration

As a first step, a pyrometer was installed and calibrated to control melt temperature. As mentioned, the radiation-temperature relation depends on the emissivity, which is difficult to calculate as it varies during the process. As constantly calibrating during melting trials is not viable, a two-color or ratio pyrometer was selected. The two-color pyrometer working principle cancels the influence of the emissivity factor by employing two independent band-pass filters for two wavelengths. This way, the radiation coming from the body is divided in two, and each detector produces its voltages whose ratio is of the temperature and is independent of the emissivity. For the measurement of objects that emit at the same wavelengths, there is no necessity to consider a correction factor. However, for different wavelength surfaces, such as non-oxidized metal surfaces or molten metals, a correction of the emissivity ratio is required by introducing a gain or an attenuation of the output signal. Thus, as the aim is to measure both the solid and liquid state metal, it is evident the necessity to adjust the ratio between the two wavelengths during trials.

Therefore, An Optris CTRatio_1MH® dual-wavelength pyrometer was selected with a measuring range between 700 °C and 1800 °C. The pyrometer was placed outside the vacuum chamber aiming from a viewport. The distance between the bottom of the crucible and the pyrometer is 710 mm with and 21.8 mm spot size. The registered temperature corresponds to the maximum value of the area covered by the spot size, which was adjusted to the top area of the ingot. Due to its configuration, the pyrometer has a fiber optic head that allows easy repositioning of the viewer utilizing a locknut clamp. By activating the laser beam to visualize the incidence of the beam, the spot size was positioned in the central area of the load's surface (Figure 3-11).

Pyrometer was calibrated by adjusting the R-slope factor or wavelength ratio to experimentally measured temperatures. An ingot with Ø 50 mm and 80 height was prepared and machined with housings for 4 type C thermocouples placed in different positions and depths along the metal load (Figure 3-11). Considering the skin effect, thermocouples were placed at the periphery of the ingot and in the center at different depths. This way, the temperature between different zones was quantified.
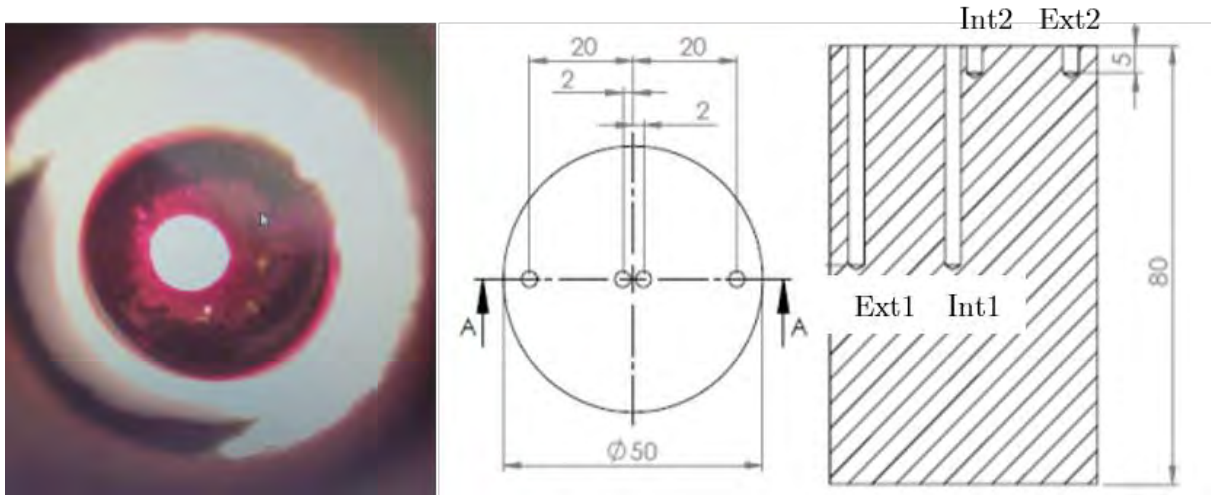
Figure 3-11. Pyrometer spot size in the ingot surface and placement of thermocouples.

An initial heating step of 5 kW was applied to obtain faster heating in the externally placed thermocouples. In Figure 3-12, thermocouples on the external surface of the ingot registered a higher temperature than those at the center. After 35 minutes and with an applied power of 11 kW, the TC_Int1 and TC_Int2 registered approximate temperatures of 1150 °C and 950 °C, respectively. In contrast, those placed at the periphery of the ingot, TC_Ext1, and TC_Ext2, were around 1300 °C. This difference of 350 °C at the center and 150 °C at the periphery results from the exposed surface's skin effect and radiation heat losses. This thermal drift resulted in threats during melting since the pyrometer recorded surface temperatures almost 400 °C below the melting range. Thus, excessive power increases at this instant of incipient melting might cause uncontrolled overheating.
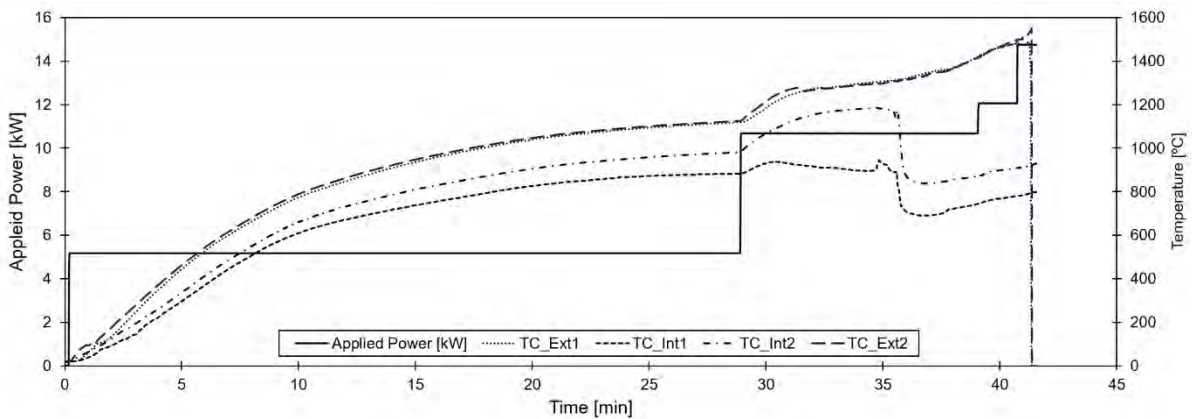
Figure 3-12. C-type thermocouple temperature evolution for calibration ingot.

To precisely adjust the R-value of the pyrometer in operating conditions, the thermocouples' temperatures as close to the melting range and in the liquid state were taken as a reference. First, the value of the thermocouple placed on the ingot surface's periphery was the reference. Then R was manually adjusted until the pyrometer registered the same temperature as the thermocouple. As a result, 1.110 was the value of R that adequately correlated with the temperature of both references. It should be considered that at that instant, the thermocouples located at greater depth are already recording liquid temperatures. Once the load's surface changed to liquid, the thermocouples on the surface lost their mechanical hold and therefore came in contact with the melt. At this moment, the submerged thermocouple was taken as a reference for the adjustment of R in liquid conditions, and it was set to 1.125.
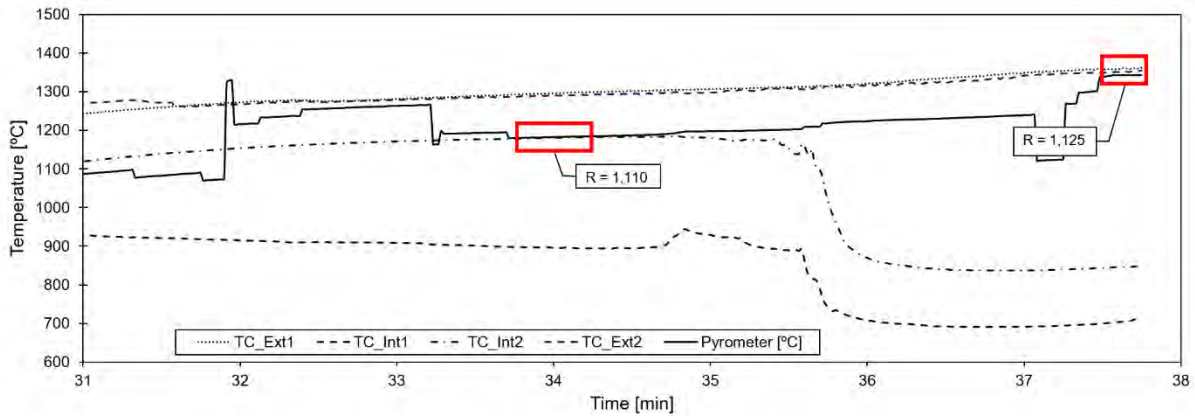
Figure 3-13. Pyrometer R-slope calibration during for solid and liquid states.

3.4. Standard melting procedure

In order to ensure an objective and comparable analysis of the results obtained from each crucible, the first step is to identify and establish standard melting conditions that ensure repeatability for all future trials. Cast bars produced with dimensions of Ø 45 mm, 160 mm height, and a weight of 2 kg were employed for all the melting trials. Before the melting test, a DSC analysis was performed on a sample of the ingots using a Netzsch STA 449 F3 Jupiter®. The analysis identified the phase transition temperatures with 1260 °C for solidus and 1359 °C for liquidus. Thus, an overheating of 90 °C was set, fixing 1450 °C as the target pouring temperature in the casting trials.
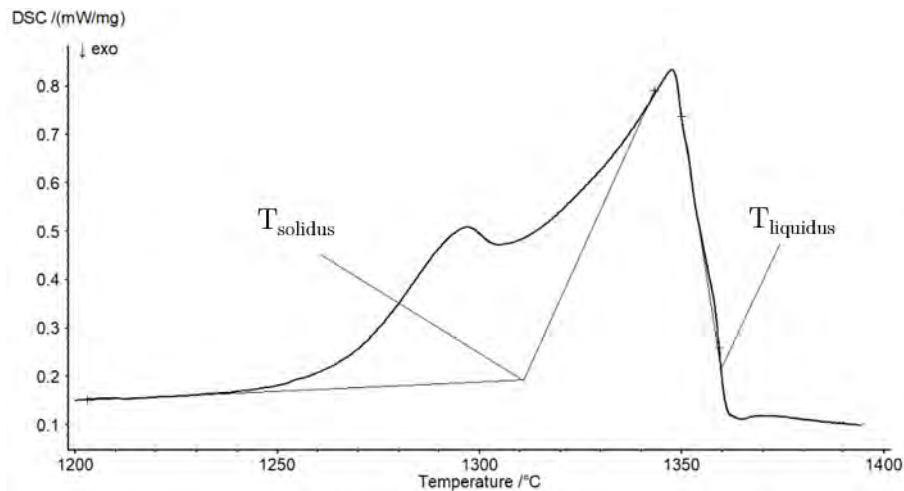
Figure 3-14. DSC calibration curve of the as-received Inconel 718.

An initial melting trial was done to calibrate the VIM installation. A standard melting procedure was established based on the DSC results and the industrial criteria for Inconel 718 melting. This was done to bring laboratory conditions close to actual industrial production conditions. The power generator is oversized for the hot crucible configuration, and the small mass of the melting material leads to employing the power generator with only a reduced percentage of its capacity. As a result of the low thermal inertia of the melt, rapid temperature variations occur with slight power modifications. Thus, it was decided that the best temperature control option is to adjust power manually. The pursued melting procedure was divided into five stages, explained in detail next and summarized in Table 3-5.

1. A one-hour bake-out stage was included to progressively increase the melt-box and crucible temperature to approximately half the melt temperature. This way, the thermal shock risk was reduced, and the humidity from the crucible was eliminated.

2. After stabilization, a second heating step was applied to increase the charge temperature.

3. In the melting stage, the power was again incremented to accelerate the melting of the entire charge in the shortest possible time. During this stage, dross particles were detected in all crucibles. They increased progressively and coalescence until a compact layer was formed on the surface of the molten metal presented in the upper view of the melt in Figure 3-15. This phenomenon can be observed in video format available as multimedia material [125].

4. In stage 4, the melt temperature was increased to 1500 °C, at which particles started to separate. The temperature was maintained, letting the metal stir until the surface was clear. The time required for clearing varied for each trial. The temperature was manually adapted due to the low thermal inertia of the melt, regulating the applied power with smooth transitions of 0.1 kW. A variability of ± 5 °C concerning the objective temperature was achieved during stationary states.

5. Once the melt was free of dross, the melt temperature was reduced to the casting temperature of 1450 °C and maintained for homogenization before pouring into the mold. The temperature control was done with the same procedure as in the previous stage.

Table 3-5. Power-time stages for the standard melting method.

Stage N°	Description	Power [kW]	Time [min]	Temperature [°C]
1	Bake-Out	5	60	Variable
2	Heating	11	12	Variable
3	Melting	16	Adaptative	Variable
4	Cleaning	Adaptative	15	1500
5	Maintenance	Adaptative	5	1450
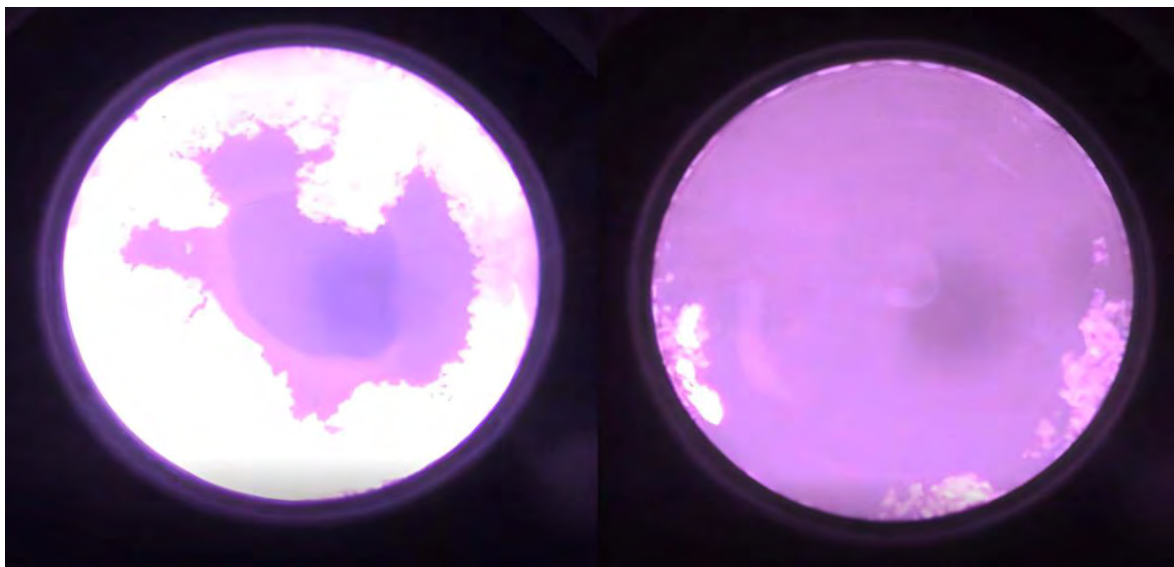
Figure 3-15. Left: Start of compact dross separation. Right: Almost the entire surface is cleaned.

The obtained Power-Temperature-Time curve is summarized in Figure 3-16 with the corresponding division of the previously described stages.
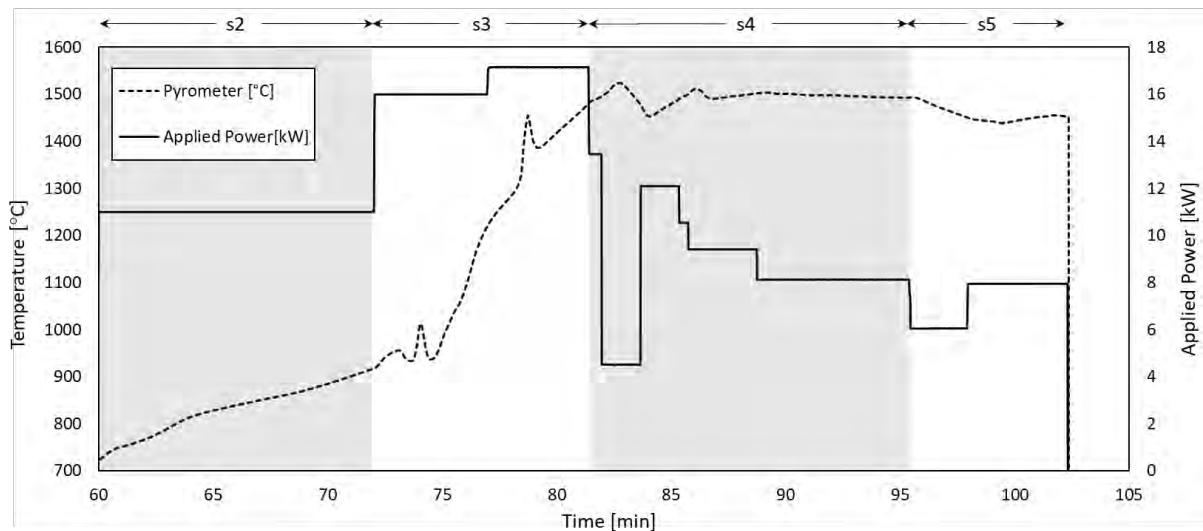
Figure 3-16. Standard melting power temperature profile.

Figure 3-17 shows the temperature rise of the water flowing through the coaxial coil cable and the inlet temperature. The conduction heat loss was derived from the difference between these temperatures and the constant flow rate. To these heat losses, radiation was added to obtain the thermal efficiency of the process as described in Equation 3.8
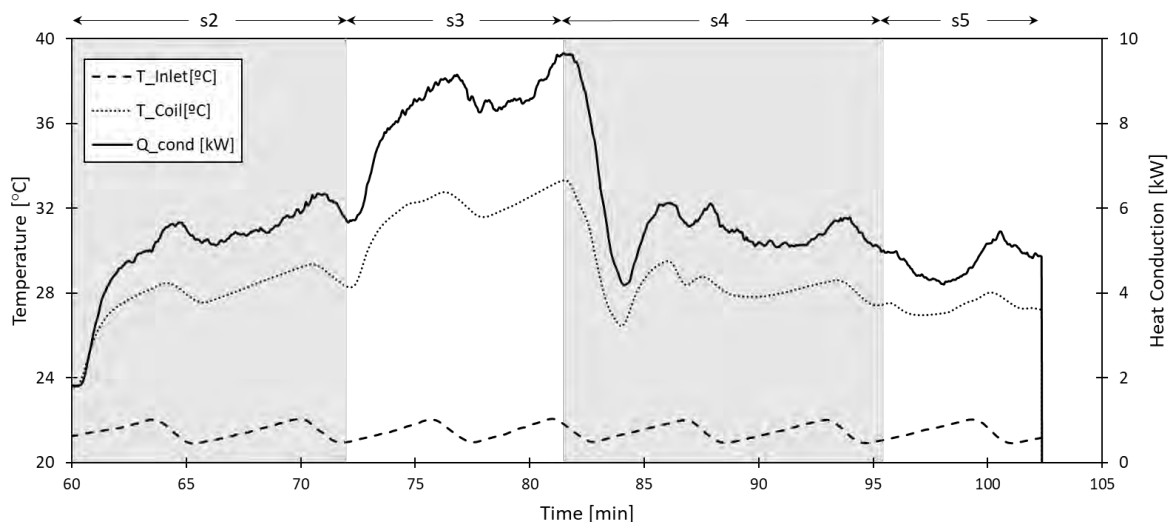
Figure 3-17. Temperature measurement and heat conduction losses.

3.4.1. Power generator electrical variables

The power generator that supplies power with a nominal power capacity of 100 kW at 10 kHz frequency was fabricated by Alecto Systems, L.L.C. It must be noted that the power generator was initially designed for a CCIM furnace with a copper crucible; thus, the operating frequencies are not the most suitable for hot crucible melting, as the typical values for a hot crucible are around 3– 5 kHz.

The power generator unit (Figure 3-18) is connected to the main line in a three-phase configuration, operating at 380 VAC and 50 Hz. The rectifier employs an uncontrolled 6-diode bridge, resulting in a constant DC voltage over time 1.35 higher than the line voltage, equivalent to approximately 515 V. The inverter converts the DC to single-phase alternating current, operating with four IBGT-type transistors connected in an H-bridge configuration. Control is achieved through a gate structure incorporating current and power transformer controllers. The current transformer regulates the inverter

output, while the power transformer provides feedback to the logic control board. The transformer ratio of 12:1 ensures a current supply to the coil, generating a stronger magnetic field.

The inverter's equivalent circuit at the output is an RLC in a series configuration circuit formed on the equivalent circuit by the melting charge, capacitor tank, and the in-between air gap. The resolution of this circuit seems simple at first glance, but the non-linearity of the load to be heated, the coil, the temperature-dependent resistivity, and the excitation frequency coil have to be considered. The current and frequency of the coil are adapted according to the resistance and inductance of the melting charge and the required power following the resonant circuit principle.

At the output, the inverter is represented by an equivalent circuit consisting of an RLC series configuration, including the melting charge, the coil, the capacitor tank, and the air gap. Although this circuit may initially appear simple, it must account for various non-linear factors, such as the temperature-dependent resistivity of the coil and the excitation frequency. The current and frequency of the coil are adjusted based on the resistance and inductance of the melting charge, following the principles of a resonant circuit. Considering these factors is crucial for accurately modeling and controlling the system's electrical operating variables measurement.
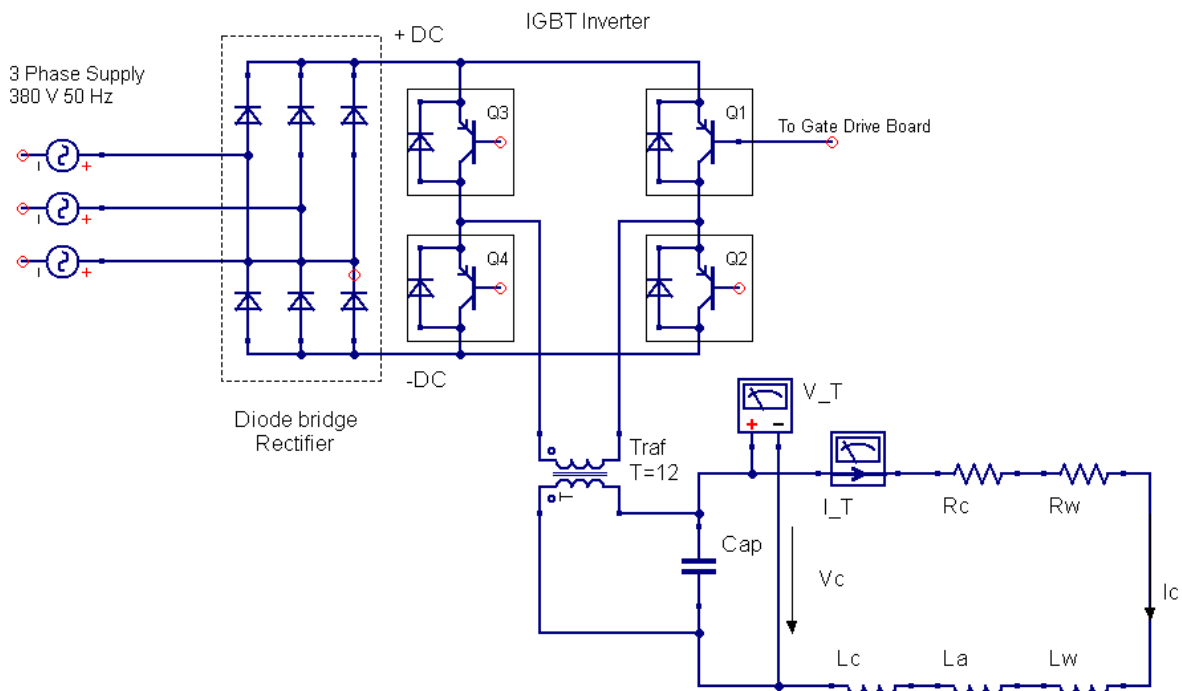
Figure 3-18. Power generator electric scheme and equivalent RLC circuit

Therefore, a specific acquisition system was developed to measure the electrical variables correctly. From the electrical circuit, the equivalent RLC circuit formed by the capacitor (Cap), inductor, and charge is in a series configuration. According to Kirchoff's law, the current flowing through the circuit is expected to be equal in all the components as it is the frequency, so the current was measured in the power generator output cable (I_T). To evaluate the voltage drop on the coil, the most optimum place is the extremes of the coil; however, the vacuum chamber and high temperatures limit this possibility. So a compromise solution was adopted, placing the transducer (V_T) in the coaxial cable connecting the vacuum chamber and the power generator.

It was necessary to use transducers specifically designed for industrial applications to handle the high currents, voltages, and frequencies present in the circuit. A Closed Loop ASIC-based Hall Effect LEM LF-2010-S® (I_T) transducer was employed for the current measurement. However, one challenge was

adapting the transducer's analog output signal (0-20mA) to the 10V scale of the NI-9217 module. This issue was resolved by designing an electronic amplifier circuit. A LEM AV 100-750® (V_T) voltage transducer was selected for voltage measurement. To visualize the waveform and amplitude, a Yokogawa DLM 2024® oscilloscope was employed.

This way, electrical variables measurements for different power conditions were carried out; current, voltage, and frequency results are summarized in Table 3-6, corresponding to the heating and melting stages of the standard melting procedure. Data from this table is employed as input on the numerical simulation of Chapter.4 Numerical modeling, for preliminary and validation simulations.

Table 3-6. Measured power generator output electrical variables for standard melting stages.

Power (P_c) [kW]	Current (I_{RMS}) [A]	Voltage (V_{RMS}) [V]	Frequency (f) [kHz]	Phase φ [deg]
5	600	90	8.4	78
8	875	105	8	74
11	1040	138	7.4	72
16	1400	162	7	68

3.5. Conclusions

This chapter focused on characterizing the materials to be utilized in subsequent experimental tests and as input parameters for the numerical model. The thermal properties of Inconel 718 in the solid state were directly measured, while reliable and consistent bibliographic references were relied upon for the liquid state due to their stability within the temperature range. Exhaustive characterization of the ceramic crucibles was conducted to determine their thermal and compositional properties, revealing significant variations depending on the chemical composition and measurement temperatures.

For conducting the tests and serving as a reference for developing the numerical model, the laboratory-scale VIM installation was introduced for the melting procedure. Necessary sensors were implemented and calibrated to ensure accurate control of the critical process variables. A standard melting procedure was established to maintain consistency across the tests. Heat losses resulting from conduction and radiation were measured under operating conditions, providing boundary conditions for the numerical model. Additionally, the electrical variables of the power generator output will be used as input parameters for the numerical development.

<div align="right">

Chapter 4

4. Numerical modeling

</div>

The numerical modeling has been divided into two steps. An induction heating model is initially developed considering the solid-state material, magnetic fields, and heat transfer have been coupled. Here, irradiation between surfaces has been introduced and discussed in detail. In the second part, the material is in a liquid state, and the fluid flow due to the magnetic force is studied, detailing the procedure for modeling the free surface's hydrodynamics and the flow recirculation. Finally, the heat transfer phenomenon is coupled with the development of a fluid flow of non-isothermal characteristics.

4.1. Induction heating

Prior to starting presenting the insights of the numerical model and simulation results, the followed methodology is resumed. Initially, the geometry is introduced, detailing the domains and corresponding boundary conditions and assigning material property parameters. Then, the mesh discretization and solver configuration are presented. This section is shared with the magnetic and heat transfer sub-models, whose mathematical formulation, the partial differential equations (PDEs), and boundary conditions are described independently, yet always considering the numerical coupling. The PDEs describing the physical phenomena were discretized with the FEM method based on COMSOL Multiphysics® v.6.0. For each submodel, its simulation results are presented and discussed.

4.1.1. Geometry, meshing, and material properties

- **Geometry**

The geometry considered for the induction heating model consists of the vacuum chamber, metal ingot, ceramic crucible, and melt-box sub-assembly composed of the protective refractory housing, coaxial copper coil, and the inner water flow (Figure 4-1).
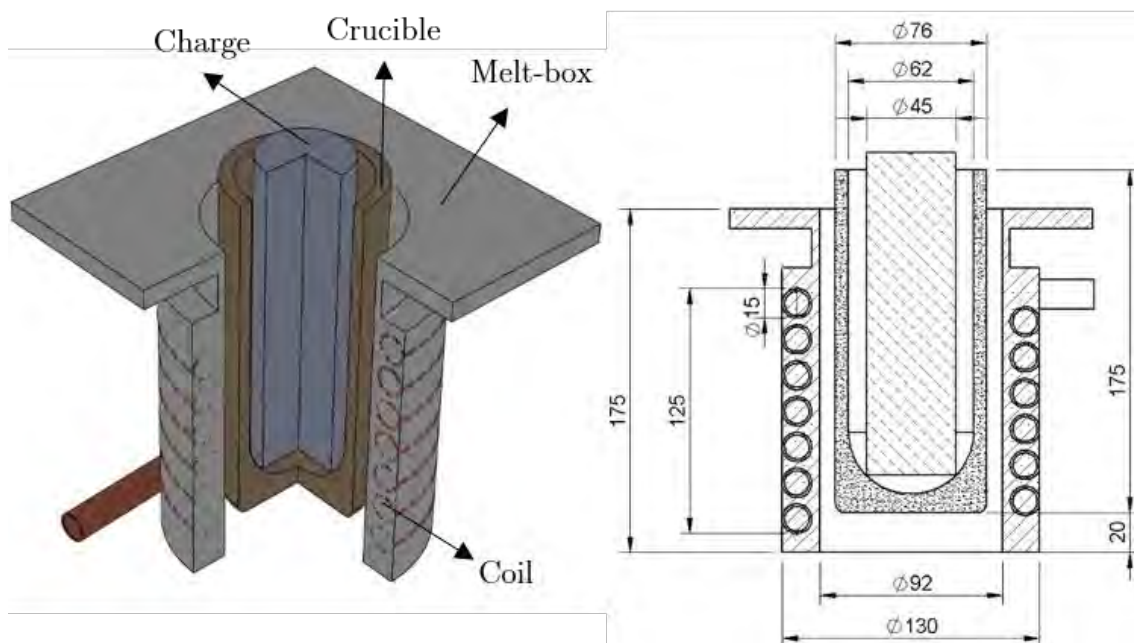
Figure 4-1. 3D geometry and section view with principal dimensions for induction heating model.

The geometry was generated using the CAD tool of the software itself to avoid errors and inaccuracies that may arise when importing files. All the elements were dimensioned according to in situ measurement of the VIM installation. The seven-turn coaxial coil surrounded the melt-box; the charge was in contact with the crucible, surrounded by the half circle corresponding to the vacuum chamber. The ingot dimensions were the ones of the standard ingot, 165 mm height by 45 mm diameter, corresponding to 2 kg weight. The revolution symmetry of the geometry was exploited by adding an axisymmetric axis. This way, the dimensions of the domains needed to discretize are reduced, solving the model in two dimensions. This solution has been typically employed for induction heating applications [69] by assuming that the potential magnetic and electric vectors (**A** and **E)** only have a component in the axial direction Z. The drawback of this method is the disregard of the coil helicity by neglecting the sinusoidal shape of the inductor. The domain and boundary assignations in the model are resumed in Figure 4-2 and Table 4-1.
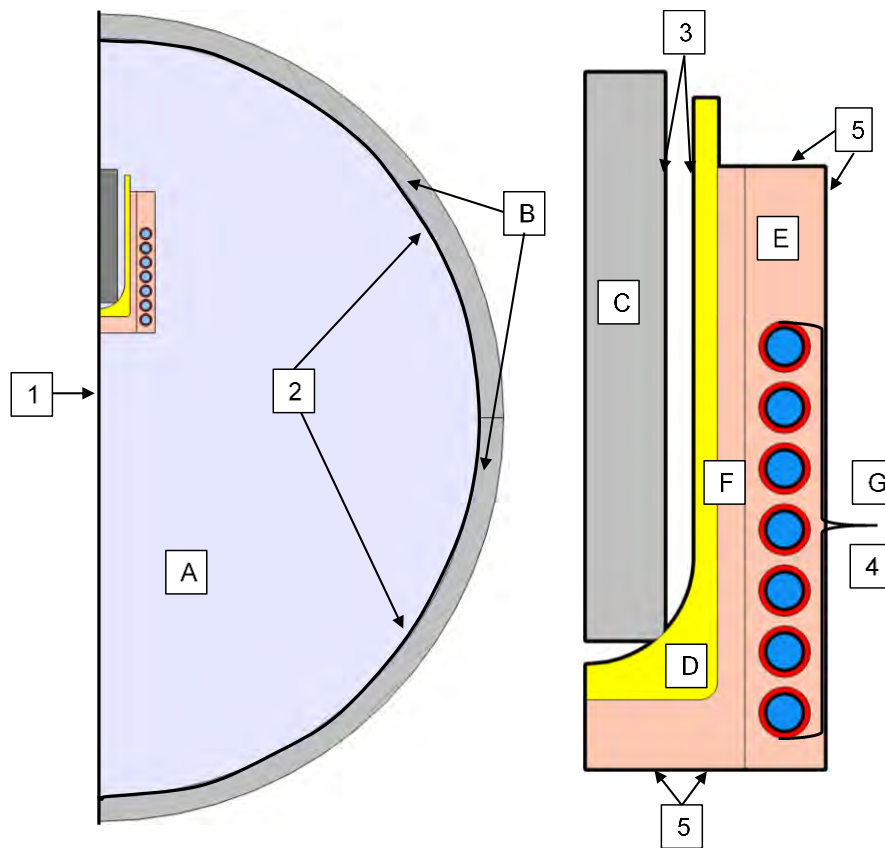
Figure 4-2. Domains and boundary conditions for the induction heating model.

Table 4-1. Resume of model domains and boundaries for the geometry.

Domain	Description	Boundary	Description
A	Vacuum Atmosphere	1	Symmetry axis
B	Chamber Structure	2	Vacuum chamber inner contour
C	Incone 718 Ingot	3	Surface-to-surface radiation
D	Crucible	4	Forced convection heat flux
E	Melt-box	5	Melt-box outer contour
F	Coaxial Coil		
G	Refrigeration water		

- **Material Properties**

The material parameters were assigned to define constitutive equations in the domains and boundaries. All the used material properties are resumed in Table 4-2. Regarding the electromagnetic properties, all materials have been considered paramagnetic $\mu_r = 1$ and electrically non-conductive $\sigma = 0$ except copper coil and Inconel 718 ingot. For the last one, characterized properties were implemented for electrical conductivity and thermophysical properties as functions of the temperature. The same can be said for the AL97I alumina crucible, where the measured results were assigned with built-in internal functions. The melt-box housing material made of Al_2O_3-CaO ceramic oxide has high thermal insulating properties. For copper and water, the assigned material properties were from the COMSOL Multiphysics® database.

Table 4-2. Resume of material properties for magnetic field and thermal sub-model.

Material	σ [S·m^{-1}]	λ [W m^{-1}K^{-1}]	C_p [J kg^{-1}K^{-1}]	ρ [kg·m^{-3}]	ϵ [$-$]
Inconel 718	$2 \cdot 10^6 \cdot T^{-0.25}$	$10.7 + 0.017 \cdot T$	$0.421 + 3e^{-4}T$	$8139 - 0.415 \cdot T$	$0.341 + 2e^{-4}T$
Copper	6e7	400	385	8960	-
Al_2O_3	-	$0.89 \cdot \ln(T) + 10.5$	$0.32 \cdot T^{0.187}$	2950	$-0.37 \cdot \ln(T) + 3.1$
Melt-box	-	$3.05 - 5e^{-4} \cdot T$	1000	2730	-
Water	-	-	-	1000	-
Air	-	-	-	1	-

- **Meshing**

In FEM, the geometry is discretized into mesh elements, and the number and quality of these elements directly influence the accuracy of the calculations. The meshing sequence in this simulation was carefully designed to capture the relevant physical phenomena and adapt the element shape and size to the different domains. In the induction coil, which is responsible for generating the magnetic field, mesh boundary layers were incorporated to capture the self-induction effects accurately. Cylindrical ingot-mapped structured elements with high quality were used to represent the coil geometry accurately. Additionally, a regular refinement step was implemented to reduce the element size and account for the skin effect, which is crucial for the precise computation of magnetic losses. For the other domains, such as the crucible, melt-box, and surrounding air, triangular free elements with small sizes were employed (Figure 4-3.a).

An adaptive mesh refinement step was included to ensure mesh independence and accurate results. This involves evaluating the global error of the magnetic vector potential **A** and refining the mesh where necessary. The initial mesh configuration consisted of 30,000 elements with an average quality of 0.88. The final configuration increased the elements to 340,000 while maintaining a quality of 0.86. This increase in elements was necessary to adapt the element size to the distribution of the induced magnetic field and accurately capture the effects of induction. The crucible's outer boundaries, which are in contact with the metal ingot, have been refined to capture the radiation effect between these surfaces. The melt-box was also refined to capture the conduction effect through the crucible and melt-box until it dissipated within the water-cooled coil. Additionally, finer mesh elements were introduced in the air domain near the melt-box to close the magnetic field loop and accurately represent the electromagnetic and thermal phenomena (Figure 4-3.b).
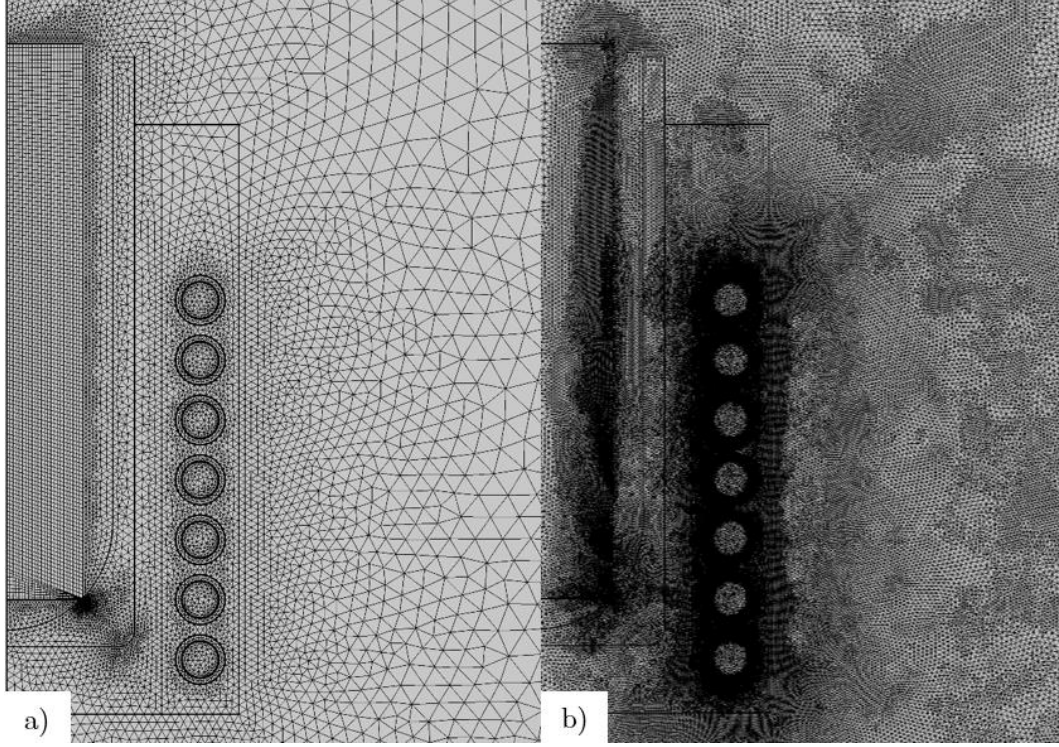
Figure 4-3. a) Initial mesh. b) Final adaptive mesh.

4.1.2. Magnetic field submodel

As described earlier, the aim is to model the induction heating process for an Inconel 718 alloy, coupling the magnetic-thermal fields. The following lines define the PDEs describing the magnetic field and heat transfer effects. Due to the different time scales, the magnetic field was calculated in the frequency domain while the temperature increment in the temporal frame as the magnetic field computation in the time frame is not feasible in the kHz frequency range. Initially, the magnetic field formulation is discussed with the corresponding numerical results.

- **Equations and boundary conditions**

Maxwell's equations are employed for the resolution of the magnetic fields. Assuming that the power generator feeds the coil with an alternating harmonic electric current $I_c = I_0 \sin(\omega_f t)$, these equations are rewritten in the frequency domain by applying a pure imaginary exponential dependence $\exp(j\omega_f t)$. For the specific case of a paramagnetic material with large electrical conductivity $\sigma > 10^6$ and without accumulation of the electrical charge. The partial differential equations for the magnetic field are summarized below:

$$\nabla \times \mathbf{H} = \mathbf{J} + j\omega_f \mathbf{D} \tag{4.1}$$

$$\nabla \times \mathbf{E} = -j\omega_f \mathbf{B} \tag{4.2}$$

$$\nabla \cdot \mathbf{B} = 0 \tag{4.3}$$

$$\nabla \cdot \mathbf{D} = 0 \tag{4.4}$$

The magnetic induction equation can be derived introducing the magnetic vector potential $\mathbf{B} = \nabla \times \mathbf{A}$, and the electric field vector potential from $\mathbf{E} = -j\omega_f \mathbf{A}$. Other important expressions are the constitutive relations that relate the material parameters and the fields.

$$\mathbf{B} = \mu_r \mu_0 \mathbf{H} \tag{4.5}$$

$$\mathbf{D} = \varepsilon_r \varepsilon_0 \mathbf{E} \tag{4.6}$$

Therefore, by combining Ohm's law, Maxwell-Ampère's law, and Faraday's law, the induced current equation for the conductive media equation can be rewritten as:

$$\mathbf{J_e} = \left(j\omega_f\sigma - \omega_f^2\varepsilon_r\varepsilon_0\right)\mathbf{A} + \nabla \times (\mu_r^{-1}\mu_0^{-1}\nabla \times \mathbf{A}) \tag{4.7}$$

$\mathbf{J_e}$ represents the external current density source determined by the input power of the coil fed by the power generator. The coil is modeled as a single conductor, essentially a solid region of copper through which the current passes. Although each turn of the coil is considered a separate domain, they are treated as a coil group to facilitate the connection between the solenoid loops. The current density, denoted as $\mathbf{J_e}$, is determined by taking the out-of-plane component of the current I_C.

$$\mathbf{J_e} = \sigma V_c/L \tag{4.8}$$

In this context, L represents the length of the coil, which corresponds to $2\pi r$, where r is the radius. By constraining the total integrated current of I_C the V_c potential can be estimated.

The current density and the voltage within the coil determine the excitation power of the coil. It is important to note that the system is fed with the experimentally measured current and voltage variables. Thus, power excitation was imposed in the coil introducing the following additional constraint

$$P_C = \frac{1}{2}\text{Re}(V_C \cdot I_C^* \cdot \cos(\varphi)) \tag{4.9}$$

Power input introduces non-linearity in the equations, necessitating the specification of the phase angle between the two vectors. Once the electrical variables of the coil and geometry are defined, the electrical parameters such as resistance, inductance, and impedance can be derived.

It is important to mention that oscillatory currents are induced when an oscillating magnetic field interferes with a conductive medium. Surface current shields the external magnetic field by inducing a new magnetic field. This new magnetic field is opposite to the external field, leading to an exponential drop in the external magnetic field. This diffusion of the induced magnetic field is the skin effect.

$$\delta = \sqrt{2/\omega_f\sigma\mu_0\mu_r} \tag{4.10}$$

These induced currents are dissipated in the form of heat by resistive heating (Q_{rh}), which is the product of the induced current and the induced voltage:

$$Q_{rh} = \frac{1}{2}\text{Re}(\mathbf{J} \cdot \mathbf{E}^*) \tag{4.11}$$

- **Boundary conditions**

The boundary conditions for the resolution of the PDEs are straightforward. To close the loop of the magnetic field vector and to confine the magnetic field inside the vacuum chamber, magnetic insulation was considered. This condition determined that the tangential component in the potential magnetic vector is zero in the vacuum chamber's inner contour boundary (N°2).

$$\mathbf{n} \times \mathbf{A} = 0 \tag{4.12}$$

While for the interface between two media or domains, the continuity boundary condition was imposed, expressed with the following relations:

$$\mathbf{n_2} \times (\mathbf{A_1} - \mathbf{A_2}) = 0 \tag{4.13}$$

$$\mathbf{n_2} \times (\mathbf{H_1} - \mathbf{H_2}) = 0 \tag{4.14}$$

4.1.3. Magnetic field numerical results

Once the magnetic field equations were defined, preliminary simulations were launched; as input variables, power stages of the 3.4 Standard melting procedure were considered, 5 kW, 11 kW, and 16 kW, corresponding to the bake-out, heating, and melting stages. The electrical variables are summarized in Table 4-3.

Table 4-3. Input electrical variable for the electromagnetic modeling.

Stage	P_C [kW]	I_C [A]	V_C [V]	φ [deg]	f [kHz]
S1	5	600	90	84.7	8.4
S2	11	1040	135	85.6	8
S3	16	1400	162	85.9	7.4

- **Magnetic flux density**

Figure 4-4 illustrates the distribution of magnetic energy dissipated as heat (Q_{rh}) on the left side and the magnetic field density (**B**) for an input power of 5 kW.
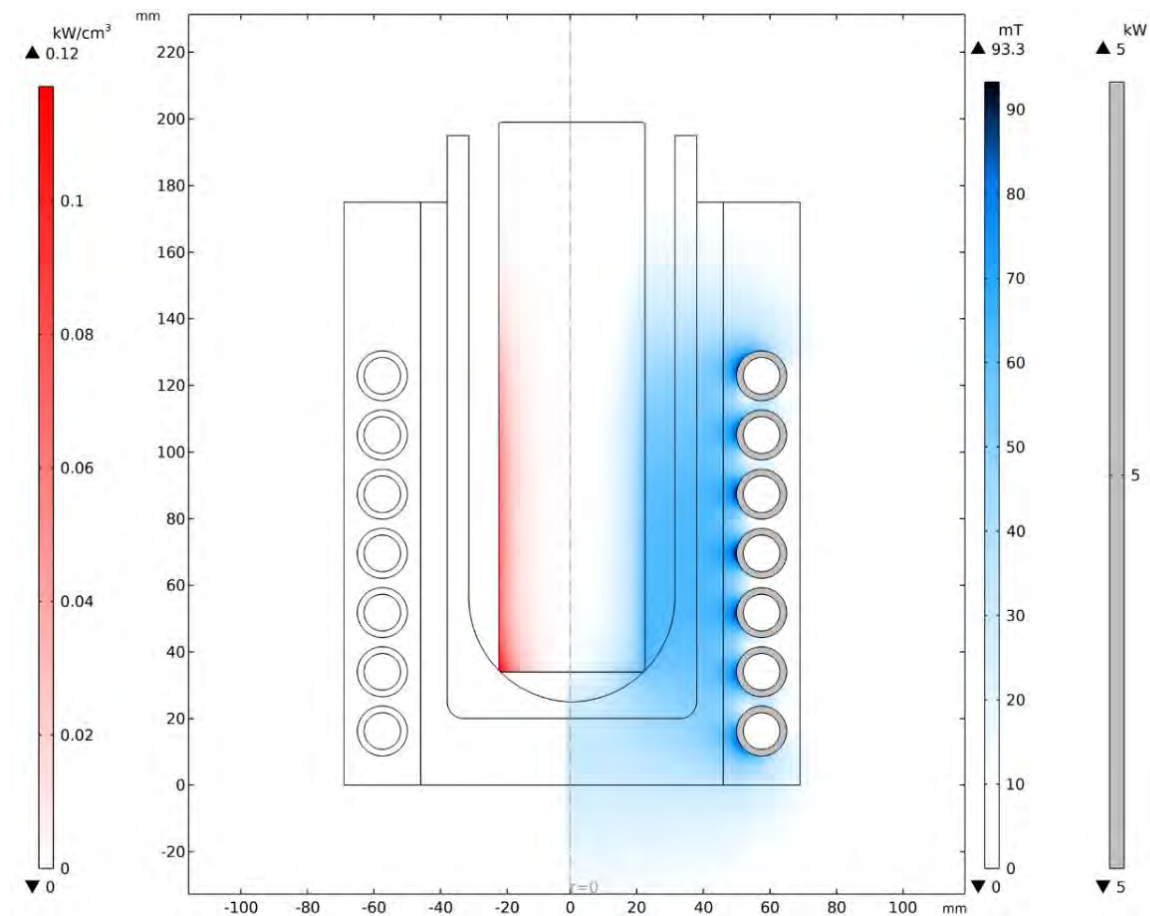
Figure 4-4. Magnetic flux density (**B**) and dissipated magnetic energy (Q_{rh}) in the load for S1.

The magnetic flux density (**B**) was localized in the superficial area of the cylindrical ingot. This effect is more clearly seen by evaluating data from the ingot outer boundary in Figure 4-5, where magnetic flux as a function of the arc length is represented for the three discussed power stages. All the boundaries are represented starting from r = 0 and z = 0 coordinates while following the outer boundary and

increasing when reaching closer to the ingot surface while decreasing by gaining height. On the contrary, there was a decrease in the top face up to almost zero in r = 0 and z = 165 mm coordinates.
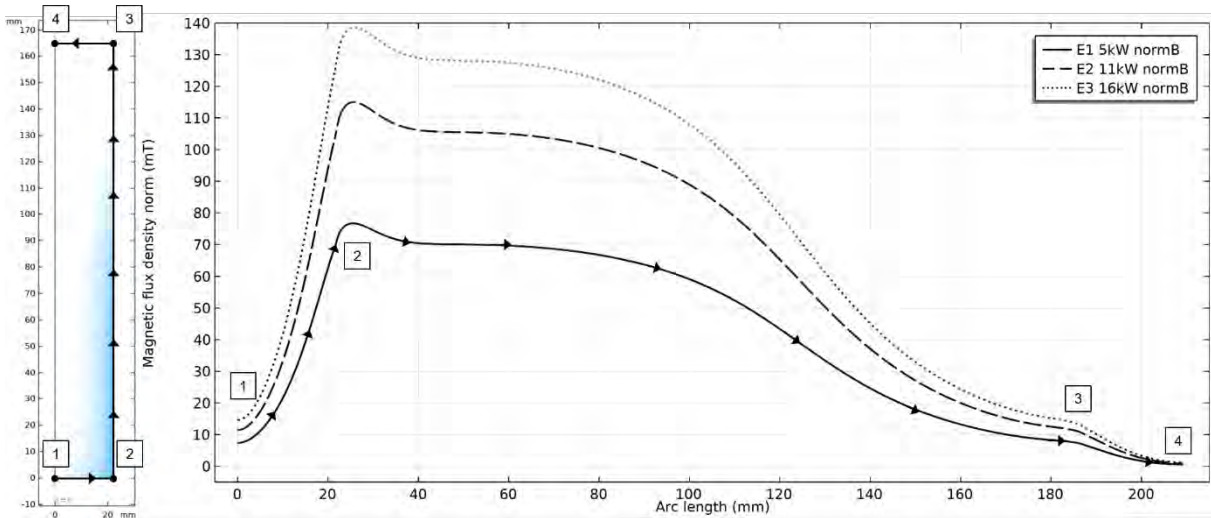
Figure 4-5. Distribution of magnetic flux density (**B**) in the surface of the charge.

The diffusion effect can be observed by evaluating the radial section's magnetic field (**B**) from r = 0 coordinate to r = 22.5 mm corresponding to the ingot radius length. Figure 4-6 resumes the magnetic flux density for the S1 power stage, considering different Z heights, starting from z = 0 mm and incrementing 40 mm to z = 165 mm. An exponential increment of the field was reported by approaching the ingot's external surface with a higher magnitude in the bottom half side of the ingot. From about half the ingot height z = 80 mm, the field barely impinges inside the ingot, especially for radial distances up to 12 mm from the ingot center. This proves the previous observation that the induction was focused on the coil's outer surface and the ingot's lower half.
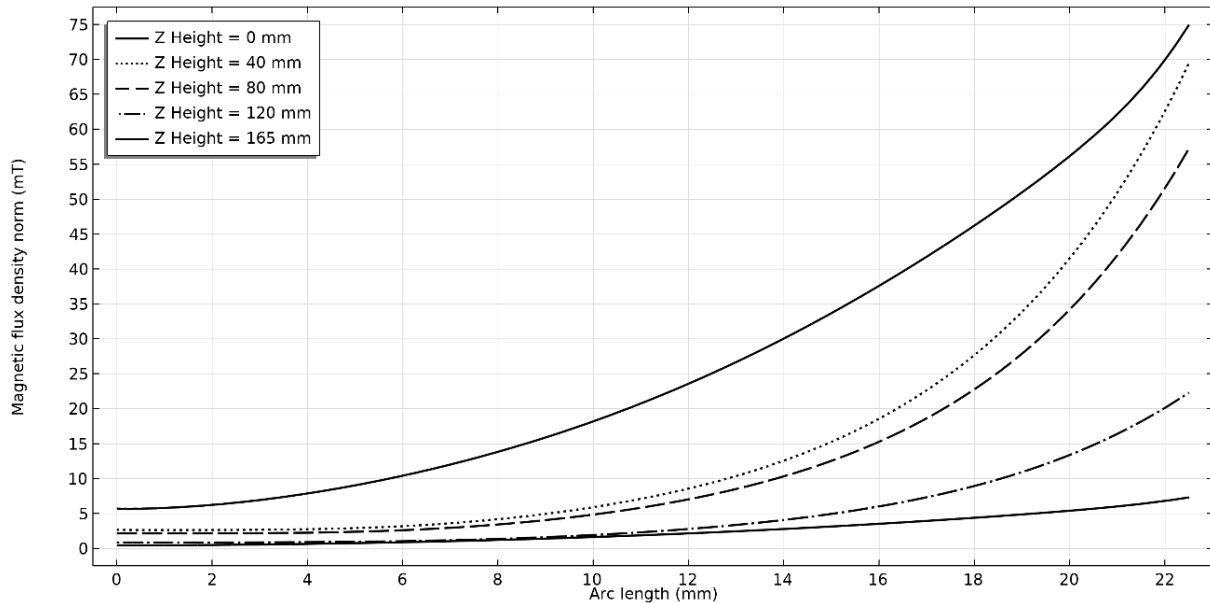
Figure 4-6. Magnetic field intensity (B) in the Radial direction at various Z heights for 5 kW.

- **Electrical efficiency**

The electrical efficiency was estimated by considering the total power balance by calculating the ratio between the coil feed power and the heat dissipation in the charge via resistive losses or induced power. The induced power was calculated by integrating equation 4.11 to complete the ingot. An approximate efficiency of 60 % was obtained for the three power cases, summarized in Table 4-4. This efficiency relates to the preliminary experimental measurements carried out in 3.4.1 Power generator electrical variables, where a decrease in thermal efficiency at higher temperatures was reported.

Table 4-4: Resume of electrical efficiency for induction.

Stage	Coil Power (P_c) [kW]	Induced power (Q_{rh}) [kW]	Electrical efficiency [%]
S1	5	3.2	64.6
S2	11	6.3	57.2
S3	16	8.9	55.4

Under alternate current excitation, the current density is higher at the coil's surface due to auto-inductance effects leading to a concentration of the current density in the outer. This results in a higher inductive reactance and lower current, leading to increased effective resistance with excitation frequency. Additionally, the change in the current density distribution in the coil loops increases due to the magnetic flux generated by the current in the adjacent wires, leading to an increase in the conductor's resistance. Figure 4-7 illustrates this effect for three frequencies (50 Hz, 1 kHz, and 10 kHz), plotting the normalized current density on the coil section leading to a localized current density in the outer contour for higher frequencies.
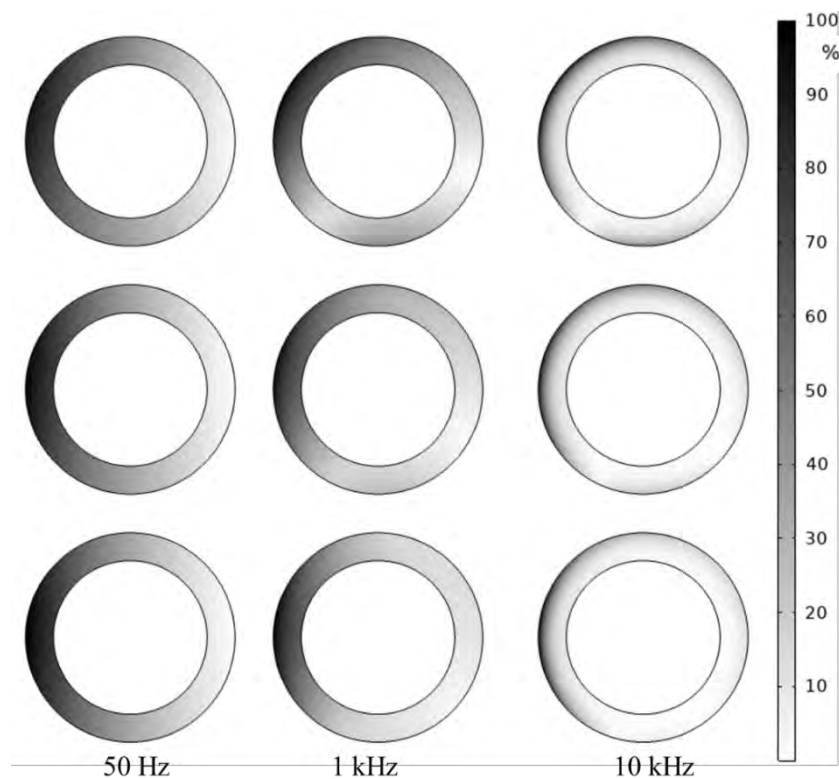
Figure 4-7. Effect of auto-induction in the current density for 50 Hz, 1 kHz, and 10 kHz.

- **Conclusions**

The analysis of the magnetic field density reveals a non-uniform distribution within the ingot, which may result in uneven heating. This can be attributed to two main factors. Firstly, the high frequency of the induced current and the high electrical conductivity of the material leads to fast diffusion of the magnetic field. This diffusion effect causes the magnetic field to spread out and become less concentrated, resulting in variations in the field intensity throughout the ingot.

Secondly, the ratio between the height and radius of the ingot plays a role in the heating uniformity. A higher ratio typically promotes more uniform heating, particularly on the surface. However, in this case, the positioning of the ingot within the crucible and melt-box was not optimal. The base of the crucible and melt-box elevates the vertical position of the ingot, causing approximately 20 % of its total length to be located outside the effective length of the coil. This configuration limitation was expected since the coil design was intended for melting, where the metal filling level would typically reach the entire coil length, ensuring more uniform heating.

As a result of these factors, the magnetic field distribution within the ingot was non-uniform, and sparse heating may occur. This non-uniformity can lead to temperature variations within the ingot and affect the melting process. It is essential to consider these aspects when optimizing the system design and coil configuration to achieve more uniform heating and melting of the ingot.

4.1.4. Magneto-thermal submodel

After examining the magnetic field distribution within the geometry, the thermal aspects of induction heating are analyzed. To accurately determine the temperature increase in the ingot, it is necessary to incorporate a heat source (Q_e) that couples both fields. The energy supplied to the system can be obtained by integrating the resistive losses (Q_{rh}), which can be expressed in terms of the induced current density (J) and electrical conductivity.

$$Q_e = \frac{J^2}{\sigma} \tag{4.15}$$

- **Equations and boundary conditions**

The temperature is a dynamic variable; thus, a transitory simulation is required. Due to the differences in the scales, the temperature is computed in the temporal frad15me while the magnetic field is modeled in the frequency. The governing equation that represents the heating of a solid body in the temporal frame can be described with the following equation:

$$\rho C_p \frac{\partial T}{\partial t} + (\mathbf{q_c} + \mathbf{q_r}) = Q_e \tag{4.16}$$

From here, it is evident that there are two principal heat transfer mechanisms, $\mathbf{q_c}$, corresponding to conduction and q_r radiation heat flux contribution. Fourier's law describes the conductive heat flux, which determines that heat transfer is proportional to the temperature gradient for a continuous media.

$$\mathbf{q_c} = -\lambda \nabla T \tag{4.17}$$

However, concerning the radiation heat flux ($\mathbf{q_r}$), the additional influence of the surface-to-surface radiation with the crucible has been included due to the ingot's large height/diameter ratio and shared vision area.

- **Surface-to-surface radiation**

The incident electromagnetic wave interacting with a body is decomposed into three components, absorption, reflection, and transmission. In this case, the ingot and crucible are solid and assumed to be opaque so that no radiation is transmitted to the ingot and crucible. Additionally, these surfaces are considered gray bodies, having a diffusive surface behavior and not accounting for spectral dependency; thus, material emissivity and absorptivity at equilibrium are equal and related to the reflection.

$$J = \rho_d G + \epsilon e_b(T) \tag{4.18}$$

The radiative heat flux leaving a surface is defined as surface radiosity (J), while the incoming radiative flux is denoted as surface irradiation (G). These two fluxes are related as the radiosity is the sum of the diffusively reflected and emitted radiation:

$$J = \rho_d G + \epsilon e_b(T) \tag{4.19}$$

Here, $e_b(T)$ is the emissive blackbody radiated power in the whole waveband and depends on the fourth power on the temperature $e_b(T) = n^2 \sigma_{SB} T^4$.

Usually, the irradiance (G) is unknown and depends on the surrounding surfaces. The irradiance received by a surface (a) emitted by another surface (b) can be defined determined by the view factor (F_{ba}) whose mathematical development can be found in Appendix 1.

The hemicube method was employed to compute the view factors. It involves dividing the surface into several small patches, projecting a hemisphere of rays onto a surface, and then computing each patch's radiation from the direction of interest [126].

Once defined, the irradiance received and radiosity emitted by the surfaces, the determination of the net fluxes is straightforward as it is a balance between the energy gain and losses, which can be expressed with the following expression:

$$\mathbf{q_r} = \epsilon(G - e_b(T)) \tag{4.20}$$

After introducing the equations relating the surface to surface radiation, it has been coupled with the general heat transfer equation and the magnetic field induction heating. The temperature dependency of the materials was introduced, directly affecting to the electrical conductivity and surface emissivity. The equations solved in the ingot domain are summarized in Figure 4-8.
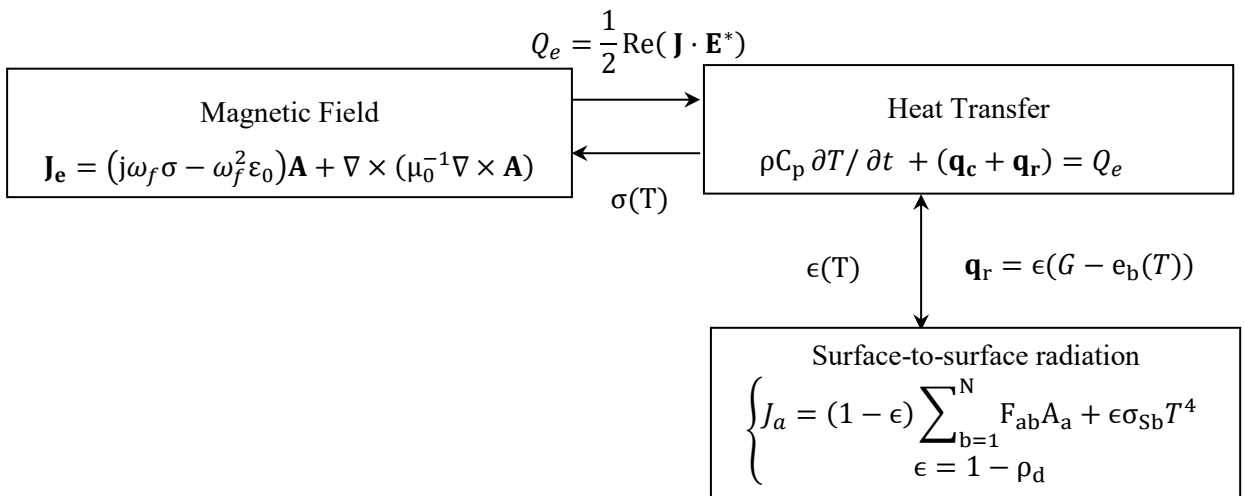
Figure 4-8. Thermo-magnetic model equations and coupling conditions.

- **Boundary conditions**

Three boundary conditions were imposed to solve the above-presented equations resumed in Table 4-5. The model considered two principal boundary conditions to replicate the heat losses, radiation of the surfaces, and forced convection of the water flow refrigeration of the coil. It is assumed that this heat dissipation effect is dominant so that the melt-box is cooled-down sufficiently; thus, possible radiation of the melt-box to the ambient can be neglected. Therefore, the rest of the boundaries surrounding the melt-box (N°6) were assumed to be thermally insulators.

Table 4-5. Boundary conditions for the thermal model.

Boundary	Boundary Condition	Equation
Surface-to-surface (N°3)	Radiation surface	$-\mathbf{n} \cdot \mathbf{q_r} = \epsilon \cdot (G - e_b(T))$
Coil internal boundary (N°5)	Forced convection	$-\mathbf{n} \cdot \mathbf{q_{dis}} = h(T_{ext} - T)$
Melt-box outer contour (N°6)	Thermal insulation	$-\mathbf{n} \cdot \mathbf{q} = 0$

Regarding the refrigeration on the inner side of the copper coil, where conducted heat was dissipated due to the forced convection of the water flow passing through, a Dirichlet-type heat flux boundary condition was imposed on the inner side of the coil (N °5). The difficulty arises in determining the heat transfer coefficient (h). It was determined by adjusting (h) to the experimentally measured heat flux on the pipe ($\mathbf{q_{dis}}$).

4.1.5. Induction heating numerical results

For a comprehensive evaluation of the induction heating process applied to the charge ingot, the bake-out and heating stages of the standard melting trial were modeled as a baseline for comparison. Therefore, the first two stages were simulated: a 5 kW power for one hour and an 11 kW for 12 minutes. A time-dependent function was imposed on the coil to adapt the power output to replicate the heating conditions. The simulation concluded at this point since the discussed model did not account for the solid-liquid phase change occurring in the melting stage of 16 kW.

- **Radiation heating**

In this case, evaluating the radiation effect between surfaces is of great interest—the cylindrical ingot shares almost the entire surface with the crucible, except for the top surface. The radiative heat flux of a surface can be determined by subtracting the radiosity from the irradiance. The three components are represented along the arc length of the ingot surface at the simulation minute 60 (Figure 4-9.a).

The analysis of radiative heat flux reveals interesting observations regarding energy exchange between the ingot and the crucible. The negative radiative heat flux in the ingot indicates it was losing energy through radiation. This outcome was expected because the contribution of the radiosity of the ingot was higher than the irradiance it received. The low temperatures of the crucible reduce the radiation leaving the crucible surface. As a result, the crucible experiences heating, as indicated by the heated region marked in red in Figure 4-9. b.

The red lines represent surfaces with a positive radiation rate, indicating a net heat gain, while the blue areas represent negative values or heat loss. It can be observed that the middle-bottom side of the ingot experiences the most significant heat losses. On the other hand, the crucible face receives irradiation from the ingot and gains heat. Additionally, it is worth noting that the radiation heat losses decrease rapidly on the middle-top side of the ingot.
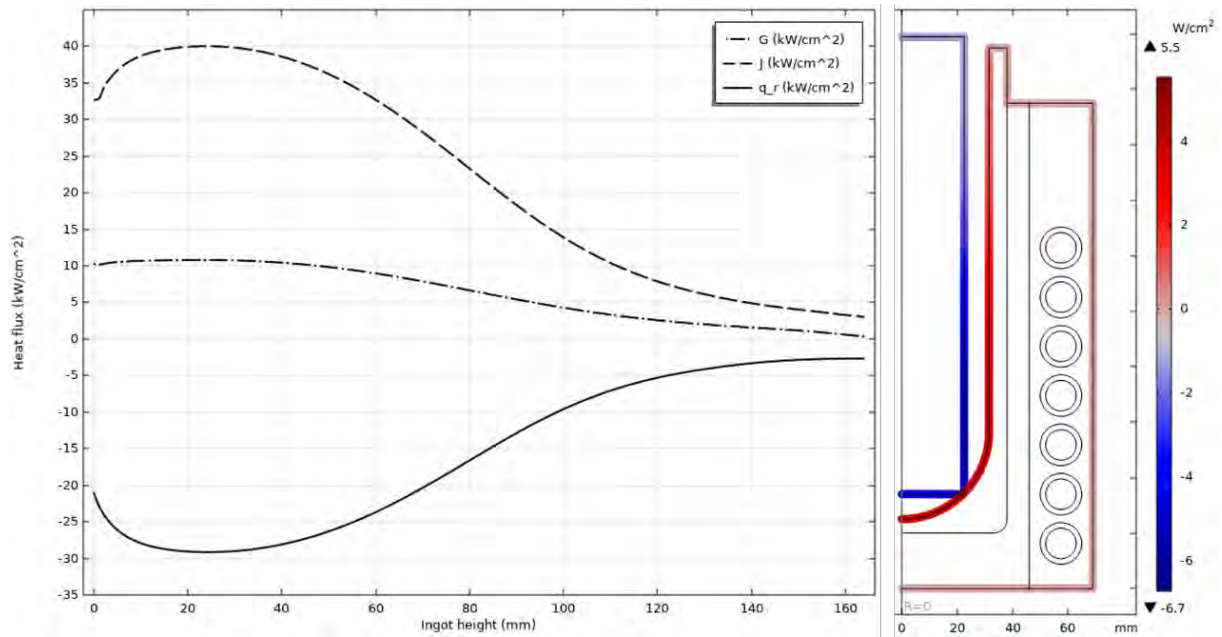
Figure 4-9. a) Radiation components for the vertical ingot surface t = 60 min.

In the transient simulation, the top surface temperature of the ingot was used as a reference to replicate the measurements obtained from a pyrometer. A numerical boundary probe covers the top surface area and obtains temperature readings. However, it is necessary to note that there was no available data from the pyrometer measurement for a significant portion of the bake-out stage, as the recording begins at 700 °C. Thus, the temperature remains unknown for most of the bake-out stage.

In the simulation, an initial temperature of 25 °C was assigned to the scalar temperature variable for all domains. The simulation covers a total duration of 72 minutes, and the temperature increment was plotted based on the maximum temperature probe on the top surface and the averaged temperature increment of the ingot (Figure 4-10.a).
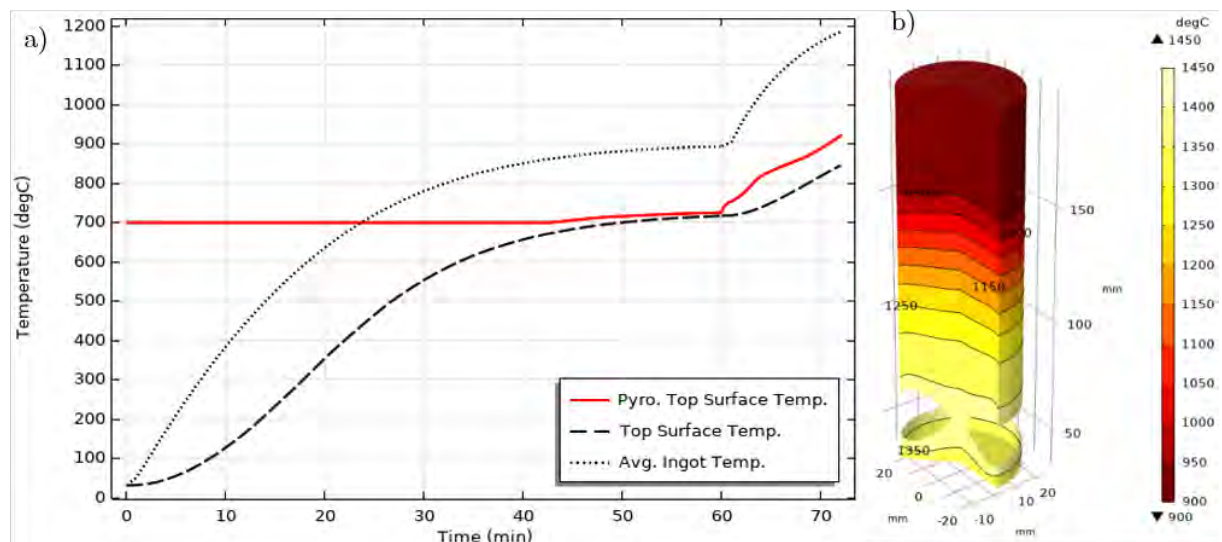
Figure 4-10. a) Simulated ingot temperature increase. b) Temperature distribution at t = 72 min.

It can be observed that the average temperature of the ingot reaches 200 °C, surpassing the temperature recorded at the top surface boundary. The temperature distribution within the ingot at the final time step of the simulation exhibited a significant temperature gradient throughout the domain (Figure 4-10.b). The mesh elements that had exceeded the solidus temperature were eliminated from the visual

representation, assuming that phase transition started; thus, the model was no longer valid. This initial melting is in line with the observed on the standard melting trial, where liquid metal appeared on the bottom side of the ingot. Therefore, the induction heating model was limited to the initial two stages. On the contrary, the top side was solid and relatively cold, as it did not even reach 1000 °C; it was expected, as the pyrometer calibration indicated that this area was the coldest zone.

- **Conclusions**

From the numerical results obtained, it can be concluded that the non-uniform heating in the ingot is related to the localized effect of the magnetic field and the dissipation of the magnetic energy due to the skin effect. This variation derives from a localized phenomenon during heating, initiating the melting of the metal almost at the base of the ingot, as seen in the preliminary tests. The contribution of the radiosity heat source for the ingot is minimum compared to the heating by induction. The pyrometer alone does not seem to be a reliable reference since its range limits the reading range, and it measures the coldest temperature of the geometry. Also, it has been observed that the model loses accuracy when the S2 heating stage begins. However, the current model did not consider the solid-liquid phase transition; thus, it should not be valid once the incipient melting starts. Therefore, it is considered necessary to perform more specific tests to obtain more temperature references in a broader range.

4.2. Induction melting model

In the second model, the focus shifts to the melt flow behavior in the presence of magnetic and thermal fields. The fluid flow problem is coupled with the magnetic and thermal fields, creating a multi-physics system. The melt flow analysis can be divided into two interconnected problems: the hydrodynamic deformation of the free surface and the continuous recirculation or stirring. These two aspects are treated separately due to their different time scales. Initially, the deformation of the free surface is examined, studying how it changes and settles into a quasi-stationary state. This part of the analysis focuses on the hydrodynamic aspects of the flow. Once the free surface reaches a stationary state, the flow recirculation is studied based on the solution obtained from the previous analysis. Afterward, the heat transfer phenomena are coupled with the flow, describing the multi-physics coupling in the induction melting process and the interaction among the different physics.

The structure of the chapter follows a similar structure to the previous model. It begins with explaining the geometry, domains, boundaries, and material properties. Mathematical equations describing the coupled phenomenon between the magnetic field and fluid dynamics are established, focusing on boundary conditions. The mesh analysis is thoroughly examined through sensitivity analysis, which relates to the numerical results and ensures the accuracy and reliability of the simulation. Next, the heat transfer physics obtained from the multi-physics model is incorporated, and the corresponding equations and boundary conditions are defined. The most relevant numerical results are presented, highlighting the important findings and insights derived from the study.

4.2.1. Geometry and material properties

- **Geometry**

Now the metal is liquid; minor modifications must be included in the previously described geometry. These changes correspond to the liquid metal where the total mass of 2 kg was maintained, but adapting the height reached by the liquid metal according to the empty volume and diameter of the crucible. The new geometry and the corresponding dimensions are in Figure 4-11.
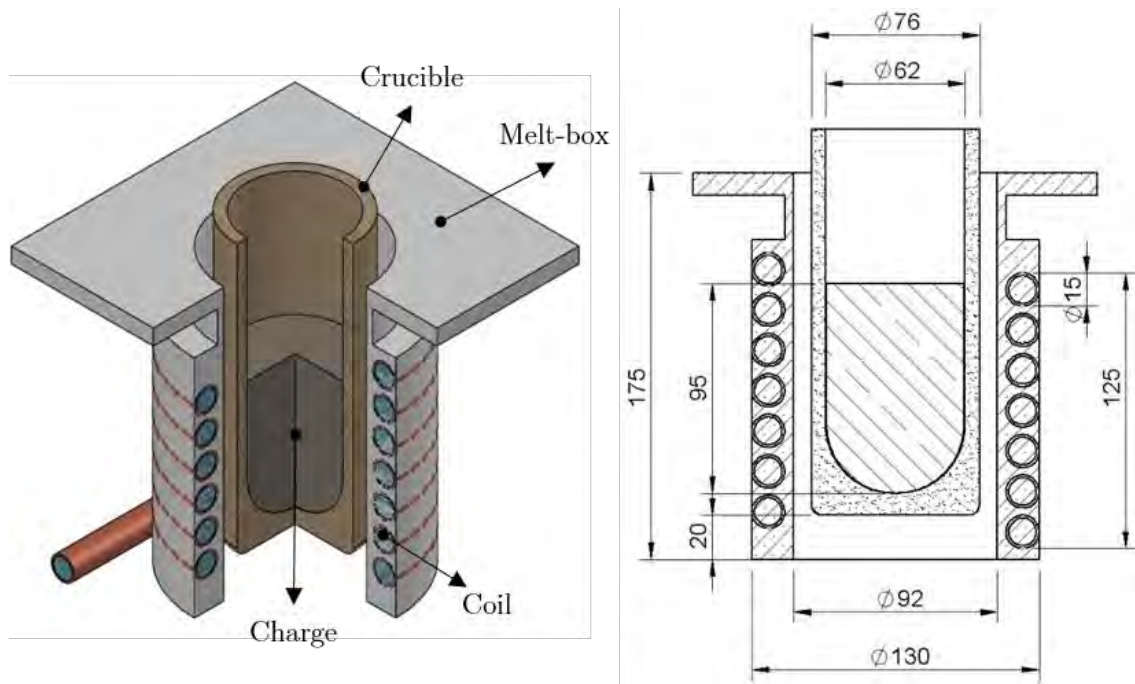
Figure 4-11. 3D melt-box and section view of the geometry with principal dimensions.

Again, the model's geometry was reduced to a 2D axisymmetric plane exploiting the periodicity of the melt-box. Domains and boundaries included in the model are summarized in Table 4-6 and Figure 4-12.
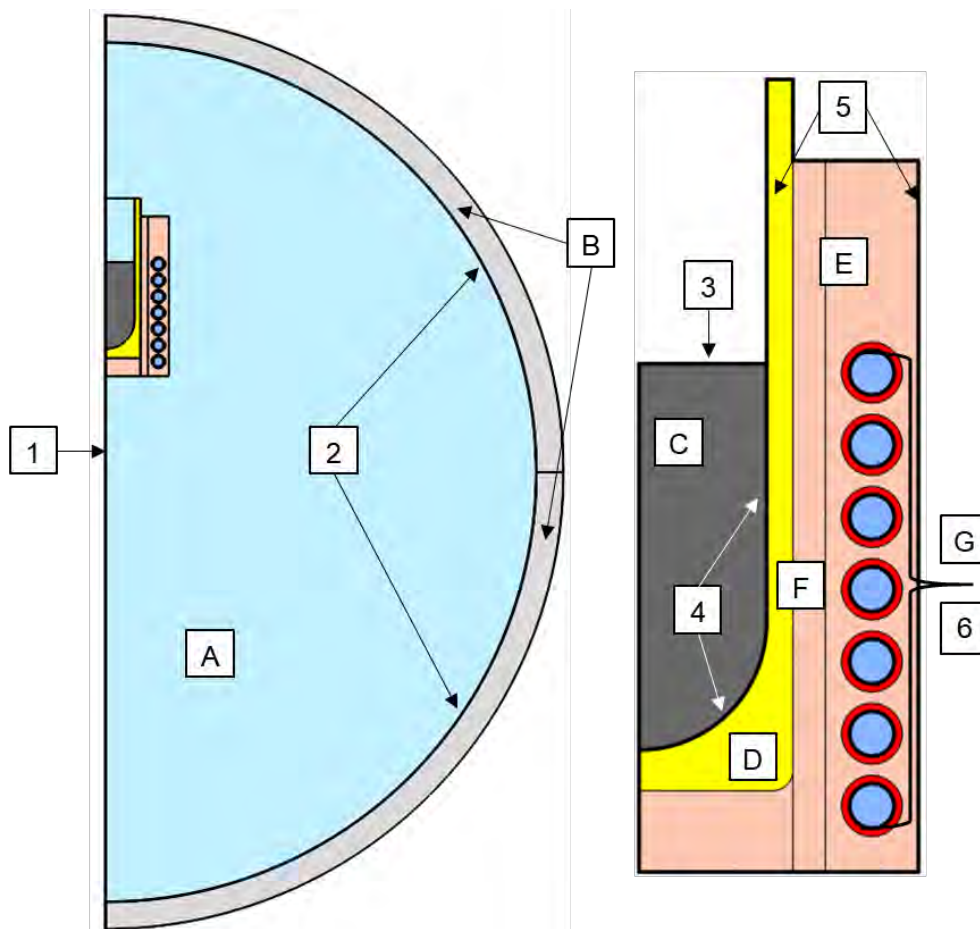
Figure 4-12. Detailed boundary conditions of the modeled geometry.

Table 4-6. Resume of model domains and boundaries for the geometry.

Domain	Description	Boundary	Description
A	Vacuum Atmosphere	1	Symmetry axis
B	Chamber Structure	2	Vacuum chamber inner contour
C	Liquid Metal	3	Metal-free surface
D	Crucible	4	Internal crucible wall
E	Melt-box	5	Melt-box outer contour
F	Coil refrigeration contour	6	Forced convection heat flux
G	Refrigeration water		

- **Material properties**

Material properties were assigned to the domains to resolve the following equations. Regarding liquid metal Inconel 718, there is a notable consistency among the bibliographic references [117], maintaining stability in the temperature range between 1450 – 1500 °C; thus, constant values were considered. Initially, liquid metal emissivity was estimated to be 0.2 according to the provided measured data. Regarding other materials, previously mentioned material parameters were implemented.

Table 4-7. Material properties for induction melting model.

Material	ρ [kg m^{-3}]	λ [Wm^{-1}K^{-1}]	C_p [J kg^{-1}K^{-1}]	σ [S m^{-1}]	μ [mPa $\cdot$ s]	γ [Nm^{-1}])
Inconel 718	7400	29.6	720	6.6e5	5.4	1.86
Al$_2$O$_3$	2950	$0.89 \cdot \ln(T)+10.5$	$0.32 \cdot T0.187$	0	-	-
Melt-box	2730	2.42	1000	0	-	-
Copper	8960	400	385	6e7	-	-

4.2.2. Magneto-hydrodynamic submodel

The coupled magnetic field and fluid dynamics model compromises the recirculation and deformation of the free surface. As mentioned in the bibliographic review, correctly determining the free surface profile and the flow field is essential for the subsequent flow heat transfer analysis and model validation. The proceeded simulation strategy is resumed in Figure 4-13. Initially, the hydrodynamic behavior of the free surface was modeled until reaching a quasi-stationary situation. Then based on the last solution, a complementary stationary study is performed to compute the fluid flow field. The following lines discuss the model's equations and the procedure for the numerical implementation.
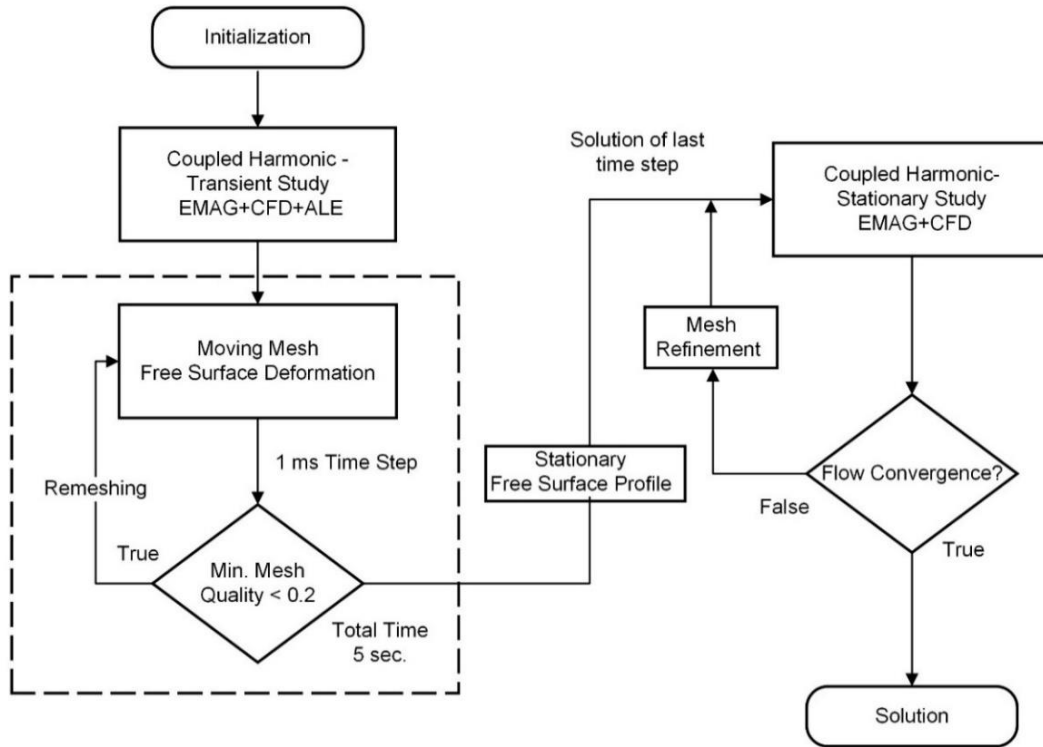
Figure 4-13. Scheme for magneto-hydrodynamic study.

- **Equations and boundary conditions**

Before the detailed analysis of the free surface hydrodynamic, it is essential to briefly mention the fluid flow and turbulence, which are described according to the Navier-Stokes equations for mass and momentum conservation in the time domain:

$$\nabla \cdot (\rho \mathbf{u}) = 0 \tag{4.21}$$

$$\rho \frac{\partial \mathbf{u}}{\partial t} + \rho (\mathbf{u} \cdot \nabla)\mathbf{u} = \nabla \cdot [-p\mathbf{I} + \mathbf{K}] + \mathbf{F} + \rho \mathbf{g} \tag{4.22}$$

Where $\mathbf{K}$ is the viscous stress tensor given by $\mathbf{K} = (\mu + \mu_T)(\nabla \mathbf{u} + (\nabla \mathbf{u})^T)$ describing the internal resistance and friction forces within the fluid.

- **Turbulence modeling**

Turbulence occurs in flows that exhibit considerable velocity gradients, forming rotating structures with a wide range of different lengths and time scales. These vortices introduce fluctuations in the velocity, pressure, and temperature fields, varying in time and space. Since resolving the Navier-Stokes equations for all turbulence scales is impossible, the equations are averaged to describe only the mean field (statistically steady flows) and the fluctuations using Reynolds decomposition.

The mathematical decomposition introduces a new term, the Reynolds stress tensor $\tau'_{ij} = \rho \overline{u'_i u'_j}$, representing the fluctuating stresses from turbulent velocity fluctuations within a fluid flow. The stress tensor describes this phenomenon by establishing statistical correlations between the velocity fluctuations at different points. Typically, the stress tensor is a symmetric second-order tensor with six independent components in three-dimensional space. Due to the nonlinearity of the Navier-Stokes equations, the solution of the averaged flow is not possible, and empirical models are introduced [127].

As mentioned in the literature review, RANS (Reynolds-Averaged Navier-Stokes) turbulence models are considered effective in capturing significant turbulence features and have shown satisfactory results for averaged flow velocities. These models allow for estimating Reynolds stresses and scalar transport by introducing closure models based on empirical data and assumptions.

Many models are based on the assumption of an analogy between the effects of viscous stresses and Reynolds stresses on the flow in terms of the proportionality between stress and strain rate. Boussinesq proposed that the Reynolds stresses should be proportional to the average strain rate.

$$\tau'_{ij} = -2\mu_T S_{ij} + 2/3\rho k \delta_{ij} \tag{4.23}$$

where term (μ_T) and representing effective viscosity resulting from unresolved turbulent eddies. As a first approximation, the standard $k - \varepsilon$ turbulence model was adopted to model the turbulent viscosity (μ_T) where the turbulent viscosity is derived from k and ε with the following relation;

$$\mu_T = \rho C_\mu \frac{k^2}{\varepsilon} \tag{4.24}$$

Two additional transport equations are added, turbulent kinetic energy (k) and turbulent dissipation rate (ε), which are included in the simulation. Detailed explanations and mathematical formulations of these closure models can be found in standard textbooks on turbulent flow dynamics [128], and the mathematical description of the turbulence model can be found in Appendix 2. a.

- **Free surface modeling**

The liquid metal stored inside the crucible is a two-phase flow problem, corresponding to the metal and the air depicted in Figure 4-14.
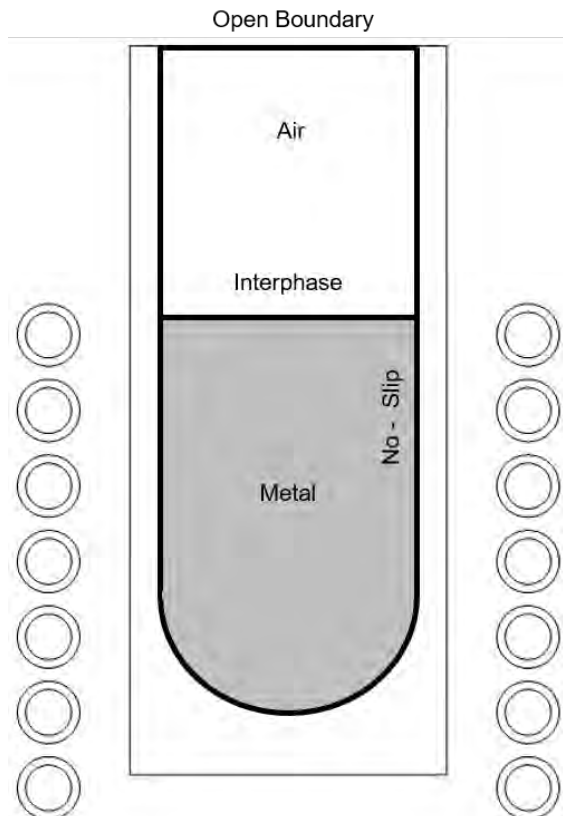
Figure 4-14. Domains and boundary conditions for free surface hydrodynamic study.

The free surface is the boundary corresponding to the interphase between the two phases. As established in the literature review, the dynamic of the free surface was affected by the hydrostatic force, hydrodynamic force, Lorentz Force, and the contribution of surface tension. The balance of these forces produces the characteristically surface profile.

The inertial term or source term ($\mathbf{F}$) works as the inertial term for mass transport. The predominant force acting on the free surface is the magnetic pressure due to the axial contribution of the Lorentz force ($\mathbf{F_L}$). The averaged component of the Lorentz Force for a harmonic field in the axisymmetric formulation can be decomposed for the axial and radial components of the force:

$$F_r = \frac{1}{2}\text{Re}\left(\mathbf{J_\phi B_z^*} - \mathbf{J_z B_\phi^*}\right) \tag{4.25}$$

$$F_z = \frac{1}{2}\text{Re}\left(\mathbf{J_r B_\phi^*} - \mathbf{J_\phi B_r^*}\right) \tag{4.26}$$

The hydrostatic force calculation is straightforward as it is the product of the volume force generated by gravity ($\rho\mathbf{g}$). Finally, what concerns the surface tension force ($\mathbf{F_{ST}}$) it is related to the surface gradient operator ($\nabla_s = \left(\mathbf{I} - \mathbf{n_i n_i^T}\right)$ = being $\mathbf{I}$ the identity matrix) and γ, the surface tension in the interphases the following expression gives it:

$$\mathbf{F_{ST}} = \gamma(\nabla_s \cdot \mathbf{n})\mathbf{n} - \nabla_s\gamma \tag{4.27}$$

- **Moving mesh interface**

Once all the forces acting in the liquid metal are defined, enabling the displacement and interaction between the two phases becomes necessary. In this case, the moving mesh method was chosen, as it does not expect any topological changes, offers easier computation convergence, and requires fewer computational resources than fixed mesh methods. The displacement of the interphase was achieved by implementing a moving mesh approach using the Arbitrary Lagrangian-Eulerian (ALE) method, allowing the mesh nodes to follow the fluid flow and accurately track the moving boundary.

The ALE method combines the advantages of Eulerian and Lagrangian methods by allowing the mesh to deform and move with the fluid while keeping the grid fixed in specific flow regions. In this method, the fluid equations are formulated in a reference frame that moves with the mesh, treating the mesh motion as an additional variable. The numerical procedure begins with defining a static mesh and introducing a mapping function that relates the reference coordinates to the current coordinates of each mesh node, using a Cartesian reference in this case. The original, undeformed mesh is referred to as the material or reference frame, while the deformed mesh represents the spatial frame. For example, in a 2D case located in the deformed mesh with coordinates (x, y), these coordinates can be related to their counterparts in the original undeformed mesh (X, Y) through a function of the form:

$$x = x(X,Y,t); y = y(X,Y,t) \tag{4.28}$$

This way, fluid equations for the $\mathbf{u}$ and p field are solved in the moving reference frame adding the variable of the mesh displacement. The flow displacement perturbs the mesh nodes so they conform with the model's moving interface and other moving or stationary boundaries. PDEs for the mesh displacement are solved to ensure a smooth mesh deformation and the propagation of the moving domain displacement; the Winslow smoothing method was applied to be suitable for unstructured meshes.

$$\frac{\partial^2 X}{\partial x^2} + \frac{\partial^2 X}{\partial y^2} = 0; \frac{\partial^2 Y}{\partial^2 x^2} + \frac{\partial^2 Y}{\partial^2 y^2} = 0 \tag{4.29}$$

The main drawback of moving mesh methods is the large stretching and elongation of grid elements leading to distortions affecting the numerical stability and convergence difficulties. Therefore, a moving mesh control was implemented in the simulation to overcome the numerical instability caused by mesh deformation. The mesh nodes were updated iteratively using the mapping function for accounting for the flow motion until convergence or the end of the simulation time was reached. If any mesh element had a quality lower than 0.2, a remeshing operation was triggered. This helped maintain the mesh's quality and integrity, ensuring convergence and stability in the numerical calculation. Once the mesh was remeshed, the simulation resumed from the previous state.

Free mesh normal direction deformation was enabled in the interphase region that separates the two domains. This allowed the mesh to adapt and follow the boundary deformation between the two domains while keeping it fixed in the axial direction. In the wall region, tangential mesh displacement was enabled to facilitate the radial movement of the triple point where the two domains and the boundary meet. This approach ensured the mesh accurately captured the boundary deformation while maintaining fixed adhesion to the wall.

The numerical coupling between the two physical fields is straightforward. The fluid flow displacement has to be included in the previously discussed induction equation to consider modifying the original magnetic field due to the free surface deformation in each simulation time step.

$$F_L = \frac{1}{2} \text{Re}(\mathbf{J} \cdot \mathbf{B}^*)$$

Magnetic Field	Hydrodynamic
$\mathbf{J_e} = \left(j\omega_f \sigma - \omega_f^2 \varepsilon_r\right)\mathbf{A} + \nabla \times (\mu_r^{-1}\nabla \times \mathbf{A})$ $+ \sigma\mathbf{u} \times (\nabla \times \mathbf{A})$	$\nabla \cdot (\rho\mathbf{u}) = 0$ $\rho\dfrac{\partial \mathbf{u}}{\partial t} + \rho(\mathbf{u} \cdot \nabla)\mathbf{u} = \nabla \cdot [-p\mathbf{I} + \mathbf{K}] + \mathbf{F} + \rho\mathbf{g}$

Moving mesh
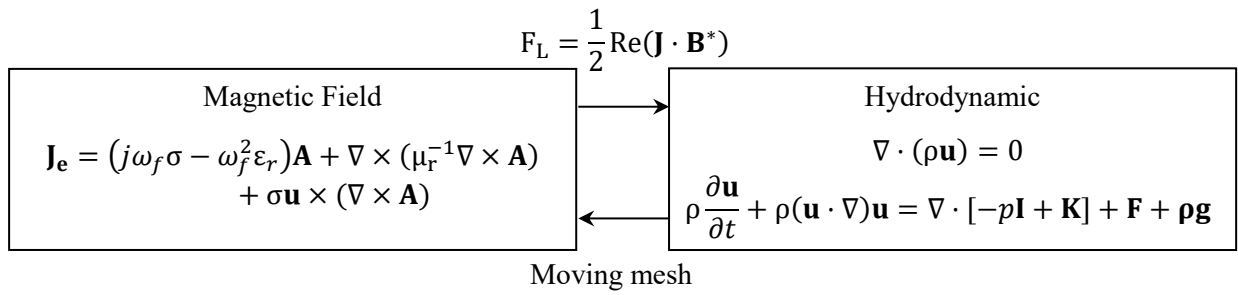
Figure 4-15. Magneto-hydrodynamic numerical coupling.

- **Boundary conditions**

The boundary conditions must be adapted to solve the fluid flow field, the turbulent variables, and the mesh displacement, which are resumed in Table 4-8. In this regard, the typical no-slip boundary in the wall was considered, imposing $\mathbf{u} = 0$. However, boundary conditions must be adapted to the resolution of the turbulence variables of the RANS $k - \varepsilon$ model. For that, the standard wall function was implemented to model the turbulent boundary layer of the wall and compute ε and k and the turbulence behavior at the near-wall region.

It considers that the velocity profile in the near wall boundary can be approximated to a logarithmic function and relates with the turbulence variables with analytical expression related to the distance from the wall (y^+). The solution and implementation can be found elsewhere [128]. And the mathematical description of the wall functions can be found in Appendix 2.a

Thus, the boundary was modified to no penetration condition where $\mathbf{u} \cdot \mathbf{n} = 0$ and the shear stress condition reads $\mathbf{K} \cdot \mathbf{n} = -\rho u_\tau/u^+ \mathbf{u}_{\text{tang}}$. The tangential velocity ($\mathbf{u}_{\text{tang}}$) relates the mesh deformation and the wall velocity of the fluid $\mathbf{u}_{\text{tang}} = \mathbf{u} - (\mathbf{u} \cdot \mathbf{n})\mathbf{n}$.

A fluid-fluid interface condition was implemented to handle the mesh displacement at the interphase boundary. This condition ensured proper coupling between the two-phase domains and allowed for the accurate resolution of the flow field. There is no mass transfer occurring across the boundary, thus

resulting in the equality of velocities between the two phases $\mathbf{u_1} = \mathbf{u_2}$. Additionally, the viscous stress tensor ($\mathbf{K}$) of the two domains was related to the normal vector ($\mathbf{n}$) at the interface, taking into account the contribution of surface tension ($\mathbf{F_{ST}}$). This formulation enabled the calculation of the interface velocity, which was equal to the mesh displacement.

The crucible top boundary was treated as an open boundary with no shear stress, and the turbulent kinematic energy and dissipation rate was assumed to be zero in this region. The mesh movement on the open boundary was fixed to ensure mass conservation.

Table 4-8. Boundary conditions for the moving mesh and hydrodynamic model.

Boundary	Physical interface		
	Flow field ($\mathbf{u}$)	Turbulence (k/ε)	Moving mesh
Wall	$\mathbf{u} \cdot \mathbf{n} = 0$ $\mathbf{K} \cdot \mathbf{n} = -\rho \frac{u_\tau}{u^+} \mathbf{u}_{tang}$	$\nabla k \cdot \mathbf{n} = 0$ $\nabla \varepsilon \cdot \mathbf{n} = \frac{C k_\mu^2}{k_v \delta_w^+ \mu}$	$\mathbf{u}_{tang} = \mathbf{u} - (\mathbf{u} \cdot \mathbf{n})\mathbf{n}$ $d_r = 0$
Fluid-Fluid Interface	$\mathbf{u_1} = \mathbf{u_2}$ $\mathbf{n} \cdot \mathbf{K_2} = \mathbf{n} \cdot \mathbf{K_1} + \mathbf{F_{ST}}$	-	$\mathbf{u}_{mesh} \cdot \mathbf{n_1} = \mathbf{u} \cdot \mathbf{n_1}$
Open Boundary	$\mathbf{K} \cdot \mathbf{n} = 0$	$\nabla k \cdot \mathbf{n} = 0$ $\nabla \varepsilon \cdot \mathbf{n} = 0$	$d_r = 0$ $d_z = 0$

- **Meshing and solver configuration**

The mesh grid definition is critical, especially when dealing with coupled, simultaneous physical interfaces like flow transport and magnetic field. The meshing sequence was divided into two steps according to the goal of the simulations. As an initial step for the mesh deformation study, unstructured triangle mesh elements were employed, adjusting the minimum element size to capture the skin effect. The coil domains meshed through boundary layer mesh to capture the resistive losses due to the auto-inductance effects in the copper windings. For the rest of the domains, triangular mesh elements were employed with extremely fine sizes. During the moving mesh simulation, an automatic re-meshing algorithm improves calculation stability and avoids generating degenerated mesh elements. In each iteration, a mesh control was applied to verify that the element's minimum quality was over 0.2, and if not, the mesh elements were adapted to the actual deformation. An example of the mesh for the last time step can be seen in the figure Figure 4-16.a.

For the stationary fluid flow simulation, a mesh refinement was performed to improve the quality of mesh elements and increase resolution, especially in the fluid-wall interface, to resolve the RANS equation in the turbulence boundary layer correctly. The grid was adjusted iteratively to ensure computation convergence based on the relative error defined by the velocity gradient of the fluid flow. In this regard, a mesh validation analysis was done to ensure the repeatability of the results, which is presented in the mesh sensitivity section of the following numerical results. For example, in Figure 4-16.b, the solutions for a maximum element length of 0.5 for the static flow analysis can be observed.

For the $\mathbf{u}$ and p fields, second-order (P2+P1) discretization was adopted, while for magnetic vector potential ($\mathbf{A}$) quadratic elements. A segregated solver was employed to solve the fields, dividing the problem into various steps corresponding to each physics and computed sequentially in each iteration. This way, smaller equation matrixes were generated. However, more iterations to converge in the solution were required. The time step was limited to 1 ms in the free surface study. A Direct PARDISO

linear solver was used to solve the linearized equation systems and simulate the magnetic and flow field and mesh displacement, while the MUMPS solver was for the turbulence variables.
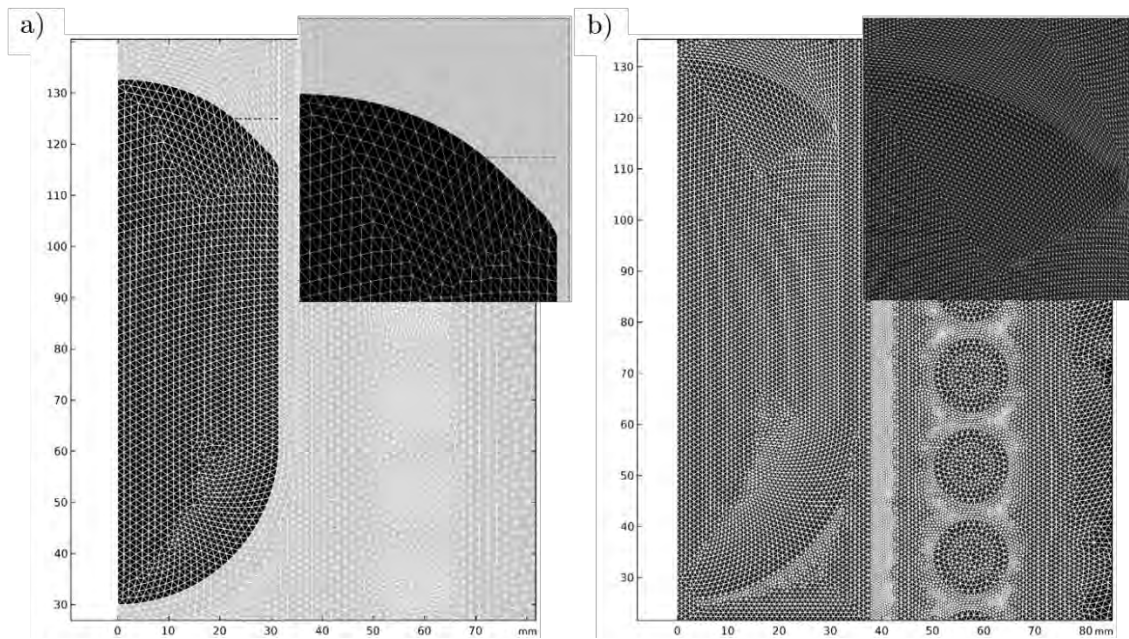
Figure 4-16. a) Final mesh for deformation study. b) Refinement for flow stationary study.

4.2.3. Magneto-hydrodynamic numerical results

- **Free surface profile**

The described set of equations was implemented in the initial liquid state model, and the coupled magnetic field studied the coupled set of equations in the frequency-transient domain. The applied power in the coil was 8 kW, corresponding to stage 4 of the 3.4. Standard melting procedure, where the melt temperature was at 1500 °C. The coupling can be observed in the transient solution where the top and bottom position of the surface is represented by numeric probes and the power in the coil (Figure 4-17).
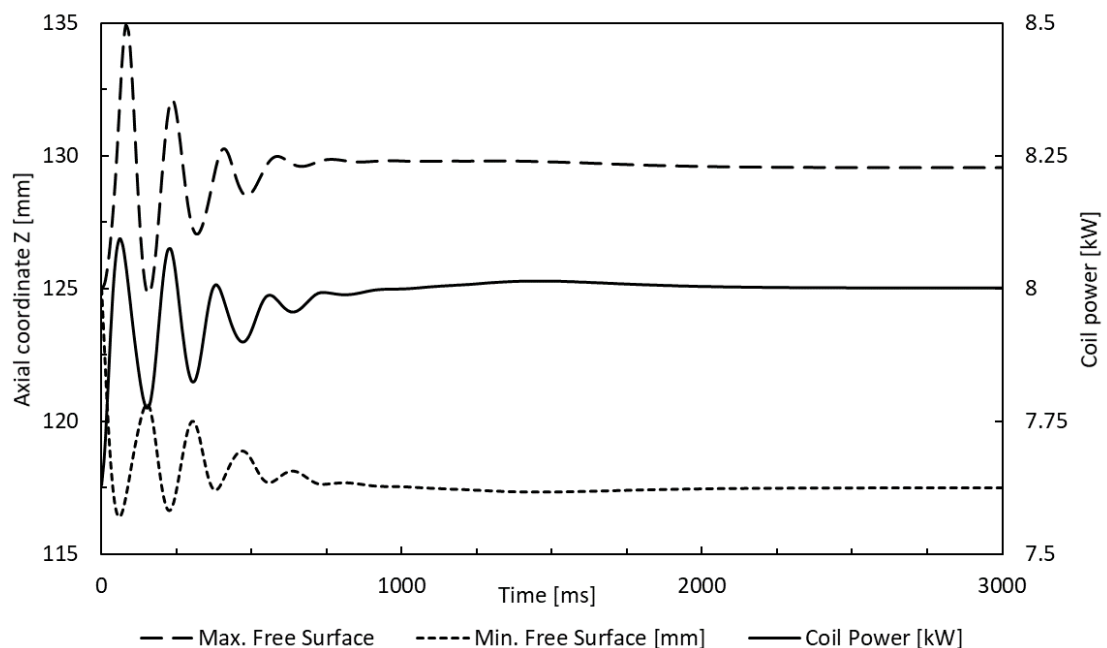
Figure 4-17. Free surface oscillations and coupling for 8 kW induced power.

The oscillations of the metal geometry during the simulation influenced the original magnetic field, leading to a delayed variation in the applied power. This accurate coupling between the physics resulted in a stationary state solution after a few seconds of simulation. However, it was observed that the initial fast oscillations were not the actual comportment observed in the experimental tests. These oscillations resulted from the instantaneous power application, not reflecting the real behavior of the power generator, which increases power progressively up to reach resonance conditions.

Therefore, a 1-second duration step function was implemented in the coil power application. This step function accounts for the progressive increment of the magnetic force in the melt, providing a more realistic representation of the power application and improving the computational convergence. The free surface deformation was simulated for three power case studies: 8 kW, 11 kW, and 16 kW. The resulting quasi-stationary surface profiles are in Figure 4-18.
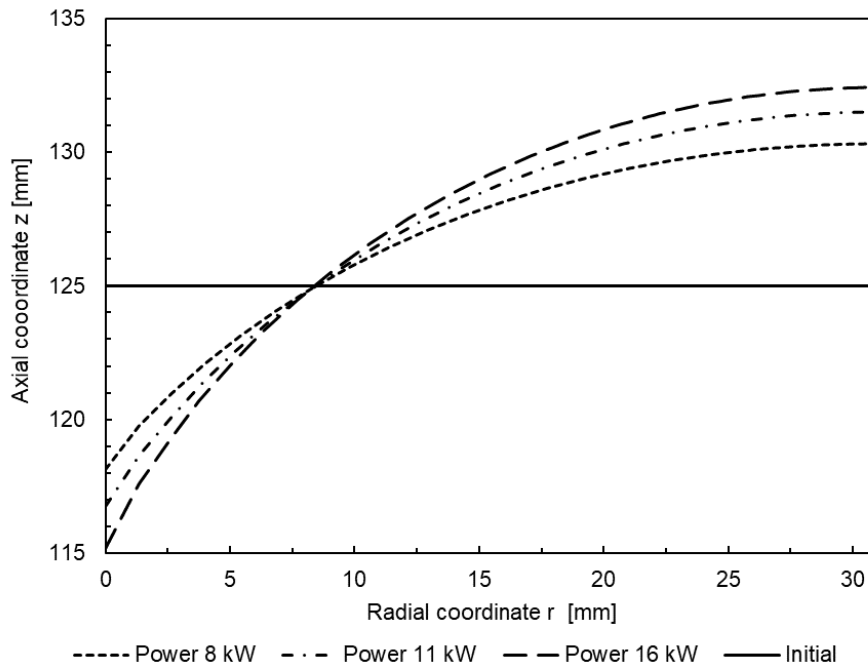
Figure 4-18. Free surface profile for considered three power stages during the standard melting trial.

It can be observed that the height difference (Δh) between the maximum and minimum points ranges from 12 to 17 mm for the applied powers of 8 kW and 16 kW, respectively. As expected, the high density of the alloy requires higher induced powers to achieve a more significant surface deformation.

- **Flow recirculation**

Once achieved, the quasi-stationary free surface profile of the flow field was studied. A coupled frequency-stationary approach was developed to evaluate the flow field pattern, as the power was maintained at 8 kW and 1500 °C, corresponding to stage 4 of the Standard melting procedure.

Slight modifications to the previous model were done, eliminating the domain corresponding to the air while maintaining the liquid metal. Also, the top surface profile was assumed to be fixed, so the boundary condition was modified to a stationary free surface described by an open boundary condition with the contribution of the surface tension, while the turbulence closure boundary conditions were $\nabla k \cdot \mathbf{n} = 0$ and $\nabla \varepsilon \cdot \mathbf{n} = 0$.

$$\mathbf{K} \cdot \mathbf{n} = 0 + F_{st} \qquad (4.30)$$

Based on the last step of the free surface deformation simulation, equal **u** and p variables were used as initial conditions, while the last deformed condition was implemented for the mesh. The solver configuration of the stationary study included an additional step to verify the mesh independence of the flow field, ensuring the correctness and precision of the solution. A mesh independence analysis was performed, which will be discussed later. Figure 4-19 represents the Lorentz force (**F$_L$**) vectors are on the left side, and the magnetic flux density (**B**) on the right side.
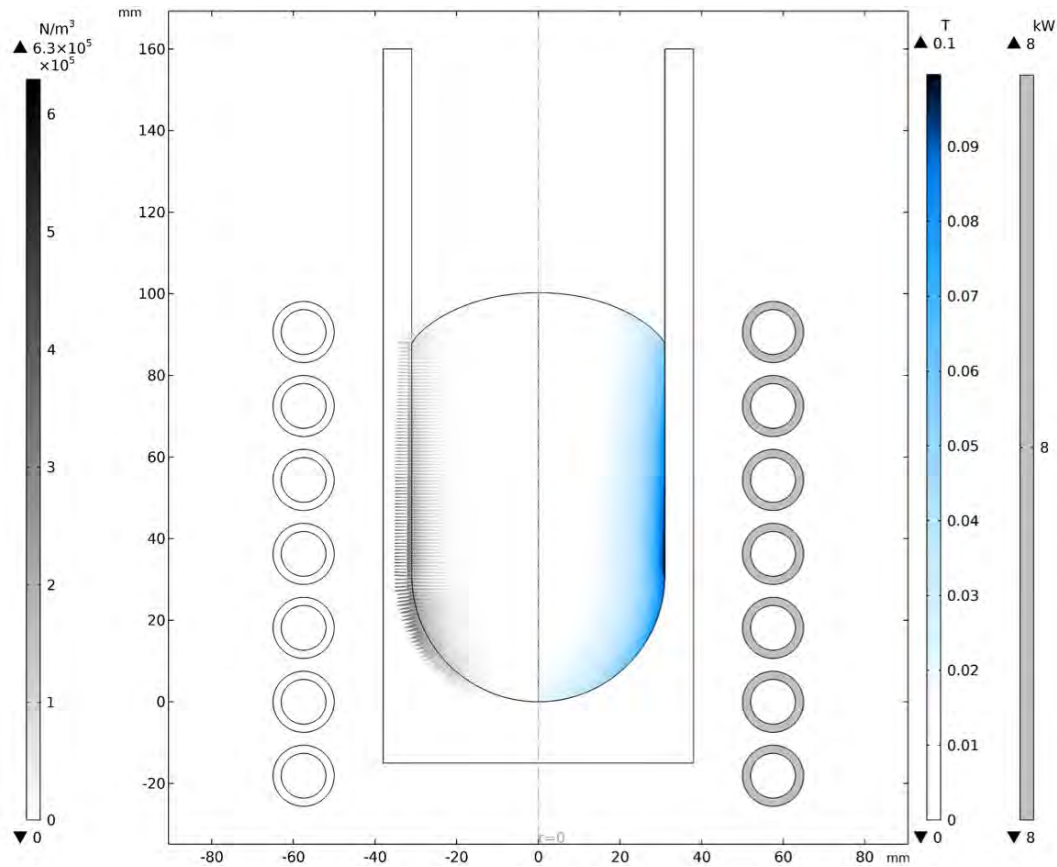
Figure 4-19. Lorentz force (**F$_L$**) vectors and magnetic flux density (**B**) for 8 kW of induced power.

Evaluating the magnetic field distribution over the metal, one can again see the skin effect and the intensity diffusion entering the metal. The highest magnetic field magnitude was at the transition between the vertical wall and the beginning of the crucible bottom curvature. The skin depth was slightly larger, 7.2 mm, due to reduced smaller electrical conductivity. Similarly, the highest magnitude of Lorentz force was in the same area, whose modulus was represented along with the vectors and a proportional scale. This suggests that the flow field might present an intensive acceleration in this region near the wall.

In order to verify the hypothesis, the flow field (**u**) and the turbulent kinetic energy (k) were examined (Figure 4-20). Concerning the flow field, two recirculatory flow patterns were distinguished, rotating in the opposite direction. The magnitude of the lower one was higher, probably due to the accelerating effect of the concave geometry of the bottom side of the crucible and the concentration of the magnetic force in that area. Flow velocity magnitude was in the order of cm/s which is a typical value according to the previous studies regarding induction melting applications reported in the bibliographical review. Another interesting flow parameter was the turbulence number being in the order of 10^4 in the transition between laminar and fully turbulent.

Regarding turbulence, by analyzing the turbulent kinematic energy (k), higher values were in the free surface and the bottom curvature. Also, it can be seen that near the wall, the kinematic energy tends to

be zero due to the limitation of employing wall functions. This indicates that the turbulence intensity should be higher in those areas and related to the free surface flow oscillations, which will be discussed in 5.2 Magneto-hydrodynamic correlation experimental trials.
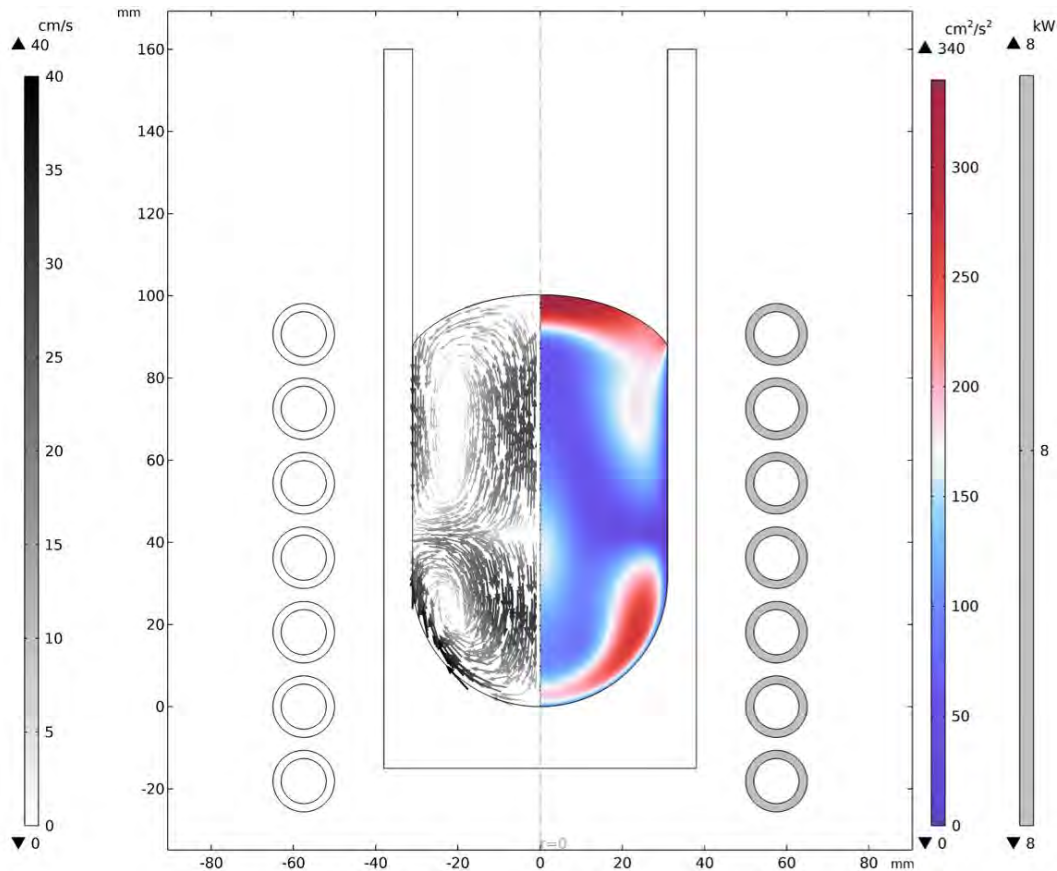
Figure 4-20. Fluid flow field and turbulent kinematic energy (k) for induced power of 8 kW.

- **Mesh sensitivity**

The results' consistency was verified through a mesh independence study; the mesh was refined by progressively minimizing the maximum element size and increasing the number of finite elements. Concatenate simulations reducing the mesh element length were performed, starting from 4 mm and halving down to 0.25 mm. In all cases, the applied power remained constant at 8 kW.

To compare the obtained results, certain critical aspects of the model were evaluated, including the total resistive heating (Q_{rh}), the magnitude of the Lorentz force ($\mathbf{F_L}$), and further related to the flow analysis, the maximum and average velocities. The results are summarized in Table 4-9.

Table 4-9. Resume of mesh independence study results.

Max Lenght (mm)	Nº Elements	Avg. Quality	Q_{rh} [kW]	$\mathbf{F_L}$ [N/m^3]	$\mathbf{u}_{avg}$ [m/s]	$\mathbf{u}_{max}$ [m/s]
4	$4.1 \cdot 10^4$	0.87	6.07	6.16	14.9	36.9
2	$5.4 \cdot 10^4$	0.89	6.08	6.17	15.6	37.8
1	$1.1 \cdot 10^5$	0.92	6.08	6.17	15.9	39.1
0.5	$2.9 \cdot 10^5$	0.94	6.08	6.17	16.4	40.4
0.25	$1.0 \cdot 10^6$	0.95	6.08	6.17	16.8	41.4

In the case of the magnetic variables, a precise consistency was achieved, the result hardly varying in principle due to the small size of the elements used. A progressive velocity increase was observed in the flow velocities case, probably related to local effects due to increased elements. However, it should be noted that it was verified the repeatability and not the accuracy; this aspect is discussed next.

- **LRN $k - \varepsilon$ turbulence model**

The above-mentioned standard $k - \varepsilon$ model is based on several assumptions that limit the accuracy of the results. The turbulence model was formulated for high Reynolds number flows, over 10^5, where the flow is completely developed, or for free stream cases. Under these circumstances, employing wall functions to calculate the velocity at the solid wall is considered a valid approach. Even if a no-slip boundary condition was imposed, there is an artificial velocity in the wall which could lead to a distortion of the heat transfer between the convective metal and the solid wall. Also, it has been reported that a lack of sensitivity to reproduce flows with adverse pressure gradients, over-estimating the shear stress and retarding the flow separation. Therefore, the size of recirculating zones and rotating flows might be underestimated [128].

A near-wall modeling approach was employed to tackle these uncertainties. The necessity to integrate the turbulence equations through the buffer and viscous sublayer reaching the wall was evident. An advanced version of RANS models employing a Low Reynolds approach in the wall region was implemented. The Low Reynolds Number (LRN) $k - \varepsilon$ formulation model is based on the previously discussed standard model; however, it is enhanced by adapting the formulation to modify the turbulence transport equations by adding non-linear damping factors. Several specific formulations considering LRN can be found in the literature; among them, the AKN model was chosen because it can predict the separation and attachment of the flow and the transition between laminar to turbulent flow [129]. The complete formulation of the LRN $k - \varepsilon$ model is resumed in the Appendix 2.b.

Regarding the near-wall flow modeling, the Low Reynolds number wall treatment approach was adapted to solve the velocity field for the viscous and buffer layers. The first mesh cell must be included in the viscous sublayer to be capable of solving the flow in the near-wall region. The requirement of a finer mesh increased the mesh quality demand; therefore, additional mesh refining was done to ensure the distance of the center of the initial mesh element. The wall treatment for a no-slip condition where the velocity was set to zero in the wall $\mathbf{u} = 0$. Thus, the turbulent kinetic energy (k) and dissipation rate ε the corresponding wall boundary condition are:

$$k = 0; \ \varepsilon = 2\frac{\mu}{\rho}\frac{k}{l_w^2} \qquad (4.31)$$

LRN turbulence models utilize damping functions to smooth the turbulent viscosity values and solve the transport equations in the near-wall region. Therefore, grid density plays a crucial role. It is recommended to have a distance between the wall and the center of the first mesh element of less than 1 in viscous units ($l_c^* < 1$).

In the initial evaluation of the independent study's mesh configuration, which had the smallest element size of 0.25 mm, it was observed that vertical sections of the wall had l_c^* values exceeding 5. To address this, the element size was further reduced in the region adjacent to the wall until the criterion of $l_c^* < 1$ was met (Figure 4-21. b). As an additional refinement, contour layers of structured elements were incorporated by specifying the number of layers, the narrowing factor, and the width of the first layer. Triangular mesh elements were used toward the domain's interior (Figure 4-21. b).

Significantly, the relative distance between the first mesh element and the physical wall was minimized by fixing a distance of 0.1 mm, thus meeting the established criterion.
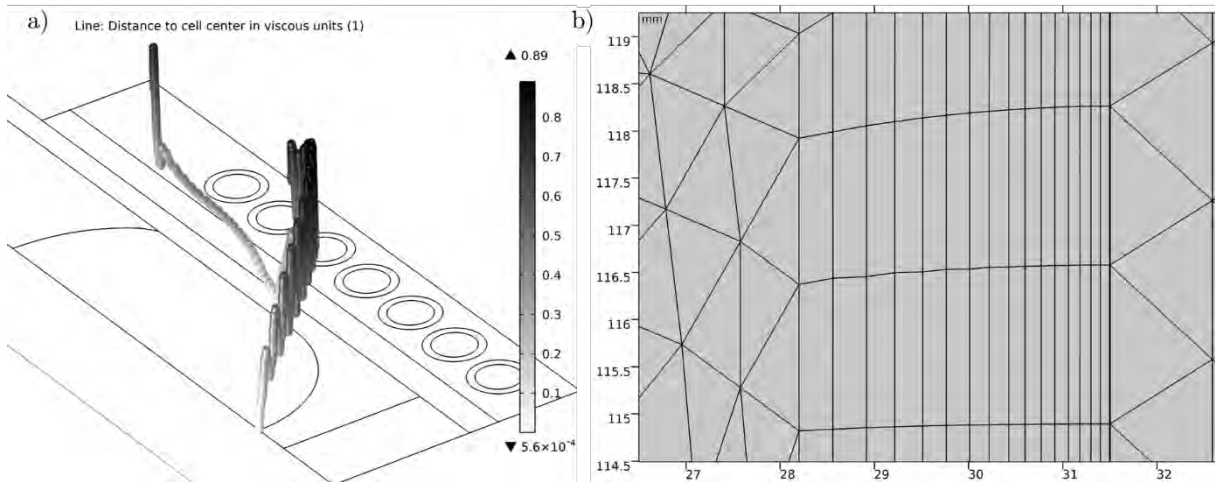
Figure 4-21. a) Depict of cell center to wall distance. b) Structured mesh in the near-wall region.

- **Turbulence model comparison**

Once the particularities of the LRN $k - \varepsilon$ turbulence model are described, the previous model was adapted, including the required turbulence modifying equations. As the initial value of the velocity and turbulence variables, the results from the previously discussed Standard (STD) $k - \varepsilon$ model were considered. Input variables for an 8 kW input power for a metal temperature of 1500 °C were included. The exact boundary conditions were applied to the model by solving a stationary velocity study. The free surface profile and the mesh was kept static from the previous analyses.

The flow field pattern indicates the formation of two opposite-direction eddies. The higher velocities were computed in the bottom curvature, probably due to the accelerating effect provided by the crucible radius. On the contrary, the velocity was almost zero in the center of the eddies. The same pattern was achieved in the two, even though the velocity magnitude was lower for the LRN $k - \varepsilon$ model, which might be reduced due to the damping functions.
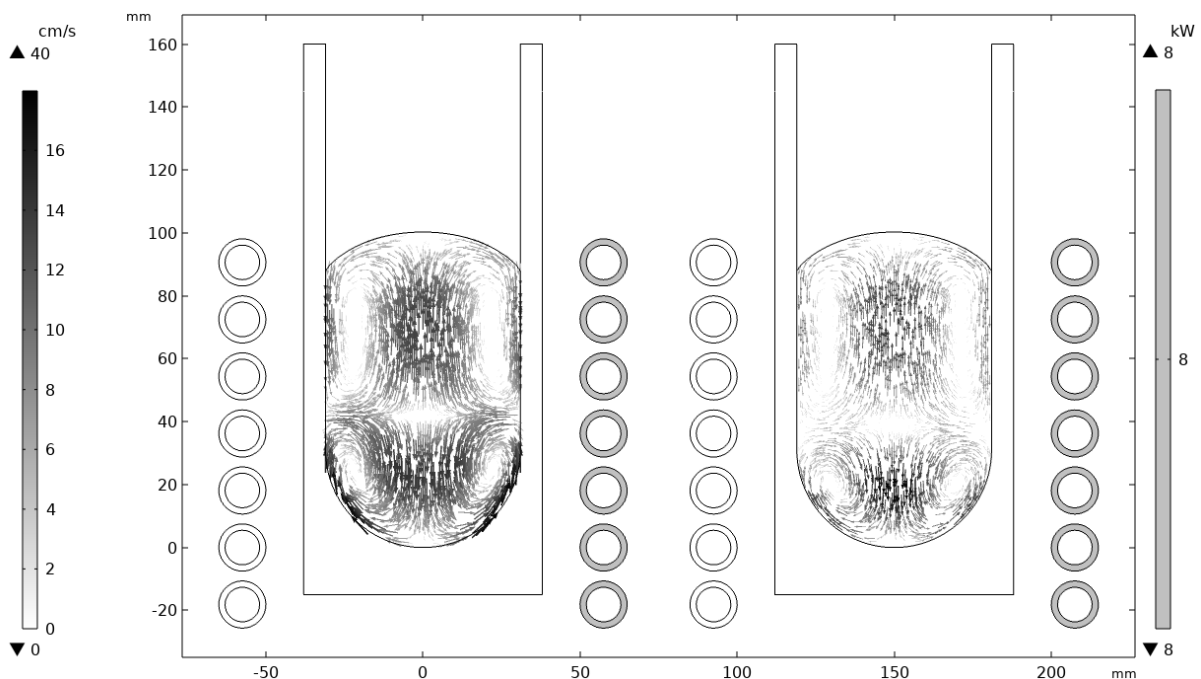
Figure 4-22. Comparison of the flow field for turbulence models. Left: STD $k - \varepsilon$. Right: LRN $k - \varepsilon$.

Regarding the symmetry axis, Figure 4-23 illustrates the r = 0 axis velocity for both the standard $k - \varepsilon$ model and the new LRN model mentioned earlier.
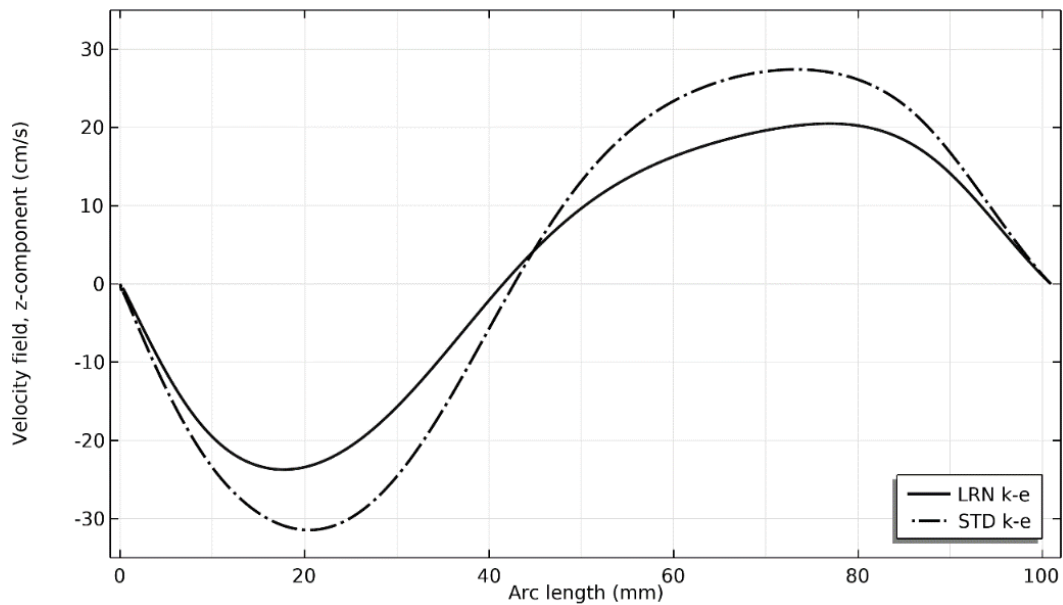
Figure 4-23. Axial velocity V_z in r = 0 comparison for LRN and STD k-e turbulence models.

The flow's radial velocity vector (Vz) reveals the presence of two distinct peaks, one positive and one negative, indicating opposite flow rotation directions. These peaks correspond to the narrowing of the flow due to recirculation, which leads to acceleration when the two streams come into contact. However, the velocity becomes zero in the zone where the two eddies are in contact, approximately 35 and 45 mm from the crucible bottom. As anticipated, the LRN model exhibits a lower velocity magnitude than the STD $k - \varepsilon$ model, and the placement of the eddies is more widely separated.

Although the two models reported similar results in terms of velocity magnitude, the LRN model's capability to solve close to the wall makes it more interesting for coupled heat transfer study. Thus, two lines crossing the center of the primary vortices, Z_1=25 mm and Z_2=75mm, were considered zones of interest (Figure 4-24).
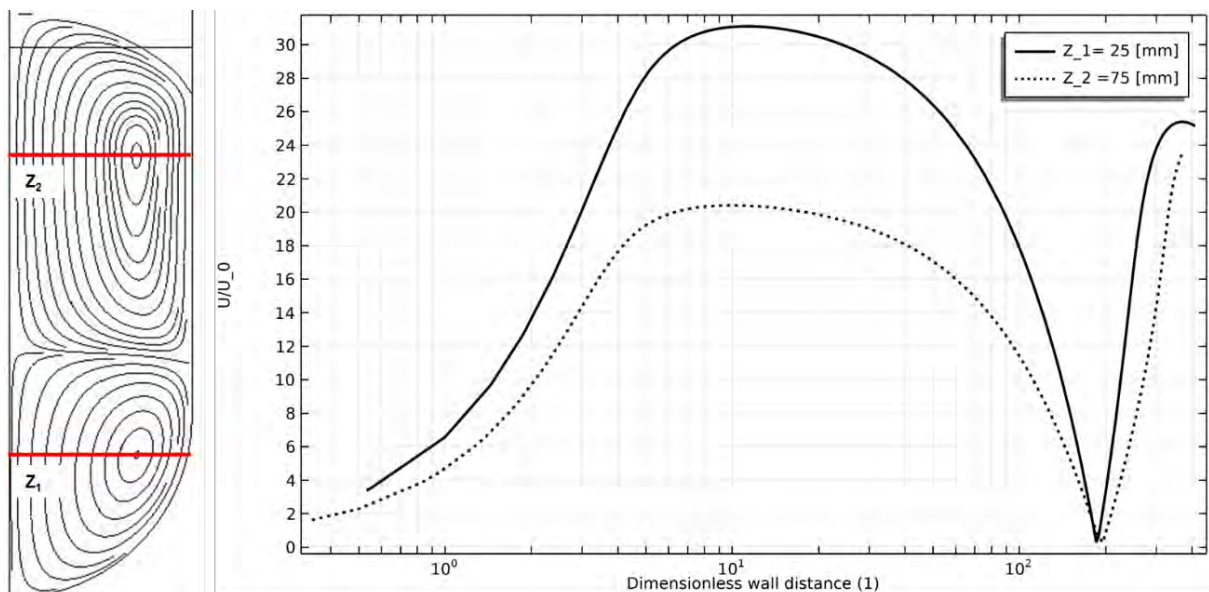
Figure 4-24. Normalized velocity and viscous wall distance for Z_1 and Z_2 section probes.

The flow field has been represented and normalized in order o observe better the fluctuations and the wall distance in viscous units and logarithmic scale. Once going away from the wall, the velocity increased almost exponentially to reach y+ around 10 when it started to decay. In the middle of the eddy, velocity is practically zero, incrementing again when approaching the axisymmetric axis with another peak not as high as the first.

Before discussing the coupling with the heat transfer, the mesh's sensitivity was verified to ensure the results' stability. As in the previous case, the maximum length of the mesh element was reduced, increasing the number. The results are summarized in Table 4-10; as in the previous case, repeatability was ensured on the magnetic-related fields, so only the velocity field is included.

Table 4-10. Mesh sensitivity analysis for fluid flow stationary simulation

Max Lenght	N° Elements	Average Quality	$\mathbf{u}_{avg}$ [m/s].	$\mathbf{u}_{max}$ [m/s]
4	$1.2 \cdot 10^5$	0.92	12.8	33.0
2	$1.5 \cdot 10^5$	0.92	12.9	33.1
1	$2.5 \cdot 10^5$	0.92	12.9	33.3
0.5	$6.4 \cdot 10^5$	0.93	13.0	35.5

4.2.4. Magneto-thermo-hydrodynamic model

In the case of induction heating, the numerical results indicated a pronounced thermal gradient on the ingot due to the skin effect. In the case of liquid metal, the electrical variables for a fixed power of 8 kW were taken as a reference to study the heating. For this purpose, the thermal field was incorporated into the magneto-hydrodynamic model presented, reproducing the turbulent heat transfer.

- **Equations and boundary conditions**

The dissipation of eddy currents into heat by the resistive losses (Q_{rh}) was done in the same manner, including the Q_e as the heat source term in the heat equation. The energy equation that describes the transport of thermal energy within the fluid and includes terms of fluid convection can be written as;

$$\rho C_p \left(\frac{\partial T}{\partial t} + (\mathbf{u} \cdot \nabla T) \right) = \nabla \cdot ((\lambda_{eff}) \nabla T) + Q_e \tag{4.32}$$

The introduced new term λ_{eff} is the sum of the contribution of the liquid metal thermal conductivity (λ) and the turbulent thermal conductivity λ_T which takes into account the enhanced heat transfer due to turbulent mixing. It depends on the flow conditions and the turbulent viscosity;

$$\lambda_T = \mu_T \, {}^{C_p} \!/\! {}_{Pr_T} \tag{4.33}$$

Therefore both fields have to be coupled; a non-isothermal approach was considered by introducing the turbulent Prandlt number (Pr_T) that relates the momentum and heat transfer of turbulent diffusion. The bibliographical review has concluded that analytical relations can be suitable for related RANS models and convective heat transfer effects.

It was mentioned that the Reynolds analogy is invalid as the local temperature and velocity gradients in the flow are not similar for low Pr number flows, which in this case is Pr=0.01; thus, the Pr_T has to be adaptive to the local flow characteristics. From the various analytical expressions, the Kays-Crawford relation was included with the following relation:

$$Pr_T = \cfrac{1}{\cfrac{1}{2Pr_{T\infty}} + CPe_T\sqrt{\cfrac{1}{Pr_{T\infty}}} - (CPe_T)^2\left[1 - \exp(-\cfrac{1}{CPe_T\sqrt{Pr_{T\infty}}})\right]} \tag{4.34}$$

Where $Pe_T = Pr\frac{\varepsilon_m}{\mu_T}$ relating the flow dissipation rate and the turbulent dynamic viscosity. While $Pr_{T\infty} = 0.85$ is the value of Pr_T Far away from the wall, and $C = 0.03$ is a constant that relates the Pr_T and Pe_T in the spatial distribution.

However, according to Weignand et al. [103], the original Kays and Crawford relation does not suit low Pr numbers in the order of 10^{-3}. For a constant value of $Pr_{T\infty} = 0.85$ Pr_T is smaller than 1.7, but when Pr tends to zero, the heat transfer is exclusively by conduction (molecular), and Pr_T should increase. Thus the author includes a correction according to the Reynolds number of the flow away from the wall. In this case, the maximum turbulence of the flow field study has been considered Re=10^4.

$$Pr_{t\infty} = 0.85 + 100/PrRe^{0.888} \tag{4.35}$$

Thus, the compendium of equations that solve the three phenomena for the liquid metal is summarized in Figure 4-25. The heat equation for solids and the heat transfer by conduction ($\mathbf{q_c}$) was solved for the rest of the thermal model domains, crucible, and melt-box. The rest of the thermal phenomena are described as heat losses in the boundary conditions.

$$F_L = \frac{1}{2}Re(\mathbf{J} \cdot \mathbf{B}^*)$$

Magnetic Field

$$\mathbf{J_e} = (j\omega_f\sigma - \omega_f^2\varepsilon)\mathbf{A} + \nabla \times (\mu^{-1}\nabla \times \mathbf{A}) + \sigma\mathbf{u} \times (\nabla \times \mathbf{A})$$

Hydrodynamic

$$\frac{\partial p}{\partial t} + \nabla \cdot (\rho\mathbf{u}) = 0$$

$$\rho\frac{\partial \mathbf{u}}{\partial t} + \rho(\mathbf{u} \cdot \nabla)\mathbf{u} = -\nabla \cdot [-p\mathbf{I} + \mathbf{K}] + \mathbf{F} + \rho\mathbf{g}$$

$$Q_e = \frac{1}{2}Re(\mathbf{J} \cdot \mathbf{E}^*)$$

Moving mesh

$$\mu_T; Re; \varepsilon$$

Heat transfer

$$\rho C_p\left(\frac{\partial T}{\partial t} + (\mathbf{u} \cdot \nabla T)\right) = \nabla \cdot ((\lambda_{eff})\nabla T) + Q_e$$
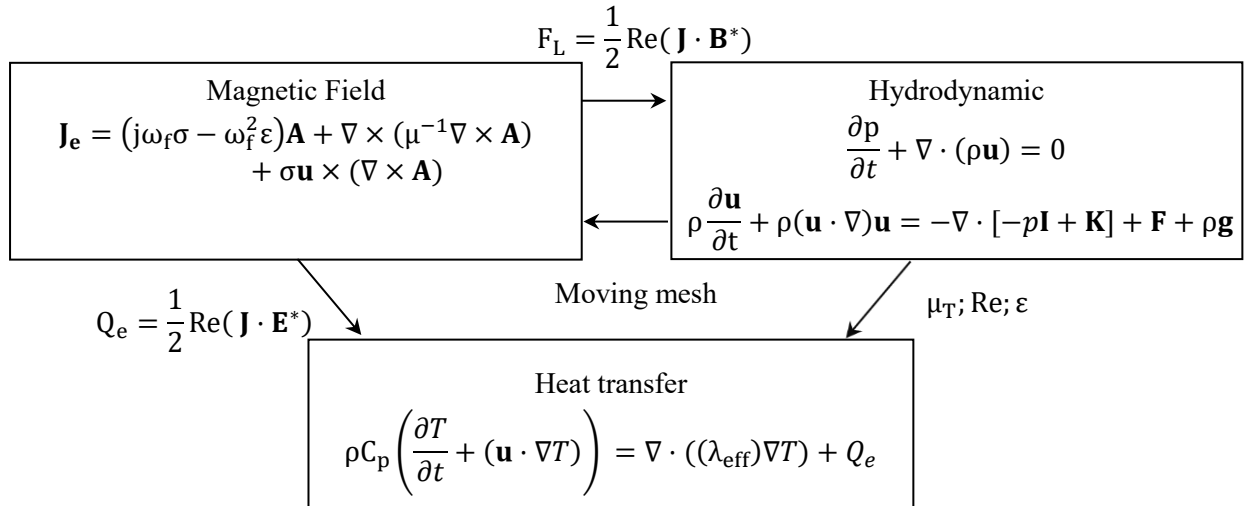
Figure 4-25. Coupled equations for the resolution of induction melting in the liquid metal.

- **Boundary conditions**

The second model incorporated boundary conditions that simulated energy loss through heat from the metal. Two main boundary conditions were considered: radiation on the free surface of the metal ($\mathbf{q_t}$) and forced convection on the inner contour of the coils ($\mathbf{q_{dis}}$). The radiation boundary condition was applied to the free surface of the metal. In the liquid state, mutual radiation between the surfaces is negligible compared to the radiation between the metal surface and its surroundings. Thus, the classical radiation boundary condition was imposed.

The forced convection boundary condition in contour Nº6 was determined based on the experimentally measured heat dissipation on the coil refrigeration of the 3.4. Standard melting procedure. This forced convective heat flux depends on the inlet and outlet temperatures and the heat transfer coefficient (h), which was parametrized to adjust the measured heat losses due to conduction through the crucible ($\mathbf{q_{dis}}$)

To ensure thermal insulation, the outer contour of the melt-box was treated as a thermal insulation boundary. It is important to note that these boundary conditions must be considered in conjunction with the previously described fluid flow and turbulence-determining boundary conditions. The summarized boundary conditions are presented in Table 4-11

Table 4-11. Boundary conditions for the coupled thermo-hydrodynamic model.

Boundary	Description	Physical interface	
		Flow field ($\mathbf{u}$)/ Turbulence (k/ε)	Thermal
Free Surface (N°3)	Radiation Surface	$\mathbf{K} \cdot \mathbf{n} = 0$ $\nabla k \cdot \mathbf{n} = 0$ $\nabla \varepsilon \cdot \mathbf{n} = 0$	$-\mathbf{n} \cdot \mathbf{q_{rad}} = \epsilon \cdot \sigma(T_\infty^4 - T^4)$
Internal Wall (N°4)	No-slip	$\mathbf{u} = 0$ $k = 0; \varepsilon = 2\dfrac{\mu}{\rho}\dfrac{k}{l_w^2}$	$-\mathbf{n} \cdot \mathbf{q} = -\lambda_{\text{eff}}\nabla T$
Coil int. boundary (N°6)	Forced Convection	-	$-\mathbf{n} \cdot \mathbf{q_{dis}} = h(T_{ext} - T)$
Crucible - Meltbox (N°5)	Thermal Insulation	-	$-\mathbf{n} \cdot \mathbf{q} = 0$

4.2.5. Magneto-thermo-hydrodynamic numerical results

In the heat transfer simulation, the initial temperature distribution of the melt-box-crucible sub-assembly and the liquid metal is estimated based on a coupled frequency-stationary simulation. The objective was to reproduce the quasi-steady state corresponding to stage 4 of the standard melting trial, where the melt temperature was 1500 °C. A constant induced power of 8 kW was established. The heat dissipation in the coil ($\mathbf{q_{dis}}$), was adjusted to have a dissipation of 5 kW corresponding to the averaged measured heat flux during the standard melting procedure. The radiation heat transfer was considered with an emissivity factor of 0.2, while the remaining material properties were described in Table 4-7. The same mesh discussed in the previous section was implemented for this simulation.

A segregated solver type was selected, with PARDISO used for the solver with second-order elements for all fields except the turbulence variables, for which MUMPS was considered. The resulting temperature field achieved in the simulation is shown in Figure 4-26 on the left side, and the heat flux magnitude and direction vectors on the right.

The maximum computed temperature was 1554 °C, approximately 50 °C superior to the pyrometer measurement. The crucible works as a thermal insulator with a rapid temperature reduction trough the crucible solid section and maintains the coil pipe inner boundary temperature to 25 °C. The total heat flux magnitude vectors crossing the domains were presented in the logarithmic scale, verifying that the heat was conducted from the crucible to the coils' inner boundary passing through the melt-box. The convective pattern between the main toroids follows the same pattern as in the velocity field, demonstrating the relationship between the two fields. Even though the convective heat flux of the melt was two orders of magnitude superior to the conduction thus, the heat transfer between the crucible and the melt was reduced due to the high thermal insulating capacity of the crucible.
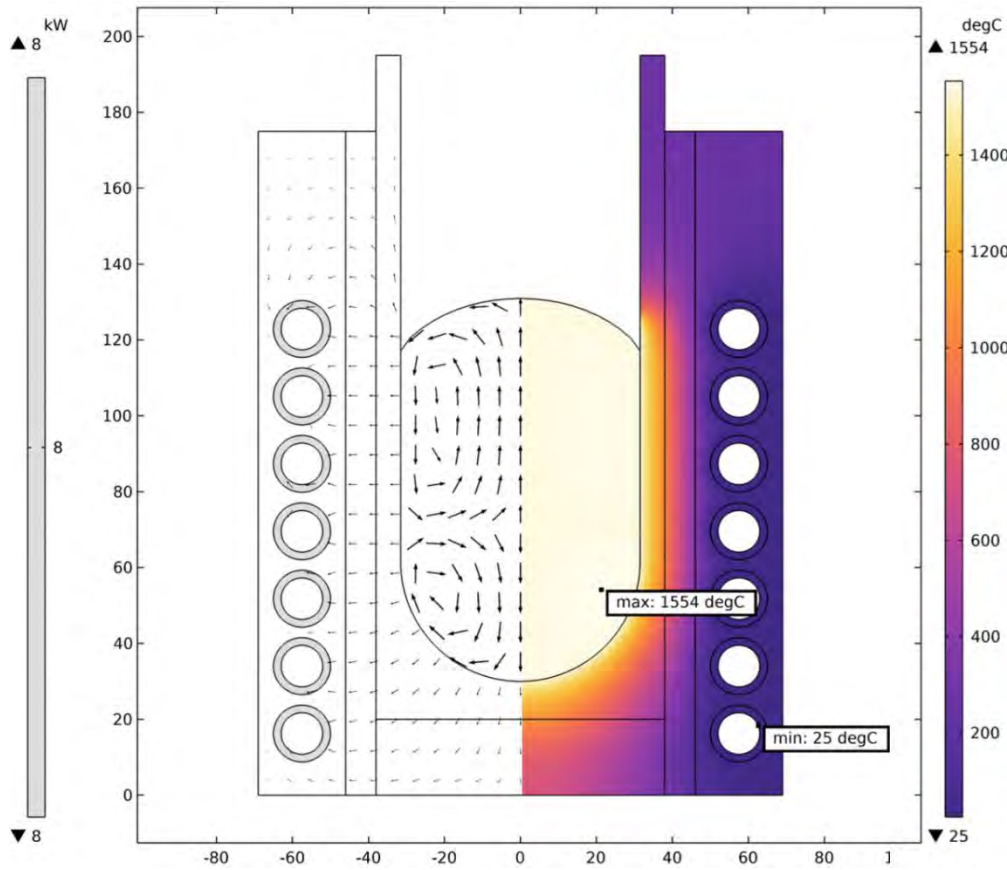
Figure 4-26. Heat flux and temperature distribution for 8 kW applied power.

Focusing on the near wall turbulent heat transfer, the Pr_T, and T_0 are shown for the $Z_1=25$ mm and $Z_2=75$ mm cut lines. As shown in Figure 4-27, the model reproduced the reduction of the Prandlt number inverse logarithmic as a function of the dimensionless wall distance starting with a value of 2.1 and decaying once it surpassed $y^+ >10$ when the flow becomes turbulent.
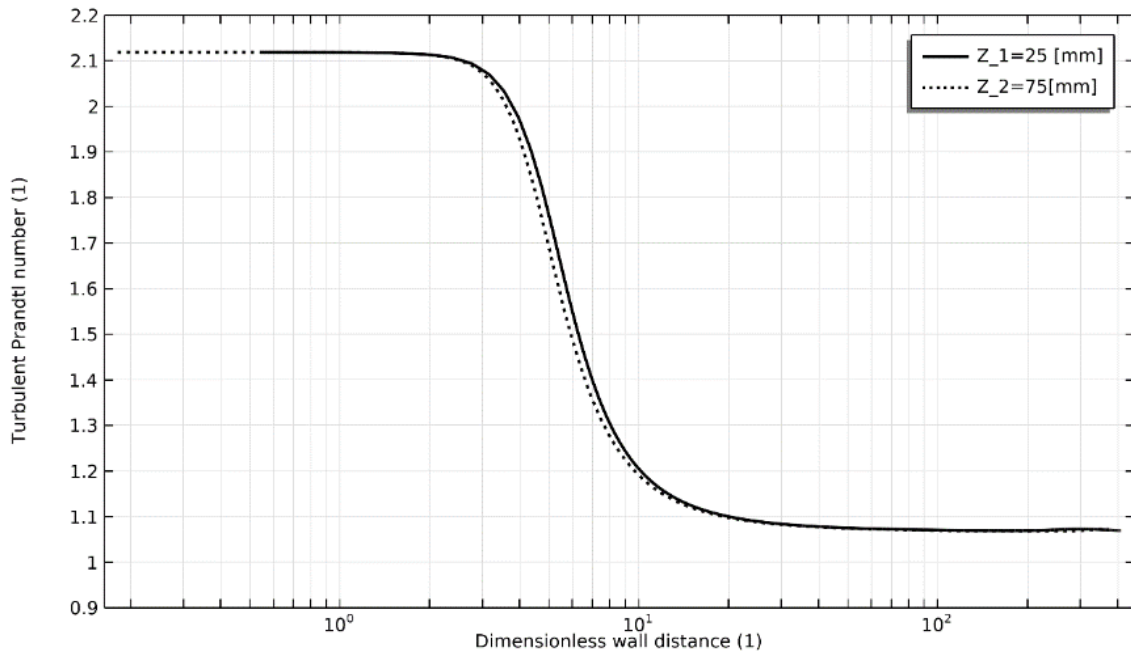
Figure 4-27. Pr_t value in function of wall distance for Z_1 and Z_2 cut lines.

The temperature has been represented in dimensionless values (T_0), subtracting the wall temperature (T_w). Initially, both temperatures are equal; in the wall, $\mathbf{u} = \mathbf{0}$ condition is fulfilled, and as moving away from the wall, the temperature increases exponentially up to almost 5 °C of increment. This confirms the previously mentioned metal homogeneous temperature distribution with a higher temperature in the central axis.

This moderate temperature increase could be related to the constant recirculation of the metal and the high thermal conductivity together with the contribution of thermal conductivity of the turbulent flow (λ_T) leading to a temperature to homogenization. Also, it must be mentioned that the stationary flow cannot model heat transfer between the eddies during the time, which might increase heat convection between them. Finally, it has to be noted that the model geometry considers a relatively small mass, 2 kg charge, under the simulation's stationary condition, which should minimize the temperature gradient.
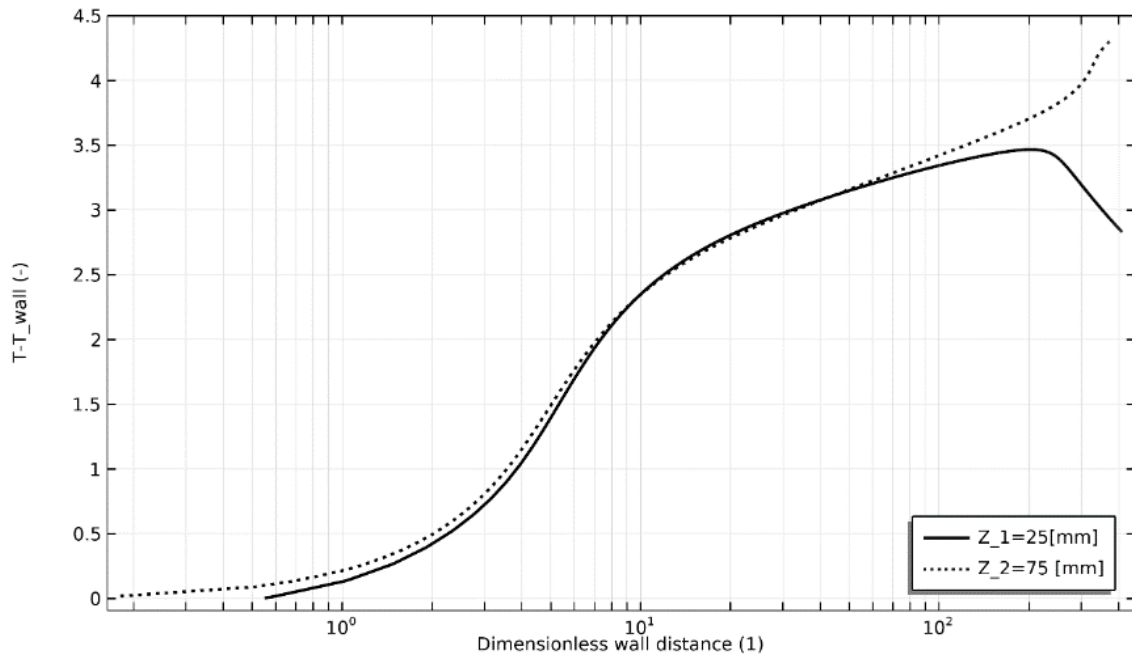
Figure 4-28. The normalized temperature in the function of wall distance for Z_1 and Z_2 cut lines.

4.3. Conclusions

It has been observed that the magnetic induction is localized and, consequently, the resistive power losses. From the magnetic field analysis, it is clear that the coil configuration is not optimal for heating loads with a high height/radius ratio since the magnetic flux is concentrated in the mid-height region of the ingot. In addition, the coil excitation frequencies contribute to this surface induction effect. Therefore, non-uniform heating of the ingot is expected with a faster temperature rise in the mid-lower zone of the ingot. The contribution of the heating by irradiation has a much smaller effect than magnetic induction.

On the one hand, it has been evidenced that the induction heating model replicates the trend of the ingot temperature increase. The pyrometer measurement range does not start until 700 °C and only records the upper surface temperature, the coldest zone. However, the numerical results suggest a considerable thermal gradient in the ingot.

Regarding the liquid state model, in the hydrodynamic model, a relatively small surface profile has been observed concerning the magneto-hydrodynamic model and the deformation of the free surface. The high density of the alloy produces a considerable normal force which compensates for the Lorentz force

produced by the magnetic field. However, it has not been possible to measure the height reached by the liquid metal due to the physical limitations of the vacuum chamber and the small size of the crucible, making the use of measuring systems impossible.

In the flow velocity field, a recirculation pattern is observed, forming two dominant vortices in opposite directions with a magnitude of about 20 cm/s, which agrees with the reports of previous works mentioned in the literature review. The two turbulence modes studied indicate a similar velocity profile, although the vortex centers are slightly displaced, and the flow velocity is different. Through mesh sensitivity studies, it has been shown that the velocity field remains stable even when the mesh size is reduced, demonstrating the model's robustness. In principle, the LRN k-e model seems more suitable as it can resolve the flow to the wall, which should be favorable when computing the heat transfer between the metal and the crucible. However, it is to be noted the necessity of specific meshing with structured elements in the near wall region to cope with the wall viscous wall distance criteria.

The multi-physical coupling between the three physics has been achieved concerning the thermal results. Although the simulation temperature and pyrometer measurement does not match perfectly, the obtained results seem promising as the error is relatively small. Verifying the Prandlt number in the near wall region indicates that the melt temperature does not vary significantly under stationary conditions. In the next chapter, it will be studied under transient conditions. In addition, the transient tests will be used to test the dynamic behavior and to understand its accuracy compared to the experimental tests described in the next chapter.

<div align="right">

Chapter 5

5. Experimental validation

</div>

The next chapter focuses on the validation of the numerical models presented in Chapter 4. Numerical modeling. To achieve this, a series of ad-hoc experimental tests were performed and compared to their corresponding numerical simulations. The aim was to establish correlations, determine the uncertainty in the simulations, and identify potential sources of error or areas for improvement in the model. The experiments utilized the VIM equipment as in 3.3. Laboratory scale VIM furnace. However, an open-air induction melting furnace was employed to study hydrodynamics and free surface deformation. Throughout the experiments, variables such as input power, temperature, and heat losses were actively monitored and recorded. Additionally, additional simulations were conducted based on the experimental measurements to replicate the testing conditions and compare the results with the experimental data.

The transient heating of the load was considered the most suitable approach to evaluate the induction heating and the resulting coupling between the two fields. Furthermore, the electrical parameters of the coil were characterized and compared with the estimates provided by the model. In terms of the liquid state, the coupling between the magnetic and hydrodynamic fields will be assessed by characterizing the free surface of the metal. Moreover, a dynamic test will be conducted to evaluate temperature under steady-state and transient conditions utilizing multiple reference points for the numerical correlation.

5.1. Induction heating correlation

The coil is the main element to generate the magnetic field necessary to induce eddy currents; thus, its accurate modeling will be key. The study's first step involves the measurement of the coil's electrical parameters and comparing them with the model results. Then, the induction heating in the solid ingot under transient conditions is studied, and the simulations are compared with the measured temperature.

5.1.1. Coil electrical characterization

In this task, the electrical characterization of the induction was carried out. Determining the equivalent resistance and impedance will be used as a reference for validating the magnetic model. A Fluke PM6304® RCL meter was used to measure the impedance. The coil was connected to this device, and a frequency sweep was performed from 50 Hz to 10 kHz, where the setup can be seen in Figure 5-1.
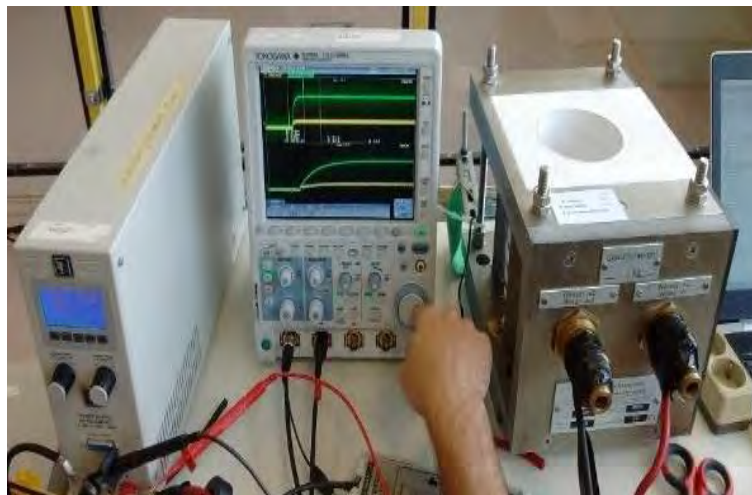
Figure 5-1. Coil electrical characterization experimental set-up.

From the measured impedance and modulus, the inductance and resistance of the coil were estimated. Two configurations were tested to verify the influence of the ingot in the coil, one with an empty melt-box and the second with an ingot. The charge, an Inconel 718 2 kg cylindrical ingot, was introduced into the crucible placed in the melt box. The results for different excitation frequencies are in Table 5-1.

Table 5-1. Electrical parameters of the coil.

	Empty		Ingot	
Frequency [Hz]	Resistance [mΩ]	Inductance[µH]	Resistance [mΩ]	Inductance [µH]
50	4.7	5.2	4.7	5.2
10^2	5.1	7.6	5.1	7.6
10^3	6.0	7.8	6.5	7.7
10^4	17.3	7.5	23.3	7.3

The coil's inductance slightly increased with the ingot placed inside. This phenomenon occurred due to the interaction caused by the charge with the magnetic field passing through it, so the magnetic coupling varies. The coil's inductance is a sensitive and challenging parameter to determine and seems to vary according to the test conditions, depending on the circuit current and the excitation frequency, so the coil is modeled to check its error concerning the measurements. Therefore, reference data is available for comparison with the model based on the measurements.

- **Coil electrical parameters**

Coil modeling is an advanced tool incorporated in COMSOL Multiphysics® that estimates electrical parameters based on the coil's dimensions. A frequency-based parametrization analysis was performed to compute the electrical parameters described in 3.4.1 Power generator electrical variables on coil characterization. A verification simulation was also carried out, introducing the ingot inside the coil. The comparison between experimentally characterized coil resistance and inductance and the modeled values generated by the coil modeling is summarized in Figure 5-2.
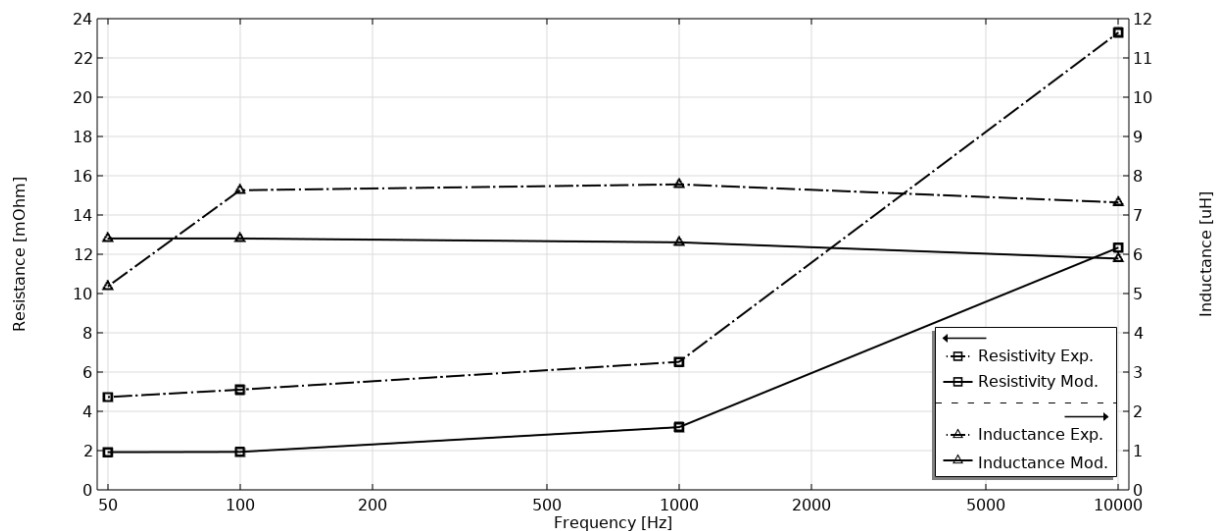
Figure 5-2. Correlation of electrical coil parameters for experimental and numerical solutions.

Even if the numerical results are in the same order of magnitude, a notable error can be observed, especially for the resistivity at the highest frequency case (10 kHz) with a more significant deviation. This underestimation of the resistivity should lead to greater electrical efficiency as there are fewer

losses due to parasitic losses. Another possibility might be that the deviation could be related to the simplification of the coil model, which does not consider the helical shape of the coil in 3D and the water connection coaxial pipe. Also, the additional resistance and inductance of the instrument measurement system increase the uncertainty of the results.

5.1.2. Experimental test and numerical correlation

The preliminary induction heating simulation is presented in 4.1.5. Induction heating numerical results evidenced non-uniform heating. However, there was only the pyrometer measuring the temperature and the uncertainty of the temperature measurement as only the pyrometer was pointing to the top surface, being the coldest surface with a temperature gradient of approximately 250 °C. Additionally, the pyrometer measuring range starts at 700 °C, making it impractical to determine the heating process until the end of the bake-out. To overcome these limitations, a specific testing setup was designed to acquire temperature-time transitory data for a more detailed study of the induction heating on the ingot. The setup incorporates a sensorized ingot with four K-type thermocouples soldered at various heights and inserted 10 mm from the surface of the ingot, as shown in Figure 5-3. These reference measurements will serve for validation and correlation purposes.
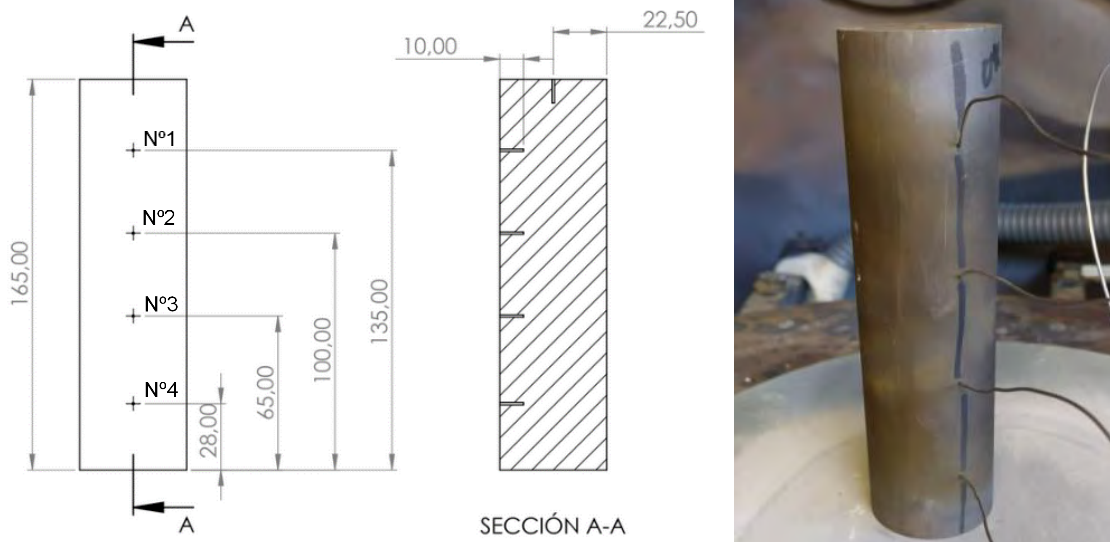
Figure 5-3. Thermocouples position in the vertical length of the ingot.

A constant power of 5 kW for 1 hour was applied for the transient thermal analysis until the system reached a steady state and stabilized the temperature. Special care was taken to ensure that the temperature limit of the thermocouples, around 1370 °C, was not exceeded during the test. Before the experiment, it was verified that the magnetic field did not interfere with the temperature readings and produced excessive signal noise. The thermal inertia was minimal during the trial, and the temperature increased rapidly, especially in the lower thermocouples. However, after 30 minutes, the temperature started to stabilize. There was a significant difference, approximately 250 °C, between the upper and lower thermocouples at the end of the test.

Next, a numerical simulation that replicates this experiment was performed. The heating power and frequency were the input variables, while four virtual probes placed in the identical coordinates as the thermocouples were the output results. Figure 5-4 compares the experimental (grey) and simulated (black) temperatures for the constant 5 kW applied power.

The experimental test shows that the temperature of the lower side thermocouples, N°3 and N°4, increased rapidly and stabilized out after 40 minutes, while the temperature increment of the upper

thermocouples, N°1 and N°2, was more gradual and continued linearly beyond half of the test duration. Regarding the simulation, the initial temperature was underestimated, particularly for the lower-side thermocouples. However, in the middle of the transient study, the temperature was overestimated, causing the simulation curve to flatten out earlier and resulting in a lower temperature towards the end. Possible reasons for these discrepancies include underestimating emissivity and lower heat dissipation in the model. Also, there could be an overestimation of the effect of irradiation between surfaces having less influence than expected.
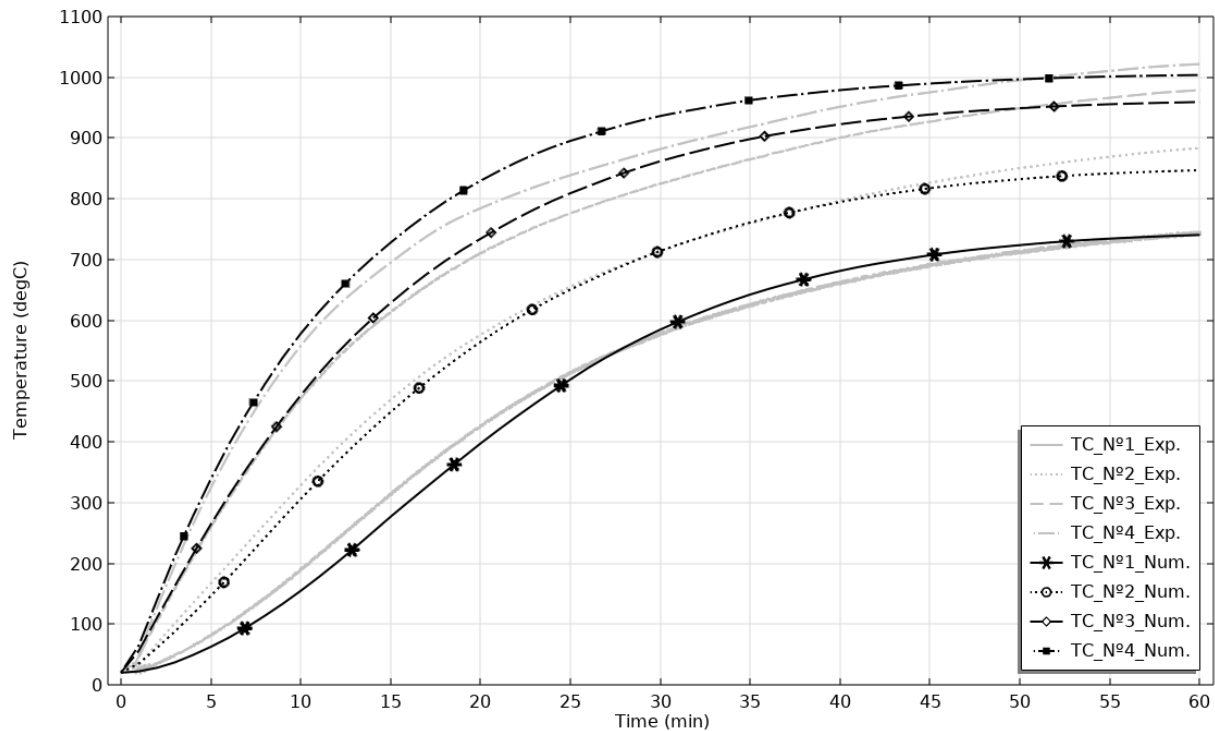
Figure 5-4. Correlation of the numerical result and experimental test for induction heating.

5.2. Magneto-hydrodynamic correlation

The following test was conducted to validate the magneto-hydrodynamic numerical coupling by measuring the free surface profile. In the theoretical simulations, the resulting surface profile under quasi-stationary conditions suggested a minor deformation with a height difference between 12 mm and 17 mm due to the low applied powers and the high density of the liquid Inconel 718 (Figure 4-18). However, the high melting temperatures of over 1350 °C and the difficulties of working in a vacuum chamber with short space, no visible light, and magnetic fields hinder the capability to acquire in-situ experimental data for free surface shape. Therefore, many technical challenges exist in validating the numerical model and completing the experimental trials for the VIM.

These difficulties can be resolved by employing an air-open induction melting furnace (Figure 5-5). In this regard, an Inductotherm® Small Steel Shell furnace with a VIP POWER-TRAK+® power generator. The operation is the same as in the previous case, with the particularity of larger dimensions of approximately one order of magnitude superior, melting 20 kg aluminum or 7.5 dm^3. Operating variables are more similar to industrial capacities, having a rated power of 50 kW at 3 kHz. The inductor coil is composed of 10 loops, and as in the previous case, the coil is coaxial with water refrigeration.

The open-air furnace configuration has the evident advantage of performing melting more easily. The elimination of the vacuum chamber allows for the installation of the acquisition systems and the observation with the naked eye, making it more suitable for hydrodynamic studies. Aluminum was

employed as a melting material with a liquidus temperature of 660 °C three times less density and having well-characterized thermophysical properties. Therefore, it will be used as a reference for validating the hydrodynamic model, performing complementary measurements, and employed as a second case study.
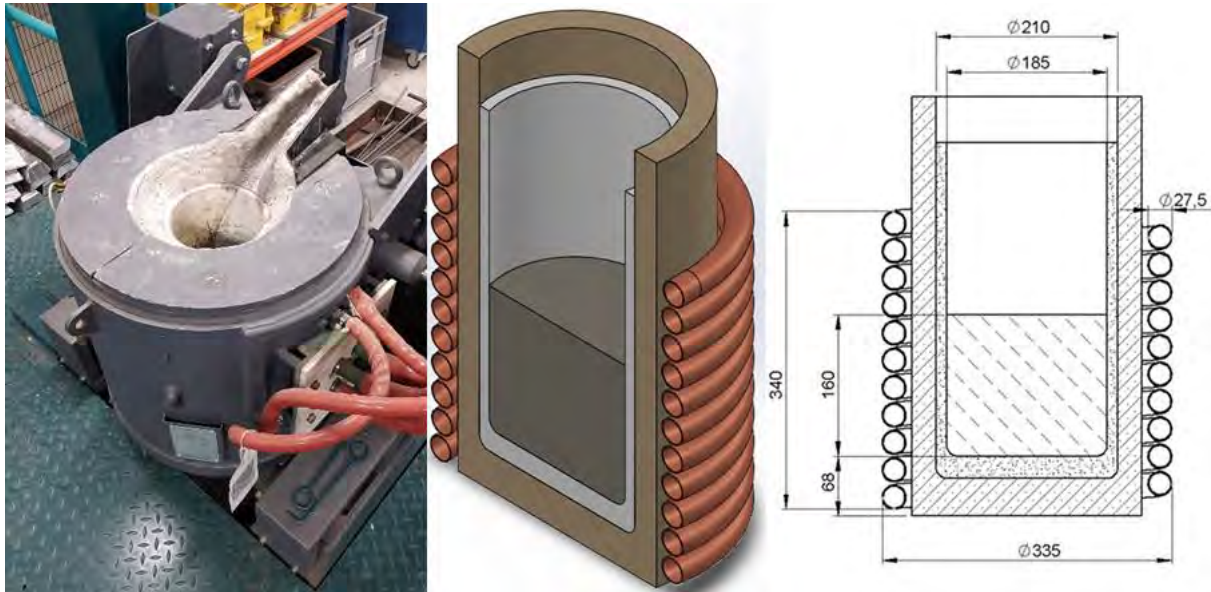
Figure 5-5. Open air induction melting furnace, 3D geometry, and section with dimensions

5.2.1. Experimental setup and measurements

The melting material underwent gradual heating using stepped power stages during the trial until the onset of incipient melting was detected. Subsequently, the power was increased to melt the charge completely. Once the metal reached a fully liquid state, the temperature was elevated to approximately 750 °C and measured using a type K thermocouple. The induced power was maintained at a fixed level to maintain the temperature, and the electrical variables were recorded from the generator.

 When the free surface of the metal reached a stable state, a device comprising 9 threaded rods with a diameter of 5 mm and a length of 390 mm was introduced into the metal (Figure 5-6).

Figure 5-6. Experimental setup for free surface deformation measuring device.

These rods were embedded in a resin block and welded on the lower side to prevent measurement distortion caused by the metal's convection force. After allowing the aluminum to wet the rods for a few seconds, the device was carefully removed, leaving a visible mark indicating the melt height and the free surface profile. Six trials were done for 5, 7.5, and 10 kg of charge weight corresponding to 12.5 %, 25 %, and 50 % of the crucible capacity. Additionally, two power conditions at 25 kW and 40 kW were tested for each filling level. The measured electrical variables of the power unit that will serve as input for the simulation are summarized in Table 5-2.

Table 5-2. Resume of conducted test and electrical parameters.

Mass [kg]	Power [kW]	Frequency [Hz]	Current [A]	Voltage [V]	Phase [deg]
5	25	2816	511	538	83
	40	2864	641	694	85
7.5	25	2820	514	541	83
	40	2908	614	644	84
10	25	2916	483	478	84
	40	2980	668	694	85

The melt deformation was assessed using contact probes, and the average height and relative error are depicted in Figure 5-7 for 25 kW and 40 kW.
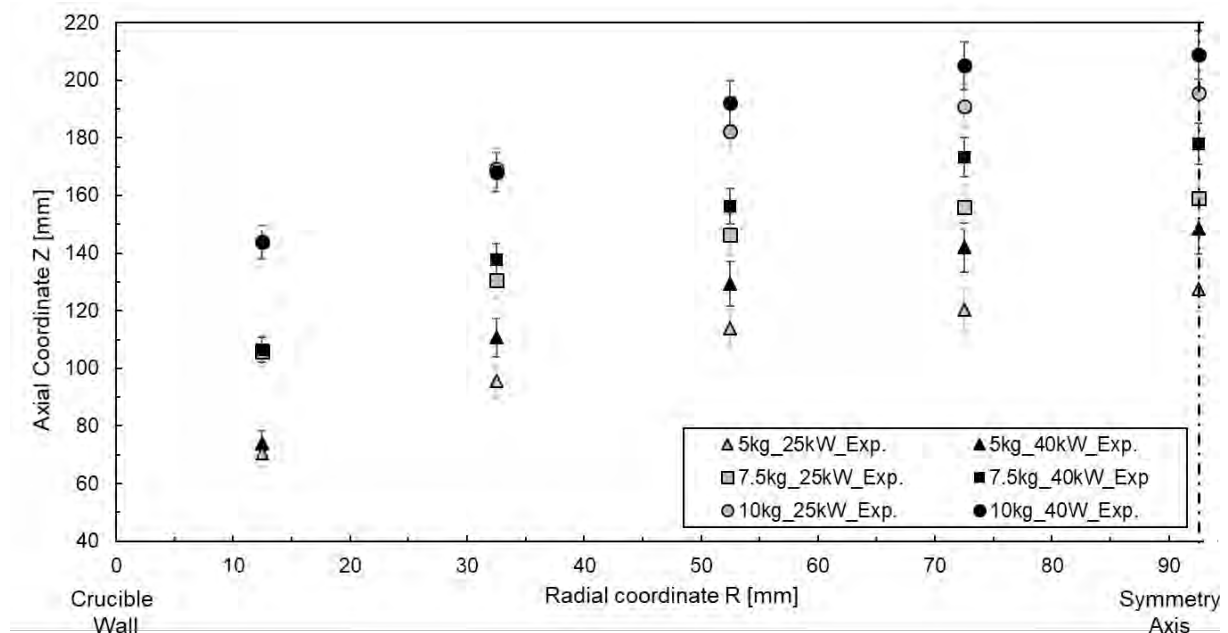
Figure 5-7. Measured surface profile for 25 kW and 40 kW and 5, 7.5, and 10 kg mass-filling.

As depicted in the figure, the characteristic meniscus shape was consistently observed across all cases, emphasizing that the initial height of the melt varied depending on the crucible's mass filling. For trials with lower filling levels, the melt's height was greater, leading to a more significant difference in height between the boundary points. This trend was also observed when comparing results obtained from trials with different power supplies, with the top surface of the melt being higher for the 40 kW supply compared to the 25 kW supply. However, the height of the lowest reference point remained similar in both cases.

It is important to note that the measuring system employed in this study has limitations and cannot provide precise information on the height of the metal near the crucible, thereby not being able to determine the contact between the metal and the wall accurately. Based on the principle of mass conservation, lower wall contacts are expected for higher melt heights.

5.2.2. Numerical results and correlation

Based on the above measurements, the same behavior was simulated in the air-open induction furnace described above. The free surface deformation was first studied at 25 kW and then at 40 kW. The implemented numerical model was the same as the 4.2.2. Magneto-hydrodynamic submodel. The previously described mesh deformation has been adapted to the new furnace's geometry and operating electrical parameters. The geometry of the open-air induction furnace was incorporated, and the meshing was adapted to the new crucible geometry (Figure 5-8).
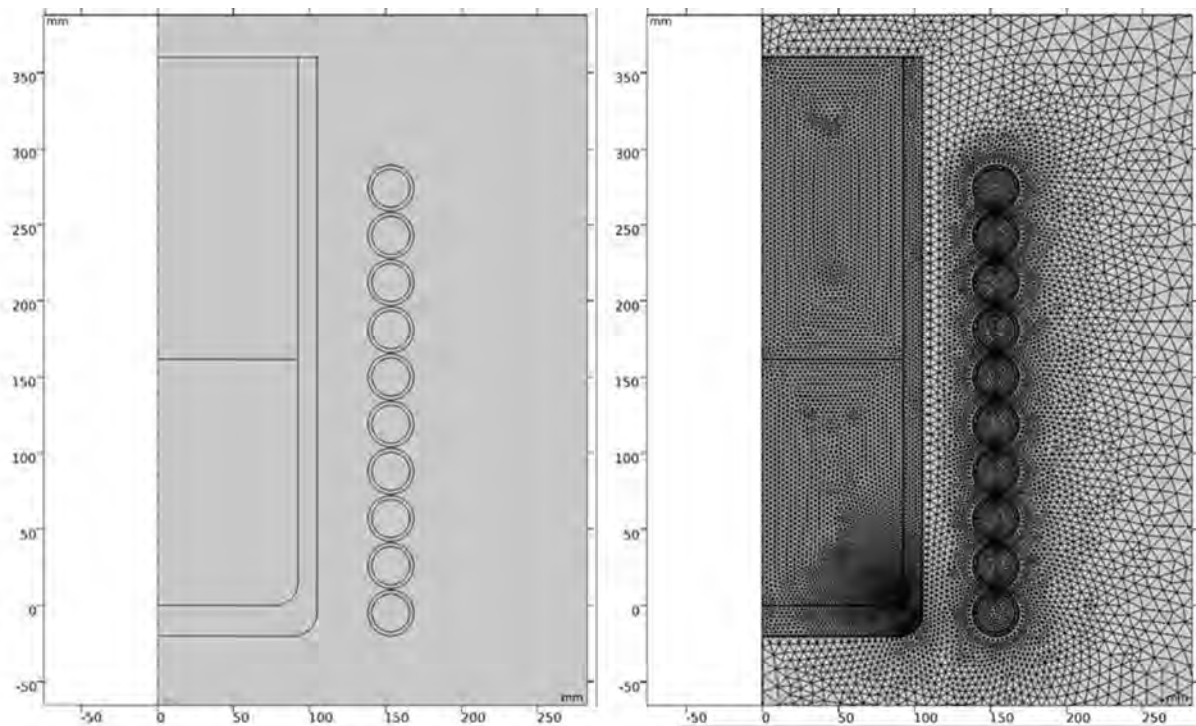
Figure 5-8. Geometry and mesh of open-air induction melting furnace implemented in the model.

Regarding material properties, it was assumed to have pure aluminum at a constant temperature of 750 °C. According to the characterization data of Leitner et al. [120], density was set at 2300 kg/m^3, viscosity 1.29 mPa·s the electrical conductivity of 3.6·10^6 S/m and surface tension of 0.85 N/m with a wetting angle of 120°.

The simulation incorporated three different mass filling levels by adjusting the initial filling level and the corresponding electrical power input variables. The coupled frequency-transient mesh deformation was then computed for 3 seconds using a fixed time step of 1 ms. A power ramp-up function was implemented to enhance simulation convergence, resulting in smoother mesh displacement. An example of the surface profile, magnetic field, and flow recirculation pattern is illustrated in Figure 5-9, representing a case with a mass of 10 kg and an induced power of 40 kW. The formation of the opposite-direction eddies in the melt, as well as the concentration of the magnetic field in the outside contour of the charge, can be observed, indicating a similar behavior as the previously described laboratory scale VIM furnace.
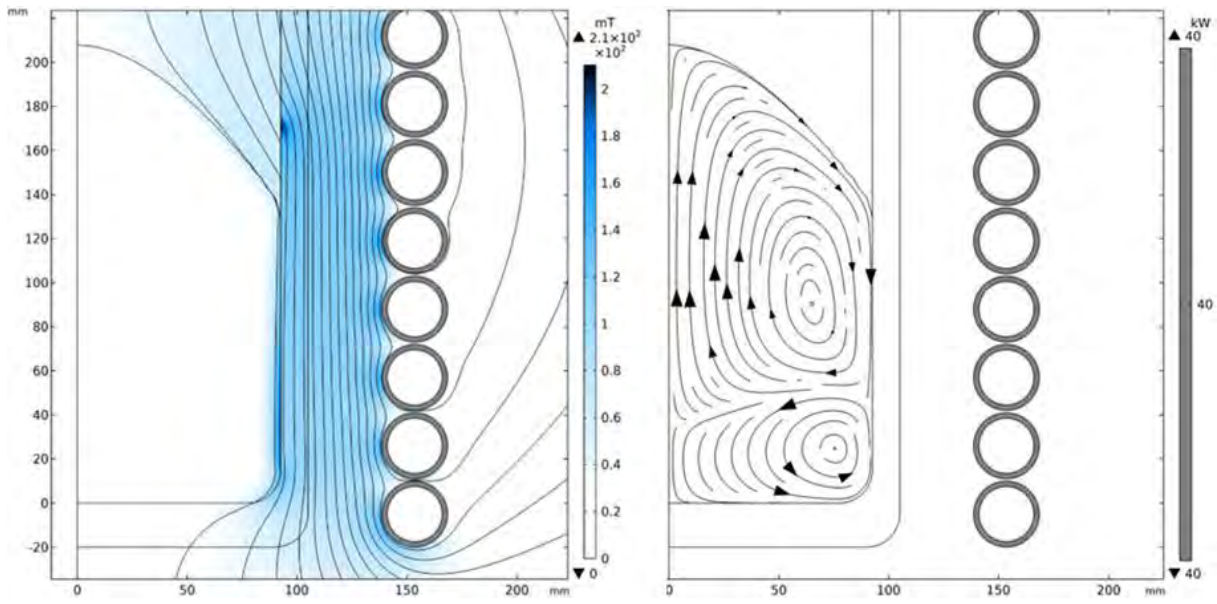
Figure 5-9. a) Magnetic field and b) fluid flow pattern for 10 kg and 25kW simulation-

The mesh was saved once the transient simulation concluded and the surface profile reached an almost quasi-stationary state. The radial and axial coordinates of the mesh elements corresponding to the interface were extracted and plotted alongside the experimental measurements obtained from height probes. Figure 5-10 plots the simulation-free surface profile and the height measured by the experimental probes for an input power of 25 kW.
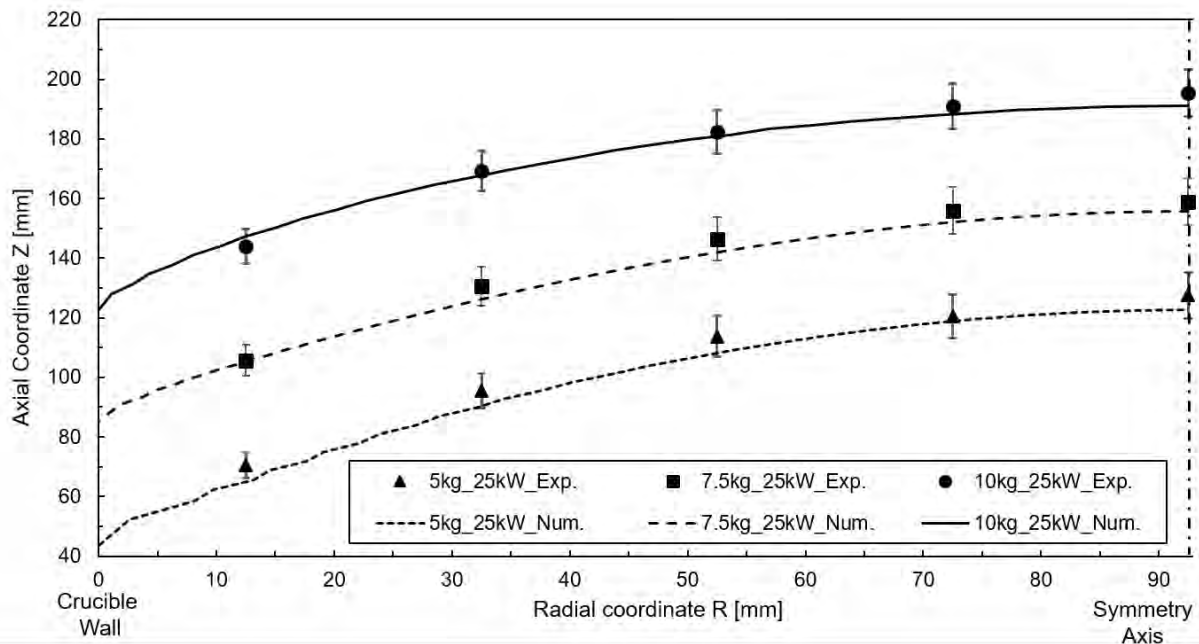
Figure 5-10. Experimental and numerical correlation of the free surface profile for 25 kW.

The numerical results effectively captured the curvature profile formed by the point coordinate measurements, exhibiting a close replication. However, a slight discrepancy was observed in the maximum height at the center of the melt, which remained consistent across all filling cases. This underestimation could be attributed to surface instabilities caused by low-frequency melt oscillations detected in the experiment. The RANS-based turbulence models utilized in the simulation cannot account for these fluctuations due to their flow-averaging nature.

An increase in surface profile roughness was observed in the vicinity of the wall, particularly for the 5 kg filling case and between the wall and the first measurement reference. This increase in roughness was attributed to mesh element distortion during displacement, as depicted in Figure 5-11.a, where the degree of mesh shape distortion, or skewness, is plotted. The mesh elements near the wall and in the interphase between the air and fluid domains experience stretching, leading to amplified distortion (indicated in red).
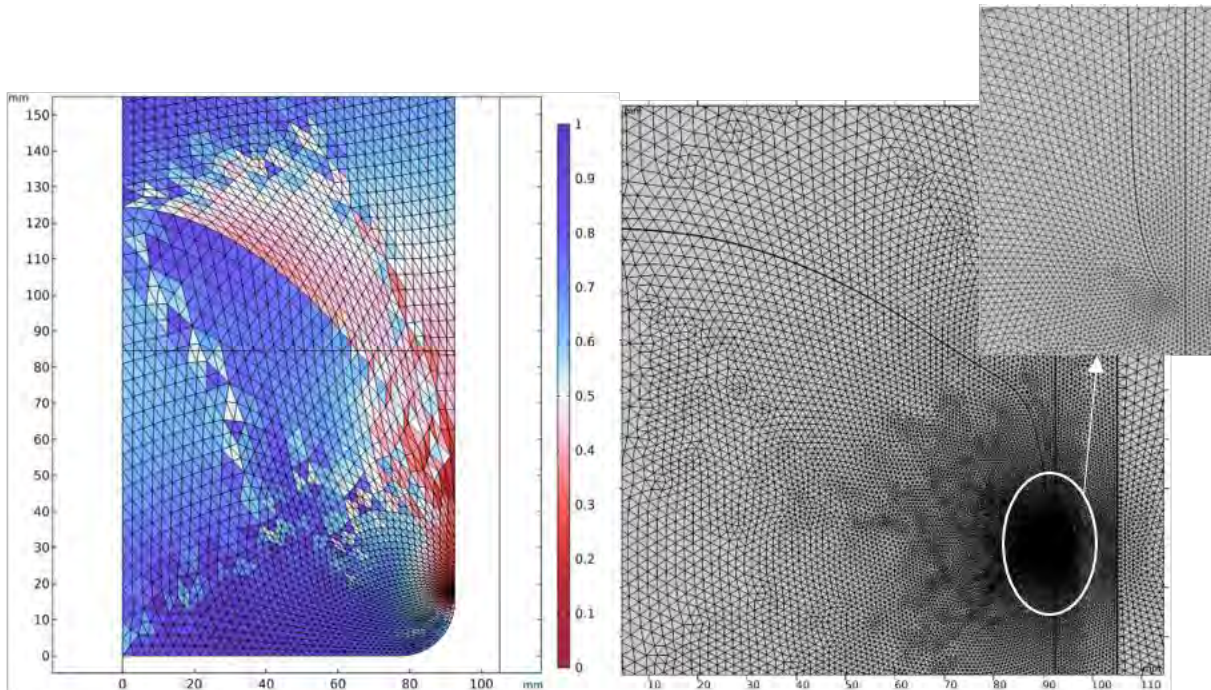
Figure 5-11. a) Mesh skewness for 5 kg 25 kW. b) Deformed and refined mesh detail.

The low filling level generates a substantial magnetic force on the free surface border, resulting in pronounced distortion and rotation of the mesh elements. Two potential solutions were considered: adaptive meshing and specific remeshing. In the case of adaptive meshing, the procedure involves increasing mesh elements in areas with significant numerical errors based on a predefined condition. However, reducing the mesh size can adversely affect element distortion and compromise computation stability, leading to premature termination. As for the remeshing method, the available algorithm in the software encounters challenges with velocity field convergence after restarting the calculation following remeshing. Attempts to facilitate convergence by reducing the time step during initialization were made, but the curved shapes of the metal pose difficulties in achieving suitable initialization of the turbulence and velocity field (Figure 5-11.b).

However, the accuracy of the numerical correlation decreased for the higher deformations associated with the 40 kW power case, as shown in Figure 5-12. In this instance, the simulation yielded a lower height than the experimental measurements. While the simulation captured the curvature of the profile, the absolute values did not align precisely, resulting in an approximate error of 10 mm for the worst-case scenario. Furthermore, the simulation did not converge sufficiently for the 5 kg filling level and 40 kW power input to achieve stable surface and reliable results.
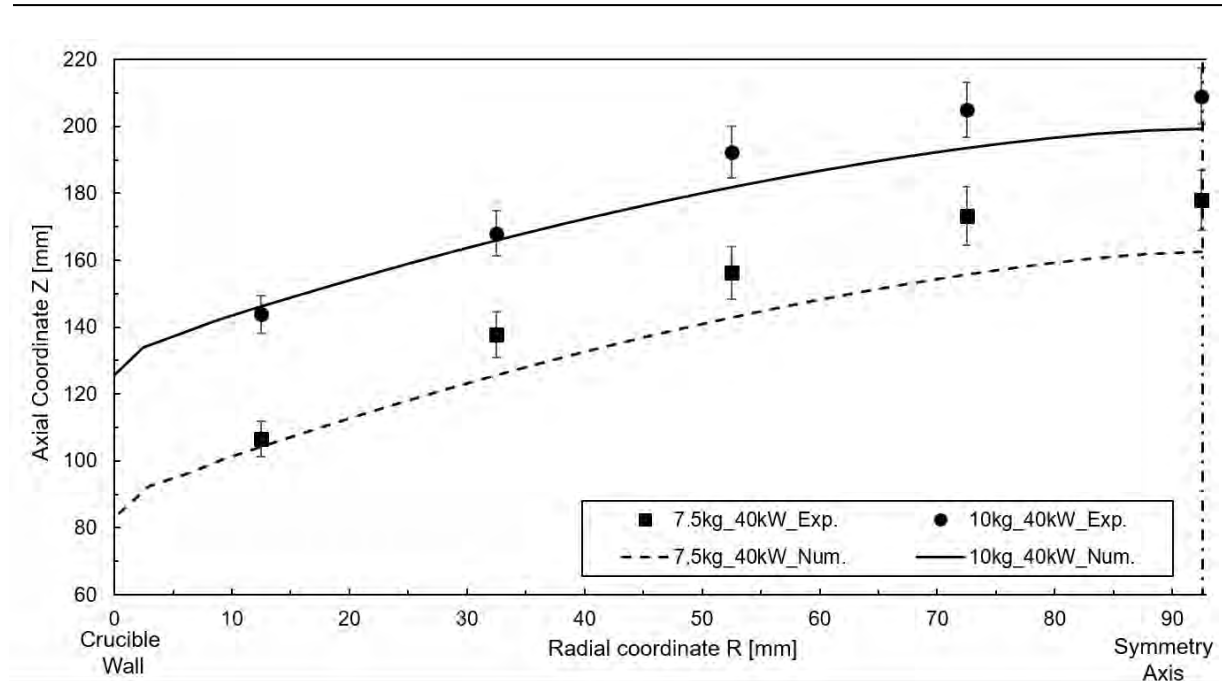
Figure 5-12. Experimental and numerical correlation of the free surface profile for 40 kW.

5.3. VIM thermal correlation

The numerical thermal results of 4.2.4. Magneto-thermo-hydrodynamic model revealed that while the metal temperature appeared homogeneous, it did not entirely align with the readings from the pyrometer. This deviation may arise from underestimating the emissivity and the fact that the model was examined under stationary conditions. Therefore, investigating the model's behavior under transient conditions plays a vital role in comprehending the heat transfer dynamics of the VIM process.

For that, varying input power conditions will be considered while additional temperature references are taken to measure the temperature response. These measurements will serve as a reference for the transient simulation by adapting the above model to the conditions for fine-tuning and addressing uncertainty concerns.

5.3.1. Experimental setup and temperature measurements

Before conducting the experimental trials, the VIM installation was configured to collect the necessary process variables for implementing the model described in 3.3.1. VIM process variables monitoring. In the VIM facility, a specific setup was devised for data acquisition. Temperatures from the thermocouples and pyrometer, the power supplied by the generator, the amount of heat dissipated by the water-cooled coil, and the vacuum chamber pressure were monitored and recorded during melting trials. To measure the thermal response of the melt to variations in applied power, a sensorized crucible was fabricated. This crucible AL97I, made of Al_2O_3, had attached two K-type thermocouples—one positioned at the base and the other on the vertical wall (Figure 5-13).

Such a device enabled more accurate melt temperature measurement throughout the VIM process. Two four-channel NI-9207 modules were employed as analog inputs to record this data at a sampling frequency of 1 Hz and imported into a real-time monitoring system according to the procedure presented in 3.3.1. VIM process variables monitoring
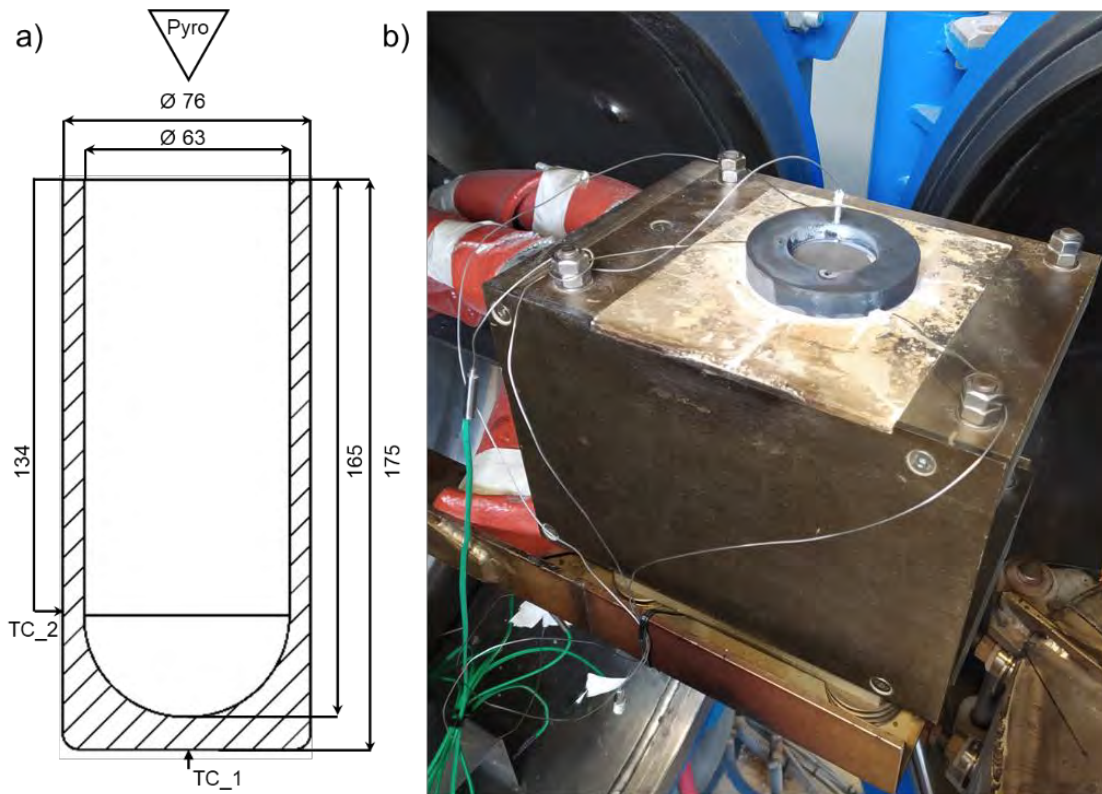
Figure 5-13. a) Crucible section and thermocouple position. b) Melt-box configuration.

- **Melting trial**

The objective of the melting trial was the transient measurement of the temperature of both the melt and crucible throughout the melting process. The trial followed a standard melting procedure involving two quasi-stationary stages to adjust the melt temperature before pouring it into the mold. A stepped power application procedure was utilized to heat the charge. Once the charge had completely melted, the coil power was adjusted to reach the target temperature of 1500 °C and maintained for 10 minutes. Then it was followed by a transition stage, during which the coil power was reduced, and the temperature gradually decreased to 1450 °C, holding steady for 15 minutes (Figure 5-14).
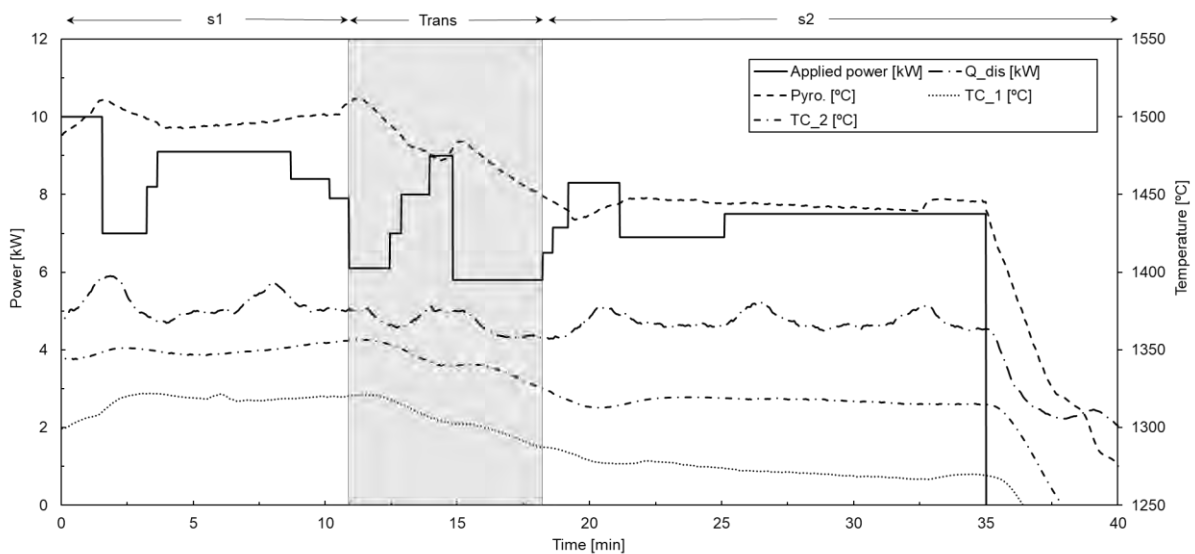
Figure 5-14. Power-temperature-time graph of melting trial in quasi-stationary stages.

It is important to note that maintaining a constant power did not result in a stable stationary temperature state due to the low thermal inertia of the melt, leading to rapid temperature variations. Therefore, slight power adjustments were necessary to sustain the target temperature.

During the trial, it was observed that the lower side thermocouple (TC_1) exhibited higher thermal inertia compared to the vertical thermocouple (TC_2), which displayed a faster response and registered a temperature approximately 25 °C higher. This difference was expected since TC_2 was located closer to the melt and, therefore, more sensitive to temperature fluctuations. These temperature stabilization stages served as reference points for the subsequent numerical model validation. The measured heat dissipation rate for the analyzed section is presented in Figure 5-14. The chiller utilized an on-off mode of operation, resulting in a maximum variable temperature difference (ΔT) of 4-8 °C.

The analysis of the obtained experimental is summarized in Table 5-3. The data for the two quasi-stationary stages with target temperature and corresponding duration, applied power, dissipating heat, and the corresponding transition stage. These references are input data for numerical simulations, posterior correlation, and validation purposes.

Table 5-3. Experimental trial stages, time steps, and process data.

Stage	Start	End	Duration [min]	P_{app} [kW]	$\mathbf{q}_{dis}$ [kW]	Temp. Objective [°C]
S-1	0	11	11	8.3	5.2	1500
Trans.	11	18.5	7.5	6.8	4.4	Variable
S-2	18.5	35	16.5	7.4	4.7	1450

For the above-measured power stages, the electrical variables of the coil were measured and later introduced as input in the numerical model. The measurements for different power stages corresponding to the RMS current, voltage, and frequency results are presented in Table 5-4.

Table 5-4. Measured electrical variables for input power.

Stage	Power [kW]	Current [A]	Voltage [V]	Frequency [kHz]	Phase [deg]
S-1	8.3	915	138	7.4	86
Trans.	6.8	810	90	8.6	85
S-2	7.4	850	105	8.3	85

5.3.2. Numerical model adaptation

- **Simulation strategy and assumptions**

For the new dynamic model, the transient temperature adjustment was incorporated to reflect the experimental data accurately. The obtained experimental data, summarized in Table 5-3 and Table 5-4, were incorporated into the model. The simulation procedure followed is depicted in a visual representation in Figure 5-15. The procedure began with computing the mesh deformation using the moving mesh method until a stationary profile was achieved. Subsequently, the mesh was refined to ensure an accurate solution for the flow velocity field, and the thermal model was coupled while maintaining the fixed free surface profile. After confirming the convergence of the calculations, the transient study was conducted until the end of the stage. In cases where there was a change in the applied power, the simulation was paused by decoupling the thermal model and recalculating the new stationary free surface. The same approach was followed for the second quasi-steady state.
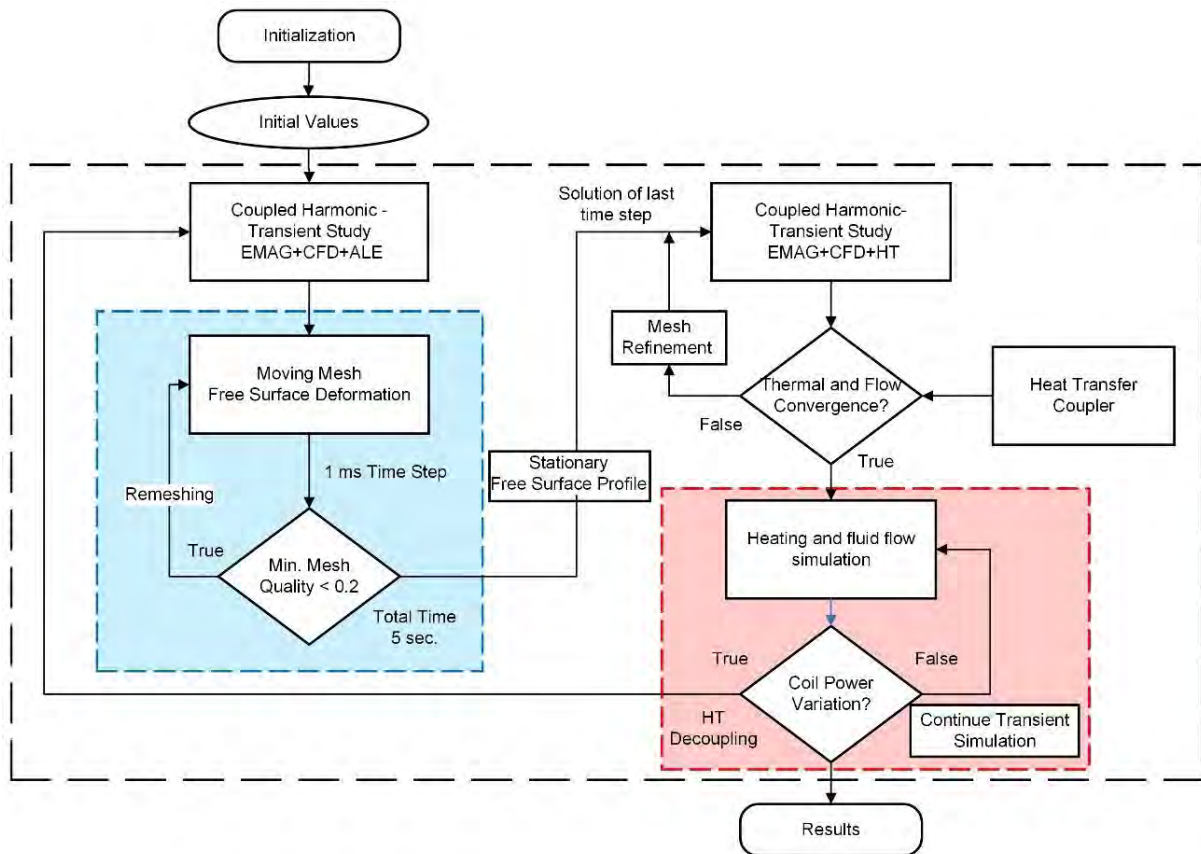
Figure 5-15. Flow chart of the simulation procedure.

- **Numerical results**

The results of the transient simulation are summarized in the following lines. Figure 5-16 illustrates the magnetic flux density within the melt-box and the fluid flow velocity field. The magnetic flux density was approximately 0.1 T, a typical value for this type of induction application. The Lorentz force vectors were concentrated in the interphase region, and their magnitude decreased as introduced into the metal. For the power stage of 8.3 kW, a slightly higher magnetic field intensity of up to 0.12 T was computed while maintaining the same distribution.

Regarding the fluid velocity, the interaction between the magnetic pressure and hydrostatic normal forces resulted in a distinct recirculation pattern. Two main toroidal flows recirculated in opposite directions. The highest flow velocities were observed in the lower zone, coinciding with the curvature of the crucible. Conversely, the velocity was nearly zero on the top surface and in the regions between the primary eddies.
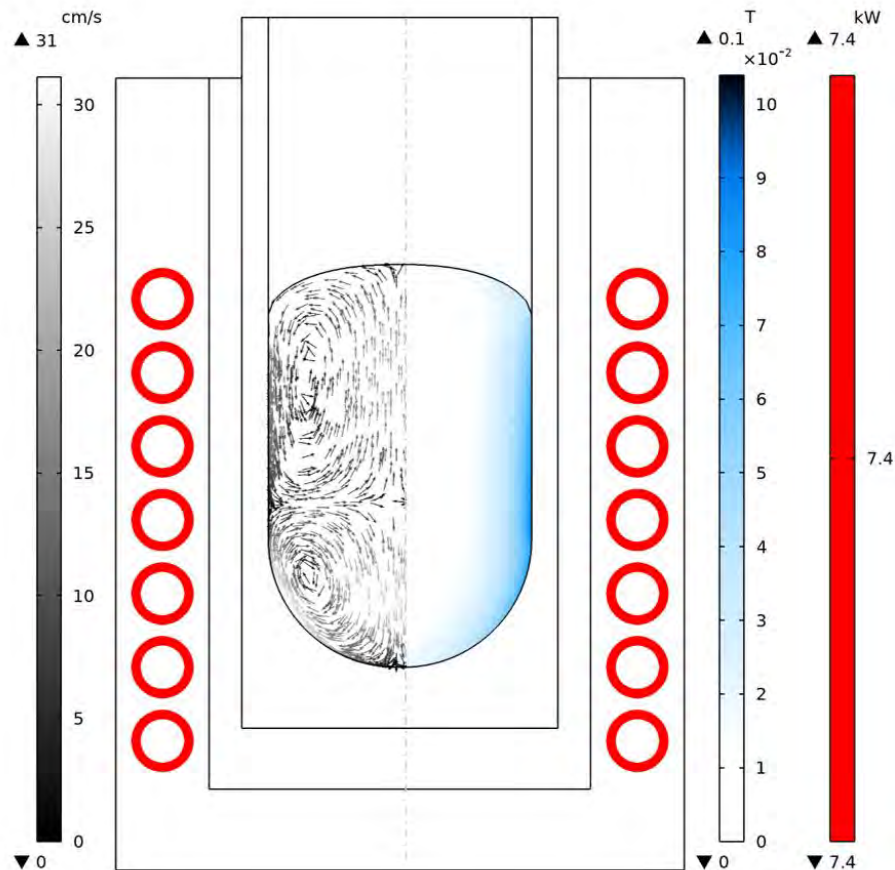
Figure 5-16. Computed magnetic flux density and fluid flow field vectors for 7.4 kW.

- **Emissivity parametrization**

To establish the initial temperature distribution accurately, overcoming the challenge of modeling transient temperature evolution, a preliminary frequency-transient study was conducted for one hour. This simulation aimed to capture the heating and solid-liquid transition during the melting trial, considering the progressive temperature increment. The results of this simulation achieved a quasi-stationary temperature state, which serves as the starting point for the subsequent transient dynamic melting simulation.

During the experimental trial conducted in the first stationary stage at 1500 °C, it was determined that the average applied power was 8.3 kW, and the heat transfer coefficient (HTC) of the inner coil boundary was adjusted to dissipate 5.5 kW of heat. However, the simulation results exhibited a higher melt temperature compared to the measurements obtained with the pyrometer. As the emissivity of the heat radiation contour was the only adjustable parameter available in the model, a sensitivity and parameterization study was carried out to evaluate the model's response in relation to this variable.

The effect of varying the emissivity value on the temperature distribution is summarized in Figure 5-17, where it can be observed that the temperature gradually decreases as the emissivity value increases. The temperature data from two floor-mounted thermocouples, TC_1 and TC_2, are also plotted, displaying a similar trend. The results indicated that the optimal emissivity value for achieving the target temperature of 1510 °C is 0.35, which is higher than the initial value considered.
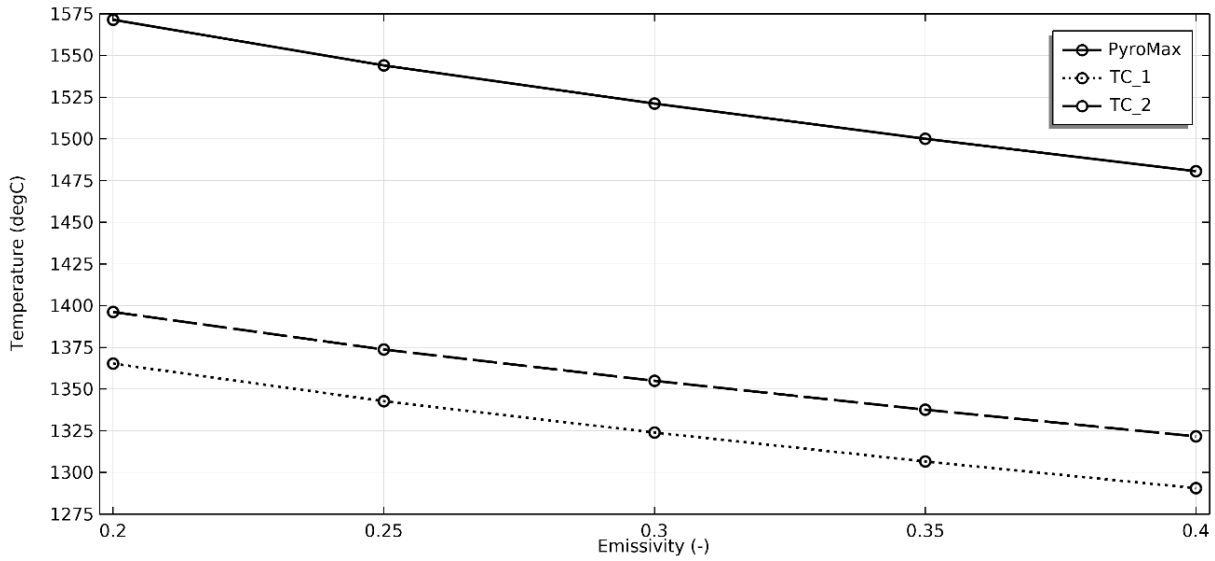
Figure 5-17. Emissivity parametrization.

The observed difference between the initially considered emissivity value and the one that best fits the target temperature of 1500 °C falls within acceptable margins. However, it is essential to acknowledge that in experimental tests, additional variables such as dross particles on the metal, fumes, and gases, as well as the variability of the pyrometer itself, can affect the actual emissivity, potentially leading to higher values than initially estimated. The preliminary quasi-stationary frequency-transient coupled simulation results are presented in Figure 5-18.
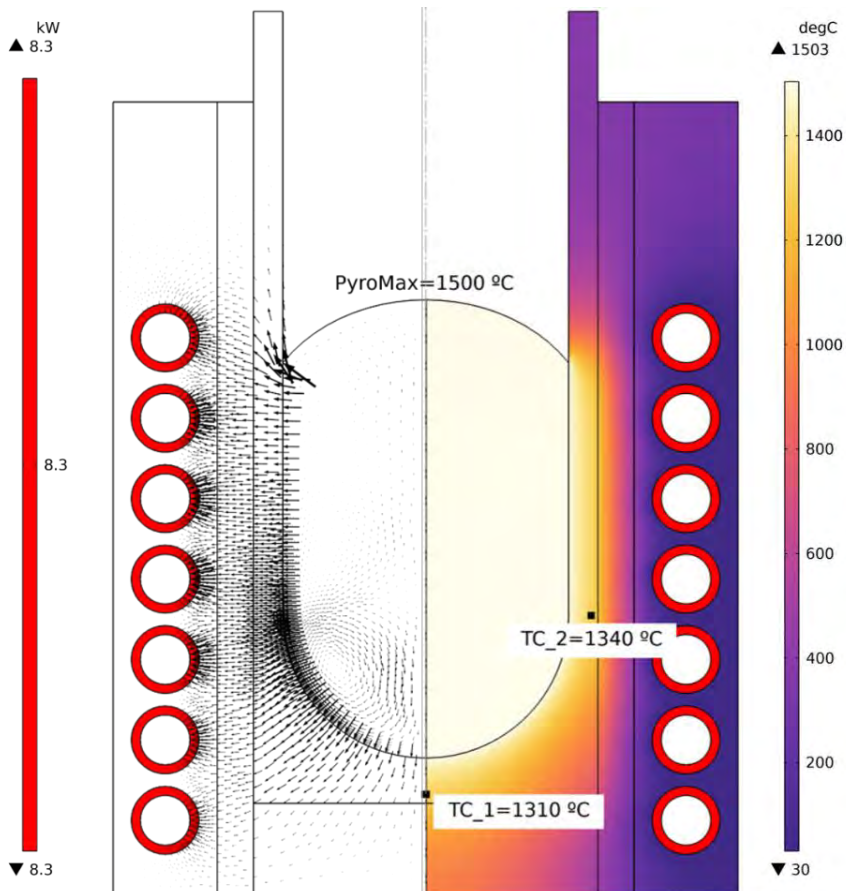
Figure 5-18. Conductive heat flux vectors and temperature distribution for 8.3 kW power.

The left side of Figure 5-18. illustrates the heat flux vectors' magnitude and direction vectors. As expected, there is an intense heat flux from the melt to the crucible, especially in the liquid metal-crucible contact area. Then the heat is conducted through the crucible after dissipating in the refrigeration coils.

The temperature distribution is depicted on the right side of the figure, with the maximum melt temperature fixed at 1500 ºC and around 1300 °C for the thermocouples. The inner boundary of the water-refrigerated coil was set at 30 °C, corresponding to the maximum temperature recorded during the melting trial. The subassembly consisting of the crucible and the melt box exhibits a high thermal insulation capacity, rapidly reducing the temperature. On the contrary, metal maintains a relatively homogeneous temperature, which will be further analyzed in the subsequent section.

5.3.3. Transient temperature correlation

Returning to the analysis of VIM melting, the power-temperature-time data (Figure 5-14) of the experimental test were employed as input parameters to simulate the temperature variations and validate the simulation results. The objective was to reproduce the two quasi-stationary temperature stages at 1500 ºC and 1450 ºC feeding the model with the power and time variables. The transient simulation will assess the model's response to dynamic power variations and the temperature response.

The model was initialized with the electrical variables, heat dissipation, and time values obtained from Table 5-3. To accurately capture the temperature variations, two reference probes were placed at the exact locations of the thermocouples, while the pyrometer measured the maximum temperature of the upper melt contour. For each stage, the averaged power was used as the input, and the heat dissipation for the water-cooled coil was adjusted, as shown in Figure 5-19.
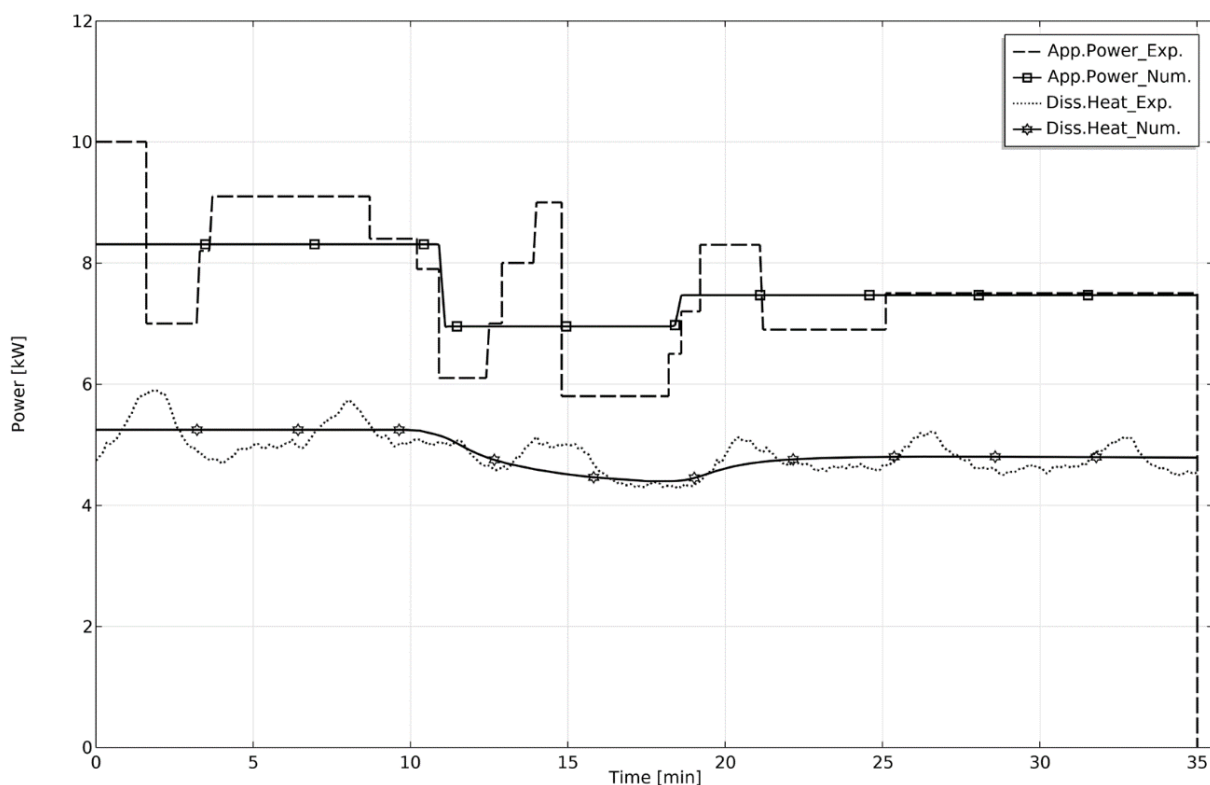
Figure 5-19. Correlation between input variables applied power and dissipated heat.

The transient temperature evolution is depicted in Figure 5-20, overlaid with the experimental measurements. The model could reproduce temperature values with a maximum error of 20 °C in relative terms for any of the measurement points. Although the model data did not exhibit signal

interference in the experimental data, the overall trends display similar behavior during the first quasi-stationary period. The transient analysis reveals that the metallic load had higher thermal inertia than the ceramic crucible. Once the transient phase ends, the system reaches a new steady state at 1450 °C for the metallic load, while the ceramic crucible decreases in temperature correspondingly to around 1300 °C. In this new steady state, the model exhibited less accuracy in relative temperature terms for the thermocouple placed on the wall (TC_2).
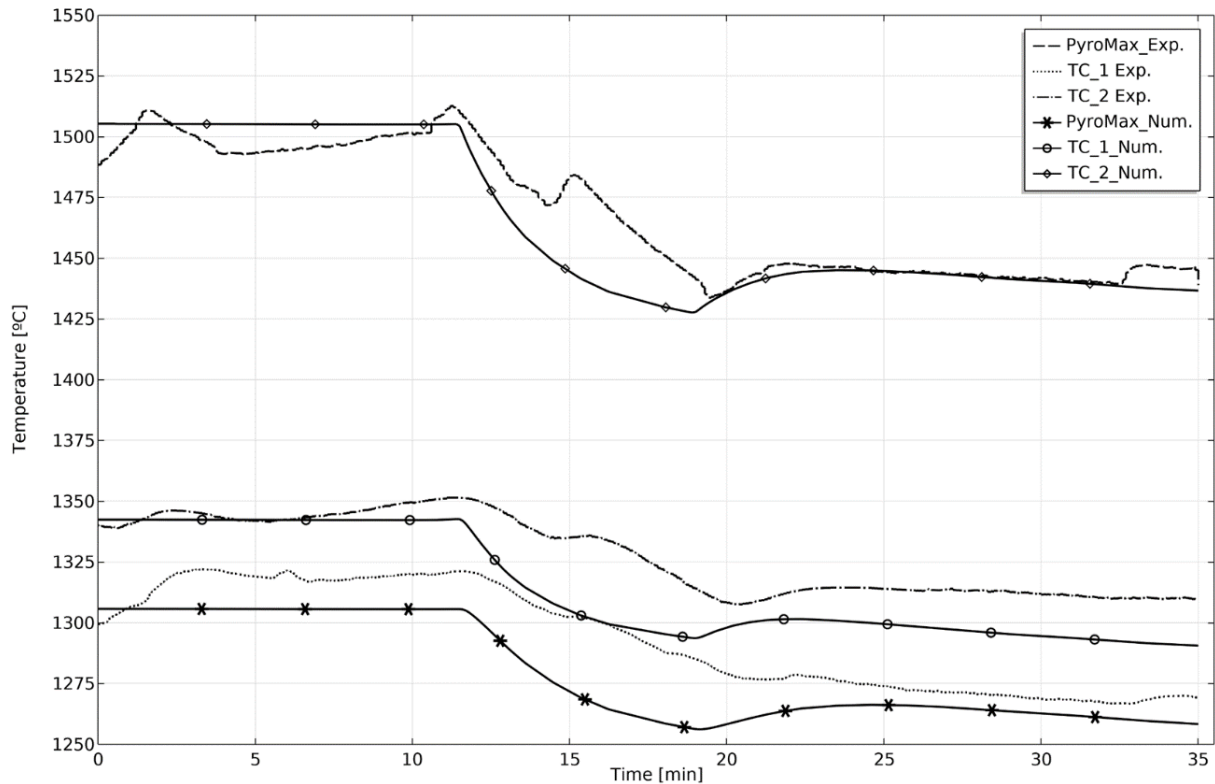
Figure 5-20. Comparison of computed temperature and experimental measurement.

The dynamic temperature response of the simulation is accurate, with a relative error of 5 %, considering the temperature transition and stabilization at the two target temperatures. The absolute temperature deviation for thermocouple TC_2 at the stationary 1450 °C is 25 °C. The melt temperature mainly influences the behavior of TC_2, as it reproduces the same trends as the metal temperature, being more sensitive to its variation.

In this regard, as was mentioned before, the thermal conductivity of the crucible plays a critical role. A sensitivity analysis was done by varying the magnitude by 10 % inside the experimental measurement uncertainty for the AL97I crucible thermal characterization. The consistency of the model was notable as it led to temperature variations of 10 °C for the pyrometer temperature reference, while for the crucible probes, there was a slight deviation.

Although the correlation could be slightly adjusted, this would result in a loss of accuracy for TC_1, which exhibits a decreasing trend. It should be noted that the simulation does not consider the power increment during the adaptation stage, where a sudden temperature change occurs, which could improve the temperature correlation.

Regarding the temperature distribution in the melt (Figure 5-21), a homogeneous field is obtained with a difference of 5 °C for the two quasi-stationary stages. As mentioned before, the homogeneous temperature distribution may be attributed to the turbulent heat transfer (λ_T), and there is continuous fast

recirculation between vortices due to the low mass and viscosity, leading to temperature homogenization.
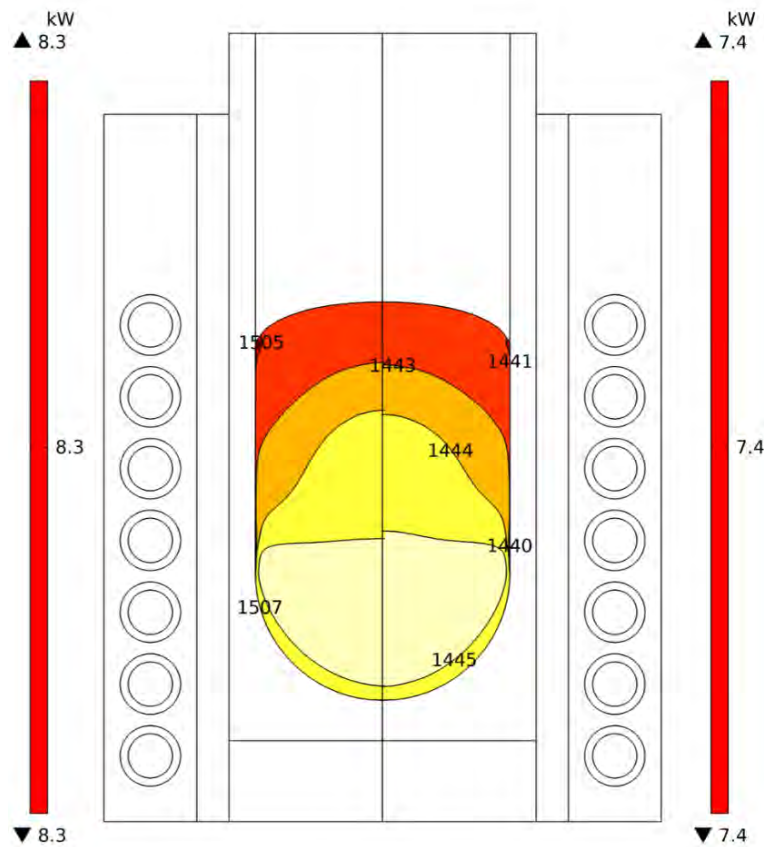
Figure 5-21. Temperature distribution for both quasi-stationary states at 1500 °C and 1450 °C.

5.4. Conclusions

The validation of the induction heating model was successfully achieved through two methods. Firstly, by comparing the experimentally measured electrical parameters with the model-generated ones and confirming their similarity. Secondly, considering the temperature differences on the ingot, additional temperature references were taken by measuring with thermocouples the heating for a one-hour extended heating test. Later, those temperature references were compared with the simulation results, indicating that the model behaves faster, achieving temperature stabilization earlier than in the experiment.

The ALE algorithm, employing the moving mesh method, proved effective in reproducing the free surface deformation during the VIM process. An acceptable correlation was achieved for different mass-filling levels under the 25 kW induced power conditions. Higher filling levels of 10 kg and 7.5 kg exhibited better correlation, partly due to minor surface deformation and optimal mesh fitting. The heightened surface profiles induced significant mesh displacement, leading to notable distortion and element rotation, necessitating the termination of the computation. To address this, the model incorporated adaptive mesh refinement and re-meshing techniques throughout the study, ensuring convergence and robustness. However, a decline in accuracy was observed for the 40 kW case, and convergence was not attained for the 5 kg filling level.

Regarding the thermal model, the free surface's emissivity was the model's unique degree of freedom, and it was parametrized to adjust the pyrometer and thermocouple measurement temperatures with the

numerical results. Emissivity was incremented to 0.35, and the temperature gap was reduced by correcting the actual pyrometer reading. Crucible thermal conductivity plays a critical role in the heat transfer phenomena, maintaining the heat in the melt.

The transient temperature simulation showed a high level of accuracy, with a relative error of below 5% for the melt temperature compared to the experimental data in both quasi-stationary and dynamic situations across all three temperature experimental references. However, the model temperature responded faster than the experimental; the possible reason to explain this delay could be the sampling frequency of the acquisition system, or it might be related to the time required by the power generator to the resonance frequency of the equivalent circuit. In addition, it must be emphasized that the modeled power was the averaged value of the stages, and that did not account for the continuous power adjustments to maintain the objective temperatures increasing the uncertainty. The temperature gradient observed in the melt was approximately 5 °C, which is attributed to the continuous recirculation of the melt, high thermal conductivity due to turbulent heat transfer, and the relatively low mass resulting in temperature homogenization.

This experimentally validated numerical model is a valuable tool for studying additional VIM installations. As well as to determine the optimal VIM operating conditions, facilitating the development of an optimized melting procedure, The following chapter will present the upscaling of this model to large-scale case studies.

Chapter 6

6. Large-scale case studies

This chapter aims to extend the experimentally validated numerical model to an industrial scale and employ it to investigate the VIM process in case studies. Specifically, two VIM furnaces with different melting capacities have been examined, thereby broadening the study of the VIM process. Firstly, this chapter addresses the specific adaptations and considerations required for modeling the respective configurations of each unique furnace. Subsequently, a summary of the most notable findings observed in each case is presented, followed by a concise comparison of the two configurations. It is necessary to highlight that ITP Aero has provided all the experimental measurements and industrial melting operating conditions, facilitating the development of the subsequent large-scale case studies.

6.1. VIM Furnace 1

The first case study furnace exhibits a distinctive feature with a single coaxial coil characterized by a circular section. This furnace can melt up to 135 kg of Inconel 718; however, for this particular study, a liner with a capacity of 105 kg was selected, allowing it to function as a single-use vessel.

Figure 6-1 illustrates the furnace, showcasing its notable design element—a leg-shaped seat that increases the axial position of the melted load. The complete geometry, including the charge, coil, liner, backup, insulating material, and the surrounding vacuum atmosphere, was generated based on the provided drawings and dimensions. As can be observed, in the case of the ten-turn coil, the metal load is placed inside it. However, the lower turns do not entirely surround the liquid metal because it is elevated due to the crucible with legs. A two-dimensional axisymmetric model was employed to simplify the discretization of the domains. The main adaptations required for this study involved the adjustment of the geometry and input electrical variables.
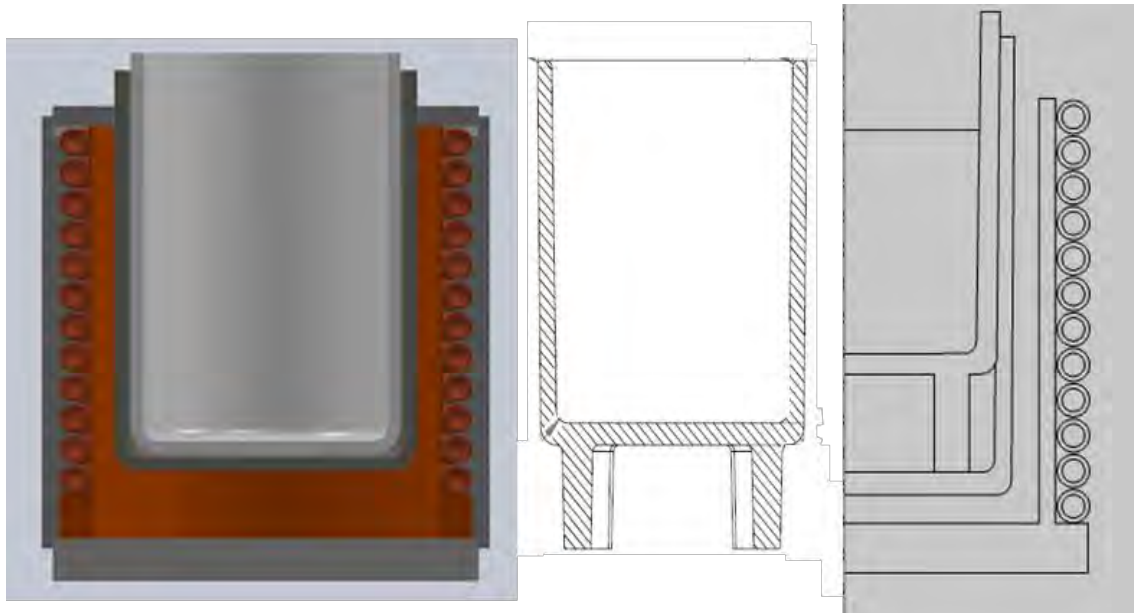
Figure 6-1. VIM Furnace 1 with Liner 105 configuration and 2D-axisymmetric geometry.

These models' equations and boundary conditions were aligned with those utilized in section 4.2.4. Magneto-thermo-hydrodynamic model. The same material properties of Table 4-7 were maintained except for the liners and crucible. Both, composed of aluminosilicate-based ceramics, were

characterized using the procedure presented in 3.2.2. Thermal characterization and specific properties were adapted in the model.

The standard industrial melting procedure is summarized in Figure 6-2, which depicts the power-temperature relationship over time for a 105 kg Inconel 718 charge. The procedure entails a gradual heating process to prevent thermal shock risks, increasing the power input until the melting power of 90 kW. The temperature readings from the pyrometer commence at 73 minutes. Once the charge is completely melted, the temperature is increased to the desired target temperature and maintained using a PID controller for a few minutes before casting the metal into molds.
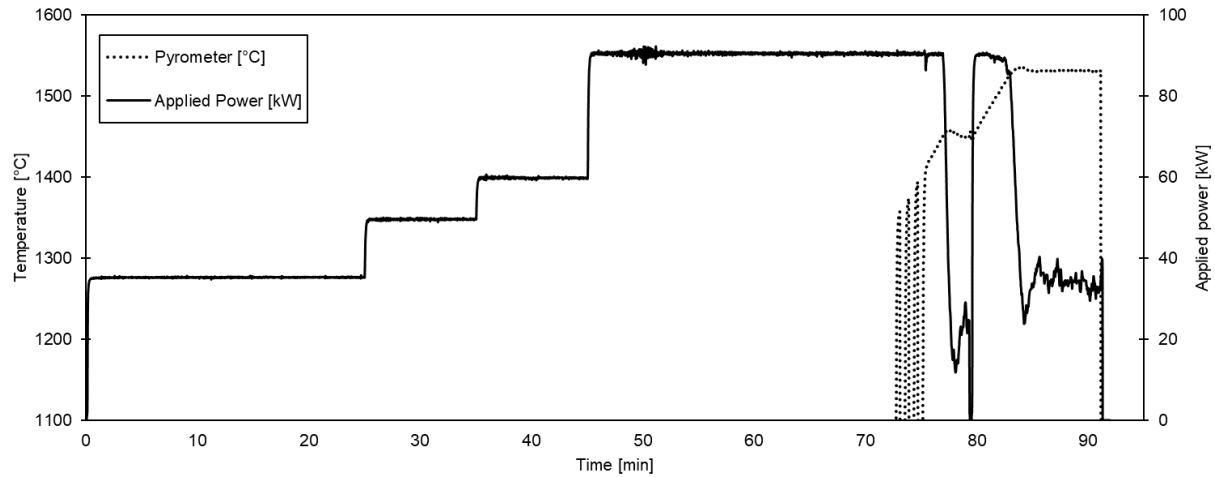
Figure 6-2. Industrial melting procedure power-temperature-time relation.

6.1.1. Coil modeling

The VIM electrical variables were experimentally characterized for the heating and melting stages presented in Figure 6-2 at 36 kW, 50 kW, 60 kW, and 90 kW. These variables, including frequency, current, and voltage, are summarized in Table 6-1. The data was inputted into the software's coil sizing function, calculating electrical parameters, coil resistance, inductance, and power.

Table 6-1. Input coil electrical variables and simulated powers.

Input variables			Output results		
f [Hz]	Ic [kA]	Vc [V]	Resistance [mΩ]	Inductance [μH]	Coil Power [kW]
1250	1.40	230	1.66	2.98	36.4
1275	1.64	250	1.70	2.96	50.2
1290	1.80	260	1.72	2.95	60.9
1390	2.15	280	1.79	2.86	91.2

On the other side, for comparison purposes, the experimentally characterized electrical parameters of the coil are presented in Figure 6-3 to compare with the simulation output. Notably, the simulated and experimental values fell within the same order of magnitude with a reasonably close agreement between the simulated and experimental results. However, the model-predicted values overestimate the inductance, while the resistance was slightly underestimated. On the contrary, the applied power was estimated correctly, which is the critical variable for the subsequent simulation of the flow field and heating.
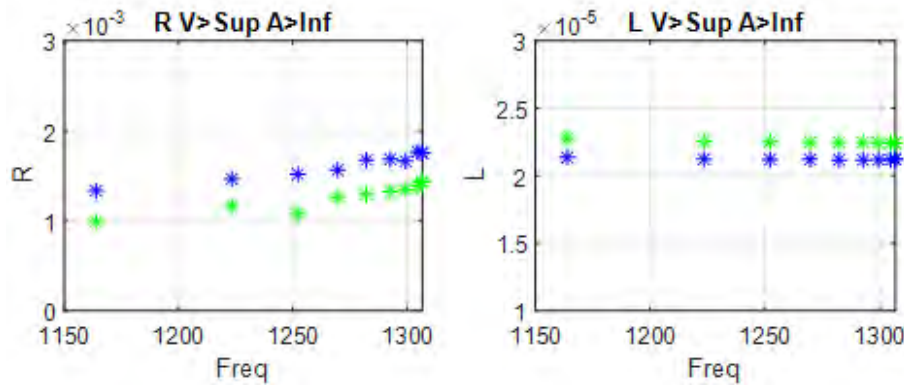
Figure 6-3. Experimental coil electrical resistance and inductance.

6.1.2. Magneto-hydrodynamic submodel

The results of the magnetic flux density (**B**) distribution along the contour of the outer surface (Figure 6-4) showed that the lower half exhibits slightly higher field values, with a concentration in the crucible's curvature. Interestingly, the density of the magnetic field was notably higher in the lower area. This pattern was consistent across all four power conditions studied, as illustrated in Figure 6-4.
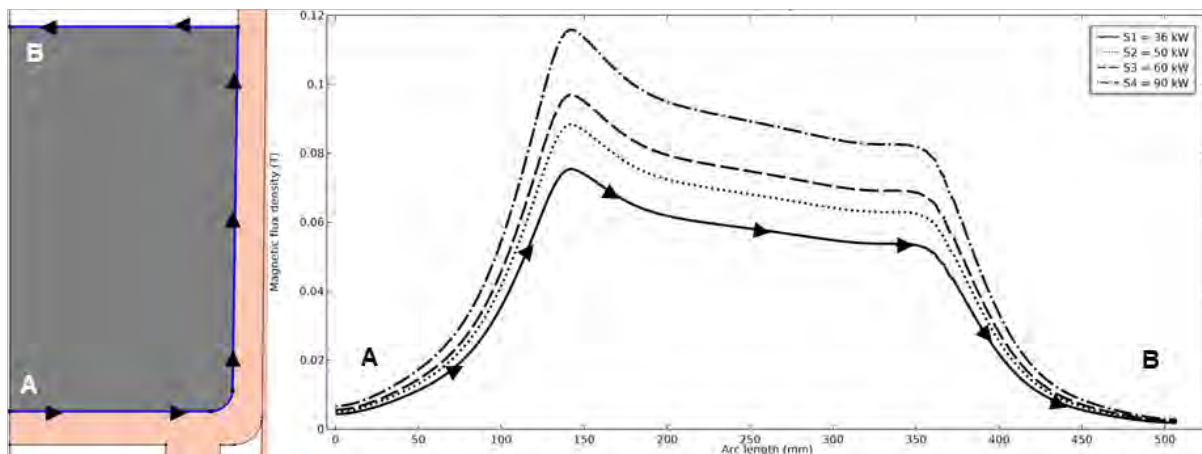
Figure 6-4. Magnetic flux density (**B**) in the outer charge contour.

However, the flux density rapidly decreased as the magnetic field entered the charge, eventually becoming almost negligible along the central axis due to the skin effect. The magnetic flux density for the cross-section is depicted on the right side of Figure 6-5, revealing a flux concentration at the charge's base. This concentration arose from the coil configuration, where nearly half of the coil did not surround the charge. As a result, the generated magnetic field concentrates on the bottom of the melt, primarily due to its role as the initial electrically conductive area encountered by the field. The reduction in field density remained consistent across the four power cases, as the coil frequency remained stable while the density's magnitude increased with the applied power. Notably, a magnetic field concentration was observed, which could result in a higher velocity field in the crucible bottom zone. This phenomenon will be further discussed in the following flow field study.

As discussed in previous chapters, the coupling between the magnetic and fluidic fields requires the simulation of the free surface deformation and the flow recirculation within the metal. To improve computational efficiency, the procedure was divided into two stages. The first stage focused on modeling the free surface profile until a quasi-stationary result was obtained. It was determined that 3 to 5 seconds were sufficient to achieve a stationary profile state.
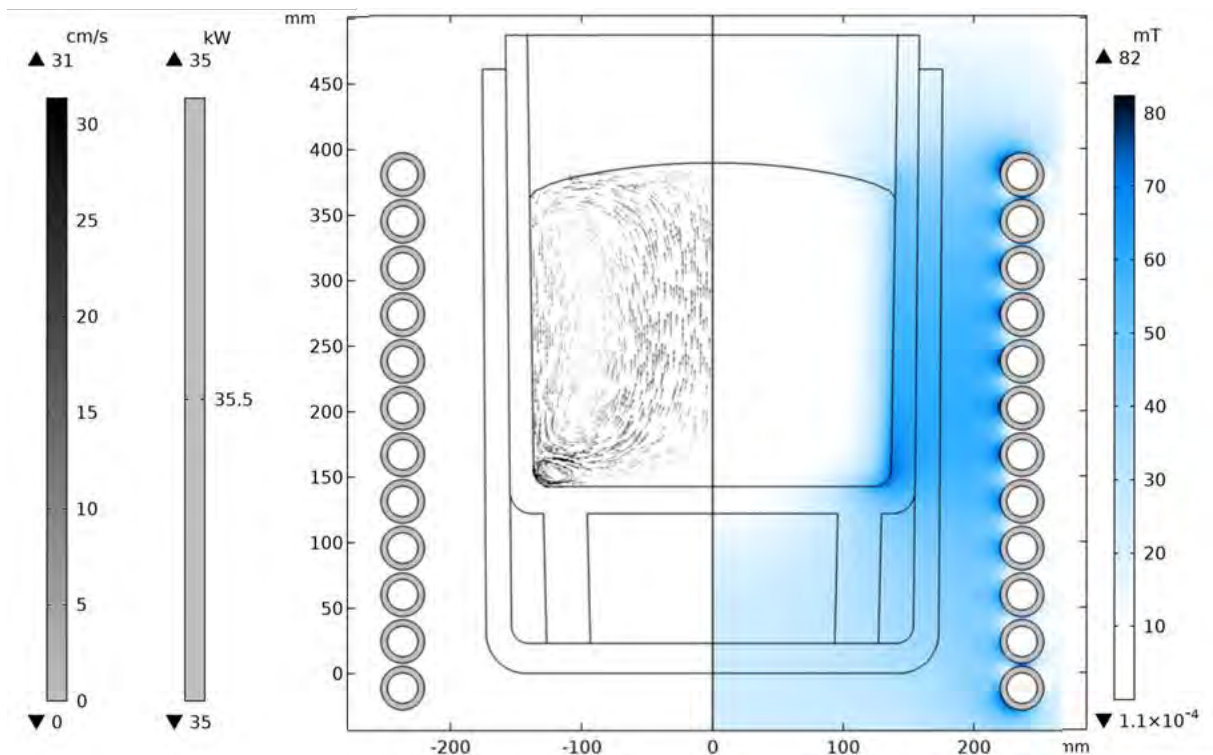
Figure 6-5. Flow field and magnetic flux density for VIM furnace 1 at 36 kW.

Figure 6-6 illustrates the free surface profiles for the melting stage at 90 kW and temperature maintenance at 36 kW. The surface profile deformation ranges between 12 and 25 mm, consistent with the previous results for the laboratory-scale VIM installation and keeping a proportional relation with the mass and the applied power. It should be noted that achieving convergence in the simulation was more challenging for the highest power case, resulting in a greater distortion of the mesh elements.
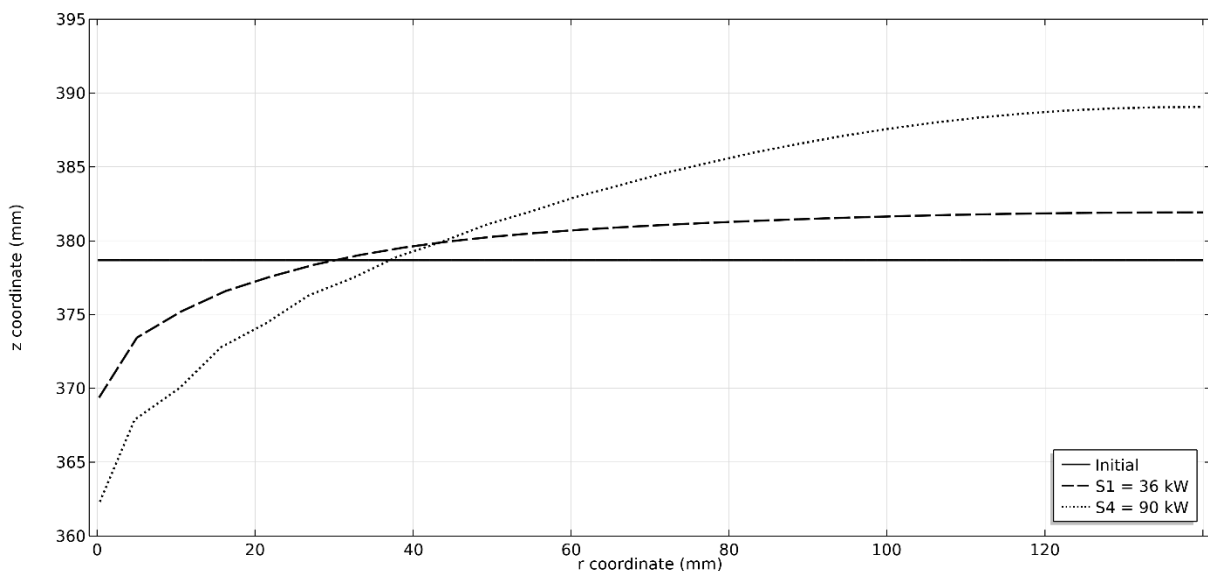
Figure 6-6. Free surface profile in a quasi-stationary state.

The second phase focused on the flow velocity plotted on the left side of Figure 6-5. An accurate reproduction of the turbulence phenomena and the resolution of the velocity gradient in the boundary layers is crucial for the posterior heat transfer simulation. Once the flow reaches a quasi-stationary condition, the velocity field remains relatively stable until there is a modification in the applied power,

leading to accelerated or decelerated metal velocities, as reported in the previous cases. The velocity field revealed the presence of two primary vortices, although the lower vortex was smaller and not fully developed. This could be attributed to the upper vortex's compression effect and the metal's weight. Also, a wider crucible, in comparison with the laboratory scale VIM furnace, derives a faster reduction of flow energy, leading to a decrease in velocity magnitude at the center of the melt.

6.1.3. Thermal submodel

The thermal model was coupled to the magneto-hydrodynamic model using the same procedure described for the laboratory-scale VIM furnace in 4.2.4. Magneto-thermo-hydrodynamic model section. The equal equations and boundary conditions were implemented, with slight modifications made to the forced convective heat flux boundary condition at the internal contour of the coil. This adaptation considered the heat dissipation from cooling water recirculation for the new furnace characteristics. The water flow rate was set at 200 l/min, and the temperature difference between the water outlet and inlet was 8 ° and maintained constant throughout the process.

The model replicates the melting process starting from minute 73, corresponding to the moment when the first temperature reference of the pyrometer reading at 1360 °C (Figure 6-2). However, since the initial temperature field is unknown, the temperature for the whole system was parametrized through a frequency-stationary study to obtain an initial metal temperature of 1360 °C. It should be noted that the mesh of the crucible wall was refined to capture heat conduction from the metal through the ceramic in greater detail.

Using this solution as a reference, a transient dynamic study reproduced the power stages. Like the laboratory-scale model, the power was implemented as a function of coil current, voltage, and frequency. It was applied stepwise, following the reference of the applied power. Four stages were identified to facilitate relatively fast calculations, with the power averaged during each stage. Additionally, smoothed transition ramps were incorporated by deriving the slope to ensure convergence of the stepwise calculation. Figure 6-2 summarizes these stages, and Table 6-2 provides further details.

Table 6-2. VIM Furnace 1 melting trial transient stages and electrical variables

	Start	End	$I_c(t)$ [A]	P_c [kW]
Stage 1	0	4	2150	90
Trans 1	4	5	Ramp1(t)	Ramp1(t)
Stage 2	5	6.5	1000	20
Trans 2	6.5	6.8	Ramp2(t)	Ramp2(t)
Stage 3	6.8	10	2150	90
Trans. 3	10	11	Ramp3(t)	Ramp3(t)
Stage 4	11	18.5	1300	36

Figure 6-7 illustrates the overlaid profiles of the simulated and experimental references for maximum surface temperature and power for the transient melting trial. It can be observed that, due to the initial uncertainty, the model overestimated the metal temperature at the end of the first 90 kW stages. However, after the transition and power adjustment of the furnace's optical pyrometer according to the thermocouple reading, a stabilization temperature of 1530 °C was achieved. Regarding the temperature distribution within the melt, a maximum gradient of 5 °C was computed during the heating and maintenance stages. It should be noted that the model does not consider PID control for the thermal

response of the metal and instead assumes a constant equivalent power of 36 kW. Despite this simplification, the model captured the same temperature trends observed in the experimental data and became more accurate as it approached the objective temperature operating conditions. Even so, the model accurately reproduced the power stages and transitions.
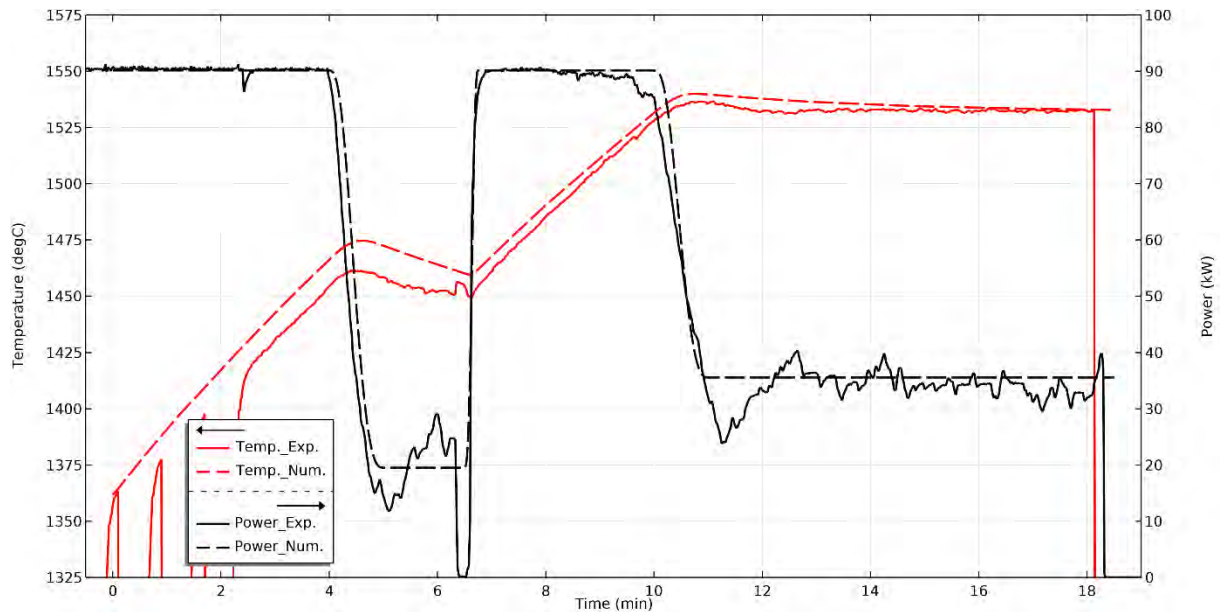
Figure 6-7. Power-temperature-time correlation for modeling and experimental correlation.

Based on these numerical results, an average correlation error of 5 % was obtained, similar to the correlation error achieved in the previous reduced-scale model at the laboratory scale. However, the current model does not account for non-linearities in the induced power, variations in cooling flow, convective atmospheric effects, or other potential artifacts as in the laboratory model. These factors contribute to a more pronounced discrepancy between the model and experimental data. Once again, the main limitation is the lack of knowledge regarding the temperature distribution at the start of the transient study. Since the model was based on a quasi-stationary condition defined by the pyrometer temperature, it does not fully represent the complete temperature system and may result in deviations from the actual behavior.

6.2. VIM Furnace 2

Regarding the second case study, it is worth noting that the furnace configuration is slightly different from the previous case having a narrower crucible height-to-diameter ratio. The furnace coil is divided into two halves: upper and lower, each consisting of five turns. These halves operate in parallel, requiring independent coil modeling. Additionally, the cross-section of the furnace coil has an oval geometry, in contrast to the previous cases, where it was entirely circular. Like the previous case, each physical aspect is studied separately and then integrated to compare the numerical results with the experimental data obtained from industrial-scale melting tests.

The specific geometry is depicted in Figure 6-8, showcasing the geometry section and CAD import for the two-dimensional axisymmetric view. The considered case study involves a liner configuration with a melting capacity of 50 kg of Inconel 718. This configuration's height-to-diameter (H/D) ratio is 1.67, nearly twice as high as in the VIM Furnace 1 case.
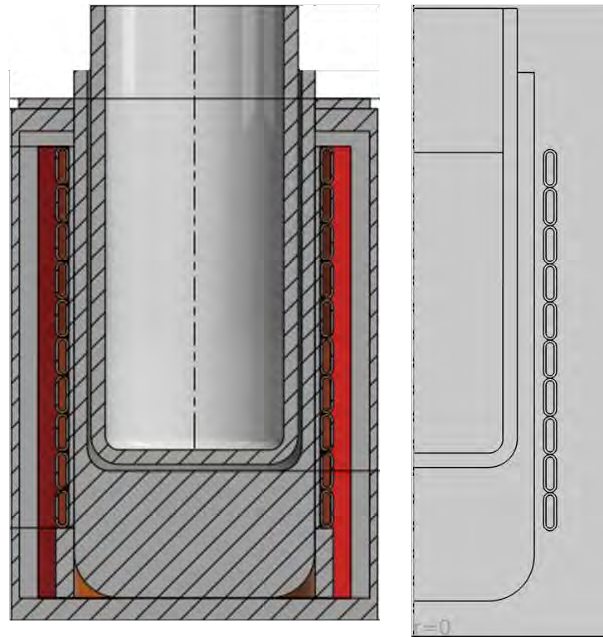
Figure 6-8. Depict of 2D section geometry and 2D-axisymmetric reduction of the model.

The melting procedure entailed rapid heating and melting of the material by utilizing the maximum power permitted by the furnace, which amounted to nearly 170 kW. Once the metal is completely melted and reaches the target temperature of 1500 °C, it is held at that temperature for a few minutes before being cast. This procedure is summarized in Figure 6-13, where an initial fast heating phase, referred to as P_{mode}, lasts for a few minutes, followed by a fast power reduction for the temperature maintenance mode named T_{mode}. Thus, the furnace's operation is investigated under these two power stages.

6.2.1. Coil modeling

As a first step, each coil was sized independently and compared with the facilitated measurements (Figure 6-9). Notable differences in the electrical parameters for the superior (green) and inferior (blue) coils can be observed by plotting the resistance, inductance, and, consequently, the power of each coil.
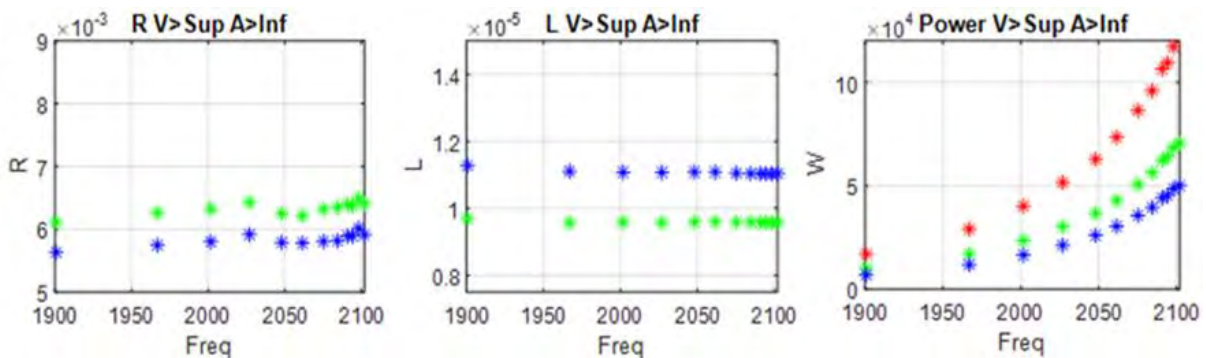
Figure 6-9. Measured experimental electrical parameters for the coils of VIM Furnace 2.

The superior coil operates at a higher power, which may be due to the better positioning of the load and improved magnetic coupling compared to the lower coil. In the case of the lower coil, a section of the coil lacks a metal load, resulting in potentially different load-coil couplings between the two coils. Therefore, the initial focus is to model the coils based on the electrical parameters obtained from the characterization.

Following the previously presented procedure, the coil was modeled feeding with the provided data, coil frequency, current, and voltage. These variables were parameterized in a sweeping study to determine

the operating powers corresponding to the experimental tests. Figure 6-10 presents the electrical parameters of the two halves of the coils and the power generated in each coil.
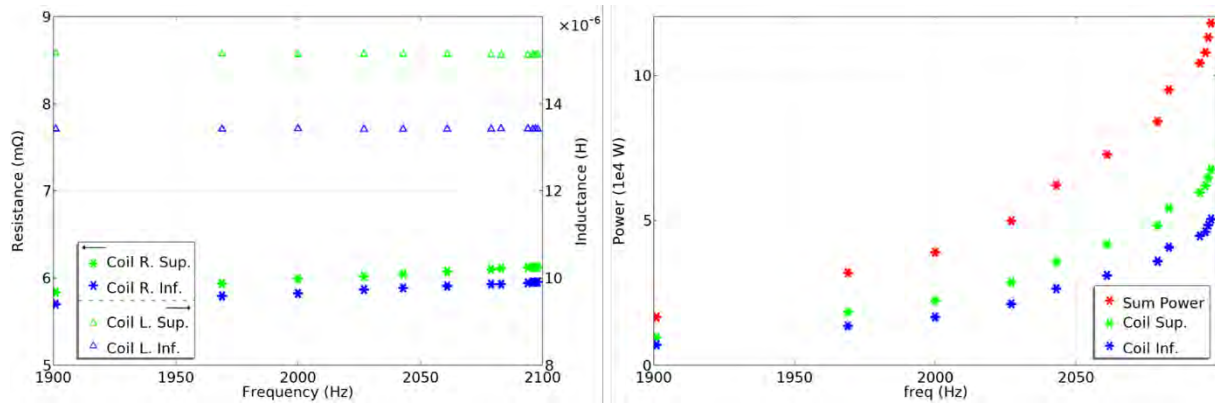
Figure 6-10. Modeled electrical parameters of the two coils and induced power.

There was a proper correlation between the experimental and numerical components, although there was a slight disparity in the inductance (triangles). Conversely, the resistance (asterisks) exhibits the opposite trend while the same power incremental trend can be observed concerning the power.

6.2.2. Magneto-hydrodynamic model

The two specific operating conditions were studied concerning the distribution of induced magnetic flux density, T_{mode} and P_{mode}. Figure 6-11 illustrates the magnetic field intensity (**B**) for the contour representing the shared surface between the metal and the crucible, revealing a similar profile for both power stages.
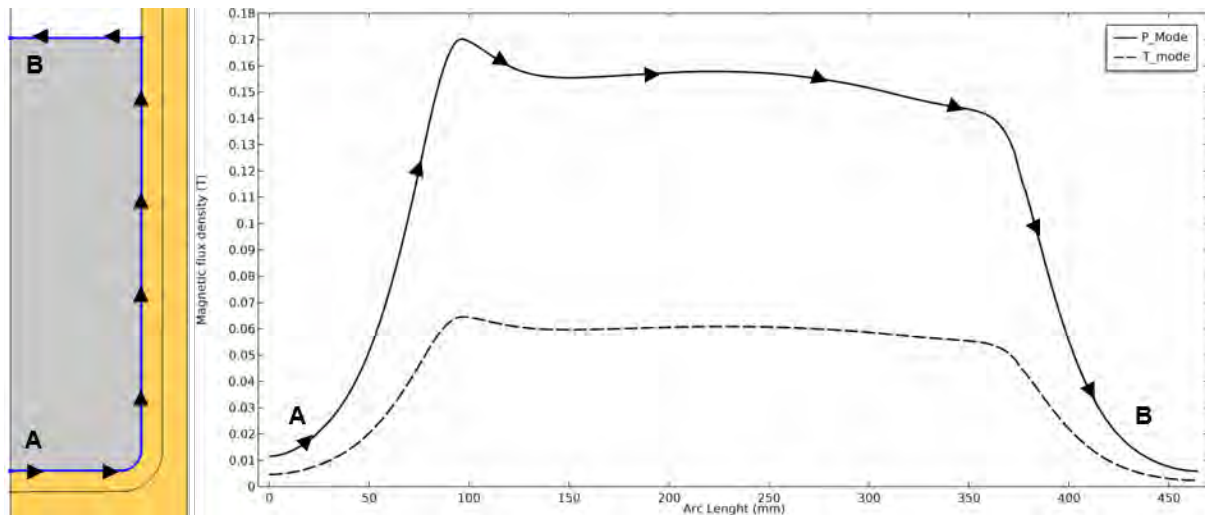
Figure 6-11. Magnetic field intensity (**B**) for the charge arc length section.

However, under T_{mode}, a more uniform condition was achieved. Both power conditions exhibited a similar magnetic field profile due to the minimal variation in frequency, being almost identical, with the magnitude increasing for the P_{mode}. In general terms, the field distribution in the contour appears to be more uniform when compared to VIM Furnace 1, as the coil surrounds liquid metal, avoiding the appearance of concentrated magnetic field zones.

In this regard, analyzing the magnetic flux in the two-dimensional section offers more valuable information depicted on the right side of Figure 6-12. The highest field density was concentrated near the bottom edge of the melt due to its proximity to the coil and central position. The effective coupling

between the magnetic field and velocity is illustrated in Figure 6-12, where the right side depicts the velocity field's magnitude and the recirculating pattern, emphasizing the independent power distribution for each half of the coil.
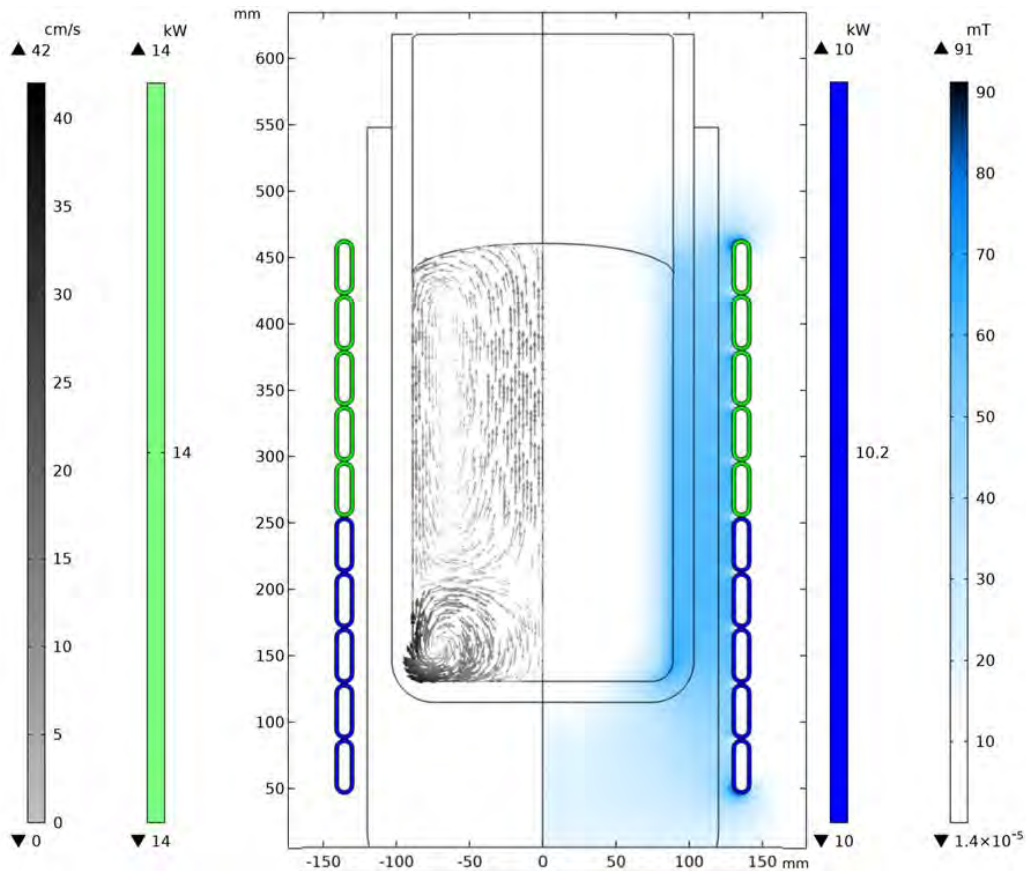
Figure 6-12. Fluid flow and magnetic flux density for VIM Furnace 2 at T_{mode}.

The radius of the upper vortex was relatively larger than that of the lower vortex, which appears to be limited by the upper vortex, resulting in compression against the base of the liner. Furthermore, the narrower inner diameter of the liner contributed to this compression, increasing the velocity of the metal. Upon analyzing the velocity values, it was observed that in P_{mode} conditions, the velocities were significantly higher, reaching almost 100 cm/s on the surface of the liquid metal. In T_{mode} conditions, the maximum velocity drops to 40 cm/s. Although the vortices are similar in both cases, the higher velocities generated in P_{mode} induce greater agitation and destabilization of the melt. These higher velocities also aid in homogenizing the temperature, albeit limited by the higher field density and increased overheating near the lower edge of the liner.

It is necessary to mention that due to the high powers and Lorentz forces generated in the metal, it was not possible to obtain convergence for the simulation of the free surface deformation at P_{mode}. Distorted mesh elements were generated as in the validation studies in the triple junction formed by the metal, the crucible wall, and the air. Therefore, the solution of the surface profile for the holding power T_{mode} was fixed for the subsequent studies.

6.2.3. Thermal submodel

As mentioned for the VIM furnace, the melting procedure 2 is simple, involving only two stages: heating at larger power (P_{mode}) and temperature maintenance (T_{mode}) (Figure 6-13). However, the difference in

the electrical parameters required the modeling of each coil independently. As a result, specific electrical variables for each coil were established and summarized in Table 6-3.

Table 6-3. VIM Furnace 2 melting trial transient stages and electrical variables

	Start	End	I_{sup} [kA]	I_{inf} [kA]	V_c [V]	P_{ind} [kW]
S - 1 (P_{mode})	0	1.2	3290	2910	400	170
Trans 1	1.2	2	Adapt	Adapt	Adapt	Adapt
S - 2 (T_{mode})	2	6.65	1280	1110	200	25

Just like in the previous case, it is not possible to determine the complete heating history of melt and liners. Therefore, the initial temperature distribution is estimated assuming stationary conditions to match the temperature measurement of the pyrometer of 1400 °C. The simulated maximum temperature for the top surface is plotted in split lines in Figure 6-13.
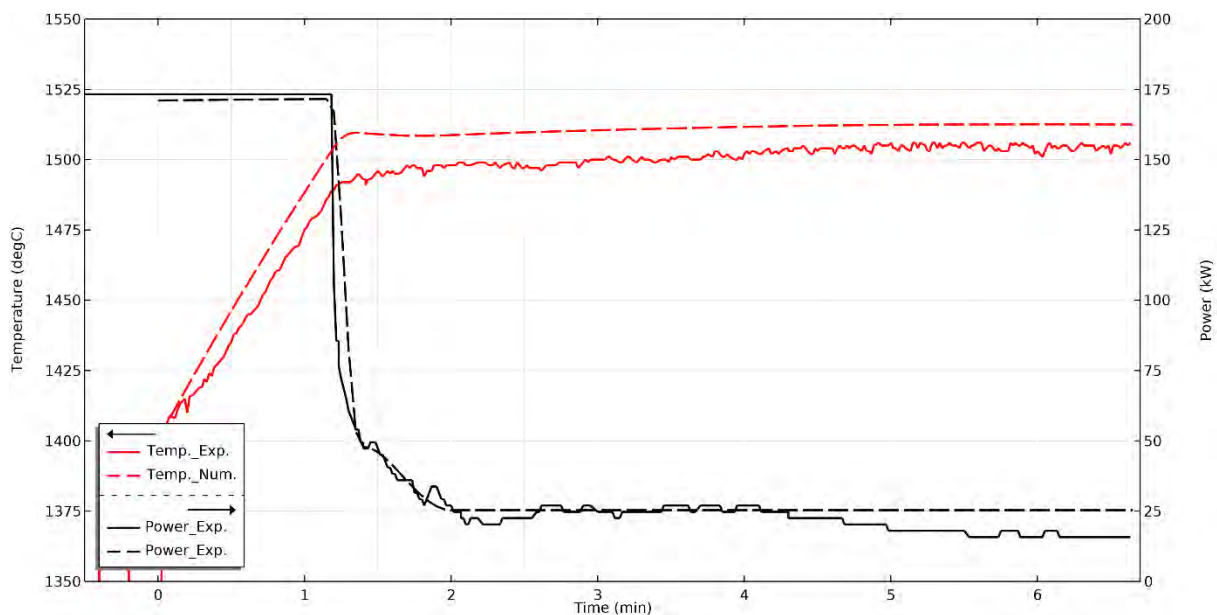
Figure 6-13. Numerical and experimental correlation of VIM furnace 2 melting trial.

The transient thermal model exhibits a more pronounced heating gradient than the experimental model. The increasing gap between the model and experimental results over time is likely attributed to the initial uncertainty in setting the model's temperature. Despite this discrepancy, the simulation results align well with the experimental reference, demonstrating adequate accuracy with an absolute error of less than 5 % in stationary conditions. Hence, it can be concluded that the model accurately predicts the system's actual behavior.

Another aspect of interest is the temperature distribution during the melting process, which helps identify the temperature gradient and the difference between the coldest and hottest zones in the liquid metal. The interest in the knowledge of the temperature distribution prior to casting is essential for the numerical study of mold filling and solidification to ensure the correct filling of the molds. Figure 6-14 illustrates the temperature distribution for the initial, middle, and final time steps for P_{mode} and T_{mode} stages.
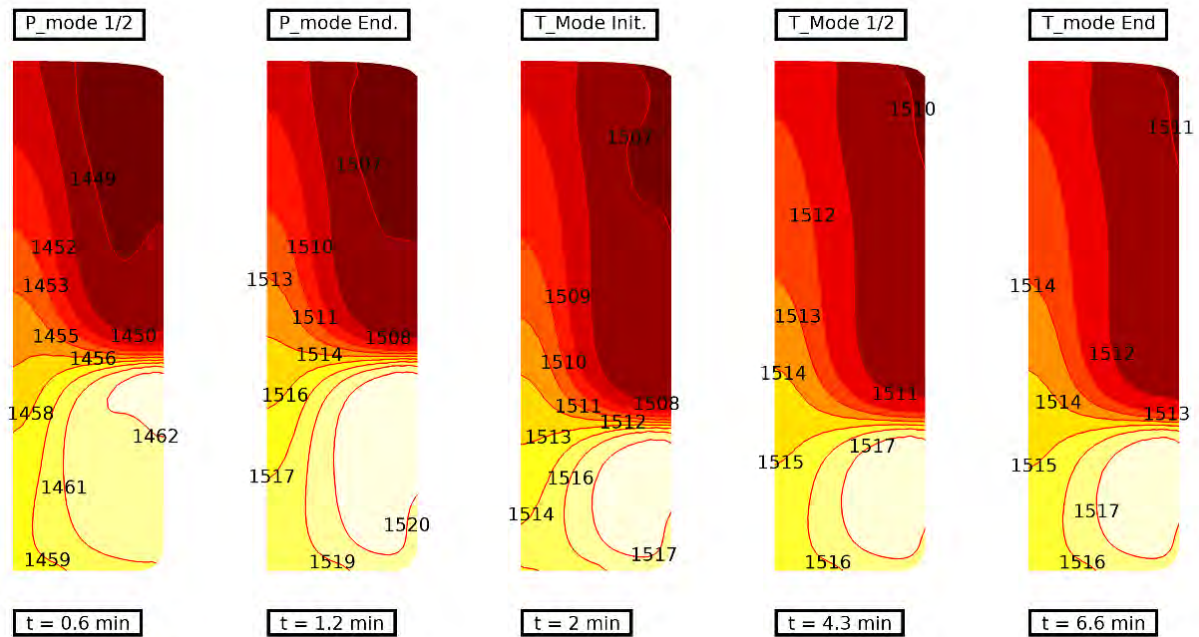
Figure 6-14. Computed temperature distribution for selected time steps during the melting.

The temperature distribution in the P_{mode} stage was initially analyzed by considering two representative situations: the middle of the stage at t = 0.6 min and the end of the stage at t = 1.2 min. The results indicate a temperature gradient of approximately 15 °C, with the hottest region being the lower vortex. Subsequently, the focus of the analysis shifted to the T_{mode} stage, which is of greater interest for ensuring temperature homogeneity prior to casting.

The maximum temperature gradient observed during this stage was 10 °C, and the temperature homogenization occurred rapidly. Specifically, temperature variations of 10 °C, 7 °C, and 6 °C were observed between the highest and lowest temperature zones at the start, middle, and end of the T_{mode} conditions, respectively. This minor temperature difference can be attributed to the lower induced power, which prevents the formation of hot zones and promotes better temperature homogenization.

6.3. Conclusions

The initial case study was conducted on an industrial scale with a significantly higher mass, two orders greater than the laboratory-scale VIM installation. Consequently, a higher power was necessary for heating the charge and maintaining the casting temperature—the modeling of the coil and the resulting magnetic field aligned well with experimental measurements. Interestingly, the flow velocity pattern revealed the presence of practically only one recirculating vortex, possibly due to the hydrostatic force of the metal, compressing the flow downwards and impeding the development of a second vortex. The thermal response of the model proved satisfactory, accurately reproducing the dynamic temperature transition, where the maximum thermal gradient of the liquid metal temperature was limited to 5 °C.

The analysis performed on the VIM Furnace 2 system, for one order of magnitude higher melt mass, uncovered variations in the operation and applied power of the induction coils, despite their parallel electrical connection. Notably, the lower coil contained non-metallic charged sections within some of its coils, affecting the induced current density and resulting in more significant temperature variations in the load and velocity vectors under different operating conditions. The P_{mode} and T_{mode} operation modes exhibited significant differences, impacting the load's melt velocity and temperature distribution. In P_{mode}, applying higher power led to forming a more prominent hot spot, causing a deviation of up to 15 °C in surface pyrometer measurements. Conversely, in T_{mode}, using lower power to adjust the

temperature resulted in a more favorable thermal distribution, with a pyrometer deviation of only 5 °C during the final instant, just before casting.

In conclusion, the developed VIM model has demonstrated its usefulness and versatility in studying various VIM systems and comparing operational scenarios. However, it is important to note that these conclusions are based on comparing independent systems, and the observed trends and behaviors may not universally apply.

Chapter 7

7. Enhancement of VIM process efficiency

The results and conclusions of the following section have been published in the Journal of Materials Research and Technology [125].

The thermal properties of ceramic crucibles, such as conductivity and heat capacity, are directly influenced by their temperature and composition. The thermal field of the numerical model has also indicated the notable thermal insulation capacity by maintaining heat in the melt.

Therefore, in order to investigate their impact on the efficiency of the VIM process, a comparative study was conducted. A series of melting trials using different crucible materials was performed, following the standard melting procedure outlined in section 3.4. Standard melting procedure. It is worth noting that the four crucible materials (AL97I, MG95I, ML72I, ZC93I) used in the melting trials were characterized in 3.2.2. Thermal characterization.

7.1. Standard melting cycle

Figure 7-1 depicts the power-time profile followed from the 60 minutes bake-out until the pouring of the melt. The AL97I trial, which serves as a reference, determines the duration of the different stages shown in the graph. Power variations in each stage are related to the power adjustments required in each trial and stage to maintain the objective e temperatures detailed in the 3.4 Standard melting procedure (1500 °C and 1450 °C in stages 4 and 5, respectively).
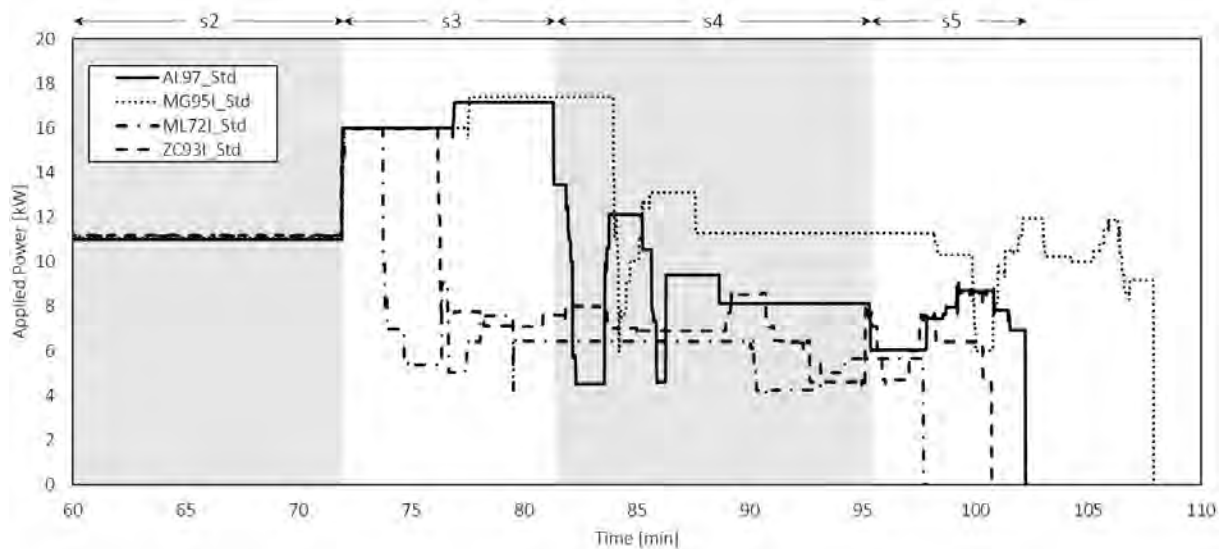
Figure 7-1. Standard melting procedure, applied power as a function of time for the four crucibles.

It must be highlighted that AL97I and MG95I required 17 kW in stage 3 to melt and reach 1500 °C for the dross cleaning. In addition, it was also necessary to apply higher power to stabilize the melt at 1450 °C in stage 5. The MG95I and the AL97I required similar power, while the ZC93I and ML72I trials needed lower power to reach the same temperature response in all stages.

The evolution of the charge temperature for the four crucibles and the division of stages is plotted in Figure 7-2. The magnetic field produces a non-uniform current induction over the charge length, initiating the melting at the base of the cylindrical ingot, which can be viewed in the video recording [125]. This incipient melting displaced the ingot radially. Sudden temperature variations in the

pyrometer between minutes 65 and 85 resulted from the ingot bottom measurement, where liquid metal appeared while the top surface continued to be cooler.

The temperature slope of stages 2 and 3 shows different heating gradients for each crucible. The ML72I and ZC93I gradient was stepper, requiring less melting time than the AL97I (8 minutes less for the ML72I and 5 minutes for the ZC93I). This is in line with the thermal measurements, where lower heat capacity and thermal conductivity were measured for the last crucibles. Thus it was expected to reduce the heat conduction consequent losses and faster heating. In contrast, the MG95I and AL97I with higher specific heat capacity and conductivity, heating, and melting were displaced in the time axis.

Once the target temperature of 1500 °C was reached, it was maintained during stage 4, adjusting the applied power following thermal inertia. This facilitated dross cleaning while preventing the melt from excessive superheating. During dross-cleaning, it was observed that the particle reduction time was not equal, with the ML72I and MG95I crucibles achieving faster metal cleaning; however, the duration was fixed to 15 minutes following the standard criteria.
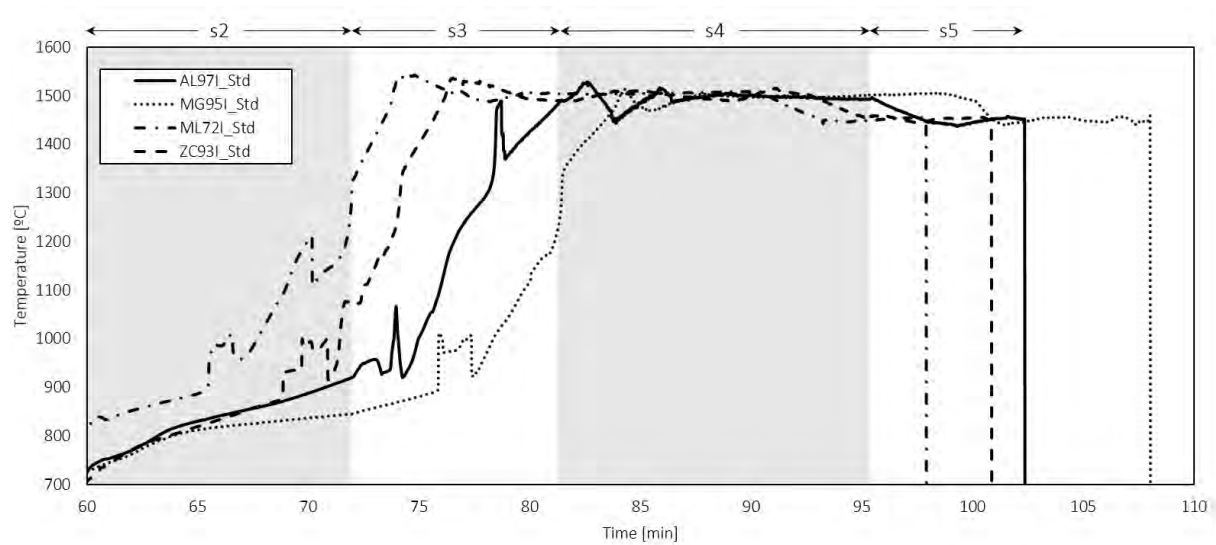
Figure 7-2. Standard melting procedure, temperature as a function of time for the four crucibles.

The energy consumption of each trial was evaluated by integrating the total lead time and the power generator supply. Table 7-1 sets out the energy consumption for the complete melting cycle and compares the energy-saving of each crucible concerning the reference trial AL97I_Std. The MG95I crucible demanded higher energy due to prolonged melting and higher power requirements. In contrast, the ZC93I and ML72I presented faster heating, with the former consuming 23% and the last 28% less energy than the baseline.

Table 7-1. Energy consumption for standard melting and crucible comparison.

Melting Trial	Energy Consumption [kJ]	Crucible Comparison [%]
AL97I_Std	846.8	-
MG95I_Std	929.3	+ 10
ML72I_Std	611.6	- 28
ZC93I_Std	648.7	- 23

7.2. Optimized melting cycle

A second trial was performed, optimizing the power profile by minimizing the dross-cleaning time in stage 4 instead of applying a standard fixed duration. Figure 7-3 illustrates the power-time graph. The standard criteria was followed until stage 2. In stage 3, the melting time was adapted to the thermal response, and it was confirmed that AL97I and MG95I required the additional step of 17 kW for 4.5 and 6.5 minutes, respectively. In contrast, a 16 kW step for 2 minutes for the ML72I and 5 minutes for the ZC93I was enough to melt the charge. Then, the applied power and time were adjusted based on the temperature evolution of the melt. The objective was to maintain the target temperature while enhancing the dross separation velocity. In this latter, less power and time were required for the ML72I and MG95I.
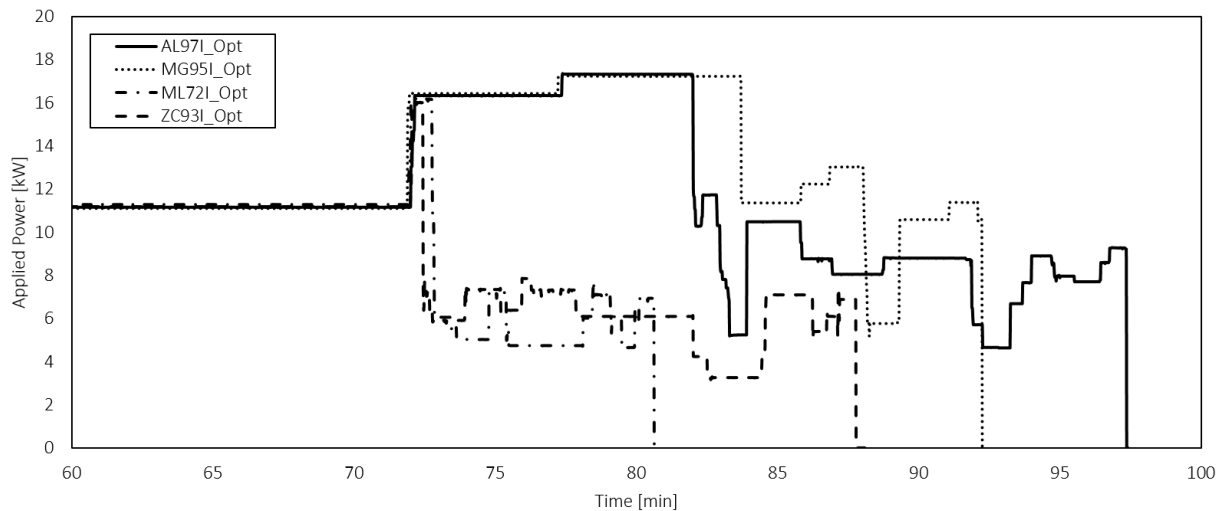
Figure 7-3. Optimized melting procedure, power as a function of time for the four crucibles.

The temperature response of the melt during temperature conditioning is shown in Figure 7-4. Once the ZC93I and ML72I were fully molten, the AL97I incipient melting started, while the MG95I required the longest time to melt completely. The dross cleaning time was minimized based on the dissipation velocity, and the temperature was maintained, which reduced the duration of stage 4—the dross cleaning times, summarized in Table 7-2. After the top melt surface was clean, the power was reduced to decrease the temperature in stage 5 and then maintained for 5 minutes for homogenization before metal pouring.
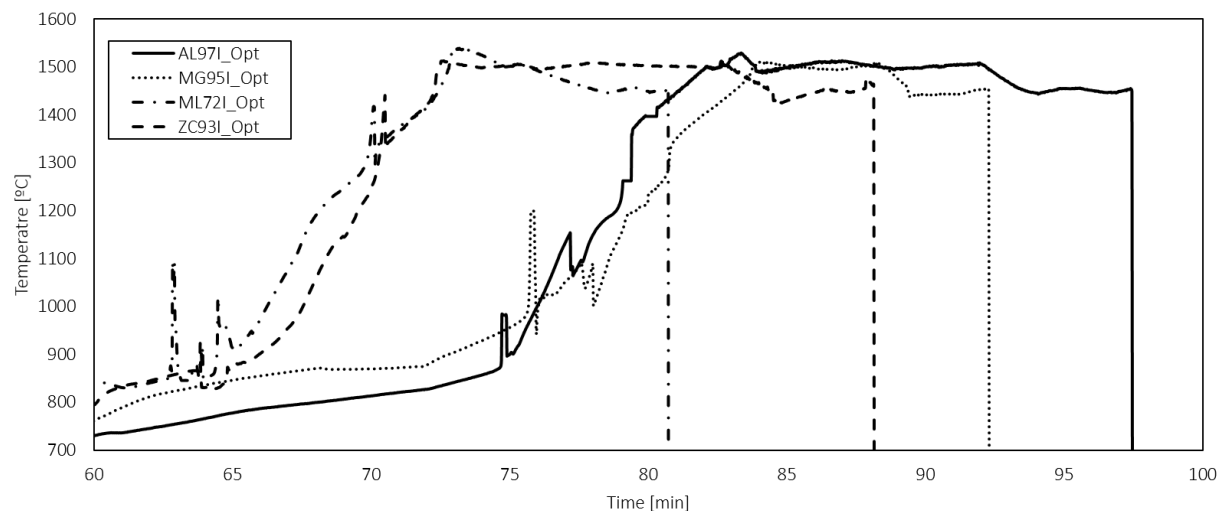
Figure 7-4. Optimized melting procedure, temperature as a function of time for the four crucibles.

The lead time saving for the optimized melting was analyzed by evaluating three critical intervals and compared to the AL97I_Opt (Table 7-2). The ZC93I and ML72I crucibles required 24% and 45% less time for the melting and dross cleaning steps than the AL97I. Again it is confirmed that melting time is directly related to thermal properties. The AL97I and MG95I melting trials had a similar total duration except for the dross cleaning, stage 4, where ML72I and MG95I were the crucibles that presented a faster dross cleaning.

Table 7-2. Detailed interval comparison between crucibles.

Evaluated interval	Stages	Duration [min]			
		AL97I_Opt	MG95I_Opt	ML72I_Opt	ZC93I_Opt
Melting time	2-3	20	22	11	11
Dross cleaning	4	13	7	5	12
Cycle time	2-5	38	34	21	28

7.2.1. Melting procedure comparison

Table 7-3, the optimized melting cycle of each crucible is compared to the previously discussed standard melting profile, revealing energy savings of between 10% and 20% for each. Evaluating the optimized melting trials with AL97I_Std baseline, reductions in energy consumption of 43% for the ML72I_Opt and 38% for the ZC93I_Opt were obtained.

Table 7-3. Energy saving by procedure comparison for tested crucibles.

Crucible Reference	Energy Consumption [kJ]		Procedure Comparison [%]
	Standard	Optimized	
AL97I	846.8	755.8	- 11
MG95I	929.3	733.1	- 21
ML72I	611.6	485.6	- 21
ZC93I	648.7	528.2	- 19

Similarly, a cycle time reduction following the optimized melting procedure is achieved for all crucibles (Table 7-4). Moreover, the lead time was reduced by 13% and 21% for ZC93I_Opt and ML72I_Opt, respectively, compared to the AL97I_Std baseline.

Table 7-4. Cycle time by procedure comparison for tested crucibles.

Crucible Reference	Cycle Time [min]		Procedure Comparison [%]
	Standard	Optimized	
AL97I	102	98	- 4
MG95I	108	93	- 14
ML72I	98	81	- 17
ZC93I	102	89	- 13

7.3. Crucible reactivity and dross analysis

The duration times of stage 4, Dross cleaning, along with video recordings, have shown that the time required for minimizing the presence of dross varied depending on the crucibles used. The thermal properties alone cannot justify why the MG95I could be faster than the ZC93I, as MG95I is the crucible with higher thermal conductivity. Thus, it is necessary to open the scope to additional aspects, such as the analysis of the dross's nature and formation and interaction with the crucible, to understand the dross-cleaning mechanisms.

Although their relationship with thermal properties is not apparent, efforts have been made to understand better the dross's characteristics and connection to the crucible. Initially, this dross tends to form clusters of small particles, indicating it is a solid element rather than gases produced during the refinement process. Two options are being considered; first, they could be oxides, but their sudden appearance at the beginning of the liquid state and their dissipation over time rule out this possibility. The second option is that they are reaction products resulting from the interaction between the ceramic crucible and the metal.

Therefore, all crucibles were examined after pouring the melt into the molds, but no identifiable remaining dross particles were found. However, solidified metal layers were observed attached to the inner walls of the crucibles. Visual analysis revealed the presence of ceramic remains, which could contain particles and possible reaction products resulting from the interaction between the metal and the crucible. Consequently, the composition of the interfacial samples and the presence of additional phases and composition variations of the tested crucibles have been analyzed using XRD and XRF techniques.

- **Dross composition**

First, a local semi-quantitative chemical composition analysis of the detached layers was done employing scanning electron microscopy (SEM) and energy-dispersive X-ray spectroscopy (EDS) with a Fei Nova Nanosem 450®. A section of the sample (Figure 7-5) corresponding to the interphase between dross and crucible was analyzed for all crucibles. MG95I_Opt crucible was selected as a representative case, the fastest for the dross cleaning stage. The measured local points are identified, and the elemental composition results are summarized in Table 7-5.
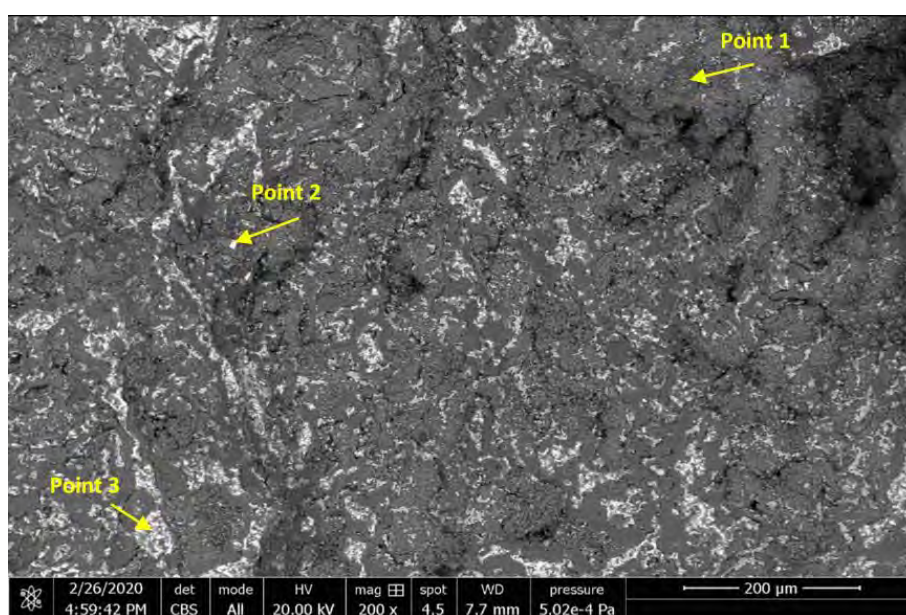
Figure 7-5. BSE of the dross-crucible face sample. EDS of oxidation products.

The main matrix composition corresponding to Point 1 is rich in Mg, O, and Al— the product of the possible reaction. In addition, several Al, Ti, and Nb-rich compounds were detected in Points 2 and 3. These metallic oxides have been detected for all crucibles in different proportions, thus, indicating the possible composition of the dross particles. The presence of complex metallic oxides together with Mg may be due to the formation of a thinner slag during melting as a consequence of the oxidation process in the MgO-based crucible.

Table 7-5. Semi-quantitative chemical composition of detected oxides for MG95I_Opt crucible.

	Chemical Composition [at.%] Spectrum								
	Ni	Cr	Fe	Nb	Mo	Mg	Ti	Al	O
Point 1	-	3.5	-	-	-	16.7	1.5	37.6	43.7
Point 2	37.7	13.6	12.3	17.6	2.7	4.2	2.4	9.5	-
Point 3	40.1	16.6	15.1	2.7	1.7	-	1.0	22.7	-
Inconel 718	52.5	19	Bal.	5	3	-	0.9	0.6	-

Regarding the remaining samples from other crucibles, the same compounds have been identified, albeit in different percentages, with the presence of oxides composed of the aforementioned alloying elements. The presence of oxygen can be attributed to either leak in the vacuum chamber, as the vacuum is not perfect and there is always a slight residual atmosphere, or the contribution from the crucibles themselves, which will be further investigated.

- **Crucible reactivity**

Tested crucibles were examined to find evidence of the melt-to-crucible reaction and the formation of new compounds. Samples from the crucibles in contact with the molten metal were extracted and grounded for XRF and XRD inspection. As received, new crucible samples were also examined for reference. The Al97I, ZC93I, and ML72I samples did not contain any relevant quantity of reaction products, while MG95I-produced compounds are presented in the XRD spectrum of Figure 7-6.
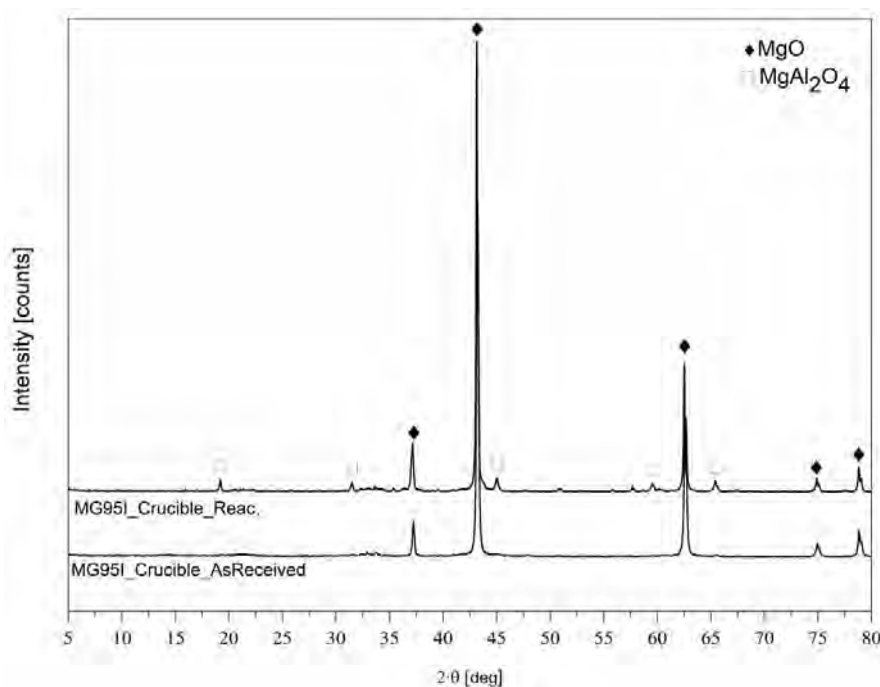
Figure 7-6. As received and reacted MG95I crucible samples XRD diffractograms.

Analysis reveals the presence of $MgAl_2O_4$ (spinel) as the main crystalline reaction product. Traces of Al_2O_3 (corundum) were also detected. According to the Ellingham diagrams, at 1500 °C, $MgAl_2O_4$ is more stable than MgO or Al_2O_3 [130]. The $MgAl_2O_4$ was likely formed from the reaction between MgO present in the crucible and Al from the alloy. This reaction could be either a direct MgO – metallic Al reaction or/and a MgO – Al_2O_3 reaction previously described by Gao et al.[48]. They evidenced a two-stage reaction for the MgO and MgO- $MgAl_2O_4$ crucibles, where the first Al_2O_3 layer was produced due to the reaction between the MgO crucible and Al of the alloy. In a secondary stage, Al_2O_3 reacted with the MgO of the crucible, deriving it into $MgAl_2O_4$. In parallel, the dissolved Mg from the first stage reduces the Al_2O_3 and Ti_2O_3 inclusions modifying the composition into stable Al-Mg oxides.

Therefore, it is reasonable to assume that MgO – Al_2O_3 reactions may occur since this would also correlate with the presence of Al_2O_3 in the diffractogram. Oxidation of the Al alloying element may be formed after the first reaction of metallic Al with crucible oxides; however, reactions between Al and free O present in the porous ceramic structures or the atmosphere cannot be discounted. The EDS analysis of the dross evidences Al-oxides' presence, indicating that this Al can only come from the alloy itself and not from the crucible and a possible loss of alloying elements in the melt. Similarly, the detected Mg-rich and Al-Ti oxides could be related to the formation of inclusions.

7.4. Conclusions

The presented results demonstrate the importance of crucibles on the overall efficiency of the VIM process for the Inconel 718 superalloy. Remarkable energy consumption saving was achieved by only varying the composition of the crucibles. Another benefit was reducing the process cycle time, which was enhanced by optimizing the melting procedure and minimizing the dross cleaning time. This optimization resulted in energy savings ranging between 10 % to 20 % and a reduction in lead times of almost 15 %.

The crucibles' thermal conductivity and heat capacity play a critical role in the heat transfer dynamics between melt and crucible. As expected from the measurements, for lower measured values, faster melting was achieved, as is the case of ML72I and ZC93I crucibles. SiO2 seems to be a critical crucible material in VIM process performance. The ML72I crucible contains approximately 25 % w.t. of SiO_2, so its employment would save energy. Moreover, the experiments performed with this crucible revealed no ceramic-metal reaction products.

The optimized melting procedure confirmed the first results and increased energy saving. However, for the dross cleaning step, the faster performance of MG95I is not possible to explain only with the crucible thermal properties.

It is not clear the mechanism behind the formation and separation of the dross. For all crucibles, the EDS analysis of the reaction products indicates the formation of Al, Ti, Mg, and Nb oxides. The composition was equal for all crucibles, varying in quantity, indicating the possible composition of the dross particles. Also, it is possible that while the melt depletes alloying elements, the crucible provides free O for forming Al-Mg-Ti oxides. All crucibles except MG95I remained chemically stable during melting. Spinel formation ($MgAl_2O_4$) in MG95I indicates that aluminum can only come from the alloy itself and not from the crucible.

These results can directly impact industrial-scale production facilities contributing to more efficient induction melting practices. Along the same line, consideration of the final thermal properties of crucibles for the future development of new compositions.

Chapter 8

8. Conclusions

In this chapter, the main conclusions derived from the work carried out are discussed first. Then, some possible ideas or lines of future work are presented, which would be interesting to pursue further.

8.1. General Outlines

The VIM process, combined with the investment casting method, is the best approach for manufacturing Ni-based superalloy aero-engine components. This process involves rapid and electrically efficient heating and melting in a vacuum atmosphere, minimizing the formation of oxides or inclusions and preventing melt contamination. However, VIM melting involves a complex and intricate technology where multiple variables and physical phenomena co-exist in challenging operating conditions, such as high temperature, magnetic fields, and vacuum atmosphere, hindering process enhancement. Therefore, the main objective of the present research project was to enhance the VIM heating and melting process for superalloy Inconel 718 while advancing the current technological understanding. A coupled multi-physics numerical model has been successfully developed to achieve this goal. Next, it has been experimentally validated to determine uncertainty and minimize deviations, ultimately improving the efficiency of the VIM process.

Regarding the numerical modeling, the present study demonstrated the feasibility of developing a coupled multi-physics model capable of capturing the internal dynamics of the melting process and establishing significant correlations among the process variables. The principal conclusions are as follows:

- Precisely controlling and monitoring the different process variables is essential for achieving a controlled process and serving as input to feed the numerical model. In this aspect, coil electrical variables, including current, voltage, and frequency, are the principal features to heat induction. The system response is measured as melt temperature variation to adjust the applied power during melting trials. At the same time, heat losses due to conduction and radiation serve to determine the boundary conditions.

- Additionally, precise measurement of Inconel 718 thermal properties is fundamental in the solid state due to temperature dependency. Significant variations among reported bibliographic data depend on the material processing history, measurement method, and conditions, necessitating experimental characterization. Conversely, bibliographic references have been relied upon for the liquid state due to data consistency and notable technical difficulties in measuring thermal properties at melting temperatures. Along the same line, ceramic oxide crucibles require a specific thermal characterization due to notable scattering in the function of the chemical composition and temperature, directly affecting the subsequent numerical modeling.

- For efficient modeling, the simulation strategy was divided into two independent models according to the material state (solid or liquid). In solid, the induction heating was effectively and accurately replicated. The contribution of heat from surface irradiation is relatively minor compared to the induced heat of the magnetic field, mainly due to the much lower surface temperature of the crucible. The positioning between the ingot and the coil is not optimal, leading to non-uniform heating and premature incipient melting. This initial melted material portion might become overheated, resulting in the burning of crucial alloying elements.

- Regarding the liquid state model, a recirculatory flow pattern was successfully reproduced in both considered turbulence models, showing similar magnitudes of the flow field, accelerating in the skin depth region and crucible bottom curvature. The repeatability of the model was verified through mesh sensitivity studies, confirming the precision of the numerical model. Moving mesh methods have been proven to be a feasible approach to computing surface deformation. Remeshing steps were included to ensure numerical convergence and avoid mesh element stretching and distortion errors.

- The thermal field was coupled through analytical solutions relating melt temperature and flow field. Numerical results show a uniform temperature distribution of the melt, opposite to the solid ingot. This uniformity is related to the continuous recirculation of the melt due to the magnetic field and the high turbulent thermal conductivity of the metal, leading to rapid temperature homogenization. However, the temperature accuracy was not entirely satisfactory, with a discrepancy of almost 50 °C between the pyrometer measurement and the model solution, which could be associated with underestimating the emissivity parameter and the additional artifacts present during experimental melting.

Regarding the experimental validation, the numerical models were validated by comparing them with ad-hoc experimental trials, which also served as a reference for adjusting the models. The main conclusions from this validation are as follows:

- Proper correlation of the induction heating was achieved with double verification simulating the temperature increment trend for thermocouple reference probes and confirming that the electrical parameters of the coil were aligned with the ones estimated by the mode

- In the liquid state, an open-air induction melting furnace was employed to characterize the free surface, requiring adaptation of the magneto-hydrodynamic model to the new furnace characteristics, being a double verification of the model`s validity. The free surface shape was correctly modeled, although the numerical solution reports a slightly lower surface profile due to the incapability to account for the melt surface instabilities due to the limitation of RANS turbulence modeling. However, the model for low mass and higher power situations led to solution divergences as mesh elements near the wall deformed too much. Even with adaptive mesh refinement, the initialization of the computation cannot converge for the turbulence and flow field, evidencing the principle limitation of the moving mesh methods.

- Parametrizing the emissivity saved the discrepancy between the pyrometer measurement and the numerical solution for the top surface temperature. The study of heat transfer under dynamic conditions revealed that the model exhibits a faster temperature response during the adaptation between the target stationary temperature stages at 1500 °C and 1450 °C, although the relative error is minor. This might derive from the averaging procedure of the applied power and heat dissipation and the incapability to consider the power generator adaptation.

The two large-scale case studies deepened knowledge of the VIM fusion process due to their unique furnace characteristics and operating conditions and served as additional validation examples for the numerical model. The intrinsic characteristics of each VIM furnace required specific adaptations, operating variables, or geometrical aspects. Thus, it is not possible to establish general rules between them. However, there were observed the following general trends,

- The importance of the crucible height/diameter ratio was proven, as it affects the flow field and the formation and distribution of recirculating eddies. Narrower crucibles result in higher velocities, as the center of the melt eddies comes in contact and slows down. Similarly, the charge

placement is also relevant, as it affects the magnetic coupling, producing higher magnetic field zones and consequent modifications of the flow pattern and primary eddy formation.

- Applying one order of magnitude higher operating powers resulted in more significant temperature differences in the melt, although the temperature tends to homogenize for low power conditions.

Finally, from the VIM efficiency improvement trials, the following conclusions are drawn:

- The low thermal conductivity of the ceramic crucibles, as indicated by the numerical results and experimentally characterized, plays a critical role in thermal efficiency. Conduction heat transfer is the primary energy loss driver; thus, a higher insulating capacity leads to higher thermal efficiency in the VIM process.

- The ceramic chemical composition is the principal variable that differentiates the heat transfer between the melt and crucible. The crucible with the least thermal conductor properties, ML72I, led to energy savings of almost 20 % and a decrease in melting time by 15 %.

- SiO_2 appears to be a crucial crucible material in enhancing VIM process performance. The ML72I crucible contains approximately 25 wt. % of SiO_2, making it thermally insulating. Furthermore, experiments with this crucible demonstrated the absence of ceramic-metal reaction products.

- Ceramic-metal reactions were found only in the MgO crucible experiment. $MgAl_2O_4$ was revealed as the main crystalline reaction product, which is more stable than MgO or Al_2O_3. This spinel is likely formed after a $MgO – Al_2O_3$ reaction, correlating with traces of Al_2O_3. Controlling this first reaction would thus be the key to avoiding the presence of these inclusions in the melt.

8.2. Future lines

The present research has provided a comprehensive and detailed understanding of the VIM fusion process. However, continuing the research to address the raised questions comprehensively is recommended. The interest of this scientific development lies in gaining a better understanding of the fusion process and enabling future technological improvements for a more efficient and faster process while ensuring metallurgical quality.

Regarding potential future research directions, the following aspects would be of interest concerning the numerical model:

- It is evident that the next step should be the integration of both solid and liquid models to consider the phase transition effect and study possible overheating in the incipient liquid.

- Expanding the study of velocity field and turbulent flow to 3D LES models would allow for the incorporation of low-frequency pulsations while incorporating heat transfer, thereby confirming the temperature homogeneity of the liquid metal.

- Similarly, calculating the deformation of the free surface using 3D models would include meniscus instabilities and improve the deformed mesh algorithm to ensure calculation convergence and mesh quality.

- Incorporating particle transport in the model for studying the addition of alloying elements to the liquid metal would allow for estimating the time required for their dissolution, optimizing fusion times, and ensuring the composition of the liquid metal.

- Developing multiscale models would be valuable, especially with the knowledge of the wall temperature. Numerically analyzing the conditions for the formation of reaction compounds

between the metal and the ceramic crucible, including concepts of Gibbs free energy and subsequent thermodynamic calculations, could be explored. Additionally, the effect of convective flow on the wall and physical erosion at the particle level could be included.

For experimental data collection and validation, the following suggestions are proposed:

- Measurement of the magnetic field generated by the coil at different power states following standard procedures and comparison with numerical results.

- Regarding the meniscus shape, using non-contact measurement methods such as laser sensors or even thermal cameras could improve measurement accuracy.

- In terms of the fusion operation, although manual control of the furnace power is relatively good, implementing a PID control could be further improved to smooth power adjustments and obtain more consistent temperature control. This would result in more stable fusion curves, simplifying the numerical correlation without the need for constant power adjustments to maintain target temperatures.

Regarding process optimization and industrial scaling:

- Conducting a Design of Experiments (DOE) to analyze new configurations and study conditions would be highly valuable, allowing for a deeper understanding and generating larger numerical results.

- Adapting the general model to the specific characteristics of each installation, such as geometry, coil parameters, operational variables, etc., is time-consuming and requires significant computational resources and result analysis. Developing surrogate models to establish relationships between the most significant operational variables could be a possible tool to streamline this process.

- Using the validated numerical tool as a reference, the numerical optimization of process variables can be studied by implementing multi-objective algorithms to define a power profile that maximizes energy efficiency, minimizes fusion time, and prevents overheating.

- Establishing the foundations for automated furnace control, where the system autonomously adjusts electrical parameters in real-time, would be pursued to ensure the furnace operates under optimal conditions.[i]

-

Bibliographic references

[1]   U. S. Energy Information Administration, "International Energy Outlook 2016," Washington County, OR, USA, 2016, 2016.

[2]   E. Svensson, P. Sommarin, J. Helber, J.-M. Piatek, and F. J. Przybylski, "Improving the energy efficiency of foundries in Europe," 2012.

[3]   M. Blesl and A. Kessler, *Energy Efficiency in Industry*, 1st ed. Springer Berlin Heidelberg, 2021.

[4]   M. Holtzer, R. Danko, and S. Zymankowska-Kumon, "Foundry Industry. Current State and Future Development," *Metalurgija*, vol. 51, pp. 337–340, 2012.

[5]   D. Lehmhus, "Advances in Metal Casting Technology: A Review of State of the Art, Challenges and Trends—Part I: Changing Markets, Changing Products," *Metals (Basel).*, vol. 12, no. 11, p. 1959, Nov. 2022.

[6]   Airbus, "Global Market Forecast | Airbus," 2023. [Online]. Available: https://www.airbus.com/en/products-services/commercial-aircraft/market/global-market-forecast. [Accessed: 07-May-2023].

[7]   A. P. Mouritz, "Superalloys for gas turbine engines," in *Introduction to Aerospace Materials*, Woodhead Publishing, 2012, pp. 251–267.

[8]   M. Donachie and S. J. Donachie, "Meting and Conversion," in *Superalloys: a technical guide*, 2nd ed., A. International, Ed. Materials Park, Ohio USA: ASM International, 2008, pp. 41–77.

[9]   A. Kracke, "Superalloys, the most successful alloy system of modern times. Past, present and future.," in *Proceedings of the 7th International Symposium on Superalloy*, 2010, pp. 13–50.

[10]   J. R. Davis, "Elevated-Temperature Characteristics of Engineering Materials," in *ASM Specialty Handbook: Heat-Resistant Materials*, J. R. Davis, Ed. ASM Specialty Handbook, 1997.

[11]   R. C. Reed, "The Superalloys: Fundamentals and Applications," in *The Superalloys: Fundamentals and Applications*, vol. 1, Cambridge University Press, 2006, pp. 1–32.

[12]   ITP Aero, "Products - ITP Aero engines and turbines manufacturer," 2020. [Online]. Available: https://www.itpaero.com/en/products-and-services/products/. [Accessed: 07-Jan-2021].

[13]   R. E. Schafrik, D. D. Ward, and J. R. Groh, "Application of alloy 718 in GE aircraft engines: past, present and next five years," *Proc. Int. Symp. Superalloys Var. Deriv.*, vol. 1, pp. 1–11, 2001.

[14]   E. A. Loria, "Recent developments in the progress of superalloy 718," *JOM*, vol. 44, no. 6, p. 33, Jun. 1992.

[15]   E. A. Loria, "The Status and Prospects of Alloy 718," *JOM*, vol. 40, no. 7, pp. 36–41, Jul. 1988.

[16]   M. C. Hardy *et al.*, "Solving Recent Challenges for Wrought Ni-Base Superalloys," *Metall. Mater. Trans. A Phys. Metall. Mater. Sci.*, vol. 51, no. 6, pp. 2626–2650, Jun. 2020.

[17]   J. H. Weber, Y. E. Khalfalla, and K. Y. Benyounis, "Nickel-Based Superalloys: Alloying Methods and Thermomechanical Processing," *Ref. Modul. Mater. Sci. Mater. Eng.*, Jan. 2016.

[18]   S. Pattnaik, D. B. Karunakar, and P. K. Jha, "Developments in investment casting process—A review," *J. Mater. Process. Technol.*, vol. 212, no. 11, pp. 2332–2348, Nov. 2012.

[19]   K. Kubiak, D. Szeliga, J. Sieniawski, and A. Onyszko, "The Unidirectional Crystallization of Metals and Alloys (Turbine Blades)," in *Handbook of Crystal Growth: Bulk Crystal Growth*, vol. 2, Elsevier, 2015, pp. 413–457.

[20]   S. Lupi, "Induction Heating," in *Fundamentals of Electroheat*, Cham: Springer International Publishing, 2017, pp. 353–524.

[21]   A. Choudhury, "State of the Art of Superalloy Production for Aerospace and Other Application Using VIM/VAR or VIM/ESR.," *ISIJ Int.*, vol. 32, no. 5, pp. 563–574, May 1992.

[22] C. Lovegren, "Evaluating the Risk of Corona Discharge in Superalloy Vacuum Induction Melting Furnace Applications," *Int. J. Met.*, vol. 14, no. 4, pp. 926–936, Oct. 2020.

[23] M. Rugg and G. Gariglio, "Fundamentals and General Aspects of Power Supply Design for Induction Heating, Heat Treating, Welding, and Melting," in *Induction Heating and Heat Treatment*, vol. 4C, V. Rudnev and G. E. Totten, Eds. ASM International, 2014, pp. 565–577.

[24] F. P. Dawson and S. B. Dewan, "Transistor Voltage Source Inverter for Induction Heating," *IETE J. Res.*, vol. 37, no. 1, pp. 111–123, Jan. 1991.

[25] R. Cook and B. Terlop, "Transformer Design and Load Matching," in *Induction Heating and Heat Treatment*, vol. 4C, V. Rudnev and G. E. Totten, Eds. ASM International, 2014, pp. 673–682.

[26] G. M. Segura, "Induction heating converter's design, control and modeling applied to continuous wire heating," Universitat Politecnica de Catalunya, 2012.

[27] E. Dötsch and B. Nacke, "Components and Design of Induction Crucible Furnaces," in *Induction Heating and Heat Treatment*, ASM International, 2018, pp. 447–461.

[28] E. Dötsch, "Refractory Demands on Inductive Melting of Cast Iron," vol. 3, pp. 99–106, 2011.

[29] L. Fu, H. Gu, A. Huang, S.W. Or, Y. Zou, Y. Zou, et al., "Design, fabrication and properties of lightweight wear lining refractories: A review," *J. Eur. Ceram. Soc.*, vol. 42, no. 3, pp. 744–763, Mar. 2022.

[30] A. Choudhury and H. Kemmer, "Vacuum Induction Melting," in *ASM Metals HandBook Volume 15*, S. Viswanathan, D. Apelian, R. J. Donahue, B. DasGupta, M. Gywn, J. L. Jorstad, M. R. W., M. Sahoo, T. E. Prucha, and D. Twarog, Eds. ASM International, 2008, pp. 116–123.

[31] A. Choudhury, "Review State of the Art of Superalloy Production Application Using VIMIVAR or VIM/ESR for Aeros pace and Other," *ISIJ Int.*, vol. 32, no. 5, pp. 563–574, 1992.

[32] M. Moshtaghi and M. Safyari, "Effect of dwelling time in VIM furnace on chemical composition and mechanical properties of a Ni-Fe-Cr alloy," *Trans. Nonferrous Met. Soc. China*, vol. 22, no. 9, pp. 2124–2130, 2019.

[33] X. L. Guo, J. B. Yu, X. F. Li, Y. Hou, and Z. M. Ren, "Effect of nitrogen content on the microstructure and mechanical properties of a cast nickel-base superalloy," *Ironmak. Steelmak.*, vol. 45, no. 3, pp. 215–223, Mar. 2016.

[34] K. Qian, B. Chen, L. Shu, and K. Liu, "Nitrogen Solubility in Liquid Ni-V, Ni-Ta, Ni-Cr-V, and Ni-Cr-Ta Alloys," *Met. 2019, Vol. 9, Page 1184*, vol. 9, no. 11, p. 1184, Nov. 2019.

[35] R. Schlatter, "Vacuum induction melting," *JOM*, vol. 24, no. 5, pp. 17–25, Dec. 2015.

[36] E. Baake and B. Nacke, "Introduction and Fundamental Principles of Induction Melting," in *Induction Heating and Heat Treatment*, 4C ed., V. Rudnev and G. Totten, Eds. ASM International, 2014, pp. 405–415.

[37] P. Dorland, J. D. Van Wyk, and O. H. Stielau, "On the influence of coil design and electromagnetic configuration on the efficiency of an induction melting furnace," *IEEE Trans. Ind. Appl.*, vol. 36, no. 4, pp. 946–957, Jul. 2000.

[38] K. Pericleous, V. Bojarevics, G. Djambazov, R. A. Harding, and M. Wickins, "Experimental and numerical study of the cold crucible melting process," *Appl. Math. Model.*, vol. 30, no. 11, pp. 1262–1280, 2006.

[39] V. Bojarevics, K. Pericleous, R. A. Harding, and M. Wickins, "The development and experimental validation of a numerical model of an induction skull melting furnace," *Metall. Mater. Trans. B*, vol. 35, no. 4, pp. 785–803, Aug. 2004.

[40] S. Spitans, A. Jakovics, E. Baake, and B. Nacke, "Numerical Modelling of Free Surface Dynamics of Conductive Melt in the Induction Crucible Furnace," *Magnetohydrodynamics*, vol. 46, no. 4,

pp. 317–328, 2010.

[41] E. Baake, B. Nacke, F. Bernier, M. Vogt, A. Mühlbauer, and M. Blum, "Experimental and numerical investigations of the temperature field and melt flow in the induction furnace with cold crucible," *COMPEL - Int. J. Comput. Math. Electr. Electron. Eng.*, vol. 22, no. 1, pp. 88–97, 2003.

[42] J. Guo, Y. Liu, Y. Su, H. Ding, and J. Jia, "Skull formation and change during ISM process of Ti-15-3 alloy," *Trans. Nonferrous Met. Soc. China.*, vol. 10, pp. 14–18, 2000.

[43] M. Moshtaghi and S. M. Abbasi, "Effect of vacuum degree in VIM furnace on mechanical properties of Ni-Fe-Cr based alloy," *Trans. Nonferrous Met. Soc. China*, vol. 22, no. 9, pp. 2124–2130, Sep. 2012.

[44] R. A. Harding and M. Wickins, "Temperature measurements during induction skull melting of titanium aluminide," *Mater. Sci. Technol.*, vol. 19, no. 9, pp. 1235–1246, Sep. 2003.

[45] S. Fashu, M. Lototskyy, M.W. Davids, L. Pickering, V. Linkov, S. Tai, et al., "A review on crucibles for induction melting of titanium alloys," *Mater. Des.*, vol. 186, p. 108295, Jan. 2020.

[46] D. W. Gusching, "Inclusions in vacuum induction melted nickel-base alloys," The University of Arizona., 1981.

[47] W. H. Sutton, "Progress in the vacuum (VIM,VAR) melting of high performance alloys," *High Temp. Technol.*, vol. 1, no. 5, pp. 267–273, 1983.

[48] X. yong Gao, L. Zhang, X. hui Qu, X. wei Chen, and Y. feng Luan, "Effect of interaction of refractories with Ni-based superalloy on inclusions during vacuum induction melting," *Int. J. Miner. Metall. Mater.*, vol. 27, no. 11, pp. 1551–1559, Nov. 2020.

[49] R. L. Saha, T. K. Nandy, R. D. K. Misra, and K. T. Jacob, "Evaluation of the reactivity of titanium with mould materials during casting," *Bull. Mater. Sei*, vol. 12, no. 5, pp. 481–493, 1989.

[50] J. Li, H. Zhang, M. Gao, Q. Li, H. Liu, and H. Zhang, "Effect of vacuum level on the interfacial reactions between K417 superalloy and Y2O3 crucibles," *Vacuum*, vol. 182, p. 109701, Dec. 2020.

[51] S. Jansson, V. Brabie, and P. Jönsson, "Corrosion mechanism and kinetic behaviour of MgO–C refractory material in contact with CaO–Al2O3–SiO2–MgO slag," *Scand. J. Metall.*, vol. 34, no. 5, pp. 283–292, Oct. 2005.

[52] C. S. Kanetkar, A. S. Kacar, and D. Stefanescu, "The wetting characteristics and surface tension of some Ni-based alloys on yttria, hafnia, alumina, and zirconia substrates," *Metall. Trans. A*, vol. 19 A, no. 7, pp. 1833–1839, 1988.

[53] F. Valenza, M. L. Muolo, and A. Passerone, "Wetting and interactions of Ni- and Co-based superalloys with different ceramic materials," *J. Mater. Sci.*, vol. 45, no. 8, pp. 2071–2079, 2010.

[54] J. Zhu, A. Kamiya, T. Yamada, W. Shi, K. Naganuma, and K. Mukai, "Surface tension, wettability and reactivity of molten titanium in Ti/yttria-stabilized zirconia system," *Mater. Sci. Eng. A*, vol. 327, no. 2, pp. 117–127, 2002.

[55] J. P. Kuang, R. A. Harding, and J. Campbell, "Investigation into refractories as crucible and mould materials for melting and casting γ-TiAl alloys," *Mater. Sci. Technol.*, vol. 16, no. 9, pp. 1007–1016, 2013.

[56] H. Zhang, M. Gao, R. Cui, L. Ma, H. Zhang, and X. Tang, "Physical erosion of yttria crucibles in Ti–54Al alloy casting process," *J. Mater. Process. Technol.*, vol. 211, no. 12, pp. 2004–2011, Dec. 2011.

[57] A. O. Surendranathan, *An Introduction to Ceramics and Refractories*, 1st ed. CRC Press, 2014.

[58] X. Jin, L. Dong, H. Xu, L. Liu, N. Li, X. Zhang, et al., "Effects of porosity and pore size on mechanical and thermal properties as well as thermal shock fracture resistance of porous ZrB2–

SiC ceramics," *Ceram. Int.*, vol. 42, no. 7, pp. 9051–9057, May 2016.

[59] K. Makarian, S. Santhanam, and Z. N. Wing, "Thermal shock resistance of refractory composites with Zirconia and Silicon-Carbide inclusions and alumina binder," *Ceram. Int.*, vol. 44, no. 11, pp. 12055–12064, Aug. 2018.

[60] J. Wojsa, J. Podwórny, and R. Suwak, "Thermal shock resistance of magnesia-chrome refractories - Experimental and criterial evaluation," *Ceram. Int.*, vol. 39, no. 1, pp. 1–12, Jan. 2013.

[61] F. Damhof, W. A. M. Brekelmans, and M. G. D. Geers, "Predictive FEM simulation of thermal shock damage in the refractory lining of steelmaking installations," *J. Mater. Process. Technol.*, vol. 211, no. 12, pp. 2091–2105, Dec. 2011.

[62] W. Shi and B. Pinto, "Energy Savings Through Thermally Efficient Crucible Technology: Fundamentals, Process Modeling, and Applications," *JOM*, vol. 69, no. 12, p. 2797, 2017.

[63] M. M. Akiyoshi, A. L. Christoforo, A. P. Luz, and V. C. Pandolfelli, "Thermal conductivity modelling based on physical and chemical properties of refractories," *Ceram. Int.*, vol. 43, no. 6, pp. 4731–4745, 2017.

[64] J. García Ten, M. J. Orts, A. Saburit, and G. Silva, "Thermal conductivity of traditional ceramics. Part I: Influence of bulk density and firing temperature," *Ceram. Int.*, vol. 36, no. 6, pp. 1951–1959, Aug. 2010.

[65] D. S. Smith, A. Alzina, J. Bourret, B. Nait-Ali, F. Bennec, N. Tessier-Doyen, et al., "Thermal conductivity of porous materials," *J. Mater. Res.*, vol. 28, no. 17, pp. 2260–2272, Sep. 2013.

[66] E. Litovsky, T. Gambaryan-Roisman, M. Shapiro, and A. Shavit, "Heat transfer mechanisms governing thermal conductivity of porous ceramic materials," *Trends Heat, Mass Momentum Transf.*, vol. 3, no. January, pp. 147–167, 1997.

[67] J. D. Lavers, "State of the art of numerical modeling for induction processes," *COMPEL - Int. J. Comput. Math. Electr. Electron. Eng.*, vol. 27, no. 2, pp. 335–349, 2008.

[68] F. Dughiero, M. Forzan, and S. Lupi, "Solution of coupled electromagnetic and thermal problems in induction heating applications," in *1996 Third International Conference on Computation in Electromagnetics*, 1996, no. 420, pp. 301–305.

[69] C. Chaboudez, S. Ciain, R. Glardon, D. Mari, J. Rappaz, and M. Swierkosz, "Numerical modeling in induction heating for axisymmetric geometries," *IEEE Trans. Magn.*, vol. 33, no. 1, pp. 739–745, 1997.

[70] F. Bay, V. Labbe, Y. Favennec, and J. L. Chenot, "A numerical model for induction heating processes coupling electromagnetism and thermomechanics," *Int. J. Numer. Methods Eng.*, vol. 58, no. 6, pp. 839–867, Oct. 2003.

[71] M. H. Tavakoli, H. Karbaschi, and F. Samavat, "Influence of workpiece height on the induction heating process," *Math. Comput. Model.*, vol. 54, no. 1–2, pp. 50–58, Jul. 2011.

[72] M. Patil, R. Kumar Choubey, and P. Kumar Jain, "Influence of coil shapes on temperature distribution in induction heating process," *Mater. Today Proc.*, Sep. 2022.

[73] J. R. Yang, R. R. Chen, H. S. Ding, J. J. Guo, J. C. Han, and H. Z. Fu, "Thermal characteristics of induction heating in cold crucible used for directional solidification," *Appl. Therm. Eng.*, vol. 59, no. 1–2, pp. 69–76, 2013.

[74] M. Kranjc, A. Zupanic, D. Miklavcic, and T. Jarm, "Numerical analysis and thermographic investigation of induction heating," *Int. J. Heat Mass Transf.*, vol. 53, no. 17–18, pp. 3585–3591, Aug. 2010.

[75] P. A. Davidson, *An Introduction to Magnetohydrodynamics*, Cambridge University Press, 2001.

[76] M. Ščepanskis, "The Modelling of the Behaviour of Solid Inclusions in the EM Induced Recirculated Turbulent Flows of Liquid Metal," University of Latvia, 2014.

[77] E. Taberlet and Y. Fautrelle, "Turbulent stirring in an experimental induction furnace," *J. Fluid Mech.*, vol. 159, pp. 409–431, 1985.

[78] C. Vivès and R. Ricou, "Fluid flow phenomena in a single phase coreless induction furnace," *Metall. Trans. B*, vol. 16, no. 2, pp. 227–235, Jun. 1985.

[79] A. Umbrashko, "Heat and mass transfer in electromagnetically driven recirculated turbulent flows," University of Latvia, 2010.

[80] J. M. Galpin and Y. Fautrelle, "Liquid-metal flows induced by low-frequency alternating magnetic fields," *J. Fluid Mech.*, vol. 239, pp. 383–408, 1992.

[81] A. Bojarevičs, A. Cramer, Y. Gelfgat, and G. Gerbeth, "Experiments on the magnetic damping of an inductively stirred liquid metal flow," *Exp. Fluids*, vol. 40, no. 2, pp. 257–266, 2006.

[82] M. Ščepanskis, A. Jakovičs, E. Baake, and B. Nacke, "Solid inclusions in an electromagnetically induced recirculated turbulent flow: Simulation and experiment," *Int. J. Multiph. Flow*, vol. 64, pp. 19–27, Sep. 2014.

[83] N. El-Kaddah, J. Szekely, E. Taberlet, and Y. Fautrelle, "Turbulent recirculating flow in induction furnaces: A comparison of measurements with predictions over a range of operating conditions," *Metall. Trans. B*, vol. 17, no. 4, pp. 687–693, Dec. 1986.

[84] E. D. Tarapore and J. W. Evans, "Fluid velocities in induction melting furnaces: Part I. Theory and laboratory experiments," *Metall. Trans. B*, vol. 7, no. 3, pp. 343–351, Sep. 1976.

[85] V. Bojarevics, K. Pericleous, and M. Cross, "Dynamic of an axisymmetric electromagnetic 'crucible' melting," *Transf. Phenom. Magnetohydrodyn. Electroconducting Flows*, 1999.

[86] K. Pericleous, "Computing the dynamic interaction of magnetic fields and turbulent conducting fluids in metals processing," *Proc. Conf. Comput. Model. Mater. Miner. Met. Process.*, pp. 5–22, 2001.

[87] P. Buliński, J. Smołka, S. Golak, R. Przyłucki, L. Blacha, R. Białecki, et al., "Effect Of Turbulence Modelling In Numerical Analysis Of Melting Process In An Induction Furnace," *Arch. Metall. Mater.*, vol. 60, no. 3, pp. 1575–1580, Sep. 2015.

[88] E. Baake, A. Mühlbauer, A. Jakowitsch, and W. Andree, "Extension of the k-ε model for the numerical simulation of the melt flow in induction crucible furnaces," *Metall. Mater. Trans. B*, vol. 26, no. 3, pp. 529–536, May 1995.

[89] F. Felten, Y. Fautrelle, Y. Du Terrail, and O. Metais, "Numerical modelling of electromagnetically-driven turbulent flows using LES methods," *Appl. Math. Model.*, vol. 28, no. 1, pp. 15–27, Jan. 2004.

[90] M. Kirpo, "Modeling of Turbulence Properties and Particle Transport in Recirculated Flows Maksims Kirpo," University of Latvia, 2008.

[91] E. Baake, B. Nacke, A. Umbrashko, and A. Jakovics, "Large eddy simulation modeling of heat and mass transfer in turbulent recirculated flows," *Magnetohydrodynamics*, vol. 39, no. 3, pp. 291–298, 2003.

[92] F. Negrini, M. Fabbri, M. Zuccarini, E. Takeuchi, and M. Tani, "Electromagnetic control of the meniscus shape during casting in a high frequency magnetic field," *Energy Convers. Manag.*, vol. 41, no. 15, pp. 1687–1701, Oct. 2000.

[93] X. R. Zhu, R. A. Harding, and J. Campbell, "Calculation of the free surface shape in the electromagnetic processing of liquid metals," *Appl. Math. Model.*, vol. 21, no. 4, pp. 207–214, Apr. 1997.

[94] P. Buliński, J. Smołka, S. Golak, and R. Przyłucki, "Coupled numerical model of metal melting in an induction furnace: sensitivity analysis and validation of model," *Prz. Elektrotechniczny*, vol. 92, no. 3, pp. 49–52, Mar. 2016.

[95]   S. Spitans, A. Jakovics, E. Baake, and B. Nacke, "Numerical modeling of free surface dynamics of melt in an alternate electromagnetic field: Part I. Implementation and verification of model," *Metall. Mater. Trans. B Process Metall. Mater. Process. Sci.*, vol. 44, no. 3, pp. 593–605, 2013.

[96]   G. Grötzbach, "Challenges in low-Prandtl number heat transfer simulation and modelling," *Nucl. Eng. Des.*, vol. 264, pp. 41–55, 2013.

[97]   H. Abe, H. Kawamura, and Y. Matsuo, "Surface heat-flux fluctuations in a turbulent channel flow up to Reτ=1020 with Pr=0.025 and 0.71," *Int. J. Heat Fluid Flow*, vol. 25, no. 3, pp. 404–419, Jun. 2004.

[98]   X. Lei, Z. Guo, Y. Wang, and H. Li, "Assessment and improvement on the applicability of turbulent-Prandtl-number models in RANS for liquid metals," *Int. J. Therm. Sci.*, vol. 171, p. 107260, Jan. 2022.

[99]   L. Bricteux, M. Duponcheel, G. Winckelmans, I. Tiselj, and Y. Bartosiewicz, "Direct and large eddy simulation of turbulent heat transfer at very low Prandtl number: Application to lead–bismuth flows," *Nucl. Eng. Des.*, vol. 246, pp. 91–97, May 2012.

[100]   F. Roelofs, P. Planquart, and L. Koloszar, "Best practice guidelines for nuclear liquid metal CFD," in Thermal Hydraulics Aspects of Liquid Metal Cooled Nuclear Reactors, Elsevier, 2018, pp. 407–419.

[101]   A. J. Reynolds, "The prediction of turbulent Prandtl and Schmidt numbers," *Int. J. Heat Mass Transf.*, vol. 18, no. 9, pp. 1055–1069, Sep. 1975.

[102]   W. M. Kays, "Turbulent Prandtl Number—Where Are We?," *J. Heat Transfer*, vol. 116, no. 2, pp. 284–295, May 1994.

[103]   B. Weigand, J. R. Ferguson, and M. E. Crawford, "An extended Kays and Crawford turbulent Prandtl number model," *Int. J. Heat Mass Transf.*, vol. 40, no. 17, pp. 4191–4196, Oct. 1997.

[104]   M. Duponcheel, L. Bricteux, M. Manconi, G. Winckelmans, and Y. Bartosiewicz, "Assessment of RANS and improved near-wall modeling for forced convection at low Prandtl numbers based on LES up to Re s ¼ 2000," *Int. J. Heat Mass Transf.*, vol. 75, pp. 470–482, 2014.

[105]   F. Roelofs, A. Shams, I. Otic, M. Böttcher, M. Duponcheel, Y. Bartosiewicz, et al., "Status and perspective of turbulence heat transfer modelling for the industrial application of liquid metal flows," *Nucl. Eng. Des.*, vol. 290, pp. 99–106, Aug. 2015.

[106]   R. H. Nichols and C. C. Nelson, "Wall Function Boundary Conditions Including Heat Transfer and Compressibility," *AIAA J.*, vol. 42, no. 6, pp. 1107–1114, May 2012.

[107]   B. L. Smith, "Adaptation of the law of the wall boundary treatment to include volumetric heating effects," *Appl. Math. Model.*, vol. 33, no. 3, pp. 1306–1322, Mar. 2009.

[108]   D. L. McElroy, R. K. Williams, J. P. Moore, R. S. Graves, and F. J. Weaver, "The Physical Properties of Inconel Alloy 718 from 300 to 1000 K," in *Thermal Conductivity 15*, Springer US, 1978, pp. 149–151.

[109]   G. Pottlacher, H. Hosaeus, E. Kaschnitz, and A. Seifter, "Thermophysical properties of solid and liquid Inconel 718 Alloy," *Scand. J. Metall.*, vol. 31, no. 3, pp. 161–168, Jun. 2002.

[110]   D. Basak, R. A. Overfelt, and D. Wang, "Measurement of specific heat capacity and electrical resistivity of industrial alloys using pulse heating techniques," *Int. J. Thermophys.*, vol. 24, no. 6, pp. 1721–1733, Nov. 2003.

[111]   S. H. Lee, S. W. Kim, and K. H. Kang, "Effect of heat treatment on the specific heat capacity of nickel-based alloys," *Int. J. Thermophys.*, vol. 27, no. 1, pp. 282–292, Jan. 2006.

[112]   A. S. Agazhanov, D. A. Samoshkin, and Y. M. Kozlovskii, "Thermophysical properties of Inconel 718 alloy," in *XXXV Siberian Thermophysical Seminar Journal of Physics: Conference Series*, 2019, vol. 1382, p. 12175.

[113] R. A. Overfelt, C. A. Matlock, and M. E. Wells, "Viscosity of superalloy 718 by the oscillating vessel technique," *Metall. Mater. Trans. B*, vol. 27, no. 4, pp. 698–701, Aug. 1996.

[114] R. F. Brooks, A. P. Day, R. J. L. Andon, L. A. Chapman, K. C. Mills, and P. N. Quested, "Measurement of viscosities of metals and alloys with an oscillating viscometer," *High Temp. - High Press.*, vol. 33, no. 1, pp. 73–82, 2001.

[115] H. Hosaeus, A. Seifter, E. Kaschnitz, and G. Pottlacher, "Thermophysical properties of solid and liquid Inconel 718 alloy," *High Temp. - High Press.*, vol. 33, no. 4, pp. 405–410, 2001.

[116] H. P. Wang, C. H. Zheng, P. F. Zou, S. J. Yang, L. Hu, and B. Wei, "Density determination and simulation of Inconel 718 alloy at normal and metastable liquid states," *J. Mater. Sci. Technol.*, vol. 34, no. 3, pp. 436–439, 2018.

[117] K. C. Mills, *Recommended values of thermophysical properties for selected commercial alloys*. Woodhead Publishing, 2002.

[118] J. O'Flynn, C. A. Whitman, and S. F. Corbin, "Thermal property measurements of metal injection moulded Inconel 625 and Inconel 718 using combined thermal analysis techniques," *Powder Metall.*, vol. 63, no. 4, pp. 277–287, Aug. 2020.

[119] D. Vitiello, B. Nait-Ali, N. Tessier-Doyen, T. Tonnesen, L. Laím, L. Rebouillat, et al., "Thermal conductivity of insulating refractory materials: Comparison of steady-state and transient measurement methods," *Open Ceram.*, vol. 6, p. 100118, Jun. 2021.

[120] M. Leitner, T. Leitner, A. Schmon, K. Aziz, and G. Pottlacher, "Thermophysical Properties of Liquid Aluminum," *Metall. Mater. Trans. A Phys. Metall. Mater. Sci.*, vol. 48, no. 6, pp. 3036–3045, Jun. 2017.

[121] S. G. Teodorescu, R. A. Overfelt, and S. I. Bakhtiyarov, "An Inductive Technique for Electrical Conductivity Measurements on Molten Metals 1," *Int. J. Thermophys.*, vol. 22, no. 5, pp. 1521–1535, 2001.

[122] B. P. Keller, S. E. Nelson, K. L. Walton, T. K. Ghosh, R. V. Tompson, and S. K. Loyalka, "Total hemispherical emissivity of Inconel 718," *Nucl. Eng. Des.*, vol. 287, pp. 11–18, 2015.

[123] L. del Campo, R.B. Pérez-Sáez, L. González,-Férnandez, X. Esquisabel, I. Férnandez, P. González-Martín, et al., "Emissivity measurements on aeronautical alloys," *J. Alloys Compd.*, vol. 489, no. 2, pp. 482–487, Jan. 2010.

[124] X. Chamorro, N. Herrero-Dorca, D. Bernal, and I. Hurtado, "Induction Skull Melting of Ti-6Al-4V: Process Control and Efficiency Optimization," *Metals (Basel).*, vol. 9, no. 5, p. 539, May 2019.

[125] P. Garcia-Michelena, X. Chamorro, N. Herrero-Dorca, D. Bernal, I. Hurtado, E. Ruiz-Reina, et al., "Effect of the crucible composition on the Inconel 718 vacuum induction melting process efficiency," *J. Mater. Res. Technol.*, Feb. 2023.

[126] T. R. Steiner, "High temperature steady-state experiment for computational radiative heat transfer validation using COMSOL and ANSYS," *Results Eng.*, vol. 13, p. 100354, Mar. 2022.

[127] H. K. Versteeg and W. Malalasekera, *An Introduction to Computational Fluid Dynamics*, 2nd ed. Essex, England: Pearson Education Limited, 2007.

[128] D. C. Wilcox, *Turbulence Modeling for CFD, Volume 1*. DCW industries, 2006.

[129] K. Abe, T. Kondoh, and Y. Nagano, "A new turbulence model for predicting fluid flow and heat transfer in separating and reattaching flows—I. Flow field calculations," *Int. J. Heat Mass Transf.*, vol. 37, no. 1, pp. 139–151, Jan. 1994.

[130] M. A. Sainz, A. D. Mazzoni, E. F. Aglietti, and A. Caballero, "Thermochemical stability of spinel (MgO·Al2O3) under strong reducing conditions," *Mater. Chem. Phys.*, vol. 86, no. 2–3, pp. 399–408, Aug. 2004.

Appendix 1. View factor and surface-to-surface radiation

The irradiance received by a surface (a) emitted by another surface (b) can be defined as $G_{a,b}A_a = F_{ba}A_b J_b$ where $F_{a,b}$ is the view factor from surface b to a.

$$F_{a,b} = \frac{1}{A_a}\int_{A_a}\int_{A_b} \frac{\cos\theta_a \cos\theta_b}{\pi D_{ab}^2}\,dA_a dA_b \tag{1}$$

Where D_{ab} is the distance from the surface A to B and $\cos\theta$ the angle of separation between the normal vector of surface A to B. This way, the irradiance of the surface (G_a) is the sum of the radiation energy from other surfaces:

$$G_a = \sum_{b=1}^{N} \frac{F_{ba}A_b J_b}{A_a} \tag{2}$$

This can be simplified by considering the reciprocity relation among the view factors $F_{ba}A_b = F_{ab}A_a$ and by substituting the irradiance into the radiosity equation, derives into:

$$J_a = (1-\epsilon)\sum_{b=1}^{N} F_{ab}A_a + \epsilon\, e_b(T) \tag{3}$$

Once defined, the radiosity of a surface is the difference between irradiation and outgoing radiation that gives the heat radiation at the surface $\mathbf{q_r} = A_a(J_a - G_a)$ and the irradiance can be eliminated by employing the above-presented equation for the radiosity:

$$q_r = \frac{A_a \epsilon_a}{1-\epsilon} - (n^2 \sigma_{SB} T_a^4 - J_a) \tag{4}$$

Appendix 2.a $k-\varepsilon$ turbulence model

The standard $k-\varepsilon$ turbulence model introduces two additional transport equations and two dependent variables; the turbulent kinetic energy k and the dissipation rate ε. The following equations are the ones implemented in the model of COMSOL Multiphysics®.

The transport equations for k read:

$$\rho\frac{\partial k}{\partial t} + \rho\mathbf{u}\cdot\nabla k = \nabla\cdot\left(\left(\mu + \frac{\mu_T}{\sigma_k}\right)\nabla k\right) + P_k - \rho\varepsilon \tag{5}$$

While the turbulent production rate P_k is defined as:

$$P_k = \mu_T\left((\nabla\mathbf{u}:(\nabla\mathbf{u}+\nabla\mathbf{u}^T)) - \frac{2}{3}(\nabla\cdot\mathbf{u})^2\right) - \frac{2}{3}\rho k\nabla\cdot\mathbf{u} \tag{6}$$

And the transport equation of ε reads:

$$\rho\frac{\partial\varepsilon}{\partial t} + \rho\mathbf{u}\cdot\nabla\varepsilon = \nabla\cdot\left(\left(\mu + \frac{\mu_T}{\sigma_\varepsilon}\right)\nabla\varepsilon\right) + C_{\varepsilon 1}\frac{\varepsilon}{k}P_k - C_{\varepsilon 2}\rho\frac{\varepsilon^2}{k} \tag{7}$$

The turbulent viscosity is derived from k and ε with the following relation;

$$\mu_T = \rho C_\mu \frac{k^2}{\varepsilon} \tag{8}$$

The constants σ_k, σ_ε, $C_{\varepsilon 1}$, $C_{\varepsilon 1}$ and C_μ to close are the standard values of $k - \varepsilon$ formulation [128]

$$\sigma_k = 1.0 \; ; \; \sigma_\varepsilon = 1.3 \; ; \; C_{\varepsilon 1} = 1.44 \; ; \; C_{\varepsilon 2} = 1.92 \; ; \; C_\mu = 0.09 \tag{9}$$

Wall functions

The analytical expression that describes the flow near the wall implemented in COMSOL Multiphysics is the following ones. The theoretical lift-off from the wall expressed in viscous units is defined as:

$$\delta_w^+ = \max(\frac{h}{2}\frac{\rho C_\mu^{\frac{1}{4}}\sqrt{k}}{\mu}, 11.06) \tag{10}$$

The first argument derives from the law of the wall, while the second is the distance from the wall where the logarithmic layer meets the viscous sublayer.

The wall lift-off, δ_w, is defined as

$$\delta_w = \frac{\delta_w^+ \mu}{\rho u_\tau} \tag{11}$$

Where the friction velocity is u_τ is given by;

$$u_\tau = \max(C_\mu^{\frac{1}{4}}\sqrt{k}, \frac{\|u\|}{u^+} \tag{12}$$

$$u^+ = \frac{1}{k_v \log(\delta_w^+)} + B \tag{13}$$

Where k_v is the von Kárman constant (default 0.41), and B is a constant 5.2.

For a no-penetration boundary condition $\mathbf{u} \cdot \mathbf{n} = 0$ a shear stress condition

$$\mathbf{n} \cdot \mathbf{K} - (\mathbf{n} \cdot \mathbf{K} \cdot \mathbf{n})\mathbf{n} = -\rho u_\tau \frac{\mathbf{u}}{u^+} \tag{14}$$

Where $\mathbf{K}$ is the viscous stress tensor:

$$\mathbf{K} = \mu(\nabla \mathbf{u} + (\nabla \mathbf{u})^T \tag{15}$$

The turbulent kinetic energy is given by $\mathbf{n} \cdot \nabla k = 0$, and the boundary condition for ε reads:

$$\varepsilon = \frac{C_\mu^{\frac{3}{4}}k^{\frac{3}{2}}}{k_v \delta_w} \tag{16}$$

Appendix 2.b. Low Reynolds number $k - \varepsilon$ model

The low Reynolds number models adapt the turbulence transport equation introducing damping functions. In this case, the AKN model has been adopted, which for a compressible the k and ε reads as:

$$\rho \frac{\partial k}{\partial t} + \rho \mathbf{u} \cdot \nabla k = \nabla \cdot \left(\left(\mu + \frac{\mu_T}{\sigma_k} \right) \nabla k \right) + P_k - \rho \varepsilon \tag{17}$$

$$\rho \frac{\partial \varepsilon}{\partial t} + \rho \mathbf{u} \cdot \nabla \varepsilon = \nabla \cdot \left(\left(\mu + \frac{\mu_T}{\sigma_\varepsilon} \right) \nabla \varepsilon \right) + C_{\varepsilon 1} \frac{\varepsilon}{k} P_k - C_{\varepsilon 2} \rho \frac{\varepsilon^2}{k} \tag{18}$$

Where the production rate P_k is written as:

$$P_k = \mu_T \left((\nabla \mathbf{u} : (\nabla \mathbf{u} + \nabla \mathbf{u}^T)) - \frac{2}{3} (\nabla \cdot \mathbf{u})^2 \right) - \frac{2}{3} \rho k \nabla \cdot \mathbf{u} \tag{19}$$

The principle modification with the standard $k - \varepsilon$ is introduced with the turbulent viscosity term.

$$\mu_T = \rho f_\mu C_\mu \frac{k^2}{\varepsilon} \tag{20}$$

While the damping functions, f_μ and f_ε reads and additional functions are introduced

$$f_\mu = \left(1 - e^{-\frac{l^*}{14}} \right)^2 \cdot \left(1 + \frac{5}{R_t^{3/4}} e^{\left(-\frac{R_t}{200} \right)^2} \right) \tag{21}$$

$$f_\varepsilon = \left(1 - e^{-\frac{l^*}{3.1}} \right)^2 \cdot \left(1 + 0.3 e^{\left(-\frac{R_t}{6.5} \right)^2} \right) \tag{22}$$

$$l^* = \frac{(\rho u_\varepsilon l_w)}{\mu} ; R_t = \frac{\rho k^2}{\mu \varepsilon} ; \mu_\varepsilon = \left(\frac{\mu \varepsilon}{\rho} \right)^{\frac{1}{4}} \tag{23}$$

While the constants of the model are given by:

$$\sigma_k = 1.4 ; \sigma_\varepsilon = 1.4 ; C_{\varepsilon 1} = 1.5 ; C_{\varepsilon 2} = 1.92 ; C_\mu = 0.09 \tag{24}$$

Low Reynolds Number Wall Treatment

The no-slip condition $\mathbf{u} = 0$ is set due to the damping term for the k and ε. Since all the velocities have to be dissipated on the wall $k = 0$ is imposed on the wall. While for the ε the next analytical relation is computed

$$\varepsilon = 2 \frac{\mu}{\rho} \frac{k}{l_w^2} \tag{25}$$

ERRATA SHEET

Reads now	**Should be**
Page i	**Page i**
Enhancement of Vacuum Induction Melting trough Numerical and Experimental Investigation	Enhancement of Vacuum Induction Melting through Numerical and Experimental Investigation
Page 2	**Page 2**
iii. Improve accuracy and reduce uncertainty trough experimental validation of theoretical results in a laboratory-scale facility.	iii. Improve accuracy and reduce uncertainty through experimental validation of theoretical results in a laboratory-scale facility.
Page 31	**Page 31**
input for the numerical models developed in Chapter ¡Error! No se encuentra el origen de la referencia.. ¡Error! No se encuentra el origen de la referencia..	input for the numerical models developed in Chapter 4. Numerical modeling.
Page 48	**Page 48**
simulation of Chapter ¡Error! No se encuentra el origen de la referencia.. ¡Error! No se encuentra el origen de la referencia. for preliminary and validation simulations	simulation of Chapter. 4 Numerical modeling, for preliminary and validation simulations
Page 78	**Page 78**
the crucible works as a thermal insulator with a rapid temperature reduction trough the	the crucible works as a thermal insulator with a rapid temperature reduction through the
Page 131	**Page 131**
J. Mater. Res. Technol., Feb. 2023	*J. Mater. Res. Technol.*, vol. 23, pp. 3351–3361, Mar. 2023.